
Fast and faithful Effective One Body models for gravitational waves from generic compact binaries

DISSERTATION

zur Erlangung des akademischen Grades
doctor rerum naturalium (Dr. rer. nat.)



vorgelegt dem Rat der

PHYSIKALISCH-ASTRONOMISCHEN FAKULTÄT

der

FRIEDRICH-SCHILLER-UNIVERSITÄT JENA

von

Rossella GAMBÀ (M.Sc.)

geboren am 12.12.1995 in Borgomanero (Italien)

REVIEWERS:

1. PROF. DR. SEBASTIANO BERNUZZI (FRIEDRICH-SCHILLER-UNIVERSITÄT JENA)
2. PROF. DR. EMANUELE BERTI (JOHNS HOPKINS UNIVERSITY)
3. PROF. DR. MARK HANNAM (CARDIFF UNIVERSITY)

DEFENSE DATE: 25.09.23

Declaration of Authorship

Ich erkläre hiermit ehrenwörtlich, dass ich die vorliegende Arbeit selbständig, ohne unzulässige Hilfe Dritter und ohne Benutzung anderer als der angegebenen Hilfsmittel und Literatur angefertigt habe. Die aus anderen Quellen direkt oder indirekt übernommenen Daten und Konzepte sind unter Angabe der Quelle gekennzeichnet.

Bei der Auswahl und Auswertung folgenden Materials haben mir die nachstehend aufgeführten Personen in der jeweils beschriebenen Weise unentgeltlich geholfen:

1. Prof. Sebastiano Bernuzzi
2. Dr. Alessandro Nagar
3. Dr. Sarp Akcay
4. Dr. Matteo Breschi

Weitere Personen waren an der inhaltlich-materiellen Erstellung der vorliegenden Arbeit nicht beteiligt. Insbesondere habe ich hierfür nicht die entgeltliche Hilfe von Vermittlungs- bzw. Beratungsdiensten (Promotionsberater oder andere Personen) in Anspruch genommen.

Niemand hat von mir unmittelbar oder mittelbar geldwerte Leistungen für Arbeiten erhalten, die im Zusammenhang mit dem Inhalt der vorgelegten Dissertation stehen.

Die Arbeit wurde bisher weder im In- noch im Ausland in gleicher oder ähnlicher Form einer anderen Prüfungsbehörde vorgelegt.

Die geltende Promotionsordnung der Physikalisch-Astronomischen Fakultät ist mir bekannt.

Ich versichere ehrenwörtlich, dass ich nach bestem Wissen die reine Wahrheit gesagt und nichts verschwiegen habe.

Ort, Datum

Unterschrift

Acknowledgements

As is customary, I would like to commence this dissertation by expressing my heartfelt gratitude to the numerous individuals who have accompanied me on this journey.

First and foremost, I want to thank my mentor, Prof. Sebastiano Bernuzzi, for his unwavering support and guidance throughout my academic career. His encouragement and constructive feedback have been instrumental in my growth and development as a researcher. I am also deeply indebted to Dr. Alessandro Nagar, who introduced me to the captivating world of Gravitational Waves and patiently guided me at the outset of my career.

I am immensely grateful to my colleagues, past and present, Matteo Breschi, Francesco Zappa, Alejandra Gonzalez, Sarp Akcay, Ssohrab Borhanian, Piero Rettegno, Simone Albanesi, and Gregorio Carullo, for their invaluable friendship and helpful advice. Additionally, I wish to thank the members of the CORE Collaboration, the Prometeo-Virgo group, the *Extreme matter* and *Waveform* subgroups of the *CBC* group of LIGO-Virgo-Kagra Collaboration (LVK), and the DFG-RTG *Physik Combo* group for their insightful discussions and contributions.

I am deeply thankful to my friends and family, who have been a constant source of encouragement and inspiration. Similarly, I owe boundless gratitude to my boyfriend Nicolò and my parents Cristina and Mario, for their enduring love and support, which sustained me through the toughest times of this journey. Thank you for always being there for me, no matter how far.

I gratefully acknowledge support by the EU H2020 under ERC Starting Grant, no. BinGraSp-714626 and from the Deutsche Forschungsgemeinschaft (DFG) under Grant No. 406116891 within the Research Training Group (RTG) 2522/1. The computational experiments were mainly performed on the ARA cluster at the Friedrich-Schiller-Universität Jena supported in part by DFG grants INST 275/334-1 FUGG and INST 275/363-1 FUGG and ERC Starting Grant, no. BinGraSp-714626. This research has made use of data obtained from the Gravitational Wave Open Science Center (GWOSC) [1, 2], a service of LVK. LIGO is funded by the U.S. National Science Foundation. Virgo is funded by the French Centre National de Recherche

Scientifique (CNRS), the Italian Istituto Nazionale della Fisica Nucleare (INFN) and the Dutch Nikhef, with contributions by Polish and Hungarian institutes. KAGRA is funded by Japanese National Research Foundation, with contributions by Korean and Taiwanese institutes.

Abstract

Rossella GAMBA

Fast and faithful Effective One Body models for gravitational waves from generic compact binaries

The detection and analysis of Gravitational-waves (GWs) from compact binary systems relies on accurate modeling of the expected signals emitted by such sources. In this *Thesis* we develop computationally efficient yet accurate models for coalescing binary black holes (BBHs) and binary neutron stars (BNSs), relying on the effective-one-body (EOB) framework as implemented in the `TEOBResumS` family of models. Building on its multipolar aligned-spin avatar, we improve `TEOBResumS` to include the description of spins precession via an efficient hybrid post-Newtonian (PN)-EOB scheme, thus obtaining a new state-of-the-art inspiral-merger-ringdown (IMR) model for BBHs and the first multipolar precessing model for coalescing BNSs. We validate our model in terms of numerical relativity (NR) faithfulness, finding that `TEOBResumS` agrees to more than 97% with NR results over a considerable portion of the parameter space. Its efficiency is demonstrated by directly employing the model in the parameter estimation (PE) of a handful of events detected by the LVK collaboration (GW150914, GW190412 and GW170817) without the need of surrogates or reduced models. Employing a flavor of `TEOBResumS` able to model the evolution of systems coalescing along non-circular trajectories, we then study the phenomenology of the GWs that are produced by systems merging along initially unbound orbits. After comparing our waveforms with a set of highly eccentric NR simulations, we analyze GW190521 under the hypothesis that it originated from a dynamical capture of two black holes (BHs). Our results suggest that GW190521 may be the the first detected GW signal to correspond to such a system. Finally, we refine the `TEOBResumS` description of matter effects: after critically assessing the importance of resonant tidal effects for quasi-circular and eccentric BNS mergers, we considerably improve the model performance by including high-order PN information and few NR-informed parameters.

Zusammenfassung

Rossella GAMBA

*Schnelle und genaue Effektive Ein-Körper-Modelle für
Gravitationswellen von generischen kompakten binären*

Der Nachweis und die Analyse von Gravitational-waves (GWs) aus kompakten Doppelsternsystemen hängt ab von einer genauen Modellierung der erwarteten Signale, die von solchen Quellen ausgesendet werden. In dieser *Thesis* entwickeln wir rechnerisch effiziente und dennoch genaue Modelle für die Koaleszenz von binary black holes (BBHs) und binary neutron stars (BNSs), wobei wir uns auf das effective-one-body (EOB)-Rahmenwerk stützen, das in der `TEOBResumS`-Modellfamilie implementiert ist. Aufbauend auf dem multipolaren Modell für ausgerichtete Spins verbessern wir `TEOBResumS`, um die Beschreibung der Präzessionsbewegung der Spins durch ein effizientes hybrides post-Newtonian (PN)-EOB-Schema, wodurch wir ein neues hochmodernes inspiral-merger-ringdown (IMR)-Modell für BBHs und das erste multipolare Präzessionsmodell für koaleszierende BNSs erhalten. Wir validieren unser Modell im Hinblick auf die numerical relativity (NR)-Treue und stellen fest, dass `TEOBResumS` in einem beträchtlichen Teil des Parameterraums zu mehr als 97% mit den NR-Ergebnissen übereinstimmt. Seine Effizienz wird durch die direkte Anwendung des Modells auf die parameter estimation (PE) einer Handvoll von Ereignissen, die von der LIGO-Virgo-Kagra Collaboration (LVK)-Kollaboration entdeckt wurden (GW150914, GW190412 und GW170817), ohne die Notwendigkeit von Surrogaten oder reduzierten Modellen. Unter Verwendung einer Variante von `TEOBResumS`, die in der Lage ist, die Entwicklung von Systemen zu modellieren, die entlang nicht-kreisförmiger Trajektorien koaleszieren, untersuchen wir die Phänomenologie von GWs, die von Systemen erzeugt werden, die entlang ursprünglich ungebundener Bahnen verschmelzen. Nach dem Vergleich unserer Wellenformen mit einer Reihe von hochexzentrischen NR-Simulationen analysieren wir GW190521 unter der Hypothese, dass er aus einem dynamischen Einfang von zwei black holes (BHs) entstanden ist. Unsere Ergebnisse legen nahe, dass GW190521 das erste entdeckte GW-Signal sein könnte, das einem

solchen System entspricht. Schließlich verfeinern wir die `TEOBResumS`-Beschreibung von Materieeffekten: Nach einer kritischen Bewertung der Bedeutung von resonanten Gezeiteneffekten für quasi-kreisförmige und exzentrische BNS-Verschmelzungen kritisch bewertet, verbessern wir die Leistung des Modells erheblich, indem wir PN-Informationen hoher Ordnung und wenige NR-informierte Parameter.

Published content and contributions

Publications as leading author

For each of the following manuscripts, I contributed to the drafting of the entire text, the production of all figures and tables, the production of all results, the implementation and the development of all computational methods.

1. **Gamba, Rossella** and Sebastiano Bernuzzi.
Resonant tides in binary neutron star mergers: analytical-numerical relativity study. 7 2022, <https://arxiv.org/abs/2207.13106>
2. **Gamba, Rossella**, Sarp Akçay, Sebastiano Bernuzzi, and Jake Williams.
Effective-one-body waveforms for precessing coalescing compact binaries with post-Newtonian twist.
Phys. Rev. D, 106(2):024020, 2022.
3. **Gamba, Rossella**, Matteo Breschi, Gregorio Carullo, Piero Rettengo, Simone Albanesi, Sebastiano Bernuzzi, and Alessandro Nagar.
GW190521: A dynamical capture of two black holes.
Accepted in Nature Astronomy, 6 2021.
4. **Gamba, Rossella**, Sebastiano Bernuzzi, and Alessandro Nagar. Fast, faithful, frequency-domain effective-one-body waveforms for compact binary coalescences.
Phys. Rev. D, 104(8):084058, 2021.
5. **Gamba, Rossella**, Matteo Breschi, Sebastiano Bernuzzi, Michalis Agathos, and Alessandro Nagar.
Waveform systematics in the gravitational-wave inference of tidal parameters and equation of state from binary neutron star signals.
Phys. Rev. D, 103(12):124015, 2021.

Publications as coauthor

1. Jacopo Tissino, Gregorio Carullo, Matteo Breschi, **Gamba, Rossella**, Stefano Schmidt, and Sebastiano Bernuzzi.
Combining effective-one-body accuracy and reduced-order-quadrature speed for binary neutron star merger parameter estimation with machine learning.
10 2022, <https://arxiv.org/abs/2210.15684>
Contributions: Wrote the text in Sections I and V, helped with the implementation of TEOBResumSPA.
2. Alice Bonino, **Gamba, Rossella**, Patricia Schmidt, Alessandro Nagar, Geraint Pratten, Matteo Breschi, Piero Rettengo, and Sebastiano Bernuzzi.
Inferring eccentricity evolution from observations of coalescing binary black holes.
7 2022, <https://arxiv.org/abs/2207.10474>
Contributions: Wrote or edited all sections, helped with the setup of the PE runs, ideated the study.
3. Matteo Breschi, **Gamba, Rossella**, Ssohrab Borhanian, Gregorio Carullo, and Sebastiano Bernuzzi.
Kilohertz Gravitational Waves from Binary Neutron Star Mergers: Inference of Postmerger Signals with the Einstein Telescope.
5 2022, <https://arxiv.org/abs/2205.09979>
Contributions: Produced the posterior distributions for some of the binaries analyzed in Section IV.
4. Angelica Albertini, Alessandro Nagar, Piero Rettengo, Simone Albanesi, and **Gamba, Rossella**.
Waveforms and fluxes: Towards a self-consistent effective one body waveform model for nonprecessing, coalescing black-hole binaries for third generation detectors.
Phys. Rev. D, 105(8):084025, 2022.
Contributions: Produced the data behind Fig. 15 and Fig. 16, edited the text.
5. Gunnar Riemenschneider, Piero Rettengo, Matteo Breschi, Angelica Albertini, **Gamba, Rossella**, Sebastiano Bernuzzi, and Alessandro Nagar.
Assessment of consistent next-to-quasicircular corrections and postadiabatic approximation in effective-one-body multipolar waveforms for binary black hole coalescences.

- Phys. Rev. D*, 104(10):104045, 2021.
Contributions: Wrote the script for Fig. 7, edited the text.
6. Matteo Breschi, **Gamba, Rossella**, and Sebastiano Bernuzzi.
 Bayesian inference of multimessenger astrophysical data: Methods and applications to gravitational waves.
Phys. Rev. D, 104(4):042001, 2021.
Contributions: Wrote part of the text for Section IV D, helped with the implementation of TEOBResumS within `bajes`.
 7. Daniel A. Godzieba, **Gamba, Rossella**, David Radice, and Sebastiano Bernuzzi.
 Updated universal relations for tidal deformabilities of neutron stars from phenomenological equations of state.
Phys. Rev. D, 103(6):063036, 2021.
Contributions: Wrote Section V, produced Fig. 12 and Fig. 13.
 8. Stefano Schmidt, Matteo Breschi, **Gamba, Rossella**, Giulia Pagano, Piero Rettengo, Gunnar Riemenschneider, Sebastiano Bernuzzi, Alessandro Nagar, and Walter Del Pozzo.
 Machine Learning Gravitational Waves from Binary Black Hole Mergers.
Phys. Rev. D, 103(4):043020, 2021.
Contributions: Helped with the implementation of TEOBResumS.
 9. Alessandro Nagar, Piero Rettengo, **Gamba, Rossella**, and Sebastiano Bernuzzi.
 Effective-one-body waveforms from dynamical captures in black hole binaries.
Phys. Rev. D, 103(6):064013, 2021.
Contributions: Wrote or edited Sections II and III, produced Fig. 2 and Fig. 5.
 10. Sarp Akcay, **Gamba, Rossella**, and Sebastiano Bernuzzi.
 Hybrid post-Newtonian effective-one-body scheme for spin-precessing compact-binary waveforms up to merger.
Phys. Rev. D, 103(2):024014, 2021.
Contributions: Provided scripts for generating SEOB and PhenomPv3 waveforms, provided scripts for mismatch computations.
 11. Alessandro Nagar, Geraint Pratten, Gunnar Riemenschneider, and **Gamba, Rossella**.
 Multipolar effective one body model for nonspinning black hole binaries.

Phys. Rev. D, 101(2):024041, 2020.

Contributions: Provided the SEOB data behind Fig. 6.

Publications with LIGO-Virgo-KAGRA Collaboration

1. B. P. Abbott *et al.*, “GW190425: Observation of a Compact Binary Coalescence with Total Mass $\sim 3.4M_{\odot}$,” *Astrophys. J. Lett.*, 892 (2020) no.1, L3.

Contributions: Text and results of Section 4.1 and, part of the text of Appendix D, text and results of Appendix E

Talks and seminars

1. University of Barcelona (UB), 2022: **invited** talk on “TEOBResumS, an advanced waveform model for O4”;
2. University of Illinois-Urbana Champaign (UIUC), 2022: seminar on “Modeling the full spectrum of gravitational waves from binary neutron stars”;
3. Penn State University (PSU), 2022: seminar on “Gravitational waves from binary neutron stars”;
4. PAX VIII (MIT), 2022: **invited** panelist for the Waveform Modeling session;
5. PHAROS (Rome), 2022: **invited** talk on “Gravitational waves from binary neutron stars”;
6. DPG (Heidelberg), 2022: short talk on “The interpretation of GW190521 as a dynamical capture of two binary black holes”;
7. National Autonomous University of Mexico (UNAM), 2021: seminar on “The interpretation of GW190521 as a dynamical capture of two binary black holes”;
8. IPAM (UCLA), 2021: **invited** lecture on waveform systematics for binary neutron star signals;
9. La Sapienza (Rome), 2020: seminar on waveform systematics for binary neutron star signals;
10. University College Dublin (UCD), 2020: seminar on waveform systematics for binary neutron star signals;

11. H2020 (Austria), 2020: **invited** talk on the impact of the crust equation of state on the analysis of GW170817 and waveform systematics;

List of Acronyms

ADM	Arnowitt-Deser-Misner	BBH	Binary black hole
BH	Black hole	BNS	Binary neutron star
BF	Bayes' factor	CBC	Compact binary coalescence
CE	Cosmic Explorer	EFE	Einstein field equations
EM	Electromagnetic	EOB	Effective-one-body
EOM	Equations of motion	EOS	Equation of state
ET	Einstein Telescope	FD	Frequency domain
FFT	Fast Fourier transform	GR	General relativity
GSF	Gravitational Self Force	GW	Gravitational-wave
HM	Higher mode	IFO	Interferometer
IMBH	Intermediate-mass black hole	IMR	Inspiral-merger-ringdown
LIGO	Laser Interferometer Gravitational-Wave Observatory	LO	Leading Order
LSO	Last Stable Orbit	LVK	LIGO-Virgo-KAGRA
MCMC	Markov-chain Monte Carlo	NG	Next-generation
NQC	Next-to-quasicircular corrections	NLO	next-to LO
NNLO	next-to-next-to LO	NR	Numerical relativity
NS	Neutron star	ODE	Ordinary Differential Equation
PE	Parameter estimation	PM	Post-Minkowskian
PN	Post-Newtonian	PP	Point-particle
PSD	Power spectral density	QNM	Quasi-normal mode
ROQ	Reduced-order-quadrature	SNR	Signal-to-noise ratio
SPA	Stationary-Phase Approximation	SXS	Simulating eXtreme Spacetimes
TD	Time domain	TOV	Tolman-Oppenheimer-Volkoff

List of Constants

Name	Symbol = Value
Pi	$\pi = 3.14159265358979 \dots$
Euler's number	$e = 2.71828182845904 \dots$
Speed of light	$c = 299792458 \text{ m s}^{-1}$
Universal gravitational constant	$G = 6.674 \times 10^{-11} \text{ m}^3 \text{ kg}^{-1} \text{ s}^{-2}$
Solar mass	$M_{\odot} = 1.98847 \times 10^{30} \text{ kg}$

Contents

Declaration of Authorship	i
Acknowledgements	ii
List of Acronyms	xii
List of Constants	xiii
Contents	1
Introduction	3
1 TEOBResumS-GIOTTO	11
1.1 Hamiltonian	12
1.2 Dynamics, radiation and inspiral waveform	15
1.3 Merger-ringdown completion	16
1.4 Acceleration techniques	18
1.5 Validating an EOB model	20
2 Hybrid PN-EOB model for generic spins binaries	24
2.1 Twist and Reference frames	25
2.2 Spin dynamics	27
2.2.1 Time evolution of the orbital frequency	27
2.2.2 Coupling of the PN spin evolution to the EOB dynamics	28
2.2.3 BBH Merger-Ringdown	29
2.2.4 BNS Frequency-domain waveforms	30
2.3 Validation	32
2.3.1 Faithfulness	32
2.3.2 BBH IMR EOB/NR comparison	34
2.3.3 Comparison with NRSur7dq4	40
2.3.4 Waveform’s timing evaluation	41

2.4	Parameter estimation	41
2.4.1	GW150914	41
2.4.2	GW190412	42
2.4.3	GW170817	43
3	TEOBResumS-DALÍ: an EOB model for non-circularized systems	44
3.1	An EOB model for dynamical captures	45
3.1.1	Phenomenology of hyperbolic mergers	47
3.1.2	Validation of the model	50
3.2	GW190521	54
4	Matter effects in GWs: resonant tides and NR information	62
4.1	Resonant tides	64
4.1.1	Effective Love number model	67
4.1.2	Comparison with numerical-relativity data	69
4.1.3	Model selection on GW170817	75
4.2	A new tidal model for TEOBResumS	77
4.2.1	EOB Tidal model	77
4.2.2	Effect of the analytical information	82
4.2.3	Numerically informing the model	84
4.2.4	EOB/NR comparisons	87
4.3	Closed form representation of tidal sector	89
4.3.1	Phase	90
4.3.2	Amplitude	92
4.3.3	Validation	93
	Conclusions	96
A	Waveform Systematics for BNS systems	100
A.1	Faithfulness of Numerical Relativity waveforms	103
	Bibliography	106

Introduction

Gravitational-waves (GWs), predicted by Albert Einstein’s theory of general relativity (GR) in 1916 [3], have been the subject of intense research for more than a century. The first indirect evidence of their existence came in 1974 with the discovery of the Hulse-Taylor pulsar [4, 5]. This binary system, consisting of two neutron stars (NSs), provided strong support for the existence of GWs [6, 7] and validated the predictions of GR. It was not until 2015 that the Laser Interferometer Gravitational-Wave Observatory (LIGO) directly detected the gravitational waves emitted by two merging black holes (BHs) [8]. This detection ushered in a new era of astronomy, demonstrating that GWs can provide a unique way of studying some of the most violent events in the universe, events that could not be observed through traditional telescopes. Since the first historical detection, GW astronomy has produced a wealth of discoveries, thanks to the combined contributions of LIGO and the European interferometer Virgo [9]. At the time of writing this dissertation, the two observatories had confidently detected about 90 binary black hole (BBH) systems [10, 11], two binary neutron star (BNS) systems [12–14] and two mixed black hole-neutron star (BHNS) binaries [15]. These detections have provided new insights into the astrophysical processes that govern the evolution of compact objects and the formation of BHs and NSs [14, 16, 17], given valuable information regarding cosmology [18] and the study of cold, dense matter [12, 19–26], as well as enabled tests of GR in a regime previously unexplored [27–29]. In order to both maximize the chances of detection and extract the source parameters from a signal, typical GW data analysis pipelines rely on matched filtering techniques [30–34]. Such methods cross-correlate the noisy output of the detector with an “optimal” filter, which provides a representation for the GWs emitted by the source and hidden within the detector noise. Waveform modeling and parameter estimation (PE) are therefore irremediably intertwined in GW astronomy.

The general relativistic two-body problem The theoretical modeling of GWs has a rich history that spans over a century. Its beginnings can be found in a seminal paper by Albert Einstein, who predicted in 1916 – as a consequence of his theory of

GR – that dynamical systems lose energy to gravitational radiation. He found that the energy loss per unit time due to the emitted gravitational radiation is related to the third time derivative of the system’s mass quadrupole moment, and proportional to c^{-5} . In the simple case of bound binary systems, then, the emission of energy via GWs should lead to a progressive decrease of the distance between the objects, causing them to inspiral and eventually merge. However, at the time, such losses were considered to be of no consequence for any practical reason. In the 4th edition of the famous Landau-Lifshitz book [35], the authors state that *“it is necessary to note that the numerical value of this energy loss, even for astronomical objects, is so small that its effects on the motion, even over cosmic time intervals, is completely negligible”*.

Ignoring the subdominant effects of GW emission, shortly after the formulation of GR many authors attempted to generalize the description of the motion of bodies beyond the Newtonian level, assuming weak gravitational field ($G \ll 1$) and exploiting a slow-motion and near-zone expansion ($v/c \ll 1$, where v is the typical speed of the system) [36–39]. The first successful endeavor to apply this “post-Newtonian (PN)” formalism dates to 1938, when Infeld, Hoffmann and Einstein himself [40] computed the equations of motions for an N-body system up to order c^{-2} , i.e. 1PN level. This formalism, as expected, proved to be accurate enough to describe e.g. the dynamics of bodies in the solar system.

It was not until the 1970s that the first efforts to develop waveform models accounting for dissipation due to gravitational radiation (which as stated above is $\mathcal{O}(c^{-5})$, i.e. 2.5PN) began. This push towards more accurate modeling of the motion of bodies in GR was prompted by the discovery of the Hulse-Taylor pulsar PSR 1913+16, consisting of two compact objects each with a mass about 1.4 times the mass of the Sun, and more in general of the discovery of strongly self-gravitating bodies (BHs and NSs) [41, 42]. The measurement of a secular acceleration of the orbital motion of PSR 1913+16 sparked lively discussions within the scientific community [43], and re-ignited interest in the experimental relevance of gravitational radiation. The 2.5PN accurate equations of motion (EOM) for a binary system were obtained few years after the discovery of Hulse and Taylor, and were instrumental in the correct interpretation of the experimental data [44–46], which were found to agree remarkably well with the theoretical predictions. Notably, together with the 2.5PN EOM, also came the addressing of some criticalities of PN theory which had been previously overlooked [43, 45], namely the treatment of the internal structure of the bodies and the regularization of the relaxed Einstein field equations (EFE) (see e.g. [47, 48]). Given the success

of PN theory and the renewed interest of the community in the relativistic two body problem, considerable efforts went into the computation of 3PN-accurate corrections to the EOM [49–51], which were completed at the beginning of the new millennium. The computation of 4PN corrections, instead, began about 10 years ago relying on a variety of techniques [52–64], and more recently 5 and 6PN terms have started being derived [65–67]. Notably, beyond the approximation of the bodies as point masses, PN expressions for finite-size effects such as spins (see e.g. [47] for a review) and tides [68–77] have – too – been successfully computed.

As significant advancements in PN theory were being made, other methods of approximately solving the EFE for binaries also achieved notable successes. One notable example is that of post-Minkowskian (PM) expansions [44, 78–86], which represent a natural generalization of PN series, relaxing the low-velocity assumption. PM techniques have been employed in the 1980s to clarify the computation of retarded interactions within PN theory, and have recently regained popularity via their link to (gravitational) scattering amplitudes and the scattering angle, which themselves can be employed to obtain precious information on the description of bound systems. Drawing inspiration from the motion of test masses on a fixed background, the Gravitational Self Force (GSF) formalism accounts for the self-field effects that modify the leading order (LO) geodesic motion of a small mass moving in the background geometry generated by a much heavier body [87–94]. This approach, pioneered by DeWitt and Brehme in 1960 [95, 96], is based on an expansion of the metric in terms of the (small) mass ratio ν of the system, and mainly finds applications in the description of extreme mass ratio inspirals, such as the motion of stellar mass BHs around supermassive BHs [97–99]¹. Currently, up to 2GSF corrections have been computed [93, 94].

Beyond purely analytical techniques, in 2005 numerical relativity (NR) – that is, the endeavor of formulating and solving the EFE numerically on a computer – succeeded in evolving a BBH systems of comparable masses through inspiral, merger and ringdown [100–102]. This breakthrough represented the culmination of half a century of work, begun by Hahn and Lindquist [103] and carried on by a number of different groups over multiple decades. Simulating BBHs and BNSs on a computer posed a highly non-trivial challenge, which required alternative formulations of the EFE such that they admit a well posed initial boundary value problem [100, 104–113]; studies in numerically stable gauge conditions [114–118]; efforts in specifying constraint-satisfying initial data [102, 119–121]; attempts in extracting physical results in a gauge

¹Note however recent studies have investigated the applicability of GSF for comparable-mass systems [93, 94].

invariant manner [121] and more. The overcoming of this challenge allowed the study of the strong-field dynamics of a binary system in a regime which is inaccessible to PN theory, and provided invaluable insight in the description of the plunge-to-postmerger stages of both BBH and BNS systems. Such a wealth of information, however, comes at an extremely high computationally cost.

Five years before the NR breakthrough, between 1999 and 2001, Buonanno and Damour laid the foundations to the effective-one-body (EOB) formalism, developed as an alternative to the PN expansion [122–127]. The aim of this framework was that of overcoming the intrinsic strong-field limitations of PN theory, and provide an analytical description of the motion and radiation of a binary system throughout its entire evolution, from the early inspiral until the postmerger (or ringdown). The EOB framework maps the general-relativistic two-body problem into the effective problem of describing the evolution of a test mass moving in a (modified) Kerr metric. By relying on a Hamiltonian formulation of the dynamics and on systematic resummation of PN results, EOB models are faithful also in the high-velocity, strong-field regime.

Today, the state of the art in GW modeling involves the use of hybrid waveforms that combine the strengths of the PN, EOB, and NR models. The EOB-NR semi-analytic family of waveforms for BBH and BNS [128–130] is based on the EOB framework, which is informed by NR in both the conservative and dissipative sectors to achieve robustness and predictivity also beyond merger [131–149]. Phenomenological models fit hybrid EOB-NR waveforms to obtain computationally cheap, yet accurate, waveforms which cover the coalescence from inspiral (for which no NR simulation is available) up to merger [150–168]. Finally, NR surrogates [169–173] directly interpolate via machine-learning techniques large sets of NR simulations, and are able to provide fast and extremely accurate waveforms within their reign of validity. All these hybrid models are accurate and computationally efficient, making them ideal for use in GW data analysis. The quality and quantity of simulations themselves, too, has largely improved in recent years, with a considerable effort spent towards the development of evolution codes. Some notable examples are *Cactus* [174, 175] and the *Einstein* toolkit [176] – on which the *Llama* [177, 178], *GRHydro* [179], *WhiskyTHC* [180] codes are based – *SpeC* [181, 182], *SpECTRE* [183], *BAM* [121, 184], *bamps* [185, 186], *GRChombo* [187], the recent *GR-Athena++* [188], and more.

Observations of GWs from compact binary systems GW models find their application in GW searches and PE pipelines. The former rely on large, pre-computed banks of waveforms, covering a large portion of the parameter space (masses, spins

etc.) of the binaries. A detection is claimed with a certain significance if the data of the interferometers, once matched-filtered with the templates in the bank, surpasses a threshold value of signal-to-noise ratio (SNR) [189–195]². The latter, instead, aims at computing the probability distributions for the parameters of a given signal in a data set via Bayesian methods [32, 199, 200], such as Markov-chain Monte Carlo (MCMC) and nested sampling (e.g. [201–204]). Thanks to the developments in modeling previously discussed, the LIGO-Virgo observatories have so far detected almost 100 GW events. In the following, we summarize some of the properties of the ones we consider the most relevant for the contents of this *Thesis*.

GW150914 [10, 205] was the first historic event observed by the LIGO collaboration. The transient is compatible with the gravitational radiation emitted by the merger of a non-spinning BBH system with total mass of $\sim 60M_{\odot}$, located ~ 400 Mpc away from the Earth. This detection established the existence of stellar mass BBHs, proving also that such systems can merge within a Hubble time [206].

Two years after GW150914 the LIGO-Virgo Collaboration (LVC) observed GW170817, the first GW signal from the coalescence of a BNS system. This detection was followed by a short gamma-ray burst, GRB170817a [13, 207, 208], and a kilonova transient, AT2017gfo [209–217], with electromagnetic (EM) signatures from radio to X-ray wavelengths. The follow-up of the source lasted for more than a year, and non-thermal emission from the GRB170817A afterglow was also detected [e.g., 218, 219]. The combined observation of the same event over these complementary channels marked the birth of multi-messenger astronomy [13]. Combined analyses of the data allowed for the determination of the first constraints on the equation of state (EOS) of NSs above nuclear saturation density [e.g. 220–225], and allowed for a measurement of the Hubble parameter via GWs [226].

GW190412 was the first highly asymmetrical BBH event (with mass ratio $\approx 3 - 4$) detected, which was also one of the louder events of the third LIGO-Virgo-Kagra Collaboration (LVK) observing run with an SNR of 19 [227, 228]. Thanks to the large mass ratio of the system, subdominant harmonics were confidently observed. Further, the detection of GW190412 provided the opportunity to test GR in a regime previously unexplored.

Finally, GW190521 is one of the most mysterious events detected so far. It is compatible with the quasi-circular merger of two heavy BHs, resulting in an intermediate-mass BH [229, 230]. The masses of the component BH fall in the pair instability

²Unmodelled searches techniques have also been employed, see e.g. [196–198]

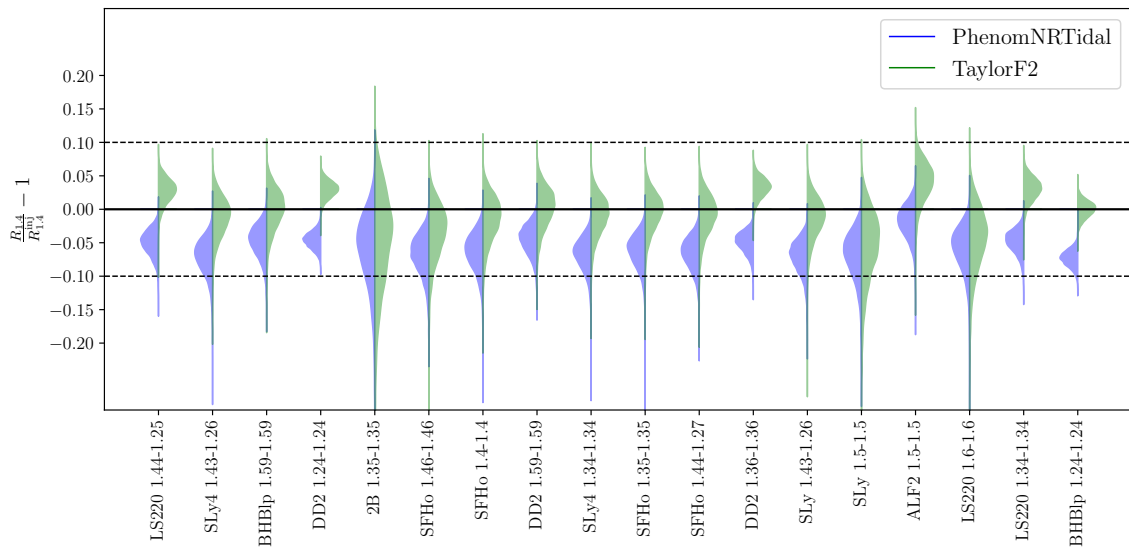


FIGURE 1: Fractional deviation between the radius of a $1.4M_{\odot}$ NS with a specified EOS, $R_{1.4}^{\text{inj}}$, and the reconstructed posteriors for a set of 18 different simulated GW signals. Each signal is generated with an EOB model, and analyzed with a phenomenological (blue) and a PN approximant (green). The under/over estimation in $R_{1.4}$ can amount up to $\pm 5\%$ and can be entirely ascribed to waveform systematics.

supernova mass gap, thus challenging standard BHs formation scenarios [17, 230–236], and suggesting that the system was formed in a dense environment [237]. The peculiar phenomenology of this event, characterized by short duration and almost complete lack of a premerger signal, offers a number of possible interpretations to be proposed. GW190521 was shown to be compatible with a quasi-circular merger with precessing BHs; with a highly eccentric system [238, 239]; a boson-star head-on collision [240]; a high-mass BH-disk system [241] or an intermediate mass ratio inspiral [242] (see also [243]).

Waveform systematics A major issue in the inference of the source parameters from GW PE is the systematic error introduced by inaccuracies or lack of physics of waveform approximants. Although significant waveform systematics (larger than statistical uncertainties) have yet to be observed, the analyses of GW190521, GW190412 as well as GW170817 highlighted that some noticeable differences among the source parameters estimated via different models are already present, suggesting that such error sources might represent a limiting factor in both single event and population inferences. Focusing on BNS systems, recent studies [244–252] have pointed out that

tidal parameters – which encode information on the star’s EOS – can be strongly biased depending on the employed matter and point mass descriptions of the waveform approximant. As a consequence, while the NS radius could be constrained at $\sim 5\%$ level at SNR 80 with current generation detectors, systematics can be at the $\sim 10\%$ level, thus dominating the result (see Fig. 1) [251]. The scenario will be further exacerbated by the increasing sensitivities of Next Generation (NG) detectors [8, 9, 253–256], in view of which GW models will require an accuracy increase of two to three orders of magnitude [257] in order to perform systematics-free PE as well as offer a robust baseline to perform accurate tests of GR. It is clear, then, that in order to truly exploit the scientific potential of GW observatories, GW astronomy will have to rely on physically complete and exceptionally accurate models, able to handle the description of systems of various nature (BBHs, BNSs, BHNSs), with potentially large spins and evolving along generic orbits.

Summary of contents This *Thesis* is centered around the modeling of the GWs emitted by BBH and BNS within the EOB framework. We focus on the `TEOBResumS` model, and include (or improve) the description of physical effects such as the precession of the orbital plane of the system due to the spins of the astrophysical objects [258, 259], the amplitude and phase modulations that occur for highly eccentric orbits [146, 260, 261], and the modifications to the GW phase and amplitude due to matter effects for binary systems containing at least one NS [262–264]. We often validate the model against NR waveforms from the Simulating eXtreme Spacetimes (SXS) [182, 265–276] and Computational Relativity (CORE) [277, 278] collaborations, and apply the developed models to the analysis of real GW events via the Bayesian Jenaer Software (BAJES) pipeline [34].

The *Thesis* is organized as follows. Chapter 1 is dedicated to a brief review of the EOB framework, as implemented within the `TEOBResumS` model. In Chapter 2, we extend `TEOBResumS` to describe waveforms emitted by precessing BBH and BNS systems, and re-analyze the GW150914, GW190421 and GW170817 events. In Chapter 3, we discuss the extension of `TEOBResumS` to model binary systems coalescing along generic (non quasi-circular) orbits, focusing on dynamical captures of BBHs. We then consider GW190521, and analyze its data under the assumption that it was generated by the capture of two BHs in a dense stellar environment. In Chapter 4, we improve the tidal sector of `TEOBResumS`. After critically evaluating the impact of resonant tidal effects via comparisons with high resolution NR waveforms, we first include higher order PN effects as well as NR information in our model, and then develop a closed-form

tidal approximant following the philosophy of the various NRTidal models. Finally, in the Conclusions we summarize the main results presented in this work, and detail future plans and perspectives. We include a brief discussion of waveform systematics for BNS systems in App. A.

Chapter 1

GIOTTO: a state of the art EOB model for quasi-circular binaries

The EOB framework [83, 84, 122–125, 128, 279–283] represents an analytical alternative to PN expansions to obtain the waveform from and the dynamics of a compact binary coalescence (CBC). This framework is based on three separate building blocks: a Hamiltonian, which describes the conservative motion of a test mass in a deformed Kerr (or Schwarzschild) metric, a radiation reaction force which accounts for dissipative effects during the evolution of the system and a prescription of the waveform through inspiral, merger and (for BBHs) ringdown. In this chapter, we briefly review the basics of the EOB framework and introduce the EOB model that we build upon in the following chapters, `TEOBResumS`. In particular, we will summarize the features of the model denoted as `TEOBResumS – GIOTTO`, developed and discussed in detail in Refs. [142, 144, 284–286]. A more in-depth discussion on the inclusion of matter effects and generic orbits is left to future chapters.

In the following, we will assume that the two objects have masses (m_1, m_2) , with the convention that $m_1 \geq m_2$. The mass ratio is defined as $q \equiv m_1/m_2 \geq 1$. The total mass is denoted by $M = m_1 + m_2$, the reduced mass by $\mu \equiv m_1 m_2 / M$, the symmetric mass ratio by $\nu \equiv \mu / M$ and the mass fractions $X_i \equiv m_i / M$, with $i = 1, 2$. The spin vectors of the binary components are denoted as $\mathbf{S}_1, \mathbf{S}_2$, while the dimensionless spins are $\chi_1 \equiv \mathbf{S}_1 / m_1^2$, $\chi_2 \equiv \mathbf{S}_2 / m_2^2$. We will often use phase-space dimensionless variables $(r, p_{r_*}, \varphi, p_\varphi)$, related to the physical ones $(R, P_{R_*}, \varphi, P_\varphi)$ by $r = R / GM$ (relative separation), $p_{r_*} = P_{R_*} / \mu$ (radial momentum), $p_\varphi = P_\varphi / (\mu GM)$ (angular momentum), and $t = T / (GM)$ the dimensionless time. The radial momentum p_{r_*} is defined as $p_{r_*} = (A/B)^{1/2} p_r$, where A and B are the EOB metric potentials (see

below). We denote the plus and cross GW polarizations as h_+ , h_\times , and define

$$h = h_+ - ih_\times = \sum_{\ell \geq 2, m} {}_{-2}Y_{\ell m} h_{\ell m}, \quad (1.1)$$

where ${}_{-2}Y_{\ell m}$ are the -2 spin-weighted spherical harmonics and $h_{\ell m}$ the multipolar GW modes.

1.1 Hamiltonian

Orbital Hamiltonian The conservative EOB Hamiltonian is obtained by mapping the conservative dynamics of the “real” system – described by the PN center of mass Arnowitt-Deser-Misner (ADM) Hamiltonian $\hat{H}_{\text{ADM}}(q, p)$ – into the “auxiliary” geodesic motion of a test particle of mass μ in an effective metric $g_{\mu\nu}^{\text{eff}}$. The latter is given by

$$g_{\mu\nu}^{\text{eff}} = -A(r; \nu)c^2 dt^2 + B(r; \nu)dr^2 + r^2(d\theta^2 + \sin^2\theta d\varphi^2), \quad (1.2)$$

where $A(r; \nu)$ and $B(r; \nu)$ are the two EOB metric potentials. Inspired by the Bohr-Sommerfeld quantization conditions and “thinking quantum-mechanically”, the potentials are determined – at a given PN order – by (i) imposing that they reduce to the correct (Schwarzschild) test-particle limit for $\nu \rightarrow 0$ (ii) computing the Delaunay Hamiltonian in terms of action-angle variables for both problems¹, and (iii) imposing that

$$\frac{\mathcal{E}_{\text{eff}}}{\mu c^2} = 1 + \frac{E_{\text{real}}}{\mu c^2} \left(1 + \alpha_1 \frac{E_{\text{real}}}{\mu c^2} + \alpha_2 \left(\frac{E_{\text{real}}}{\mu c^2} \right)^2 + \alpha_3 \left(\frac{E_{\text{real}}}{\mu c^2} \right)^3 + \alpha_4 \left(\frac{E_{\text{real}}}{\mu c^2} \right)^4 + \dots \right), \quad (1.3)$$

where $\alpha_1, \alpha_2, \alpha_3, \alpha_4$ etc. are parameters to be determined. An equivalent procedure based on the determination of the canonical transformation linking EOB and ADM coordinates can also be followed to the same end [124].

Further specifying the case to that of equatorial ($\theta = \pi/2$) orbits, the above procedure at a fixed PN order yields $\alpha_1 = \nu/2$ and $\alpha_{i \geq 2} = 0$, leading to the following EOB Hamiltonian:

$$H_{\text{eob}} = M \sqrt{1 + 2\nu(\hat{H}_{\text{eff}} - 1)} \quad (1.4)$$

$$\hat{H}_{\text{eff}} = \frac{1}{\nu} \sqrt{A(1 + p_\varphi^2 u^2 + Q) + p_{r^*}^2} \quad (1.5)$$

¹Note that beyond 2PN accuracy one also has to account for a non-geodesic term Q in the effective dynamics

with $u = 1/r$.

Currently, A is known up to 5PN, while Q and $D = AB$ are known to 5.5 PN, respectively [287–290]. Their expressions (omitting non-local terms in Q) can be read from e.g. Eq. (2) to (5) in [291]. The analytical results obtained are of striking simplicity. It turns out, for instance, that the entire 2PN dependence of \hat{H}_{ADM} – there encoded in seven ν -dependent coefficients – is condensed in only two simple additional contributions in $A(r; \nu)$ and $B(r; \nu)$, and similar “condensations” happen at higher PN orders. This simplification can at least partially be referred to the reformulation of the PN mechanics into the effective one, which in this sense represents a “resummation” of the real dynamics. The fact that all α_i with $i \geq 2$ are exactly equal to zero further suggests that the relation between the effective and the real energy is *exactly* quadratic. This intuition was proved in Ref. [83], which also showed how the relativistic dynamics of a two-body system is equivalent, at first PM order, to the relativistic dynamics of an effective test particle moving in a Schwarzschild metric – thus motivating assumption (i) above.

In order to further ensure robustness and predictivity also in the strong field regime, additional resummations are performed on the metric potentials typically either via Padé approximants or logarithmic functions [131, 142, 292]. The *TEOBResumS-GIOTTO* model, for instance, resums $A(r)$ via a Padé (1,5), while the D potential is resummed with a Padé (0,3) [142]². Notably, this model also augments the $A(r)$ potential with a pseudo 5PN NR-informed parameter, a_c^6 , determined via comparisons to simulations of non-spinning BBH coalescences.

Spinning systems The inclusion of spin-orbit effects in the EOB Hamiltonian closely follows the procedure mentioned above [125, 126, 280, 281, 291, 293–296]. While the results listed here are specified to systems whose spins are aligned with the orbital angular momentum, the techniques employed to obtain them are general and have been extended to generic spins. PN results [297–299], expressed in center of mass ADM coordinates, are mapped into \hat{H}_{eff} by means of successive canonical transformations [291, 295]. The resulting Hamiltonian reads:

$$\hat{H}_{\text{eff}} = \sqrt{A(1 + p_\varphi^2 u_c^2 + Q) + p_{r_*}^2} + p_\varphi (\hat{G}_{\hat{S}} \hat{S} + \hat{G}_{\hat{S}_*} \hat{S}_*). \quad (1.6)$$

In the expression above, $\hat{S} = (X_1^2 \chi_1 + X_2^2 \chi_2)$, $\hat{S}_* = X_1 X_2 (\chi_1 + \chi_2)$ and $\hat{G}_{\hat{S}}, \hat{G}_{\hat{S}_*}$ are two gyro-gravitomagnetic contributions, currently known up to 5.5PN [280, 293, 300–304],

²Different resummation choices have been explored for the generic-orbits model, see Ref. [291].

which account for spin-orbit effects. These quantities are gauge-dependent, this freedom corresponding to the choice of a spin-supplementary condition. In *TEOBResumS*, the DJS gauge [124, 280] is employed, which eliminates all explicit dependence of the gyro-gravitomagnetic factors on the orbital angular momentum p_φ ³.

Spin squared terms [305, 306] are instead included within the *TEOBResumS* EOB Hamiltonian via the definition of a “centrifugal radius” r_c [125, 296], related to the usual radial variable r (at LO) through:

$$r_c^2 = r^2 + \tilde{a}_0^2 \left(1 + \frac{2}{r}\right), \quad (1.7)$$

with $\tilde{a}_0 = X_1\chi_1 + X_2\chi_2$. Following intuitions deriving from the structure of the Kerr Hamiltonian in Boyer-Lindquist coordinates, under the mapping $r \rightarrow r_c$ the A potential becomes

$$A(r_c) = A_{orb}(r_c; \nu) \frac{(1 + 2u_c)}{1 + 2u}, \quad (1.8)$$

and, similarly

$$D = \frac{r^2}{r_c^2} D_{orb}(u_c; \nu). \quad (1.9)$$

Following the same philosophy employed for the orbital potentials, both gravitomagnetic terms are typically resummed and NR-informed [280, 281, 291, 294, 295, 307]. *TEOBResumS* employs an inverse-Taylor resummation [296] for both of them, resumming their next-to-next-to-leading order (NNLO) expressions, and informing them via a single phenomenological parameter, c_{N3LO} , computed via phasing comparisons against a handful of simulations of spinning BBH binaries [144, 285].

³This choice, while convenient for calculations, implies that the model is singular at the light ring, see e.g. [292]

1.2 Dynamics, radiation and inspiral waveform

The EOB Hamiltonian of Eq. 1.4 implies a set of four Ordinary Differential Equations (ODEs) for the EOB variables $r, \varphi, p_{r^*}, p_\varphi$:

$$\frac{dr}{dt} = \left(\frac{A}{B}\right)^{1/2} \frac{\partial \hat{H}^{\text{EOB}}}{\partial p_{r^*}}(r, p_{r^*}, p_\varphi) \quad (1.10a)$$

$$\frac{d\varphi}{dt} = \Omega = \frac{\partial \hat{H}^{\text{EOB}}}{\partial p_\varphi}(r, p_{r^*}, p_\varphi) \quad (1.10b)$$

$$\frac{dp_{r^*}}{dt} = -\left(\frac{A}{B}\right)^{1/2} \frac{\partial \hat{H}^{\text{EOB}}}{\partial r}(r, p_{r^*}, p_\varphi) \quad (1.10c)$$

$$\frac{dp_\varphi}{dt} = 0 \quad (1.10d)$$

with the last equation enforcing orbital angular momentum conservation. Given that we are not interested in the geodesic motion of bodies, but rather want to study effects due to radiation, the second ingredient that enters the EOB framework is a prescription for the radiation reaction force, which accounts for dissipation due to GW emission and modifies the Hamilton's equations for p_{r^*} and p_φ :

$$\frac{dp_{r^*}}{dt} = \left(\frac{A}{B}\right)^{1/2} \left(-\frac{\partial \hat{H}^{\text{EOB}}}{\partial r}(r, p_{r^*}, p_\varphi) + \hat{\mathcal{F}}_r \right), \quad (1.11)$$

$$\frac{dp_\varphi}{dt} = \hat{\mathcal{F}}_\varphi(r, p_{r^*}, p_\varphi) \quad (1.12)$$

where $\hat{\mathcal{F}}_\varphi$ and $\hat{\mathcal{F}}_r$ represent the azimuthal and radial components of the radiation reaction.

Once more, $\hat{\mathcal{F}}_\varphi$ and $\hat{\mathcal{F}}_r$ need to be resummed. Due to difficulties in robustly resumming $\hat{\mathcal{F}}_r$, and given that this quantity vanishes along circular orbits, a typical choice is setting $\hat{\mathcal{F}}_r = 0$. Regarding $\hat{\mathcal{F}}_\varphi$, numerous techniques have been employed over the years to obtain robust expressions for this quantity [144, 279, 308–311], the most recent being based on a factorization and (inverse-Taylor or Padé) resummation of the multipolar modes $h_{\ell m}$ [144]. During the quasi-circular inspiral, $\hat{\mathcal{F}}_\varphi$ is given by:

$$\hat{\mathcal{F}}_\varphi = -\frac{1}{\Omega} \sum_{\ell \geq 2} \sum_{m=-\ell}^{m=\ell} F_{\ell m} \quad (1.13)$$

$$F_{\ell m} = \frac{1}{8\pi G} (m\Omega)^2 |R h_{\ell m}|^2 \quad (1.14)$$

where $F_{\ell m}$ is the (instantaneous) GW flux. The modes $h_{\ell m}$ are then factorized as

$$h_{\ell m} = h_{\ell m}^{(N,\epsilon)} \hat{S}_{\text{eff}}^{(\epsilon)} \hat{h}_{\ell m}^{\text{tail}} e^{i\delta_{\ell m}} \rho_{\ell m}^{\ell}. \quad (1.15)$$

In Eq. 1.15, ϵ denotes the parity of $\ell+m$, $h_{\ell m}^{(N,\epsilon)}$ is the LO Newtonian term, which can be computed from the quadrupole formula [279]; $S_{\text{eff}}^{(\epsilon)}$ is a source term, which equals \hat{H}_{eff} or the angular momentum, depending on the parity of ϵ [279]; $\hat{h}_{\ell m}^{\text{tail}}$ accounts for tail effects, and resums an infinite number of leading logarithms [308, 309]; $e^{i\delta_{\ell m}}$ corrects the phase of the waveform accounting for terms not included in the tail term, such as subleading logarithms; $\rho_{\ell m}$ is a “residual relativistic wave amplitude” [144, 279, 310, 311]. Appropriate factorization and resummation of the $\rho_{\ell m}$ terms is critical, and can lead to sensible improvements of EOB waveforms [310, 311]. The choices followed by *TEOBResumS* are listed, for all modes up to $\ell = m = 4$ as well as the $\ell = m = 5$ mode, in Tab. I of Ref. [144]. The same table also lists the PN information included in both the purely orbital and spinning sectors of the $\rho_{\ell m}$. Once the multipolar modes are computed, $\hat{\mathcal{F}}_{\varphi}$ is obtained by factorizing the LO contribution to Eq. (1.13), given by the (2, 2) multipole, and accounting for horizon absorption (in case the binary is a BBH):

$$\hat{\mathcal{F}}_{\varphi} = -\frac{32}{5} \nu r_{\omega}^4 \Omega^5 \hat{f}. \quad (1.16)$$

where $\hat{f} = \sum_{\ell m} F_{\ell, m} / F_{22}^{\text{LO}} + \hat{f}_{\text{Horizon}}$, and r_{ω} is a modified radial variable which satisfies Kepler’s law during the adiabatic inspiral but differs from it during plunge.

1.3 Merger-ringdown completion

The EOB description of the dynamics of coalescing BHs involves analytical PN calculations, which rely on the assumption that the two BHs can be approximated as two point masses separated by a sufficient distance. Although the resummations employed are meant to mitigate these limitations, this approach might in principle appear limited to the inspiral to merger portion of the coalescence. This is, however, not the case. Relying on intuitions coming from BH perturbation theory, in the 2000s Ref. [308] devised a strategy to match the inspiral and plunge (“insplunge”) waveform – valid until the peak of the EOB orbital frequency – with a ringdown template, characterized by the superposition of quasi-normal mode (QNM) of the final BH and valid beyond merger:

$$h_{\ell m} = h_{\ell m}^{\text{insplunge}}(t) \theta(t_{\text{mrg}} - t) + h_{\ell m}^{\text{ringdown}}(t) \theta(t - t_{\text{mrg}}). \quad (1.17)$$

Initial comparisons with NR simulations demonstrated that this simple prescription provided qualitatively correct predictions. With the increase in number and accuracy of NR simulations, the EOB model for the last phases of the coalescences evolved to directly include NR information [131, 139, 141, 269, 312–319]. Currently, the *TEOBResumS* waveform is completed via Next-to-quasicircular corrections (NQC) corrections, which improve the behavior of the waveform during plunge, and a phenomenological ringdown template.

NQCs Also known as “non-quasi-circular” corrections, they were originally introduced in the study of the test particle limit [308]. In this regime, studies of the transition from inspiral to plunge highlighted the necessity to account for non-circular terms in the radiation reaction force $\hat{\mathcal{F}}_\varphi$ in order to obtain good agreement between the “exact” numerical and analytical results [320]. They were subsequently first moved to the h_{22} waveform, in place of the radiation reaction [321, 322], and then consistently accounted for in both $\hat{\mathcal{F}}_\varphi$ and h_{22} [323]. More recent works included these terms also to the higher-order ($\ell > 2$) multipolar waveforms, for both spinning and non-spinning binaries [284–286], and highlighted the importance of including them also in the higher multipolar instantaneous fluxes to obtain good agreement with NR waveforms [324].

NQCs terms appear in the definition of the EOB multipolar waveforms (and, similarly, in the fluxes $F_{\ell m}$) as an additional multiplicative factor:

$$h_{\ell m} = h_{\ell m}^{(N,\epsilon)} \hat{S}_{\text{eff}}^{(\epsilon)} \hat{h}_{\ell m}^{\text{tail}} e^{i\delta_{\ell m}} \rho_{\ell m}^\ell \hat{h}_{\ell m}^{\text{NQC}}, \quad (1.18)$$

with

$$\hat{h}_{\ell m}^{\text{NQC}} = (1 + a_1^{\ell,m} n_1^{\ell,m} + a_2^{\ell,m} n_2^{\ell,m}) \times e^{i(b_1^{\ell,m} n_3^{\ell,m} + b_2^{\ell,m} n_4^{\ell,m})}. \quad (1.19)$$

Here, $(n_1^{\ell,m}, \dots, n_4^{\ell,m})$ are functions depending on first and second time derivative of r . The $a_i^{\ell,m}$ and $b_i^{\ell,m}$ parameters, instead, are determined by solving a set of four algebraic equations, imposing that the waveform amplitude and frequency (and their first time derivatives) equal NR fits⁴ at a certain reference time close to the peak of the EOB *pure* orbital frequency, i.e. the frequency obtained neglecting spins contributions.

In order to consistently employ these corrections within the radiation reaction force, Ref. [323] introduced an iterative procedure, which requires the re-generation of the EOB waveform, using the NQCs parameters determined at the previous iteration

⁴Such fits are employed only for the $(\ell, m) = (2, 2), (3, 1), (3, 3), (4, 1), (5, 5)$ modes. For the $(2, 1), (3, 2), (4, 2), (4, 3)$ and $(4, 4)$ modes, the quantities needed to determine the NQC parameters are extracted directly from the ringdown template described below.

already during the dynamics. Given the heavy computational cost of this iterative procedure, Ref. [286] introduced direct fits for the $a_1^{(2,2)}, a_2^{(2,2)}, b_1^{(2,2)}, b_2^{(2,2)}$ coefficients as a function of the intrinsic parameters of the source.

Ringdown waveform The ringdown template employed in *TEOBResumS* is given by a QNM-factorized waveform, multiplied by a NR-informed correcting factor [139, 142, 144, 285, 317]:

$$h_{\ell m}^{\text{ringdown}}(\tau) = e^{-\sigma_1 \tau} \bar{h}_{\ell m}(\tau), \quad (1.20)$$

where σ_1 is the complex frequency of the fundamental QNM and $\tau = (t - t_{\ell m}^{\text{peak}}) \geq 0$. Each $\bar{h}_{\ell m}$ is further factorized as

$$\bar{h}_{\ell m}(\tau) = \bar{A}_{\ell m}(\tau) e^{i\bar{\phi}_{\ell m}(\tau)}. \quad (1.21)$$

For each multipole, $\bar{A}_{\ell m}$ and $\bar{\phi}_{\ell m}$ are parameterized as in Eq. (5.4)-(5.10) of Ref. [285]. These templates depend on a total of five multipole-specific parameters, $(\hat{A}^{\text{peak}}, \omega^{\text{peak}}, c_3^A, c_3^\phi, c_4^\phi)$, which are fit to NR waveforms from the SXS catalog, and two global parameters $(M_{\text{bhf}}, a_{\text{bhf}})$ which represent the mass and spin of the remnant BH. The ringdown model is then completed by the determination of $t_{\ell m}^{\text{peak}}$, computed in terms of the time-shift between the peak of each mode and the $\ell = m = 2$ one.

1.4 Acceleration techniques

In order to compute an EOB waveform for a simple aligned-spins, quasi-circular binary it is then necessary to (i) obtain appropriate quasi-circular initial conditions [309, 325], (ii) solve the Hamilton equations given by Eqs (1.10) with the radiation reaction of Eq. (1.16), (iii) compute the NQC-augmented modes and (iv) attach the ringdown model (for a BBH system), (v) interpolate the waveform multipoles to a uniform-in-time grid and compute the waveform polarizations. While delicate, steps (i), (iii) and (iv) are computationally cheap. On the other hand, numerically integrating the system (1.10) with standard techniques can prove to be rather computationally expensive, especially for binaries which evolve for hundreds of thousands of orbital cycles. Additionally, for such systems, the waveform multipoles interpolation can also require long times. For these reasons, EOB-based models are generally considered to be very accurate but poorly suited to be directly employed in GW PE.

Post-adiabatic dynamics A number of techniques and approximations can be employed to reduce the computational cost of generating waveforms with EOB models. Reduced order models (ROMs) and surrogates decrease the waveform evaluation time by e.g. speeding up likelihood evaluations or interpolating between waveforms, with non-appreciable loss of faithfulness to the original model [326, 327]. EOB waveforms can alternatively be speeded up using dedicated analytical methods. Ref. [328] introduced an iterative procedure, the post-adiabatic (PA) approximation, to obtain fully analytical solutions to the EOB EOM throughout the entire inspiral, with considerable gains in speed. This procedure provides a solution to the system (1.10), and is based on the simple intuition that for quasi-circular binaries at large separations the radiation reactions force acts as a small correction to the conservative motion.

In the adiabatic limit, $\hat{\mathcal{F}}_\varphi = 0$ and – along exactly circular orbits – $p_{r_*} = 0$ and $p_\varphi = j_0$, the latter obtained imposing $\partial_r \hat{H}_{\text{EOB}} = 0$ at a given radius r . At first PA order, radiation reaction is small but non-negligible, and $p_{r_*} \neq 0$. The latter can be computed by combining the EOB EOM for dr/dt and dp_φ/dt into $dp_\varphi/dr = \hat{\mathcal{F}}_\varphi (dr/dt)^{-1}$. At 2PA level, one computes the correction to $p_\varphi \neq j_0$ using the previously obtained value of p_{r_*} , this time solving $dp_{r_*}/dr = (dp_{r_*}/dt)(dr/dt)^{-1}$. This process can then be repeated to N^{th} order over a radial grid, with the time t and orbital phase φ that can be recovered by quadratures.

Efficient frequency domain waveforms Waveforms obtained via PA approximation still need to be translated into the frequency domain (FD) to be directly applicable to PE, thus requiring interpolation and Fast Fourier transform (FFT), which dominate the waveform generation time. This computational hurdle can be overcome by drawing inspiration from analytical PN approximants, which are turned into closed-form FD templates by applying the stationary-phase approximation (SPA) [30, 47, 329–331]. While PN approximants become unfaithful as the binary motion becomes non-adiabatic (high-velocities regime), the SPA itself was proven to be accurate at least up to frequencies corresponding to the Last Stable Orbit (LSO), e.g. [329, 331].

Reference [332] applied the SPA to BNS EOB waveforms in order to obtain computationally inexpensive FD templates. The FD extension of a given time domain (TD) EOB waveform is computed by applying the SPA to the single multipolar TD modes $h_{\ell m}(t) = a_{\ell m} e^{i\phi_{\ell m}(t)}$ to obtain

$$\tilde{h}_{\ell m}^{\text{SPA}} = \tilde{A}_{\ell m}^{\text{SPA}} e^{i\Psi_{\ell m}^{\text{SPA}}} = \frac{a_{\ell m}(t_f)}{\sqrt{\ddot{\phi}_{\ell m}(t_f)/2\pi}} e^{i[\psi_f(t_f^{\ell m}) - \pi/4]}, \quad (1.22)$$

with $\psi_f(t) \equiv 2\pi ft - \phi(t)$ and where t_f denotes the stationary point of $\psi_f(t)$. The two GW polarizations in FD are then computed by combining the multipolar modes with spin-weighted spherical harmonics.

The resulting FD **TEOBResumS** model retains the same accuracy as the TD **TEOBResumS** up to merger for any low-mass signal, and for waveforms with initial frequency $f_0 \lesssim 15$ Hz its speed is comparable to that of other commonly used phenomenological or surrogate approximants. The model so obtained was applied to direct PE of GW170817 and GW190425 [14], employed for the construction of the efficient surrogate model **MLGW – BNS** [333] and interfaced with a reduced-order-quadrature (ROQ) model to speed up likelihood evaluations.

1.5 Validating an EOB model

The goodness of a GW model can be evaluated by comparing it to any set of NR simulations, which have not been employed to inform the model itself. Such comparisons can be performed in a number of complementary ways in order to correctly assess and understand the analytic systematics that affect a model. When working with EOB models, in particular, it is important to recall that the waveform is the byproduct of the description of the effective dynamics, which – too – can and should be tested appropriately. Given that a large part of this dissertation will be dedicated to the validation of various flavors of EOB models, we introduce here a few quantities which will often be employed in future chapters.

Phasing The first kind of comparison that can be performed to benchmark a model against NR is what is usually referred to as “TD phasing”, and simply consists in superposing two waveforms – typically the h_{22} multipoles directly – in the TD. In order to obtain meaningful comparisons, it is necessary to “align” the two waveforms, i.e. to find a global time and phase shift $(\Delta\phi, \Delta t)$ such that

$$\chi^2 = \int_{t_i}^{t_f} [\phi_h(t + \Delta t) - \phi_k(t) - \Delta\phi]^2 dt, \quad (1.23)$$

is minimized. In Eq. (1.23), ϕ_h, ϕ_k are the (2,2) GW phases of the two waveforms (h, k) to be aligned, and (t_i, t_f) specify the time window over which the minimization is performed. Once the $\Delta\phi$ and Δt are known from the (2,2) mode, the other modes can be aligned by employing the same Δt and appropriately rescaling $\Delta\phi$. One example

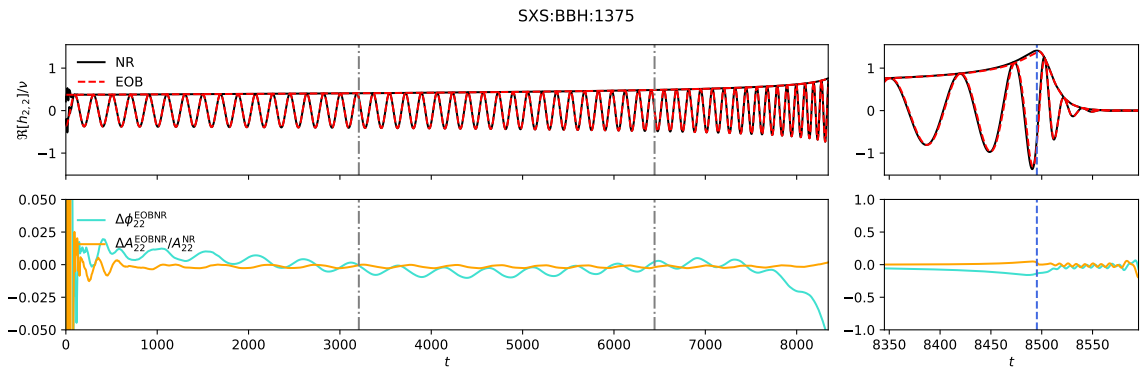


FIGURE 1.1: Example TD phasing. In the top panel we plot the real part of h_{22} , and compare *TEOBResumS* (red-dashed) with a BBH NR waveform from the SXS catalog (black) with $q = 8$ and dimensionless spins $\chi_1 = -0.9$, $\chi_2 = 0$. The bottom panel, instead, shows the relative amplitude difference $\Delta A^{\text{EOBNR}}/A^{\text{NR}}$ (orange) and the phase difference $\Delta\phi^{\text{EOBNR}}$ throughout the evolution of the binary. Dotted gray lines mark the alignment window, while the dashed blue line indicates merger.

phasing is shown in Fig. 1.1, which compares *TEOBResumS-GIOTTO* to one $q = 8$ spin-aligned SXS simulation, with $\chi_1 = -0.9$, $\chi_2 = 0$. The agreement between the two waveforms can be quantified in terms of accumulated phase difference at merger, and is – in this specific case – equal to ~ -0.1 rad.

Although conceptually very simple, correctly aligning waveforms in the TD is an art, more than a science. Slightly different choices of alignment window can lead to rather different results. Usually, it is desirable to choose the alignment window so that (i) it covers the early inspiral, where the waveforms are expected to agree well, (ii) $\Delta\phi$ remains flat during the inspiral and (iii) $|\Delta\phi|$ increases monotonically throughout plunge, merger and ringdown. Unfortunately, however, it is not always possible to obtain satisfactory results following these simple guidelines.

Unfaithfulness To further quantify the agreement of a model with NR, it is standard to evaluate the EOB/NR unfaithfulness (or mismatch) $\bar{\mathcal{F}}$, which describes the *global* agreement between a model and the NR data, given the noise curve (or power spectral density (PSD)) of a detector.

When waveforms are constructed exclusively via $\ell = |m| = 2$ modes, the EOB/NR unfaithfulness is defined as

$$\bar{\mathcal{F}} = 1 - \max_{\phi_0, t_0} \frac{(h_{\text{EOB}}, h_{\text{NR}})}{\sqrt{(h_{\text{NR}}, h_{\text{NR}})(h_{\text{EOB}}, h_{\text{EOB}})}}, \quad (1.24)$$

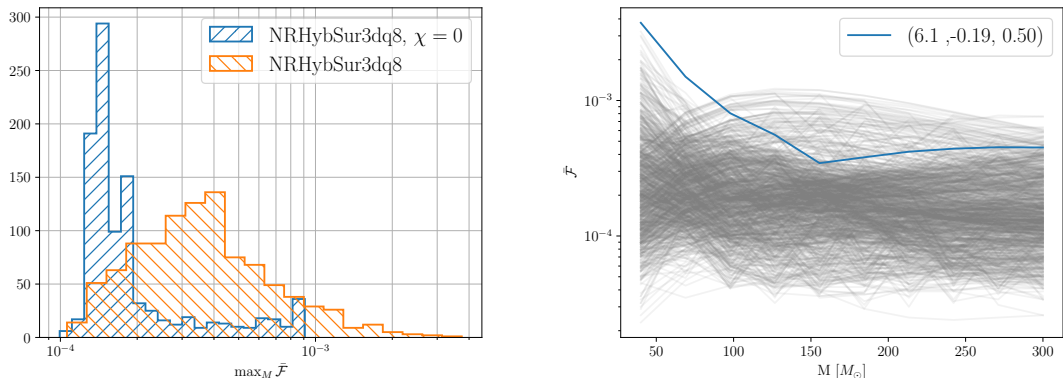


FIGURE 1.2: Mismatches between **TEOBResumS** and the NR surrogate **NRHybSur3dq8** for 1000 configurations of mass ratio and spins, computed as discussed in the text. The left panel shows the distributions of the largest unfaithfulness – maximized over the total mass M – for each configuration, while the right panel shows the unfaithfulness as a function of M for spinning configurations, corresponding to the orange distribution shown on the left.

where (\cdot, \cdot) denotes the Wiener inner product in waveform space between the EOB and NR waveform and ϕ_0, t_0 are a reference time and phase, which carry no astrophysical significance and are therefore maximized over. The action of the inner product on two generic waveforms h, k is given by

$$(h, k) = 4\Re \int_{f_{\min}}^{f_{\max}} \frac{\tilde{h}(f)\tilde{k}^*(f)}{S_n(f)} df, \quad (1.25)$$

where $S_n(f)$ is the PSD of the detector. For the comparisons carried out in this *Thesis*, we typically employ either the Einstein Telescope PSD [334], or the advanced LIGO PSD of [335]. Unless otherwise specified, f_{\min} and f_{\max} are instead taken as the initial frequency of the NR simulation and the merger frequency (for BNS systems) or an arbitrarily high frequency threshold covering also the ringdown (e.g., 2048 Hz) for BBHs.

For instance, the unfaithfulness of **TEOBResumS** against the *entirety* of the simulations of aligned-spins BBHs of the SXS catalog can be inspected from Fig. 6 of [144]. When considering waveforms built with the $\ell = |m| = 2$ mode only, the largest values of $\bar{\mathcal{F}}$ are obtained for systems with large spins, see e.g. Fig. 4 of [144]. Figure 1.2, instead, displays the unfaithfulness of **TEOBResumS** against the NR surrogates **NRHybSur3dq8**, valid for systems with $q < 8$ and spins $|\chi_i| < 0.8$. We consider 1000 different configurations of mass ratio and spins, and for each compute the unfaithfulness over a range of masses $M \in [40, 300]$, from 20 to 2048 Hz with the aLIGO PSD.

Gauge-invariant Energetics Differently from Phenomenological models or surrogates, the EOB framework is based on the description of an effective dynamics, that of a test particle on a deformed Kerr metric, with a known mapping between the real and effective dynamics (see Eq. (1.6)). Therefore, although the EOB variables r, φ, p_{r^*} are coordinate-dependent, EOB models naturally compute the evolution throughout the coalescence of two gauge-invariant quantities: the system's (binding) energy E_b and its angular momentum \hat{j} :

$$E_b \equiv \frac{E - M}{\mu} = \frac{\nu \hat{H}_{\text{EOB}} - 1}{\nu}, \quad (1.26)$$

$$\hat{j} \equiv p_\varphi. \quad (1.27)$$

These values can be compared to the same quantities obtained from NR:

$$E_b \equiv \frac{M_{\text{ADM}}^0 - \Delta \mathcal{E}_{\text{rad}} - M}{\mu} \quad (1.28)$$

$$\hat{j} \equiv \frac{\mathcal{J}_{\text{ADM}}^0 - \Delta \mathcal{J}_{\text{rad}}}{M\mu} \quad (1.29)$$

where $(M_{\text{ADM}}^0, \mathcal{J}_{\text{ADM}}^0)$ denote the total initial ADM mass-energy and angular momentum and $(\Delta \mathcal{E}_{\text{rad}}, \Delta \mathcal{J}_{\text{rad}})$ are the radiated energy and momentum, which can be evaluated via direct integration of the waveform multipoles (see e.g. Eq. 3-4 in [336]). These comparisons can be used to directly test the goodness of the EOB dynamics, i.e. of the effective Hamiltonian and radiation reaction [285, 292, 336–338]. For instance, different mass ratio regimes give complementary information on the conservative and dissipative dynamics (recall that $\hat{\mathcal{F}}_\varphi \sim \nu$). Further, they can be used to test the impact of the NR information on the waveform and its consistency with the underlying dynamics.

Chapter 2

Hybrid PN-EOB model for generic spins binaries

The accurate modelling of the GWs emitted by coalescing BBH and BNS systems represents a significant challenge in current GW astronomy, due to the complexity of the physical effects to be described. Among them, in the past decade the GW community has dedicated significant attention to the phenomenon of spins precession, which arises when the binary's angular momentum and spin vectors are not aligned, leading to modulations in the amplitude and phase of the GW signal. According to stellar evolution theory, BBHs may be affected by spins precession depending on their formation channels: while BBH systems formed in galactic fields should possess spins mostly aligned with the orbital angular momentum [339–344], dynamically-formed BBHs are expected to have randomly oriented spin tilts [345–348].

These considerations highlight the need of waveform models that properly capture precession effects. In this context, a vast array of methods has been developed over the last decade, including analytical approximations, numerical simulations, and hybrid methods. Between them, some of the most notable waveform models for precessing binaries are those belonging to the Phenom family [160–166], those based on surrogates of NR [172] and those based on the EOB framework [138, 258, 349]. In this chapter we focus on the description of precessing compact binaries within the latter, and improve on the `TEOBResumS` model first presented in Ref. [258]. In particular, we extend the precessing waveform model to (i) incorporate higher modes in the waveform for both BBH and BNS; (ii) incorporate the ringdown description for BBH, so to obtain a complete inspiral-merger-ringdown (IMR) approximant, (iii) provide an alternative, fast, frequency-domain approximant for BNS inspiral-merger and long BBH inspiral events based on the nonprecessing approach of Ref. [251]. `TEOBResumS` IMR precessing model for BBH is validated by directly computing (mis)matches against a significant number

of NR **SXS** waveforms and against the waveform model **NRSur7dq4**. We also indirectly test its performance against the state-of-the-art **IMRPhenomXPHM** model, by comparing EOB/NR and Phenom/NR mismatches. Finally, we perform full PE to further compare the model to other existing approximants, and estimate the source parameters of the BBH merger events GW150914 [205], GW190412 [228], and GW170817 [12], the first BNS inspiral-merger event.

On top of the standard quantities introduced in Chapter 1, we recall here two definitions that pertain to the mass-weighted projections of the spins parallel and perpendicular to the Newtonian orbital angular momentum of the system \mathbf{L}_N . For $q \geq 1$, the parallel scalar is given by [125, 350, 351]

$$\begin{aligned}\chi_{\text{eff}} &\equiv (X_1 \boldsymbol{\chi}_1 + X_2 \boldsymbol{\chi}_2) \cdot \hat{\mathbf{L}}_N \\ &= (\hat{\mathbf{S}} + \hat{\mathbf{S}}_*) \cdot \hat{\mathbf{L}}_N \\ &= \tilde{a}_0\end{aligned}\tag{2.1}$$

where $\hat{\mathbf{L}}_N \equiv \mathbf{L}_N/|\mathbf{L}_N|$. This is a conserved quantity of the orbit-averaged precession equations over the precession timescale [351]. The perpendicular scalar, first introduced in Ref. [164], is defined as

$$\chi_p \equiv m_1^{-2} \max \left\{ |\mathbf{S}_{1,\perp}|, q \frac{4+3q}{3+4q} |\mathbf{S}_{2,\perp}| \right\},\tag{2.2}$$

where $\mathbf{S}_{i,\perp} \equiv \mathbf{S}_i - (\hat{\mathbf{L}}_N \cdot \mathbf{S}_i) \hat{\mathbf{L}}_N$ are the components of \mathbf{S}_i perpendicular to $\hat{\mathbf{L}}_N$ for $i = 1, 2$.

2.1 Twist and Reference frames

In binaries containing spinning objects, the spin-orbit and the spin-spin interactions contribute significantly to the phase evolution and can modulate distinguishably the amplitude of the emitted GWs. When the spins of the binary components $\mathbf{S}_1, \mathbf{S}_2$ are not aligned with the orbital angular momentum \mathbf{L} of the system, all three vectors precess around the total angular momentum vector $\mathbf{J} = \mathbf{L} + \mathbf{S}_1 + \mathbf{S}_2$ [352]. Accordingly, the orbital plane of the binary is not fixed throughout its evolution, but rather precesses, inducing non-trivial modulations in the gravitational waves detected by an inertial observer. In this scenario, the dominant emission of gravitational radiation

happens along the direction perpendicular to the orbital plane, i.e., along the Newtonian orbital angular momentum \mathbf{L}_N [353–356]. It is then possible to identify a special “co-precessing” non-inertial frame, which follows the evolution of \mathbf{L}_N . In this frame, the modulations of amplitude and phase due to precession effectively disappear [357] and the waveform can be well approximated by that emitted from an aligned spin system. Then, given the evolution of the co-precessing frame (i.e., of the vectors $\mathbf{S}_1, \mathbf{S}_2$ and \mathbf{L}_N) and a co-precessing waveform, it is possible to rotate the latter into the inertial source frame and obtain the associated precessing waveform [353, 354, 358]. This technique is usually referred to as the “twist”, due to the time-dependent rotation which relates the two frames. To perform the twist, one can in principle use either the frame set by the Newtonian orbital angular momentum \mathbf{L}_N or \mathbf{L} . Since, by definition, \mathbf{L}_N remains orthogonal to the orbital plane, we employ this frame for the twist. Reference [359] has shown that the differences in the \mathbf{L} -frame vs. \mathbf{L}_N -frame twisted waveforms as compared with precessing NR waveforms are marginal. Accordingly, we define our inertial source frame such that its z axis is aligned with the initial ($t = 0$) Newtonian orbital angular momentum $\mathbf{L}_N(0)$, and the x axis is identified by the vector $\mathbf{r}(0)$ connecting the bodies. Then, following usual conventions, we choose the line of sight vector $\hat{\mathbf{N}}$ to have spherical angles $(\iota, \pi/2 - \phi_{\text{ref}})$ and define the initial spin components, $\mathbf{S}_1(0), \mathbf{S}_2(0)$, in this so-called L_0 frame. We then track the evolution of \mathbf{L}_N with respect to this frame via its spherical angles α and β , defined using the Cartesian components of the unit vector $\hat{\mathbf{L}}_N$

$$\alpha = \arctan(\hat{\mathbf{L}}_{Ny}/\hat{\mathbf{L}}_{Nx}), \quad (2.3)$$

$$\beta = \arccos(\hat{\mathbf{L}}_{Nz}). \quad (2.4)$$

A third angle γ , which identifies the co-precessing frame univocally with respect to the L_0 frame [355], is given by

$$\dot{\gamma} = \dot{\alpha} \cos \beta, \quad (2.5)$$

where the overdot denotes differentiation with respect to time. With α, β , and γ , the twisted (precessing) multipolar waveform $h_{\ell m}^T$ is obtained via an Euler rotation

$$h_{\ell m}^T = \sum_{m'=-m}^m h_{\ell m'}^A D_{m',m}^{*\ell}(-\gamma, -\beta, -\alpha), \quad (2.6)$$

where $h_{\ell m}^A$ are the spin-aligned waveforms in the co-precessing frame and $D_{m',m}^{*(\ell)}(-\gamma, -\beta, -\alpha)$ are the Wigner D matrices, defined as

$$D_{m',m}^{(\ell)}(\alpha, \beta, \gamma) = e^{-im'\alpha} e^{-im\gamma} d_{m',m}^{\ell}(\beta) \quad (2.7)$$

with

$$\begin{aligned} d_{m',m}^{\ell}(\beta) &= \sum_{k_i}^{k_f} (-1)^{k-m+m'} \\ &\times \frac{\sqrt{(\ell+m)!(\ell-m)!(\ell+m')!(\ell-m')!}}{k!(\ell+m-k)!(\ell-k-m')!(k-m+m')!} \\ &\times \left[\cos \frac{\beta}{2} \right]^{2\ell-2k+m-m'} \left[\sin \frac{\beta}{2} \right]^{2k-m+m'}. \end{aligned}$$

Finally, the plus and cross GW polarizations h_+ and h_{\times} are obtained from the twisted modes as

$$h_+ - ih_{\times} = \sum_{\ell,m} h_{\ell m}^T {}_{-2}Y^{\ell m}(\iota, \pi/2 - \phi_{\text{ref}}), \quad (2.8)$$

where ${}_{-2}Y^{\ell m}(\iota, \phi)$ are the standard spin weight $s = -2$ spherical harmonics. Our baseline model for the spin-aligned co-precessing waveforms is **TEOBResumS v2** [144, 285], a multipolar EOB model for quasi-circular BBH and BNS coalescences.

2.2 Spin dynamics

2.2.1 Time evolution of the orbital frequency

To obtain the time and frequency evolution of the Euler angles α, β and γ we follow Ref. [258] and solve the PN spin-evolution equations for $\mathbf{S}_1, \mathbf{S}_2$, and $\hat{\mathbf{L}}_N$ at the next-to-next-to-next-to-next-to-leading order (N3LO). To avoid clutter, we present the evolution equations up to the next-to-leading order (NLO), which can be cast into classical precession equations

$$\dot{\mathbf{S}}_i = \boldsymbol{\Omega}_i \times \mathbf{S}_i, \quad (2.9a)$$

$$\dot{\hat{\mathbf{L}}}_N = \boldsymbol{\Omega}_{\text{NLO}} \times \hat{\mathbf{L}}_N, \quad (2.9b)$$

for $i = 1, 2$. The precession frequencies are given by

$$\boldsymbol{\Omega}_1 = v^5 \left[\nu \left(2 + \frac{3}{2} \frac{X_2}{X_1} \right) \hat{\mathbf{L}}_N + \frac{v}{2} \left\{ \mathbf{S}_2 - 3 \left[\left(\frac{X_2}{X_1} \mathbf{S}_1 + \mathbf{S}_2 \right) \cdot \hat{\mathbf{L}}_N \right] \hat{\mathbf{L}}_N \right\} \right], \quad (2.10a)$$

$$\boldsymbol{\Omega}_{\text{NLO}} = -\frac{v}{\nu} (\boldsymbol{\Omega}_1 + \boldsymbol{\Omega}_2), \quad (2.10b)$$

where v is the relative speed of the binary components and $\boldsymbol{\Omega}_2$ is obtained from $\boldsymbol{\Omega}_1$ with $1 \leftrightarrow 2$. The N3LO expression for this system of nine coupled ODEs is explicitly given in equations (4a)-(4b) and (7) of Ref. [258], together with an expression for the evolution of the orbital frequency under radiation reaction for which we employed a TaylorT4-resummed PN expression in our previous work: $\dot{\omega}^{\text{PN}}$ [331, 357]. Specifically, we employed the expressions from Ref. [360] up to 3.5PN, which are integrated together with the spin ODEs in order to evolve the system under radiation reaction.

2.2.2 Coupling of the PN spin evolution to the EOB dynamics

When analyzing long signals, neglecting the evolution of the spins in the aligned-spin dynamics can lead to non-negligible errors. In principle, one should evolve the full EOB equations, coming from a general Hamiltonian where the orbital plane is not fixed. Similarly, the waveform and radiation reaction of the model, too, would need to be extended to incorporate the effect of the planar components of the spins. This general approach would increase the already significant computational cost related to the solution of the Hamilton equations. Luckily, it was found [361] that good agreement with NR waveforms can be achieved by simply replacing in the waveform and radiation reaction the fixed values of χ_i with the time-dependent projections of the spin vectors onto the orbital angular momentum, i.e., $\hat{\mathbf{L}}_N(t) \cdot \boldsymbol{\chi}_i(t)$.

In our model, we (optionally) employ the spin dynamics to compute the projections of the spins onto $\hat{\mathbf{L}}_N$. We proceed as follows: (i) the PN spin-dynamics is independently evolved with the N3LO description of the precession equations with $\dot{\omega}^{\text{PN}}$ detailed above; (ii) we interpolate the spin and angular momentum components as functions of the ‘‘spin’’ orbital frequency ω coming from our PN evolution; (iii) at each step of the EOB evolution, we compute the EOB orbital frequency and evaluate $\boldsymbol{\chi}_{i,z}(\omega = \omega_{\text{EOB}}) \equiv \hat{\mathbf{L}}_N(\omega = \omega_{\text{EOB}}) \cdot \boldsymbol{\chi}_i(\omega = \omega_{\text{EOB}})$ via the splines calculated above; (iv) finally, these quantities are inserted into the appropriate places in the EOB dynamics. This generic procedure is applied both when numerically evolving the ODE system and when applying the PA approximation of Ref. [284].

To gauge the impact of the spins’ projection on the waveform, we compute the mismatches (see Sec. 2.3.1) obtained between `TEOBResumS` waveforms with an inclination of $\iota = \pi/3$, evolved either with or without spin projection, for a set of waveforms with $q \in [1, 6]$, $M \in [50, 225]M_\odot$, $\chi_p \in [0., 0.8]$ and $\chi_{\text{eff}} \in [-0.45, 0.65]$. We find that, although a large portion of the mismatches lie below the 10^{-3} threshold, the effect of the spin projection can be relevant for binaries with large in-plane spin components, for which the parallel components of the spins to the orbital angular momentum varies more, and can lead to mismatches larger than 1%.

2.2.3 BBH Merger-Ringdown

To model the final state of the BBH one can employ the fits of Ref. [319] with minor modifications to account for the non-null planar components of the BHs’ spins. Following Ref. [156], we define the remnant spin as:

$$\chi_f = \sqrt{(\chi_{f\parallel})^2 + (S_\perp/M_f)^2}, \quad (2.11)$$

where $\chi_{f\parallel}$ and M_f are estimated from the fits of Ref. [319] using the parallel component of the spins to the orbital angular momentum at merger, and \mathbf{S}_\perp is given by

$$\mathbf{S}_\perp = \mathbf{S}_1(\omega_{\text{mrg}}) - \mathbf{S}_{1\parallel}(\omega_{\text{mrg}}) + (1 \leftrightarrow 2). \quad (2.12)$$

Figure 2.1 displays the accuracy of the fits when compared to a handful of `SXS` NR simulations. We also compare the output of the fit above to the values obtained with the “simple” aligned-spin fit, and with the fits provided by the surrogate model of Refs. [172, 362]. Notably, while the mass of the remnant is approximated (by all approaches) at the level of 10^{-3} , the difference $|\chi_f^{\text{NR}} - \chi_f^{\text{surr}}|$ is up to ten times smaller with respect to the other approaches. This result is not surprising, and is in line with the discussion presented in Ref. [172]. Therefore, although all the results presented in this paper will employ Eq. (2.11), we also implemented the option to take χ_f and M_f as input parameters. This way, by externally computing the remnant properties with the surrogate model (using the `surfInBH` package), we can easily obtain a precise description of the final BH.

For a complete model of the ringdown phase, it is necessary to also extend the Euler angles α, β, γ beyond the merger. The precession of the orbital momentum effectively stops at the merger, and the direction of the spin of the final BH can be thought of as constant, and well-enough approximated by the direction of the angular momentum at

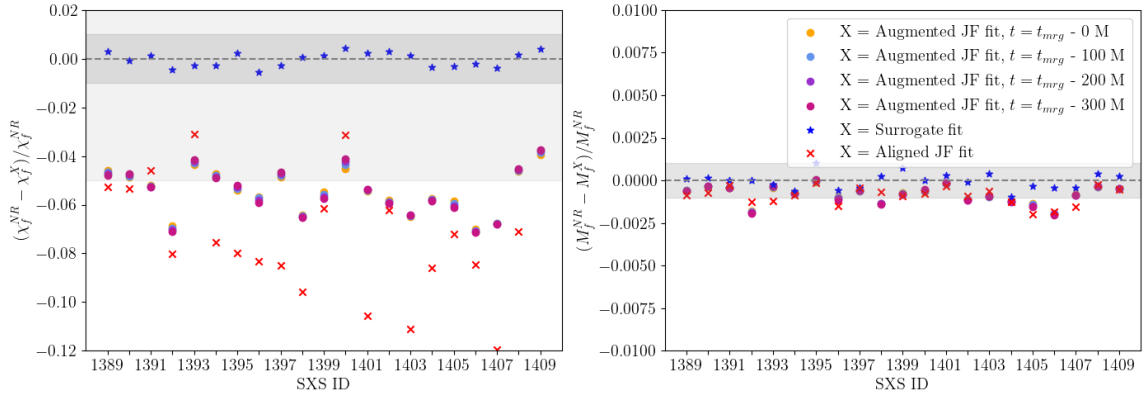


FIGURE 2.1: Relative differences in the dimensionless spin χ_f of the final BH (left) and its mass M_f (right) between NR simulations and fits of Ref. [172] (blue stars) and the various Jimenez-Forteza (JF) fits of Ref. [319]. The latter are evaluated with the initial z component spins (red crosses) or corrected to account for the precession by employing the spins at a reference time before merger like in Eq. (2.11). While the remnant mass is always estimated at the order of 10^{-3} and the two methods give comparable results, the surrogate fit for the remnant spin is up to an order of magnitude more precise. In the left panel, light (dark) gray bands highlight the 5% (1%) relative error interval; in the right panel the 1‰ one.

merger. Therefore, one option is to simply prolong the angles by fixing them to their value at merger. Alternatively, it was observed that the evolution of the α angle can be approximately described through the difference of the $\ell = 2$ fundamental QNMs [138, 363]

$$\alpha(t) = \begin{cases} \alpha(t_{\text{mrg}}) + (\omega_{220} - \omega_{210})(t - t_{\text{mrg}}), & \boldsymbol{\chi}_f \cdot \hat{\mathbf{L}}_{Nf} > 0, \\ \alpha(t_{\text{mrg}}) + (\omega_{2-10} - \omega_{2-20})(t - t_{\text{mrg}}), & \boldsymbol{\chi}_f \cdot \hat{\mathbf{L}}_{Nf} < 0, \end{cases} \quad (2.13)$$

where $\boldsymbol{\chi}_f = \boldsymbol{\chi}_1(\omega_{\text{mrg}}) + \boldsymbol{\chi}_2(\omega_{\text{mrg}})$ and $\omega_{\ell m 0}$ are the fundamental QNMs for $\ell = 2$ and $m = 2, 1, -1, -2$ [312]. One can then fix β to its value at the merger. γ is subsequently computed by integrating its evolution equation (2.5). Both options for the post-merger evolution of α are currently available in `TEOBResumS` public code, and users can choose between one or the other. The default behavior is given by the QNMs extension, which gives marginally better results when computing mismatches between EOB and NR waveforms (see Sec. 2.3).

2.2.4 BNS Frequency-domain waveforms

As discussed in Chapter 1.4, spin-aligned EOB models can be straightforwardly extended to the FD by applying a SPA to the multipolar modes $h_{\ell m}(t)$. The FD, spin-aligned modes $\tilde{h}_{\ell m}(f)$ can then be twisted and combined into plus and cross

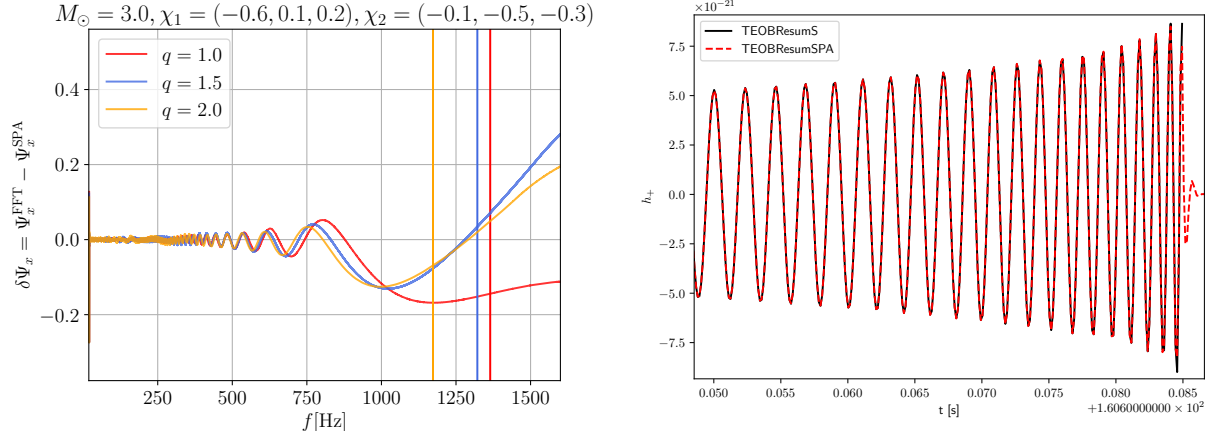


FIGURE 2.2: Comparison between TD and FD models. Left: phase differences between the FD cross polarizations h_{\times} obtained either by twisting SPA-transformed modes or directly via FFT. The three fiducial BNS systems considered have varying mass ratios $q = \{1, 1.5, 2\}$ and fixed spins, total masses and tidal parameters. Vertical colored lines denote the merger frequency. At merger, the largest phase difference amounts to ≈ -0.2 radians. Right: TD plus polarizations corresponding to the $q = 2$ system displayed in the left panel.

polarization as [166]:

$$\tilde{h}_{+} = \frac{1}{2} \sum_{\ell \geq 2} \sum_{m' > 0} e^{im'\gamma} \tilde{h}_{\ell m'} \times \sum_{m=-\ell}^{\ell} \left[e^{-im\alpha} d_{mm'-2}^{\ell} Y^{\ell m} + (-1)^{\ell} e^{im\alpha} d_{m-m'-2}^{\ell} Y^{\ell m*} \right], \quad (2.14a)$$

$$\tilde{h}_{\times} = \frac{1}{2} \sum_{\ell \geq 2} \sum_{m' > 0} e^{im'\gamma} \tilde{h}_{\ell m'} \times \sum_{m=-\ell}^{\ell} \left[e^{-im\alpha} d_{mm'-2}^{\ell} Y^{\ell m} - (-1)^{\ell} e^{im\alpha} d_{m-m'-2}^{\ell} Y^{\ell m*} \right]. \quad (2.14b)$$

The sign differences in our expressions with respect to those presented in Ref. [166] come from the EOB convention that the phase of the TD multipoles $h_{\ell m}$ with $m > 0$ is positive. Hence, $\tilde{h}_{\ell m}(f) = 0$ for $m > 0$ and $f < 0$. The Euler angles α, β, γ are all evaluated at the SPA frequencies $2\pi f/m$.

Figure 2.2 displays the phase difference in the frequency domain of the cross polarization h_{\times} computed between the FFT of precessing TEOBResumS TD signals and the SPA-based model described above. We consider three nominal BNS systems with fixed spins $\chi_1 = (-0.6, 0.1, 0.2)$, $\chi_2 = (-0.1, -0.5, -0.3)$ inspiralling from an initial frequency $f_0 = 20$ Hz, tidal polarizability parameters $\Lambda_1 = \Lambda_2 = 400$, total mass $M = 3M_{\odot}$ and mass ratios of 1, 1.5, and 2. For all three cases considered, we find that the phase difference at the merger (represented by the vertical lines) lies below

0.2 rad. The visual agreement in the TD between the inverse-FFT'd SPA waveform and the TD template can instead be inspected from the right panel of Fig. 2.2. The conclusions of Ref. [332] regarding the validity of the SPA up to merger can be applied also to precessing BNS systems. At the same time, the SPA-based model is less computationally expensive than its TD counterpart thanks to the non-uniform time grid which is employed for the inspiral. Moreover, and more importantly, it opens to the possibility of generating waveforms directly over a non-uniform frequency grid, optimized for PE, allowing the application of techniques such as relative binning [364] or multibanding [365].

2.3 Validation

In this section we compare our EOB model to (i) the set of 99 precessing SXS simulations also employed in Ref. [156], supplemented with the longer precessing simulations SXS : BBH : 1389 to SXS : BBH : 1409, and (ii) 5000 NRsur7dq4 (henceforth NRsur) waveforms, spanning $q \in [1, 4]$ and $|\chi_i| \in [0.1, 0.8]$ yielding a range of $-0.8 \leq \chi_{\text{eff}} \leq 0.8$ and $0.0 \leq \chi_p \leq 0.8$. We compute the sky-averaged faithfulness (see Sec. IV of Ref. [366]) for all considered templates. Then, for a selected number of systems, we align the time-domain polarizations and compute the cumulative phase difference of the waveform $h = h_+ - ih_\times$. Overall, we find that the maximum mismatch between TEObResumS and SXS is obtained for very asymmetric, highly spinning binaries. The same statement holds for NRsur – TEObResumS mismatches.

2.3.1 Faithfulness

As discussed in Sec. 1.5, the agreement between a target model s and a generic template h is usually quantified through the faithfulness (or match) \mathcal{F} , defined as the normalized inner product between s and h , maximized over the reference time and phase t_0, φ_0 , see Eq. (1.24). However, when the template waveform incorporates higher modes or if the system is precessing, this definition is not completely independent of the extrinsic parameters of the binary. In general, the target and template waveforms are obtained from the plus and cross polarizations as:

$$k_i = F_+(\theta^i, \phi^i, \psi^i)k_+(\iota^i, \varphi_0^i, t_0^i, \Theta^i) + F_\times(\theta^i, \phi^i, \psi^i)k_\times(\iota^i, \varphi_0^i, t_0^i, \Theta^i), \quad (2.15)$$

where $i = s, h$ and $\theta, \phi, \psi, \iota, \Theta$ are, respectively, the right ascension, declination, polarization, inclination, and intrinsic parameters (masses, spins, tidal parameters etc.) of the binary system. Equation (2.15) can be rearranged into

$$k_i = \mathcal{A}(\theta^i, \phi^i) [\cos \kappa(\theta^i, \phi^i, \psi^i) k_+(\iota^i, \varphi_0^i, t_0^i, \Theta^i) + \sin \kappa(\theta^i, \phi^i, \psi^i) k_\times^i(\iota^i, \varphi_0^i, t_0^i, \Theta^i)], \quad (2.16)$$

where κ denotes the effective polarizability and

$$e^{i\kappa(\theta, \phi, \psi)} = [F_+(\theta, \phi, \psi) + iF_\times(\theta, \phi, \psi)] / \mathcal{A}(\theta, \phi), \quad (2.17)$$

$$\mathcal{A}(\theta, \phi) = \sqrt{F_+^2(\theta, \phi, \psi) + F_\times^2(\theta, \phi, \psi)}. \quad (2.18)$$

When only $(2, \pm 2)$ modes are considered, it can be shown that Eq. (1.24) depends on extrinsic parameters only through overall amplitude and phase factors. On the other hand, when higher modes are considered, the dependence on the extrinsic quantities is nontrivial.

We define the (template) sky-maximized (SM) faithfulness between the target strain and the waveform template as

$$\mathcal{F}_{\text{SM}} = \max_{t_0^h, \varphi_0^h, \kappa^h} \frac{(s, h)}{\sqrt{(s, s)(h, h)}}, \quad (2.19)$$

where we dropped the explicit dependence on intrinsic and extrinsic parameters in the right-hand side. Accordingly, the unfaithfulness is given by $\bar{\mathcal{F}}_{\text{SM}} = 1 - \mathcal{F}_{\text{SM}}$. This quantity is computed following the procedure outlined in Sec. IV of Ref. [366]. The maximization over κ is performed analytically, while t_0 is maximized via the inverse FFT. The maximization over the reference phase φ_0 is performed numerically through a dual annealing algorithm, similar to what is done in Ref. [166]. Finally, we mention that for precessing systems one additional degree of freedom remains: the freedom to perform a rigid rotation of the in-plane spin components about the initial \hat{z} axis, which is equivalent to choosing different initial conditions for the α (and γ) Euler angles. We further maximise \mathcal{F}_{SM} over such a rotation by once more relying on a dual annealing algorithm. We note that this procedure differs from the one employed in Ref. [138], where instead the initial (reference) frequency is varied, and the initial in-plane spin components are kept fixed to their nominal target value.

Once \mathcal{F}_{SM} (or, equivalently, $\bar{\mathcal{F}}_{\text{SM}}$) is computed as described, we normalize it over the SNR of the signal and further average over the sky angles of the target waveform,

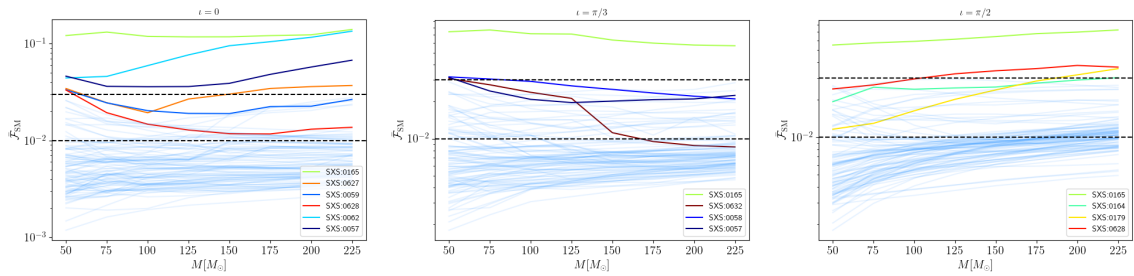


FIGURE 2.3: NR/EOB mismatch, $\bar{\mathcal{F}}_{SM}$, for the 99 SXS short precessing simulations computed with strain mode content $\ell \leq 4 + (5, \pm 5)$, plotted as a function of the total mass of the system and computed with a fixed inclination of the binary of $\iota = \{0, \pi/3, \pi/2\}$ (top, middle and bottom panels, respectively). A total of ten configurations have $\bar{\mathcal{F}}_{SM}$ which reaches up to 3%. The dashed horizontal lines in each panel mark the 3% and 1% thresholds.

in order to completely marginalize over any dependence of the mismatch on the sky position and obtain values which depend exclusively on the intrinsic parameters of the source. We consider N_φ values of $\varphi_0^s \in [0, 2\pi)$ and N_κ values of $\kappa^s \in [0, 2\pi)$, and present the average value over $N_\varphi \times N_\kappa$ values.

2.3.2 BBH IMR EOB/NR comparison

To validate the performance of our model, we compare our waveforms with a set of selected SXS NR simulations. In particular, we focus on two different sets: 99 “short” waveforms, with $\chi_p \lesssim 0.84$, $\chi_{\text{eff}} \in [-0.45, 0.65]$ and $q \lesssim 6$, and 21 “long” simulations with $\chi_p \lesssim 0.49$, $\chi_{\text{eff}} \in [-0.2, 0.3]$ and $q \lesssim 4$, spanning from ~ 60 to ~ 146 orbits. To translate the NR data from the NR frame into the source frame described in Sec. 2.1, we make use of the public catalog tools available at [367] and described in, e.g., Ref. [368]. For all unfaithfulness computations, we consider total detector-frame masses $M \in [50, 225]M_\odot$, employ the zero-detuned high-power PSD of Ref. [335] and average $\bar{\mathcal{F}}_{SM}$ over a grid $\kappa^{\text{NR}} = \{0, \pi/2, \pi, 3/2\pi\}$ and $\varphi_0^{\text{NR}} = \{0, 2\pi/5, 4\pi/5, 6\pi/5, 8\pi/5\}$. We perform our computations over the frequency range $[f_{\text{min}}, 2048]$ Hz, where f_{min} is the initial GW frequency of the NR waveform, expressed in physical units.

“Short” SXS simulations Figure 2.3 shows the sky-averaged $\bar{\mathcal{F}}_{SM}$ as a function of the total binary mass for three different choices of the binary inclination, $\iota = \{0, \pi/3, \pi/2\}$. We find that when $\iota = 0$ ($\pi/3, \pi/2$), for all but six (four) notable simulations the EOB/NR unfaithfulness lies below the 3% threshold for all values of masses considered, and that 80% (76%, 68%) of the averaged $\bar{\mathcal{F}}_{SM}$ computed are smaller than

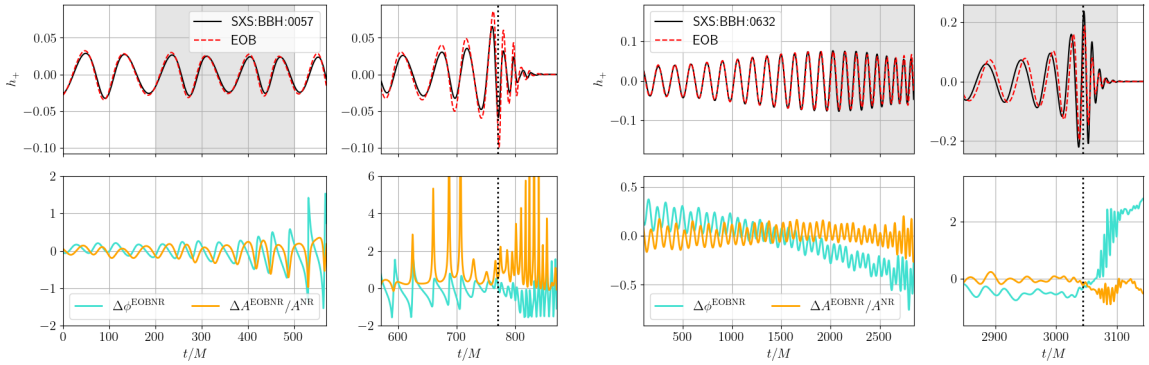


FIGURE 2.4: Visual comparison between the h_+ NR waveforms (black, solid curves) computed from `SXS:BBH:0057` (left panel) and `SXS:BBH:0632` (right panel) and the `TEOBResumS` waveforms obtained with the same intrinsic parameters (red, dashed), inclination $\iota = \pi/3$ and all modes with $\ell \leq 4$. The phase difference $\Delta\phi^{\text{EOBNR}} = \phi_{\text{NR}} - \phi_{\text{EOB}}$ is shown in cyan, and the relative amplitude error $\Delta A^{\text{EOBNR}}/A^{\text{NR}}$ in orange. Merger is indicated by a black dotted line. The waveforms are aligned by minimizing the phase difference in the time window highlighted in gray, see Eq. (30) of Ref. [168]. Both systems are characterized by very large in-plane spins at their initial reference frequency, with `SXS : BBH : 0057` also having $q > 5$. While the phase difference oscillates during the inspiral and generally remains below 1 rad, the dephasing and the amplitude relative differences increase at merger, indicating that an improved description of the final moments of the coalescence will be required.

1%. The configurations for which the EOB/NR faithfulness lies above the 3% threshold are highly asymmetrical ($q > 5$) or strongly precessing ($\chi_p > 0.7$) systems, with `SXS : BBH : 0165` being the most challenging one, as it is a $(q, \chi_{\text{eff}}, \chi_p) = (6, -0.45, 0.77)$ coalescence. In Fig. 2.4 we consider two more of these systems (`SXS : BBH : 0057` and `SXS : BBH : 0632`), and align the time-domain NR and EOB waveforms by minimizing their phase difference $\Delta\phi^{\text{EOBNR}} = \phi^{\text{NR}} - \phi^{\text{EOB}}$ over a chosen time-window (see e.g. [168]). We find that the EOB waveform correctly captures the behavior of the NR waveform up to few orbits before merger, where differences in phase and amplitude start to grow.

For comparison, we also compute $\bar{\mathcal{F}}_{SM}$ between the set of NR simulations here considered and the waveform approximant `IMRPhenomXPHM` [166], with fixed inclination $\iota = \pi/3$. Figure 2.5 shows the results of this calculation. We find that $\bar{\mathcal{F}}_{SM}^{\text{EOB}}$ varies between ~ 0.002 and 0.06, with the distribution median peaking at 0.007; while $\bar{\mathcal{F}}_{SM}^{\text{XPHM}}$ spans the interval ~ 0.002 to 0.1, with a median of 0.005. Overall, the two approximants give consistent results, with `TEOBResumS` generally performing marginally worse at high masses, and marginally better for $M < 75M_\odot$.

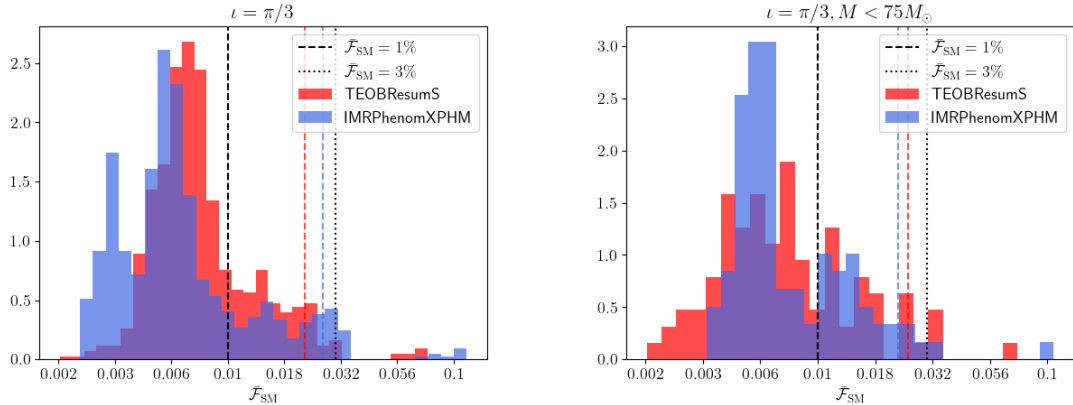


FIGURE 2.5: Left panel: the distribution of NR/TEOBResumS and NR/IMRPhenomXPHM mismatches for the 99 SXS short precessing simulations of Fig. 2.3, at a fixed binary inclination of $\iota = \pi/3$. The black dashed and the dotted black vertical lines mark the 1% and 3% thresholds, and dashed colored lines the 95th percentiles. We find that the performance of IMRPhenomXPHM is comparable to that of our EOB approximant, with $\bar{\mathcal{F}}_{SM}^{\text{EOB}}$ falling in the range 0.002 – 0.06 with median at 0.007, and $\bar{\mathcal{F}}_{SM}^{\text{XPHM}}$ falling within the interval 0.002 – 0.1 and having a median of 0.005. Right panel: the same plot as above, with total masses restricted to below $75M_{\odot}$. Overall, TEOBResumS performs slightly better than IMRPhenomXPHM for lower masses, and slightly worse for higher ones.

“Long” SXS simulations Figure 2.6 once more shows the sky-averaged $\bar{\mathcal{F}}_{SM}$ as a function of the total binary mass for three different choices of the binary inclination, $\iota = 0, \pi/3, \pi/2$. The mismatches behave similarly to what we described above in the sense that they generally degrade for increasing magnitude of in-plane spins and growing inclinations. This well-known fact can be appreciated also from Fig. 2.7, where we align the NR waveform SXS : BBH : 1397 and the corresponding EOB waveform. We compute the phase difference $\Delta\phi^{\text{EOBNR}}$ between the two, and find that for $\iota = 0$ it is constantly smaller than 0.1 rad during the inspiral, growing to ~ 0.6 rad after merger. For $\iota = \pi/3$ the phase difference displays larger oscillations, which are however always smaller than 0.5 rad. The relative difference in the amplitude $\Delta A^{\text{EOBNR}}/A^{\text{NR}} = (A^{\text{NR}} - A^{\text{EOB}})/A^{\text{NR}}$, instead, degrades after merger for the $\iota = \pi/3$ case. Nonetheless, for the case considered the behavior of both the EOB phase and amplitude remain correct during the merger.

Overall we find that all the mismatches computed lie below 3% for the inclinations considered, and 93% (98%, 87%) below 1% for $\iota = 0$ ($\iota = \pi/3, \pi/2$).

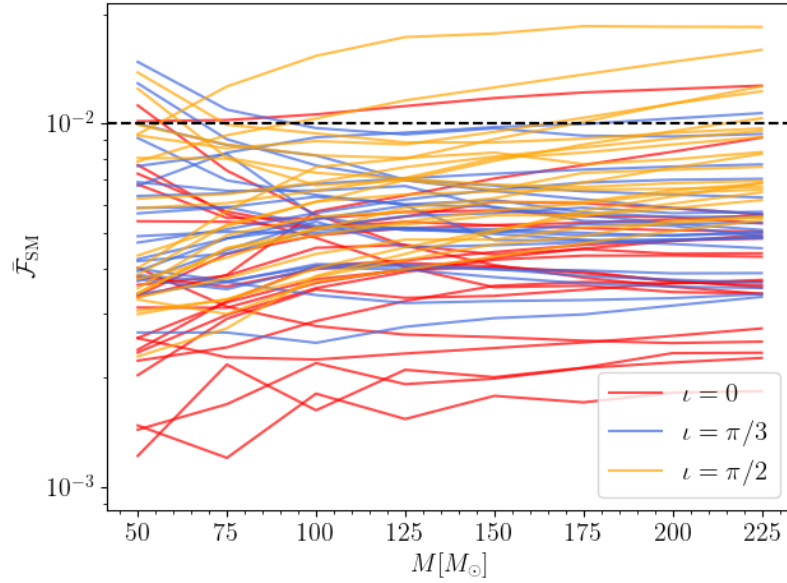


FIGURE 2.6: NR/EOB mismatch for the SXS long precessing simulations 1389 to 1409, plotted as a function of the total mass of the system and computed with a fixed inclination of the binary of $\iota = 0, \pi/3, \pi/2$ (red, blue and orange lines, respectively). The dashed black horizontal line marks the 1% threshold. No simulations have $\bar{\mathcal{F}}_{\text{SM}} > 3\%$ for any of the considered inclinations.

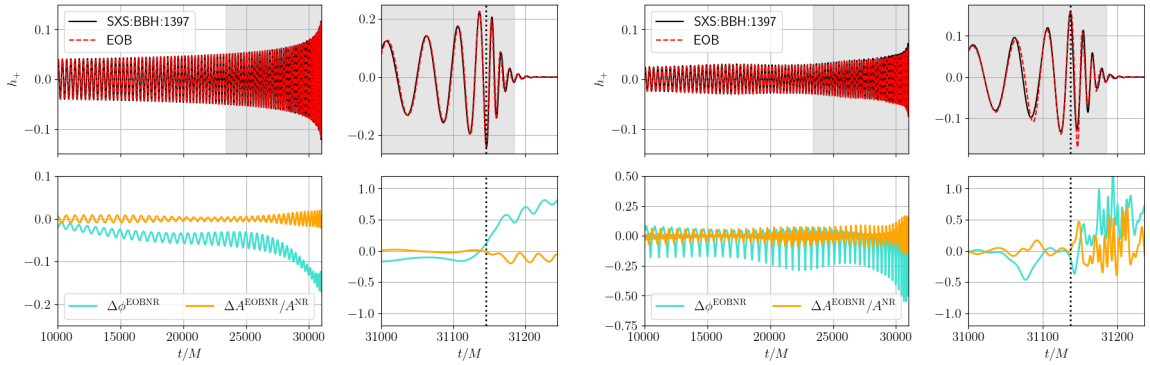


FIGURE 2.7: Visual comparison between the h_+ waveform computed from SXS:BBH:1397 (black, solid curves) with $\ell \leq 4$ and the TEOBResumS waveform obtained with the same intrinsic parameters (red, dashed) for two different inclinations, $\iota = 0$ (left panel) and $\iota = \pi/3$ (right panel). The phase difference $\Delta\phi^{\text{EOBNR}} = \phi_{\text{NR}} - \phi_{\text{EOB}}$ is shown in cyan, and the relative amplitude error $\Delta A^{\text{EOBNR}}/A^{\text{NR}}$ in orange. Merger is indicated by a black dotted line. The waveforms are aligned by minimizing the phase difference in the time window highlighted in gray. As the inclination increases, so do the importance of higher modes and the amplitude modulations due to precession.

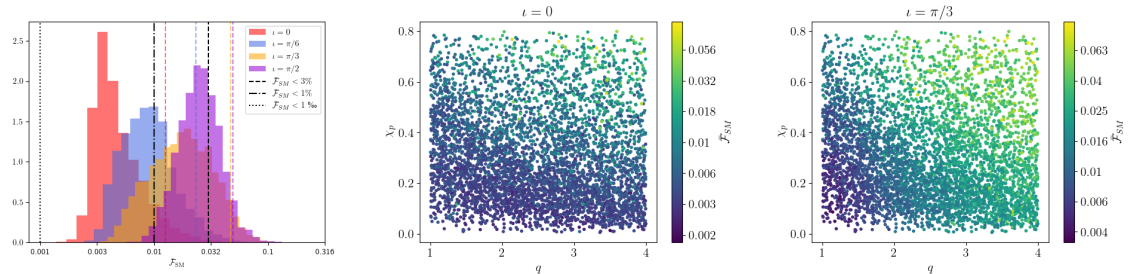


FIGURE 2.8: Top panel: NRSur7dq4/TEOBResumS sky maximized $\ell \leq 4$ mismatch for 5000 systems with $q \in [1, 4]$, spin magnitudes $\chi_i \in [0.1, 0.8]$ and random spin directions, computed from an initial frequency range of 20 to 37.5 Hz with the aLIGO design PSD noise curve up to 1024 Hz. The dotted, dot-dashed, and dashed vertical black lines mark unfaithfulness of 1%, 1%, and 3%, respectively. The colored, dashed vertical lines mark the 95th percentiles for the four distributions. Middle and bottom panels: the behavior of the mismatch over the $\{q, \chi_p\}$ parameter space for inclinations of 0 and $\pi/3$. The higher unfaithfulness values are obtained for highly asymmetrical systems, with large in-plane spins (high χ_p) and mass ratios of $q > 2$.

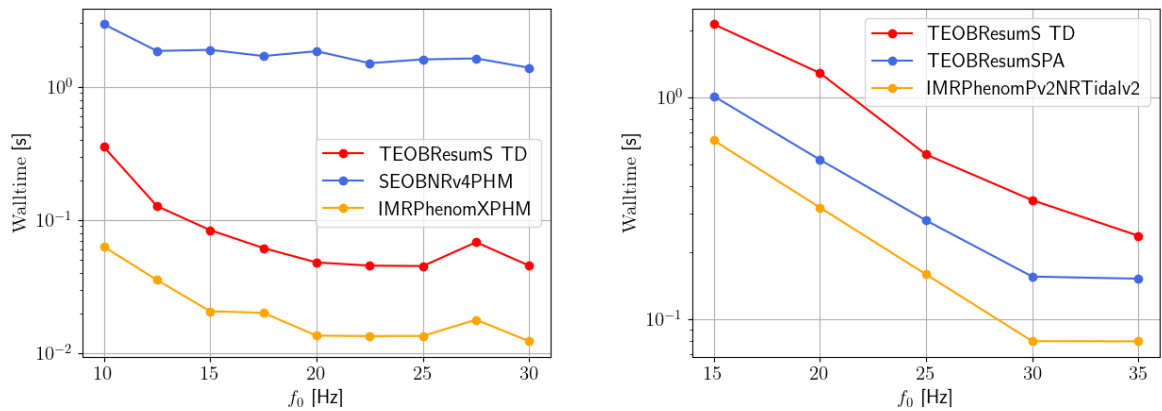


FIGURE 2.9: Left panel: BBH evaluation time for a $q = 1$, $M = 60M_\odot$ precessing system containing the $(\ell, m) = (2, 1), (2, 2), (3, 2), (3, 3), (4, 4)$ modes. Three different state of the art approximants are considered: TEOBResumS, IMRPhenomXPHM and SEOBNRv4PHM. TEOBResumS is approximately three times slower than IMRPhenomXPHM, and up to an order of magnitude faster than SEOBNRv4PHM. Right panel: BNS evaluation time for a $q = 1$, $M = 3.5M_\odot$ precessing system, whose waveform is constructed with the $(2, 2)$ mode. TD denotes the standard TD TEOBResumS model with SPA denoting the FD version of Sec. 2.2.4

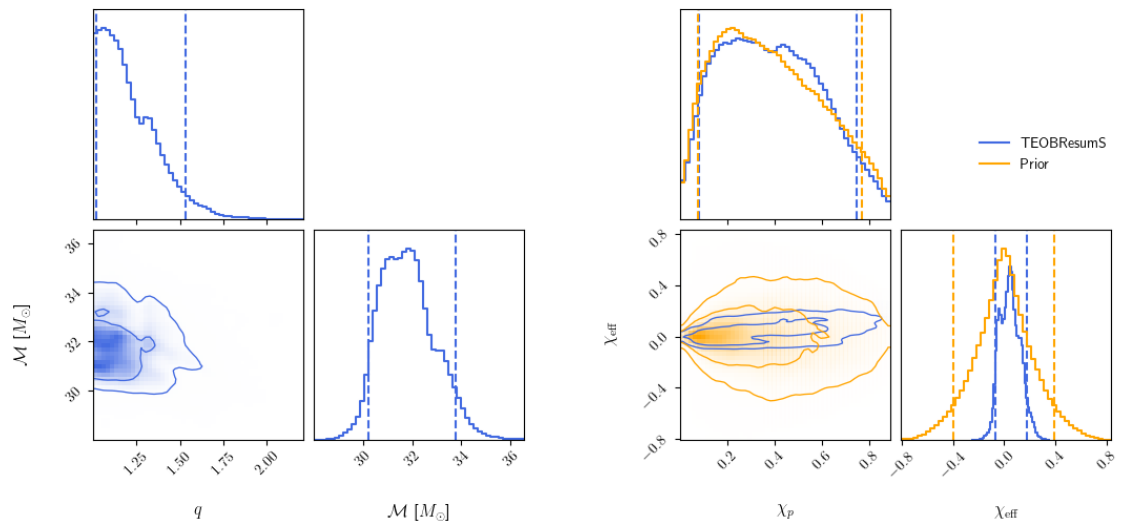


FIGURE 2.10: Posteriors for chirp mass, mass ratio and spins obtained by analyzing the GW150914 data with **TEOBResumS**, as discussed in Sec. 2.4.1. For comparison, we also plot the prior distributions for χ_{eff} and χ_p . As expected, the posterior distribution of χ_p is consistent with its prior. The masses obtained in our analysis are consistent with the ones previously reported in Ref. [34], but the uncertainties on q and \mathcal{M} are larger. This is due to the addition of four degrees of freedom, namely the in-plane spin components.

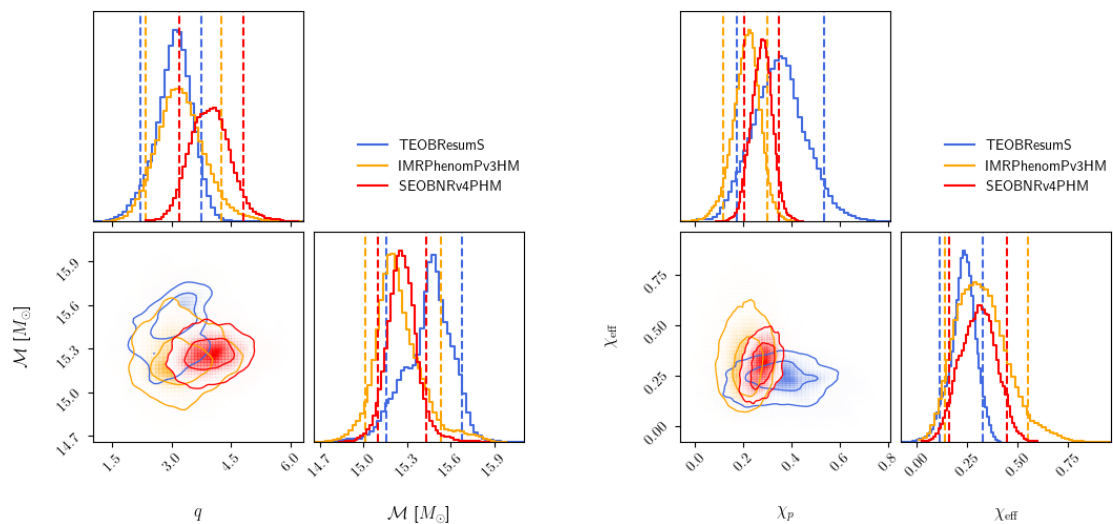


FIGURE 2.11: Posteriors for chirp mass, mass ratio and spins obtained by analyzing the GW190412 data with **TEOBResumS**, as discussed in Sec. 2.4.2. We compare our results to the public LVC posteriors obtained with the precessing models **SEOBNRv4PHM** and **IMRPhenomPv3HM**. The results of our analysis are broadly consistent with the ones obtained by LVC, although some model systematics are clearly present between the three approximants.

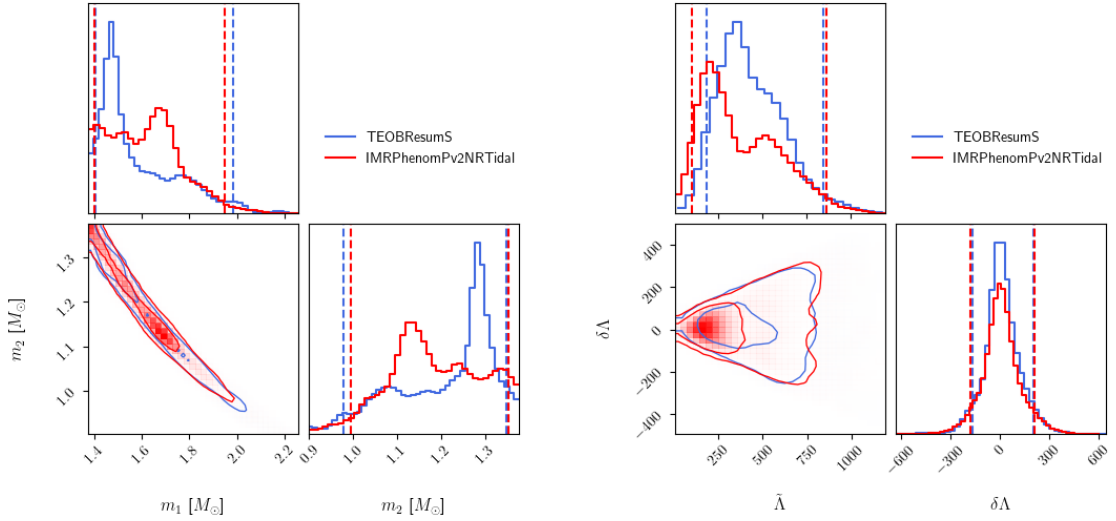


FIGURE 2.12: Marginalized, two dimensional posteriors for detector frame masses (left) and tidal parameters (right) for GW170817, obtained with the precessing `TEOBResumS` model or the phenomenological `IMRPhenomPv2NRTidal` model, from the analysis of Ref. [10]. The 90% intervals are compatible between the two models. We note that the `IMRPhenomPv2NRTidal` posteriors for $\tilde{\Lambda}$ display some bimodalities, which are due to the higher frequency cutoff employed for the analysis.

2.3.3 Comparison with NRSur7dq4

To extend the comparison to a larger number of binaries, we additionally computed $\bar{\mathcal{F}}_{\text{SM}}$ between our model and the NR surrogate model `NRSur7dq4` using all modes with $\ell \leq 4$. We considered 5000 systems with $q \in [1, 4]$, which is the calibration region of the surrogate, and spin magnitudes $\chi_{1,2} \in [0.1, 0.8]$ with uniformly distributed spin vector polar angles $\theta_{1,2} \in [0, \pi)$ and azimuthal angles $\phi_{1,2} \in [0, 2\pi)$. We set the initial GW frequency to 20 Hz for $M \geq 100M_{\odot}$ and to a linearly decreasing function of M from 37.5 to 20 Hz as M increases from 40 to 100 M_{\odot} . Figure 2.8 shows the distributions of the unfaithfulness obtained for inclinations of $\iota = 0, \pi/6, \pi/3$ and $\pi/2$. We find that, for $\iota = 0$, 98.8% of the systems considered have unfaithfulness below 3% and 87.8% below 1%, with a global distribution spanning the range $\bar{\mathcal{F}}_{\text{SM}} \in [0.0027, 0.04]$ with median 0.0046. As previously observed, the situation worsens as the inclination increases, with $\bar{\mathcal{F}}_{\text{SM}} \in [0.003, 0.05]$ for $\iota = \pi/6$, $\bar{\mathcal{F}}_{\text{SM}} \in [0.003, 0.1]$ for $\iota = \pi/3$ and $\bar{\mathcal{F}}_{\text{SM}} \in [0.006, 0.14]$ for $\iota = \pi/2$. For $\iota = \pi/3$, only 80% (21%) of the total mismatches are below the 3% (1%) threshold. The degradation of the unfaithfulness is observed especially for asymmetric binaries with large χ_p as can be discerned by comparing the middle and bottom panels of Fig. 2.8.

2.3.4 Waveform’s timing evaluation

We now test the computational efficiency of our EOB model, and compare it to other state of the art precessing approximants for BBH and BNS coalescences, `SEOBNRv4PHM`, `IMRPhenomXPHM` and `IMRPhenomPv2NRTidalv2`. We choose one reference equal mass BBH binary, with $M = 60M_{\odot}$ and $\chi_1 = (-0.6, 0.1, 0.2)$, $\chi_2 = (0.1, -0.5, -0.3)$, and a list of initial frequencies $f_0 = \{10, 12.5, 15, 17.5, 20., 22.5, 25, 27.5, 30\}$ Hz. For each initial frequency f_0^i we calculate the average time (over 20 repetitions) needed to evolve the binary and produce the h_+ and h_{\times} polarization. This process is then repeated for a BNS configuration with $q = 1$, $M = 2.8M_{\odot}$ and same spins as the previous BBH system, and a choice of initial frequencies $f_0 = \{15, 20, 25, 30, 35\}$ Hz. We performed this test on a Huawei MateBook 14 with AMD Ryzen 5 2500U processors and 8 GB RAM.

The results are displayed in Fig. 2.9. We find that, for BBH systems, `TEOBResumS` is approximately three to four times slower than `IMRPhenomXPHM` and about one order of magnitude faster than `SEOBNRv4PHM`. For BNS systems, instead, the FD model is about two times faster than its TD counterpart, and two times slower than the phenomenological `IMRPhenomPv2NRTidalv2`. We highlight that the main evaluation cost for both the TD and FD `TEOBResumS` models comes from the twisting procedure itself, rather than from the solution of the two (PN and EOB) dynamics ODE systems.

2.4 Parameter estimation

We demonstrate possible applications of our model by performing PE on real GW data. We re-analyze the data of GW150914 and GW190412, and show that the posteriors obtained are consistent with those presented in, e.g., Refs. [10, 227]. Finally, we analyze GW170817 [12, 19, 369]. All of our PE studies are performed with the `BAJES` pipeline [34] and the `dynesty` [204] sampler.

2.4.1 GW150914

For our study, we consider 8seconds of data centered around the GPS time of the event. We employ 4096 live points, and analyze the frequencies between 20 and 1024 Hz. We fix the sampling rate to 4096 Hz, and sample the component masses enforcing that the chirp mass lies in $\mathcal{M} \in [12.3, 45]M_{\odot}$, the mass ratio $q \in [1, 8]$, and the spin magnitudes $|\chi_i| \in [0, 0.89]$ with $i = 1, 2$ with an isotropic prior for the tilt angles. We

consider all modes up to $\ell = 4$, and marginalize over the timeshift. Finally, we employ 10 calibration nodes, and the PSD given in Ref. [10]. Fig. 2.10 displays the posteriors we recovered from our analysis. We find that $\mathcal{M} = 31.7_{-1.5}^{+2.0} M_{\odot}$, $q = 1.17_{-0.16}^{+0.36}$, $\chi_{\text{eff}} = 0.04_{-0.08}^{+0.09}$ and $\chi_p = 0.38_{-0.29}^{+0.37}$. Our results are consistent with the analyses presented in Refs. [10, 205, 370], performed with other approximants, and with the PE conducted in Ref. [34], which employed the non-precessing version of `TEOBResumS`. The posteriors of χ_p are consistent with the prior as GW150914 displays no evidence of precession. Notably, the introduction of additional spin components widens the credible intervals on the component masses with respect to the analysis of Ref. [34], obtained with the same approximant and similar settings.

2.4.2 GW190412

The original LVK analysis has yielded well constrained imprints of spin precession with $0.15 \lesssim \chi_p \lesssim 0.5$ and $\theta_1 = 0.80_{-0.36}^{+0.52}$ [227], support for $\chi_{\text{eff}} > 0$ with 95% credibility [227], and clear evidence of the subdominant modes carrying a significant portion of the signal SNR. A number of following studies have further improved on the original analysis by investigating in more detail the effects of the higher modes [371] and of the chosen priors [372] on the PE. The same works also carried out studies to understand the differences observed when different waveform models are employed to analyze the signal. Although such detailed investigations lie beyond the scope of this *Thesis*, it is clear that the exceptional nature of GW190412 makes it very desirable to analyze with `TEOBResumS`.

We employ 4096 live points and analyze the frequencies between 20 and 1024 Hz with a fixed sampling rate of 4096 Hz. We sample in the component masses, requiring that the chirp mass falls in $\mathcal{M} \in [8, 20] M_{\odot}$ and the mass ratio $q \in [1, 10]$. We sample in spin magnitudes $|\chi_i| \in [0, 0.89]$ with $i = 1, 2$, enforcing an isotropic prior for the tilt angles. Once again, we consider all modes up to $\ell = 4$, and marginalize over the timeshift.

Posteriors for the masses and spins are plotted in Fig. 2.11. We compare the results obtained in our PE with the publicly available LVC posterior samples, obtained with the two independent models `SEOBNRv4PHM` [138] and `IMRPhenomPv3HM` [162]. We find that `TEOBResumS` gives estimates of GW190412 parameters that are overall consistent with those computed from the other two approximants. We obtain a slightly larger chirp mass, and overall wider χ_p and tighter χ_{eff} posteriors.

2.4.3 GW170817

Though observations from millisecond pulsars yield at most dimensionless spins of $\chi \approx 0.5$ [373] and the fastest observed NS spin in electromagnetically observed binary pulsars is $\chi \lesssim 0.05$ [374, 375], the spins of the components of GW170817 are not well constrained [10, 12]. For our re-analysis we employ 6000 live points and consider 128 seconds around the GPS time of the event, analyzing the frequencies between 20 and 1024 Hz to minimize waveform systematics [332]. We sample the component masses imposing that $\mathcal{M} \in [1.1, 1.3]M_\odot$ and $q \in [1, 3]$. The dimensionless spin magnitudes are sampled in the interval $[0, 0.89]$, with an isotropic prior for the tilt angles. We sample the dimensionless tidal deformabilities Λ_1, Λ_2 over a uniform prior $[5, 5000]$. Figure 2.12 displays the marginalized, two-dimensional posteriors for the detector masses m_1, m_2 of the NSs and the tidal parameters $\tilde{\Lambda}$ and $\delta\Lambda$, which parameterize the LO and NLO tidal corrections to the PN GW phase [376]. The masses are slightly bimodal. This effect is not unexpected, and has already been previously observed [10, 369]. Evidently, it is related to the modelling of spin precession: on the one hand, allowing spin magnitudes to vary in the large interval $[0, 0.89]$ increases the correlations between spins and mass ratio; on the other hand, precession effects can more easily fit features of the data which might be due to the noise. This event too, much like GW150914, does not display evidence for precession or spinning components. Indeed, we find that χ_p is consistent with its prior, and $\chi_{\text{eff}} = 0.01^{+0.04}_{-0.02}$. Finally, we measure $\tilde{\Lambda} = 406^{+238}_{-150}$. This value is marginally larger than the one obtained with the `IMRPhenomPv2NRTidal` model, consistently with Ref. [251], but slightly smaller than the one obtained with the aligned spin model.

Chapter 3

TEOBResumS-DALÍ: an EOB model for non-circularized systems

In dense stellar regions, e.g. galactic nuclei or globular clusters, individual BHs can become gravitationally bound as energy is lost to gravitational radiation during a close passage [377, 378]. Such dynamically captured pairs may be sources of GWs, with a phenomenology that is radically different from quasi-circular inspirals [379, 380] and can be detected from larger distances and greater BH masses than quasi-circular mergers [381]. Although to date there is no definitive observational evidence of these systems, the capture of a stellar-mass object by a massive BH is also expected to be an efficient emitter of gravitational radiation for future detectors [382] as the Einstein Telescope [383] and LISA [384]. Due to the special waveform morphology, these systems might be either missed or incorrectly analyzed using standard quasi-circular templates, as already emphasized long ago [385] (see Ref. [386] for a recent review).

Physically faithful waveform models to systematically study the phenomenology of dynamical captures did not exist before the work presented in Ref. [146], and summarized in this Chapter. To the best of our knowledge, the only attempt at building a waveform model for this kind of events dates back to Ref. [385] that provided a qualitative study of the phenomenon. The model of [385] is based on geodesic motion on a Kerr BH spacetime augmented by LO Newtonian-like radiation reaction, then complemented by an effective model for a (quasi-circular) ringdown informed by NR simulations. Similarly, NR studies of BBH mergers from dynamical capture conducted thus far are few [387–389] and limited to non-spinning binaries. A few years ago, Ref. [390] showed that the EOB approach to the general relativistic two-body dynamics [122–125, 127, 280, 291] is suitable also for hyperbolic scattering events. In particular, Ref. [390] compared NR and EOB predictions for the scattering angles for

hyperbolic encounters, although it provided neither a description for the dynamical capture, nor a waveform model. Here we expand on the results of Ref. [390] and illustrate that the EOB formalism can provide a complete model, for both dynamics and radiation, for dynamical capture BH binaries. The key analytical advance is the radiation reaction and waveform along generic orbits proposed in Ref. [145]. The latter is based on the use of generic (non-circular) Newtonian prefactors in the multipolar waveform and radiation reaction. The merger and ringdown parts of the waveform are then modeled using analytical representations informed by quasi-circular (spin-aligned) numerical simulations [141, 144, 285]. We then validate our model in the capture regime by computing mismatches against six completely new simulations performed with the `GR-Athena++` code [188] and 46 highly eccentric simulations from the RIT catalog [391]. Finally, we apply the model to the analysis of one of the most mysterious signals detected by LVK: GW190521.

3.1 An EOB model for dynamical captures

Reference [145] introduced an EOB model valid along generic orbits, i.e. valid for any configuration *beyond* the quasi-circular one. Although the studies presented in Ref. [145] were limited to configurations with mild eccentricities ($e \leq 0.3$) there are no conceptual constraints that prevent from using the model in more extreme configurations, e.g. scattering or dynamical captures. The eccentric EOB model we describe here stems from the quasi-circular `TEOBResumS-GIOTTO` [142, 144, 285], discussed at length in Chapter 1.

To generalize `TEOBResumS` to generic orbits, Ref. [145] proposed to simply replace the quasi-circular LO terms, both in radiation reaction and waveform, with their exact analytical expressions valid on general orbits. In particular, the azimuthal part of the radiation reaction force reads:

$$\hat{\mathcal{F}}_{\varphi}^{\text{EOB}} = -\frac{32}{5}\nu r_{\omega}^4 \Omega^5 \hat{f}_{\varphi}^{\text{nc}} \hat{f}(\Omega). \quad (3.1)$$

Comparing this expression with Eq. 1.16, it is apparent that the only difference lies in the multiplicative factor $\hat{f}_{\varphi}^{\text{nc}}$. This quantity encodes the non-circular corrections in the angular momentum flux. It depends on time derivatives of the EOB dynamical variables r, Ω , and its explicit expression can be computed from the usual quadrupole formula (see Eq. 7 in Ref. [145]). Additionally, the *radial* radiation reaction force, usually set to zero for quasi-circular binaries, is non-negligible for binaries coalescing

on generic orbits. This quantity is modeled by resumming the 2PN expression derived in [392]. The Newtonian prefactor in the LO multipolar EOB waveform h_{22} is similarly substituted with

$$h_{22}^{N,0} = -8\sqrt{\frac{\pi}{5}}\nu(r_\omega\Omega)^2(1 + \hat{h}_{22}^{nc})e^{-2i\varphi} \quad (3.2)$$

where \hat{h}_{22}^{nc} is, again, computed by evaluating two time derivatives of the symmetric-tracefree mass multipole, $h_{22} \propto I_{22}^{(2)}e^{2i\varphi}$, and can be read from e.g. Eq. 10 of [148]. The model can generate all modes up to $\ell = m = 5$ included, although, in the presence of spin, the extension through merger and ringdown is not present for the $(\ell, m) = (3, 1), (4, 2)$ and $(4, 1)$ multipoles (see discussion in Ref. [144, 145]). Note that, for simplicity, we do *not* include NQC corrections in the plunge to merger description of the waveform. These choices are motivated by the fact that, although some NR simulations are available [385, 387, 390, 393–396], a systematic coverage of the BBH parameter space for highly eccentric or hyperbolic orbits is currently missing.

Before moving on with our presentation, we note that at the time of writing this dissertation this simple model has undergone numerous changes and improvements. Although the analyses presented in this chapter do not include them, we still wish to mention and list them to correctly represent the state of the art. In particular, Ref. [148] improved the prescription for the multipolar waveforms, computing the Newtonian prefactors also for the subdominant modes and introducing a sigmoid function to turn on/off NQC parameters and the Newtonian prefactors close to merger. It also modified the prescription for \mathcal{F}_r , suggesting a new resummation technique which improves the quasi-circular limit of this model. Focusing then on the conservative dynamics, Ref. [149] investigated the effect of high order analytical information in the EOB metric potentials, augmenting the D and Q functions with up to 5PN terms and experimenting with different Padé resummations. Going back to the radiative sector, Ref. [397] presented an improved factorization and resummation of the multipolar waveforms, modified to include up to 2PN non-circular information. Such a prescription was then validated in the extreme mass ratio limit via comparisons with numerical results for eccentric systems and dynamical captures. Finally, Ref. [398], applied the idea of using the full, resummed EOB equations of motions (which was already present in [145]), to the 2PN results of [397]. This generalization considerably improves the waveform accuracy, and the method is accurate also for highly eccentric systems.

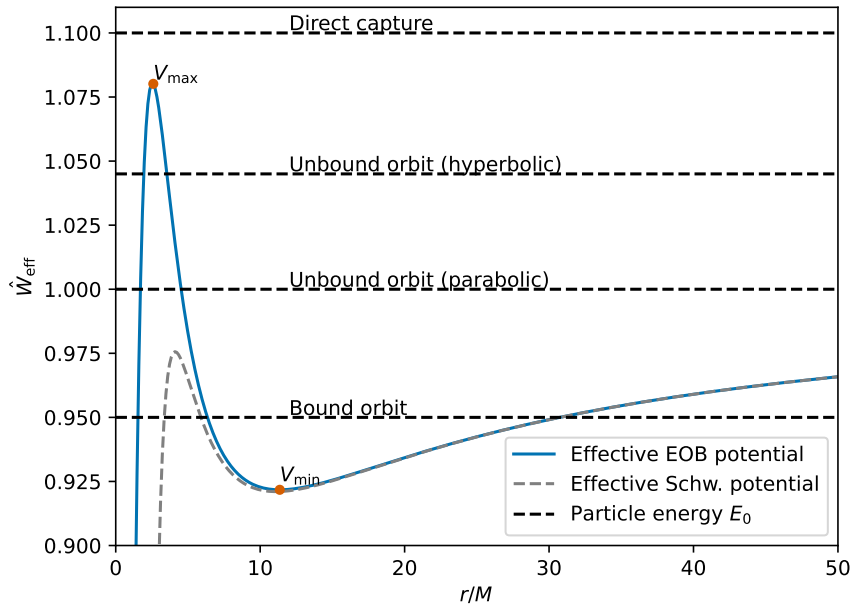


FIGURE 3.1: The EOB effective potential \hat{W}_{eff} determines, in the conservative case, the shape of the orbit. Here, we show the *TEOBResumS-DALÍ* potential (blue line) for an equal mass, non-spinning system, and compare it to the Schwarzschild potential (dashed gray line).

3.1.1 Phenomenology of hyperbolic mergers

Much like precession of the orbital plane of the binary causes amplitude and phase modulations in the GW emitted by the system, eccentricity-related effects – too – visibly modify the GWs phenomenology. In order to qualitatively understand them, it is useful to first discuss the setup of the initial data. To start, recall the form of the EOB Hamiltonian:

$$\hat{H} \equiv H/\mu \equiv \nu^{-1} \sqrt{1 + 2\nu(\hat{H}_{\text{eff}} - 1)}, \quad (3.3)$$

with $\nu \equiv \mu/M$ and \hat{H}_{eff} is the effective Hamiltonian[144–146]. For non-spinning binaries, the configuration space can be characterized by the mass ratio $q = m_1/m_2 \geq 1$, the initial energy E_0/M and the initial reduced orbital angular momentum p_φ^0 [146]. Similarly to the motion of a test particle moving around a Schwarzschild BH, the EOB behavior of a hyperbolic encounter is characterized by the EOB potential energy

$$E_{\text{EOB}} \equiv M \sqrt{1 + 2\nu(\hat{W}_{\text{eff}} - 1)}, \quad (3.4)$$

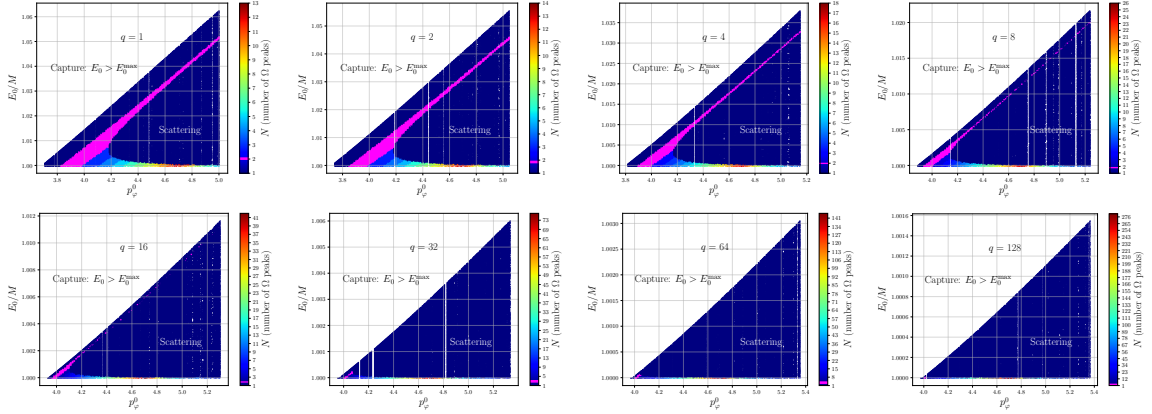


FIGURE 3.2: Analysis of the parameter space of hyperbolic encounters of non-spinning BBHs parameterized in terms of initial data $(q, E_0/M, p_\varphi^0)$. The number of multiple encounters ($N \geq 2$) increases with q , while the corresponding area on the parameter space gets smaller and smaller. Note the separation, given by the colored area, between configurations that scatter and configurations that eventually merge.

where

$$\hat{W}_{\text{eff}} = \sqrt{A(r)(1 + p_\varphi^2/r^2)} \quad (3.5)$$

is the effective potential energy. The solution $\partial_r \hat{W}_{\text{eff}} = \partial_r^2 \hat{W}_{\text{eff}} = 0$ defines the LSO parameters $(r_{\text{LSO}}, p_\varphi^{\text{LSO}})$. When $p_\varphi > p_\varphi^{\text{LSO}}$, \hat{W}_{eff} has both a maximum and a minimum and, depending on E_0/M , bound as well as unbound configurations are present. In the absence of radiation reaction, unbound configurations are defined by the condition $E_0/M > 1$. We define $E_{\text{min}}/M \equiv \nu \hat{H}(r_0, q, p_\varphi, p_r = 0)$ the energy corresponding to the initial separation and $E_{\text{max}}/M = \max_r [\nu \hat{H}(r, q, p_\varphi, p_r = 0)]$.

In the absence of GW losses, for a given p_φ , the value E_{max} corresponds to unstable circular orbits, analogously to Schwarzschild geodesics. When $E_0 > E_{\text{max}}$ the objects fall directly onto each other without forming metastable configurations (e.g., for head-on collisions, corresponding to $p_\varphi = 0$). When $1 < E_0/M \leq E_{\text{max}}/M$, the phenomenology changes from direct plunge, to on up to many close passages before merger, to zoom-whirl behavior or even scattering [390, 393, 395]. When $E_0/M < 1$, the system is bound and the orbit is either elliptic or circular. The different cases are shown in Fig. 3.1. In the presence of radiation reaction, the qualitative picture remains unchanged (as also observed in NR simulations [387]), although the threshold between the two qualitative behaviors is not simply set by E_{max} , but it is also affected by GW losses.

It is apparent that the dynamics of each configuration can be characterized by

counting the number of encounters, i.e. the number of peaks of the orbital frequency $\Omega(t) \equiv \dot{\varphi}$, each peak corresponding to a periastron passage [146]. We then consider different mass ratios, $q = \{1, 2, 4, 8, 16, 32, 64, 128\}$ to provide a comprehensive exploration of the parameter space. For each value of the angular momentum, we lower the energy and count the number of peaks of Ω . The result of this analysis is reported in Fig. 3.2. The colors characterize how many periastron passages the system has undergone before merging. Focusing first on the $q = 1$ case (top-left panel of the figure), one sees that when the energy is decreased from \hat{E}_{\max} there are different islands of initial parameters that correspond to progressively more complicated physical behaviors. The plot is split in two by an area that corresponds to the frequency developing two peaks before merger (magenta online). The $N = 1$ part of the parameter space *above* the magenta region corresponds to direct plunge. By contrast, the $N = 1$ part on the right of and below the magenta region corresponds to scattering events instead of capture. For a given value of E_0 , configurations in the first $N = 1$ region have smaller angular momentum and larger radial momentum, so that the capture is favored. On the contrary, in the second $N = 1$ region the angular momentum dominates, and thus, after a close encounter, the two objects separate again instead of merging. When the initial energy is lowered further, getting close to the stability region, the system attempts to stabilize again and the number of periastron passages before merger increases progressively also for large values of p_φ^0 . The phenomenology remains qualitatively the same *also* when the mass ratio is increased, but the region with $N = 2$ becomes narrower and narrower as q increases, notably for $q \geq 32$, when the divide between $N = 1$ configuration is barely visible on the plots (we shall quantify this behavior better below). By contrast, for energies just slightly larger than the (adiabatic) stability limit, the number of possible encounters can grow considerably, up to several tens, although limited to a region of p_φ^0 much smaller than in the equal-mass case. We qualitatively interpret this behavior as mirroring the effect that radiation reaction, that is proportional to ν , becomes less and less efficient as ν is decreased and so the system can persist in a metastable state much longer. Figure 3.3 exhibits the number of encounters versus ν . Configurations with two encounters are always the most frequent ones, although their fraction quickly decreases below 10% for $q > 4$ ($\nu < 0.16$).

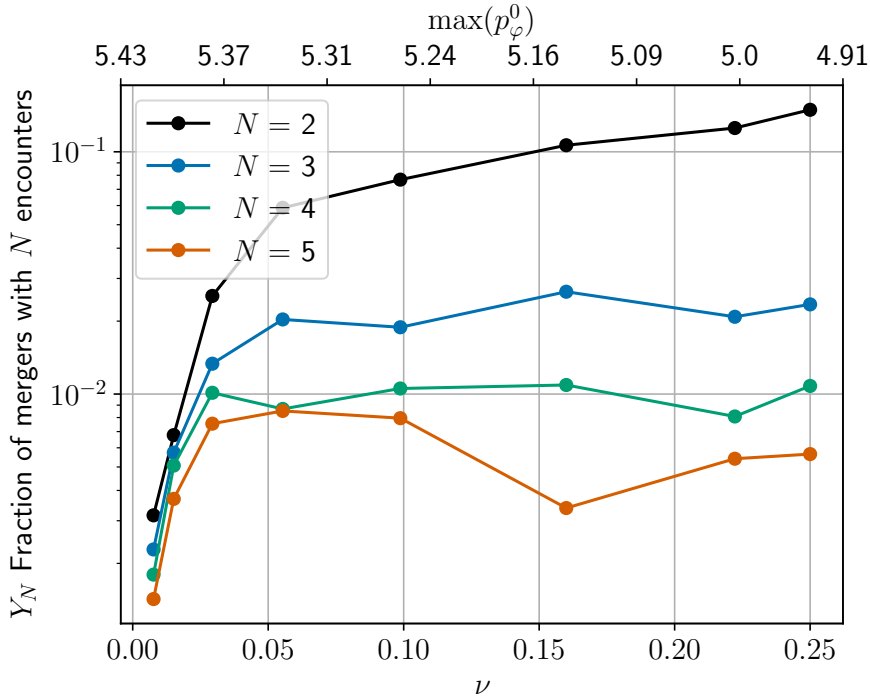


FIGURE 3.3: Fraction of BBH configurations (including also scattering events) that end up with N encounters (where the N -th encounter corresponds to merger) for non-spinning binaries. Configurations with $N = 2$ are the most frequent ones, although their frequency quickly decreases below 10% as $q > 4$ ($\nu < 0.16$).

3.1.2 Validation of the model

The model discussed in this Sec. 3.1 has been extensively validated against mildly eccentric NR simulations, scattering angle computations and test particle results [145, 147]. Although these regimes are different from the one we are interested in studying here – i.e., captures of comparable-mass bodies – some important insight can nonetheless be extrapolated from this information. In detail, Ref. [145] performed time-domain and mismatch comparisons against 28 equal-mass mildly eccentric NR simulations [145] from the SXS collaboration [182, 265–276], proving that the radiation reaction employed is highly accurate in this regime. Reference [146], instead, compared the scattering angle obtained with *TEOBResumS* with 10 equal-mass scattering simulations from Ref. [390], but for which waveforms were not available. This is a strong test of the dynamics (of both the conservative and dissipative sector), that probes the model in a very challenging physical scenario [146]. Finally, Ref. [147] employed 111 waveforms generated by a non-spinning test particle along planar geodesics in Kerr spacetime with eccentricities up to 0.9 and dimensionless Kerr spin magnitude

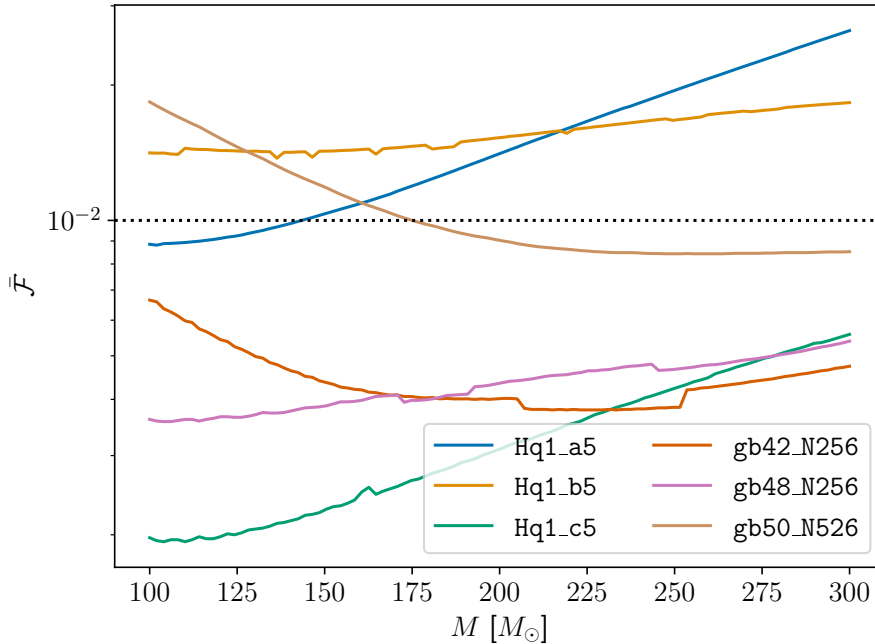


FIGURE 3.4: EOB/NR unfaithfulness for highly eccentric and capture configurations. Comparison between the NR simulations of Table 3.1, produced for this work, and the eccentric *TEOBResumS*. We consider frequencies between 11 and 512 Hz, use the Hanford PSD of GW190521 and compute \bar{F} for systems with masses $M \in [100, 300]M_{\odot}$.

up to $\tilde{a}_0 = 0.9$. This analysis was also extended to non-geodesic motion (see Fig. 13 and Fig. 14 therein). Tests against test-mass waveforms from dynamical encounters show a good performance of the quasi-circular ringdown approximation for the configurations that circularize during the last encounter, see in particular Fig. 14 of [147]. The region where the circular ringdown performs less well is the direct-capture and head-on scenario (as expected on physical grounds).

To further corroborate these observations in the regime of direct interest for captures, we produced six equal-mass, non-spinning simulations of highly eccentric systems or dynamical captures using the NR code *GR-Athena++* [188], see Table 3.1. Three simulations reproduce configurations of Gold and Bruegmann [387] (*gb42_N256*, *gb48_N256* and *gb50_N256*); the three remaining ones are instead completely new configurations (*Hq1_a5*, *Hq1_b5* and *Hq1_c5*). In order to compare NR and EOB waveforms, one needs to consistently specify initial energy, angular momentum and separation. While the first two quantities are in principle gauge-invariant, to get the

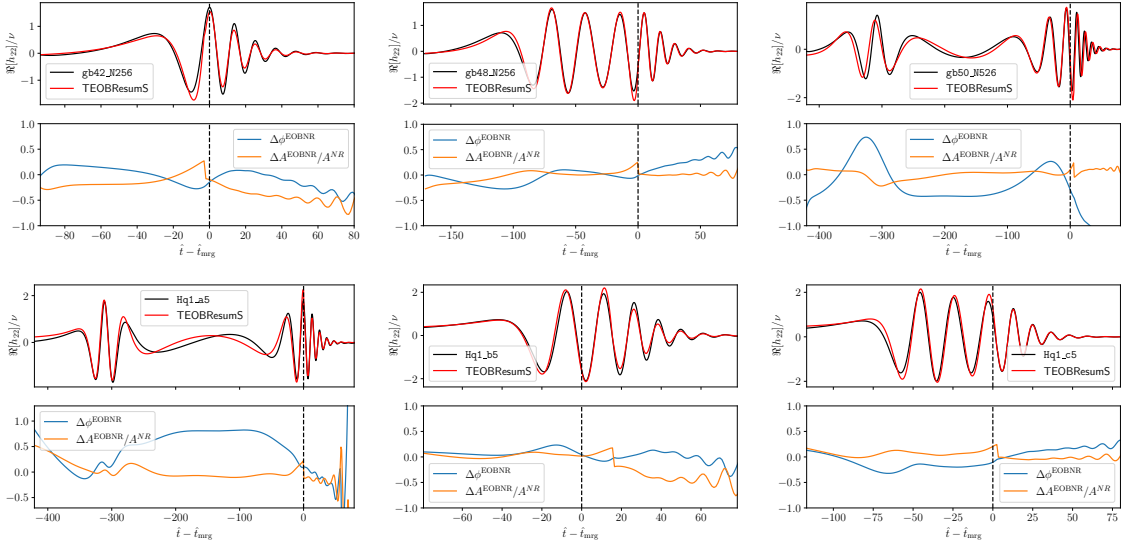


FIGURE 3.5: Time-domain EOB/NR phasing comparison. Comparing the NR waveforms of Table 3.1 to the analytical ones obtained using the eccentric **TEOBResumS**. For each configuration, the top panel displays the amplitude and the real part of the dominant multipole h_{22} , while the bottom panel shows the phase difference $\Delta\phi^{\text{EOB/NR}} = \phi^{\text{EOB}} - \phi^{\text{NR}}$ and the relative amplitude difference $\Delta A^{\text{EOB/NR}}/A^{\text{NR}} = (A^{\text{EOB}} - A^{\text{NR}})/A^{\text{NR}}$. Despite the lack of NQC corrections or of a hyperbolic-NR-informed ringdown, **TEOBResumS** quantitatively captures the NR waveform for all configurations.

latter we need to convert from ADM coordinates to EOB coordinates using a 2PN-accurate transformation [122, 392]. However, the existence of NR junk radiation, resolution effects, Schott energy (currently not accounted for in our model) can cause small differences between the NR and EOB initial data. While small variations in the energy and angular momentum can significantly change the phenomenology of the waveform, as shown in Fig. 2 of [146], small inaccuracies in the initial separation are not relevant as long as the bodies are initially far enough. In this scenario, the effect of the radiation reaction is negligible at the beginning of the evolution, and small shifts in initial separation correspond to global constant time shifts. As such, we estimate the “optimal” values of (E_0, p_φ^0) by first minimizing the mismatch on the initial energy and angular momentum over a small interval around the values extracted from the NR metadata, allowing a relative error up to 1% in energy and up to 6% in angular momentum. This procedure was performed only for a single reference value of total mass, using the expression:

$$\bar{\mathcal{F}} = 1 - \max_{t_0, \phi_0, E_0, p_\varphi^0} \frac{(h^{\text{NR}}, h^{\text{EOB}})}{\sqrt{(h^{\text{NR}}, h^{\text{NR}})(h^{\text{EOB}}, h^{\text{EOB}})}}, \quad (3.6)$$

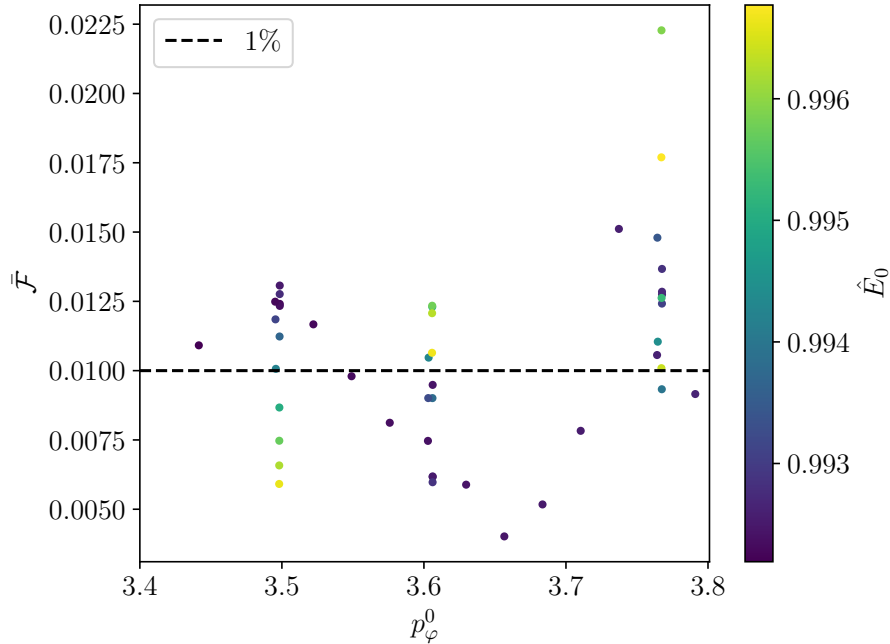


FIGURE 3.6: EOB/NR unfaithfulness for the highly eccentric NR waveforms from the RIT catalog. We compare 46 non-spinning highly eccentric datasets from RIT [391] with the eccentric TEOBResumS model. We consider frequencies between 11 and 512 Hz, use the Hanford PSD of GW190521 and compute $\bar{\mathcal{F}}$ with fixed total mass $M = 250M_{\odot}$.

In view of the next section, we use as reference total mass $M = 250M_{\odot}$, i.e. the detector frame mass of GW190521, and employ GW190521 Hanford’s PSD. The initial conditions found with this procedure are then employed to compute $\bar{\mathcal{F}}$ for all values of the total mass M considered using the standard definition of mismatch, Eq. 1.24. We considered frequencies between 11 and 512 Hz and total masses $M \in [100, 300]M_{\odot}$. We found mismatches between 0.2% and 3%, see Fig. 3.4. The corresponding time-domain EOB/NR phase comparisons of the $\ell = m = 2$ waveform are shown in Fig. 3.5. For each configuration in Fig. 3.5 we compare the real part of the EOB and NR waveform and explicitly show the phase difference $\Delta\phi^{\text{EOBNR}} \equiv \phi^{\text{EOB}} - \phi^{\text{NR}}$ and the relative amplitude difference $\Delta A^{\text{EOBNR}}/A^{\text{NR}} \equiv |A^{\text{EOB}} - A^{\text{NR}}|/A^{\text{NR}}$. Note that the NR-informed quasi-circular ringdown [144] delivers a rather faithful representation of the NR phasing, while the amplitude might be underestimated. This is consistent with the findings in the test-particle limit [147]. On top of the comparisons against the six new simulations presented, we also considered a subset of the waveforms presented in Ref. [391] and apply the same procedure detailed above. Figure 3.6 shows the unfaithfulness of

ID	r_0	E_0/M	p_φ^0	$E_{0,\text{opt}}/M$	$p_{\varphi,\text{opt}}^0$	$\Delta E/E[\%]$	$\Delta p_\varphi/p_\varphi[\%]$
Hq1_a5	100.000	1.003	3.970	1.005	3.987	-0.132	-0.440
Hq1_b5	100.000	1.008	3.970	1.010	4.049	-0.192	-2.000
Hq1_c5	100.000	1.007	3.970	1.015	4.181	-0.799	-5.323
gb42_N256	20.842	0.994	3.305	0.994	3.238	0.018	2.033
gb48_N256	20.869	0.994	3.671	0.997	3.762	-0.267	-2.476
gb50_N526	20.878	0.994	3.784	0.993	3.771	0.131	0.342

TABLE 3.1: EOB initial data to match NR simulations. The values correspond to the equal-mass, non-spinning NR data of Figs. 3.4 and 3.5. The first column of the table reports the configuration label. The quantities r_0, E_0 and p_φ^0 are the initial EOB radial separation, initial energy and initial angular momentum obtained by mapping the initial position and momenta of the punctures into EOB coordinates via the 2PN coordinate transformation between ADM and EOB coordinates [392]. The quantities $E_{0,\text{opt}}$ and $p_{\varphi,\text{opt}}^0$, instead, are the corresponding values which minimize the EOB/NR mismatch at $M = 250M_\odot$. The last two columns report the corresponding relative differences.

our model computed against all such simulations with initial eccentricity larger than 0.5, zero spins, $q \leq 8$ and initial angular momentum $p_\varphi \geq 3.4$ at initial separation $r \sim 20$. Notably, the 46 simulations selected display typical EOB/NR mismatches below 3%, with about half of them more than 99% faithful to NR.

3.2 GW190521

The GW transient GW190521 is compatible with the quasi-circular merger of two heavy ($m_1 \simeq 85M_\odot$, $m_2 \simeq 66M_\odot$) BHs resulting in a $\simeq 150M_\odot$ intermediate-mass BH (IMBH) [229, 230]. The estimated BH component masses fall in a mass gap $\simeq 65 - 120M_\odot$ for BHs formed directly from stellar collapse, and challenge standard scenarios of BHs formation [17, 230–236], suggesting the possibility of a progenitors formation through repeated mergers [237]. The short duration (~ 0.1 s) of GW190521 and the absence of a premerger signal, identified also by unmodeled (or weakly modeled) analyses [8], are critical aspects for the choice of waveform templates in matched filtering analyses and thus for the interpretation of the source. For example, under the hypothesis of a quasi-circular merger, matching the signal morphology requires fairly large in-plane components of the individual BH spins and results in a (weak) statistical evidence for orbital-plane precession. High orbital eccentricities are also compatible with the burst-like morphology of GW190521, but best-matching eccentric merger waveforms still require spin precession [238, 239]. Spin precessing BBH mergers

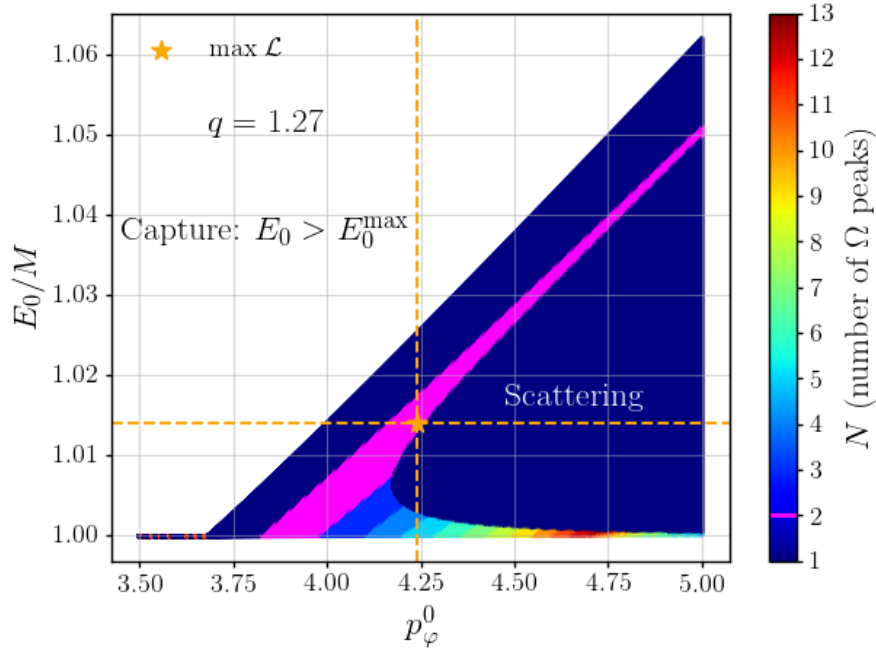


FIGURE 3.7: Parameter space for non-spinning hyperbolic encounters predicted using the *TEOBResumS* EOB model and fixing $q \equiv m_1/m_2 = 1.27$. Here (p_φ^0, E_0) are the EOB initial angular momentum and energy, while E_0^{\max} is the value corresponding to unstable circular orbit. For $E_0 < E_0^{\max}$, each color labels the number of peaks (i.e. of periastron passages) N of the EOB orbital frequency Ω . The orange star labels the maximum likelihood values $(\bar{p}_\varphi^0, \bar{E}_0)$ corresponding to the *constrained* analysis, see Table 3.2.

are known to be degenerate with head-on collisions [240]. However, a head-on BBH is disfavored with respect to a boson-star head on collision with a log Bayes' factor of -6.1 [399]. Other proposed interpretations involve a high-mass BH-disk system [241] or an intermediate mass ratio inspiral [242] (see also [243]), and indicate that the origin of GW190521 is still unsettled.

In this section we analyze GW190521 within the scenario of a BBH dynamical capture and compare this hypothesis to that of a quasi-circular merger. As discussed, dynamical captures have a phenomenology radically different from quasi-circular mergers [385–387]. The close passage and capture of the two objects in hyperbolic orbits naturally accounts for the short-duration, burst-like waveform morphology of GW190521 even in the absence of spins. Moreover, possible explanations of the high component masses rely on second-generation BHs, stellar mergers in young star clusters and BH mergers in active galactic nuclei disks [17, 231–236, 377, 378], for which dynamical captures are possible. While no observational evidence for GWs from dynamical captures existed prior to our work, such events are not incompatible with the

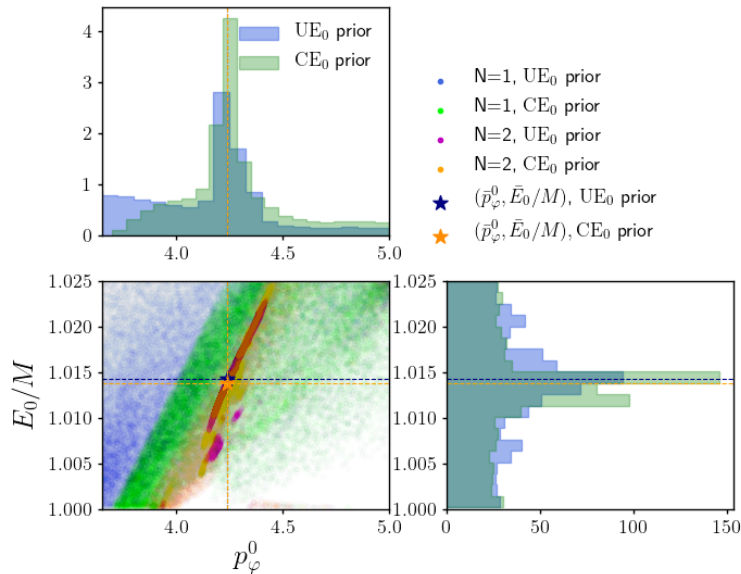


FIGURE 3.8: Marginalized two-dimensional posterior distributions of the initial energy E_0 and initial angular momentum p_φ^0 for the constrained (CE₀) and unconstrained (UE₀) energy prior choices. The colors highlight the different waveform phenomenologies, with $N = 1$ (blue and green) or $N = 2$ (magenta and orange) peaks in the orbital frequency. The maximum likelihood values $(\bar{p}_\varphi^0, \bar{E}_0)$ are highlighted with red (UE₀ prior) and dark-orange (CE₀ prior) stars.

current detection rates [382, 400], although these rates would require corrections to take into account the large masses of GW190521 [401].

The publicly released GW190521 data are analyzed around time $t_{\text{GPS}} = 1242442968$, with a 8 s time-window and in the range of frequencies [11, 512] Hz using the *bajes* pipeline [34]. We employ the PSD estimate and calibration envelopes publicly available from the GW Open Science Center [404]. The Bayesian analysis uses the *dynesty* sampler [204] with 2048 live points. We use a uniform prior in the mass components (m_1, m_2) exploring the ranges of chirp mass $\mathcal{M}_c \in [30, 200] M_\odot$ and mass ratio $q \in [1, 8]$. The luminosity distance is sampled assuming a volumetric prior in the range [1, 10] Gpc. We analytically marginalize over the coalescence phase, and sample the coalescence time in $t_s \in [-2, 2]$ s with respect to the central GPS time.

The key quantities to sample the configuration space of hyperbolic mergers are $(E_0/M, p_\varphi^0)$. The initial angular momentum is uniformly sampled within $p_\varphi^0 \in [3.5, 5]$, and further imposing $p_\varphi^0 \geq p_\varphi^{\text{LSO}}$ for any q . The initial energy is uniformly sampled in the interval $E_0/M \in [1.0002, 1.025]$ but with two different additional constraints that

Reference	This paper					LVK[229]	Gayathri et al.[238]	Romero-Shaw et al.[239]
	TEOBResumS[145, 146]	TEOBResumS[145, 146]	TEOBResumSP[259] ¹	NRSur7dq4[172]	NRSur7dq4[172]	NRSur7dq4[172]	NR[391]	SEOBv2[402]
Waveform	Unconstrained (UE ₀)	Constrained (CE ₀)	–	–	–	–	–	–
E ₀ prior	–	–	–	–	–	–	–	–
Multipoles	($\ell, m $) = (2, 2)	($\ell, m $) = (2, 2)	($\ell, m $) = (2, 2)	($\ell, m $) = (2, 2)	($\ell, m $) = (2, 2)	$\ell \leq 4$	–	–
m_1 [M _⊙]	85_{-22}^{+88}	81_{-25}^{+62}	90_{-14}^{+19}	102_{-23}^{+35}	84_{-12}^{+17}	85_{-14}^{+21}	102_{-11}^{+7}	92_{-16}^{+26}
m_2 [M _⊙]	59_{-37}^{+15}	52_{-32}^{+35}	66_{-20}^{+10}	64_{-29}^{+12}	71_{-18}^{+16}	66_{-18}^{+17}	102_{-11}^{+7}	69_{-19}^{+18}
M_{source} [M _⊙]	151_{-51}^{+73}	130_{-43}^{+75}	156_{-15}^{+25}	164_{-20}^{+30}	153_{-19}^{+29}	150_{-17}^{+29}	–	–
$m_2/m_1 \leq 1$	$0.69_{-0.52}^{+0.27}$	$0.63_{-0.43}^{+0.31}$	$0.73_{-0.15}^{+0.21}$	$0.62_{-0.30}^{+0.32}$	$0.86_{-0.30}^{+0.12}$	$0.79_{-0.29}^{+0.19}$	–	–
χ_{eff}	–	–	$-0.05_{-0.12}^{+0.09}$	$0.01_{-0.36}^{+0.24}$	$-0.03_{-0.26}^{+0.25}$	$0.08_{-0.36}^{+0.27}$	0	$0.0_{-0.2}^{+0.2}$
χ_{p}	–	–	$0.72_{-0.22}^{+0.16}$	$0.71_{-0.36}^{+0.22}$	$0.79_{-0.40}^{+0.16}$	$0.68_{-0.37}^{+0.25}$	0.7	–
e	–	–	–	–	–	–	0.67	–
E^0/M	$1.014_{-0.012}^{+0.009}$	$1.014_{-0.012}^{+0.010}$	–	–	–	–	–	–
p_{φ}^0	$4.18_{-0.62}^{+0.50}$	$4.24_{-0.37}^{+0.57}$	–	–	–	–	–	–
D_L [Gpc]	$4.7_{-2.7}^{+4.8}$	$6.1_{-3.7}^{+3.7}$	$4.5_{-1.2}^{+1.2}$	$3.9_{-1.9}^{+2.3}$	$4.8_{-2.2}^{+2.3}$	$5.3_{-2.6}^{+2.4}$	$1.84_{-0.054}^{+1.07}$	$4.1_{-1.8}^{+1.8}$
SNR _{max}	15.2	15.4	14.7	14.7	14.6	15.4	–	–
$\log(\mathcal{L})_{\text{max}}$	123.2	123.0	106.0	107.0	105.6	–	–	–
$\log \mathcal{B}_{\text{noise}}^{\text{signal}}$	84.00 ± 0.18	83.30 ± 0.18	72.95 ± 0.08	74.76 ± 0.11	74.86 ± 0.11	–	–	–

TABLE 3.2: Source parameters of GW190521. We indicate the mass of the heavier (lighter) object with m_1 (m_2), M_{source} is the total mass in the frame of the source, χ_{eff} is the effective spin along the orbital angular momentum, while χ_{p} is the effective precessing spin [229]. The second and third columns report our new results, obtained with the hyperbolic capture model [146] with the two different prior choices on the energy. The fourth, fifth and sixth columns report the results obtained in this work with the quasi-circular models TEOBResumSP and NRSur7dq4. For reference, the remaining columns report results of other analyses[229, 238, 239]. We employ the standard cosmology of Planck [403] to compute source frame masses. Median values and 90% credible intervals are quoted and natural logarithms are reported. The SNR values correspond to the matched-filter estimates.

1: spin results obtained at a reference frequency of 5 Hz.

2: lower limit at 10 Hz.

result in two different prior choices: (UE₀) *Unconstrained prior*, $E_0 \geq E_{\text{min}}$; (CE₀) *Constrained prior*, $E_{\text{min}} \leq E_0 \leq E_{\text{max}}$. The UE₀ prior spans a larger portion of the parameter space, notably including direct capture, although the dynamics remains far from the head-on collision case. The CE₀ prior is contained in the first, and restricts the parameter space to systems closer to stable configurations, for which the orbital dynamics substantially contributes to the waveform and the ringdown description is expected to be more accurate.

The results of the analysis corresponding to the UE₀ and CE₀ priors are summarized in the second and third columns of Table 3.2 respectively. The consistency of the two measurements confirms the robustness of our modeling choices. Focusing on global fitting quantities we find, respectively for the UE₀ (CE₀) priors, maximum likelihood values $\log(\mathcal{L})_{\text{max}} = 123.2$ (123.0), and Bayesian evidences $\log \mathcal{B}_{\text{noise}}^{\text{signal}} = 84.0 \pm 0.18$ (83.3 ± 0.18), while the recovered matched-filter signal-to-noise ratio (SNR) is equal to 15.2 (15.4). Employing the standard cosmology [403], we find component masses in the source frame $(m_1, m_2) = (85_{-22}^{+88}, 59_{-37}^{+18})M_{\odot}$ for the UE₀ case and $(m_1, m_2) = (81_{-25}^{+62}, 52_{-32}^{+32})M_{\odot}$ in the CE₀ case. Figure 3.8 illustrates the (E_0, p_{φ}^0) parameter space selected by the analysis, with colors highlighting configurations with

different number of encounters N . The figure shows that, despite GW190521 consisting of a single GW burst around the analyzed time, many of the configurations selected, and in particular the most probable ones, correspond to two encounters.

The phenomenology corresponding to the set of maximum likelihood parameters selected by the analysis are shown in Fig. 3.9. The EOB relative trajectory (top panel) is complemented by the corresponding waveform templates projected onto the three detectors and compared to the whitened LIGO-Virgo data around the time of GW190521. Thicker lines highlight the last part of the dynamics, which exactly covers the portion of the signal displayed in the bottom panel. The magnitude of the first GW burst predicted by the EOB analysis (not shown in the plot) is comparable to the detector noise and would occur outside the analysis window. However, we find that such first burst is not a robust feature across samples, occurring at different times and smaller amplitudes for different points and not occurring at all for others (see Fig. 3.8). Given this consideration and the small amplitude of such first burst, we do not expect an extension of the analysis segment to impact our main conclusions.

In order to compare the hyperbolic capture with the quasi-circular merger hypothesis, we perform a new quasi-circular analysis with the precessing surrogate model `NRSur7dq4` [172] and with the quasi-circular precessing flavor of `TEOBResumS`, here dubbed `TEOBResumSP` [258, 259]. To minimize systematic effects, we consistently use the `bajes` pipeline [34] with the same settings discussed above for all the runs. The prior distributions for the mass parameters and the extrinsic parameters are also identical to the ones used in the hyperbolic capture analysis with `TEOBResumS`, while the prior on the spin components is chosen to be uniform in the spin magnitudes and isotropic in the angles [229]. When including higher modes we disable phase marginalization.

In Table 3.2 we quote maximum likelihood and matched-filter SNR values obtained from the full unmarginalised posterior. The quasi-circular precessing analyses with `bajes` and `NRSur7dq4` are in agreement with those obtained by LVK [229], confirming the reliability of the infrastructure adopted for the inference. The maximum SNR recovered via our pipeline is lower by 0.7 than the one extracted from the public LVK samples. We attribute this discrepancy to differences in data-processing between pipelines, small differences in the prior boundaries and the sampling itself. The use of consistent settings in our new runs with the model used by the LVK excludes that such discrepancies affect the comparison against the non-circular analysis. The

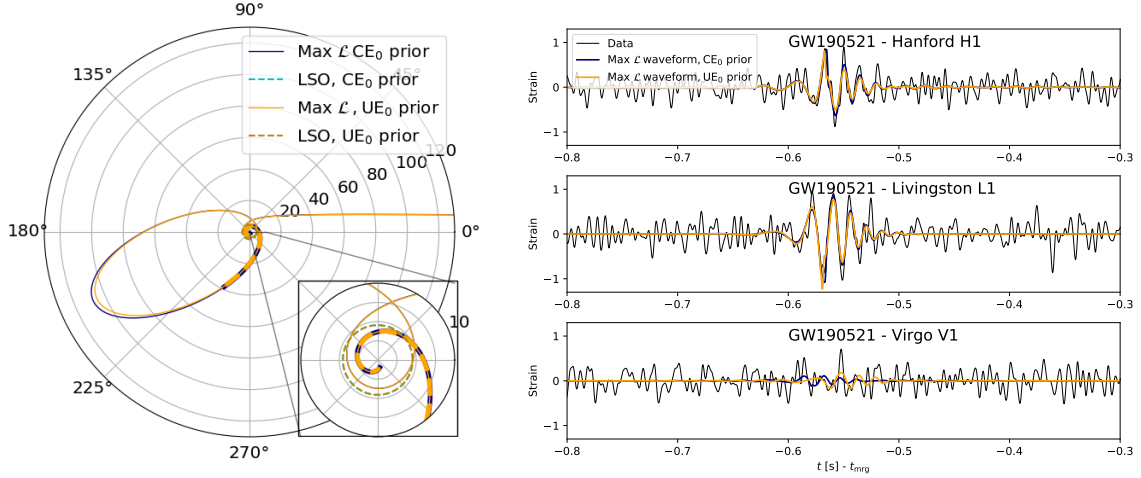


FIGURE 3.9: Maximum likelihood configurations with the two different energy priors, UE_0 (orange) and CE_0 (blue). Top: the (r, φ) EOB relative orbit. Bottom: the waveform templates projected onto the three detectors compared to the whitened LIGO-Virgo data around the time of GW190521. The most probable LSO are highlighted with gold (UE_0 prior) and cyan (CE_0 prior) dashed lines and are located, respectively, at $\bar{r}_{\text{LSO}} = 4.54$ and $\bar{r}_{\text{LSO}} = 4.52$. Corresponding mass ratios are $\bar{q} = 1.04$ and $\bar{q} = 1.27$. The inset highlights the first close encounter, that is then followed by a highly eccentric orbit that eventually ends up with a plunge and merger phase. The part of the trajectory from $\sim (t_{\text{GPS}} - 0.8 \text{ s})$ to merger, which contributes to the second GW burst, is highlighted with thicker lines in the plot. Note that the GW bursts corresponding to the first encounter occur $\sim 4 \text{ s}$ before the GW190521 time, their magnitude is comparable to the detector noise and are outside the segment of data analyzed.

TEOBResumSP analyses display consistency with the NR surrogate. When PE is performed with the dominant $(2, 2)$ mode, it yields $\log \mathcal{L}_{\text{max}} = 106.0$, $\text{SNR}_{\text{max}} = 14.7$ and $\log \mathcal{B}_{\text{noise}}^{\text{signal}} = 72.95 \pm 0.08$. This indicates that the observed increases in these statistics when employing the dynamical capture model are not driven by subtle differences between waveform families (EOB and NR surrogate).

Despite the different hypotheses on the coalescence process, our results on the component masses are in good agreement with the ones obtained from a quasi-circular model. This confirms that an IMBH is formed at the end of the coalescence also in the hyperbolic merger scenario. The consistency on the total mass is not surprising, given that the dominant contribution to this parameter comes from the determination of the ringdown frequency [229]. However, the dynamical capture model is able to fit GW data better than the quasi-circular scenario despite having four less degrees of freedom, with a 16 e-fold increase in the maximum likelihood value. For comparison,

the distribution of $\log \mathcal{L}$ of the quasi-circular analysis spans a ~ 26 e-folds range and has median ~ 9 e-folds smaller than its maximum value. If we assume this difference to be representative of the statistical uncertainty σ on the likelihood, we find that our result lies about 3σ from the median of the quasi-circular analysis and 2σ from its maximum value. Under the dynamical capture assumption, we obtain a matched-filter SNR $\rho = 15.4$, larger by almost a unity with respect to the same value obtained using quasi-circular waveforms. Similarly to the $\log \mathcal{L}$, the maximum SNR of the hyperbolic analysis lies about 1σ from the corresponding value of the quasi-circular analysis and 2σ from its median.

The fit improvement registered by these two indicators is confirmed by the Bayesian evidences, keeping into account the full correlation structure of the parameter space, which imply odds $\gtrsim 4315:1$ in favor of the dynamical encounter scenario against the quasi-circular scenario. This number is expected to be an optimistic estimate of the posterior odds, due to the prior odds disfavoring a dynamical capture scenario compared to a quasi-circular binary. However, estimates of prior odds are currently not reliable due to orders of magnitudes uncertainties on dynamical capture rates in this mass range [401] and, as such, we do not attempt to quantify them directly. Given our (conservative) Bayes factor, we estimate that the capture interpretation is favored with respect to a quasi-circular stellar-collapse scenario [17] so long as the rates of such events is larger than $5 \times 10^{-3} \text{Gpc}^{-3} \text{yr}^{-1}$. This number is computed by imposing that the posterior odds are larger than one, i.e. that $4315 \times R^{\text{dc}}/R^{\text{qc}} > 1$, where R^{dc} is the rate of dynamical capture events and $R^{\text{qc}} = 23.9 \text{Gpc}^{-3} \text{yr}^{-1}$ as estimated by LVK[17]. Notably, the Bayes' factors receive a penalty disfavoring the quasi-circular hypothesis due to the larger dimensionality of this model which is not phase marginalized and includes precessing spins degrees of freedom, although the latter are only weakly measurable. Additionally, some railing against the prior can be observed for the E_0/M and the $\text{UE}_0 p_\varphi^0$ posterior samples, which might affect the estimation of the dynamical capture evidence. However, the choice of prior bounds in this analysis was dictated either by physical boundaries, and hence cannot be relaxed, or by considerations on computational cost and model validity in a region – that of head-on mergers – which was shown to have little support for the phenomenology observed[399]. In light of the above caveats, the Bayesian evidences alone represent useful, but not decisive proof in favor of the capture scenario.

Nonetheless, these two results combined constitute data-driven indicators that the interpretation of GW190521 within the dynamical capture scenario seems preferred

over a quasi-circular spin-precessing merger [8, 243]. No other analysis shows such large improvements in evidence and log-likelihood with respect to the equal-mass, quasi-circular scenario [238, 239, 399]. At the same time, the *absolute* values of evidence and maximum likelihood estimated in some studies [243] are almost as large as those obtained in this work. These values were however obtained with a model which is less NR-faithful in the quasi-circular case than the NRSur7dq4 model considered in this work. Although a direct comparison is not possible given the different PE infrastructure, sampler, models and priors explored, this fact highlights the necessity of exploring multiple hypothesis and model selection to understand such short GW transients.

Chapter 4

Matter effects in GWs: resonant tides and NR information

GWs from coalescing BNS carry information on the stars' internal structure and composition, i.e. their EOS [69, 405]. Such information is mainly, but not exclusively, encoded in the tidal parameters of the stars themselves, which describe the tidal response of a body due to the external gravitational field of its companion [406, 407]. Precise measurements of the tidal parameters of NSs are a key science goal for current and next generation detectors [223, 408–411]. As such, it is fundamental that waveform models give faithful representations of the entire coalescence up to merger. Comparisons between current state-of-the-art models and NR simulations, however, highlight that approximants do not correctly reproduce NR waveforms in the last stages of the inspiral, when matter contributions are best measured and their impact is the largest [251, 264, 412]. Numerous studies have shown that the imperfect modeling of matter effects will have large impact on PE with NG detectors, with waveform systematics that could potentially already be relevant for signals detected in the next LVK observing run, O4 (see also App. A). In this section we describe in some detail two topics which concern the modeling of tidal effects and GWs from BNSs: (i) the measurability and impact of tidal resonances, and (ii) the inclusion of high order numerical and analytical relativity information within `TEOBResumS`.

Matter effects Although BNS and BBH systems exhibit similar dynamics when the objects are far apart, finite-size effects become increasingly important as the orbits shrink due to the emission of GWs. The system's quadrupole moment, which is the primary factor affecting the waveforms, is influenced by adiabatic tidal effects [69–72, 74–77, 129, 405–407], quadrupole-monopole terms [68, 73, 328, 413], and possible resonant excitations of the stars' modes [134, 414–419] or nonlinear fluid instabilities

at low frequencies [420–422]. All of these effects can be accurately described using PN theory, with adiabatic tidal effects representing the most important contribution due to matter.

Consider a spherically symmetric star immersed in an external field. The presence of the field induces perturbations on the star, which can be decomposed in even “gravitoelectric” and odd “gravitomagnetic” moments, denoted as G_L and H_L , where L is a multi-index $a_1 a_2 \dots a_\ell$. In the stationary (adiabatic) treatment of tidal effects, the mass and current multipoles induced by the external fields, M_L and S_L respectively, are linearly related to the tidal moments via the tidal polarizability coefficients μ_ℓ , σ_ℓ :

$$M_L = \mu_\ell G_L, \quad (4.1)$$

$$S_L = \sigma_\ell H_L. \quad (4.2)$$

These coefficients are related to the relativistic Love numbers via:

$$\mu_\ell = \frac{2k_\ell}{(2\ell - 1)!!} R^{2\ell+1}, \quad (4.3)$$

$$\sigma_\ell = \frac{(\ell - 1)j_\ell}{4(\ell + 2)(2\ell - 1)!!} R^{2\ell+1}, \quad (4.4)$$

where k_ℓ^A is the ℓ -th electric Love number of the body, j_ℓ its magnetic-type Love number and R its radius. The dimensionless tidal parameters are then defined as:

$$\Lambda_\ell = \frac{\mu_\ell}{M^{2\ell+1}} = \frac{2}{(2\ell + 1)!!} k_\ell \mathcal{C}^{-(2\ell+1)}, \quad (4.5)$$

$$\Sigma_\ell = \frac{\sigma_\ell}{M^{2\ell+1}} = \frac{(\ell - 1)j_\ell}{4(\ell + 2)(2\ell - 1)!!} \mathcal{C}^{-(2\ell+1)}, \quad (4.6)$$

where we define the compactness of a star as $\mathcal{C} = M/R$. Tidal Love numbers can be explicitly computed by solving the coupled system of perturbed EFE together with the perturbed hydrodynamical equations [406, 407], and are a function of the compactness of the star. In a BNS system, the tidal moments are each sourced by the companion body. The energy of the system, following PN arguments, is given (at LO in tidal interactions) by

$$E = \frac{\mu v^2}{2} - \frac{\mu M}{r} \left(1 + \frac{\hat{\mu}}{r^5} \right). \quad (4.7)$$

where $\hat{\mu} = (3m_1/2m_2)\mu_2^{(1)} + (3m_2/2m_1)\mu_2^{(2)}$. The variation in energy affects GW emission, and tidal effects enter the PN GW phase expansion at 5PN via the reduced

tidal parameter $\tilde{\Lambda}$, defined as:

$$\tilde{\Lambda} \equiv \frac{16}{13} \left[\frac{(m_1 + 12m_2)m_1^4 \Lambda_1}{M^5} + (1 \leftrightarrow 2) \right]. \quad (4.8)$$

Tidal effects can also be included in EOB models (see Sec. 4.2.1). The EOB electric tidal coefficients, are usually denoted as $\kappa_{\ell,+}^i$, where $i = A, B$ labels the body. They are related to the tidal Love numbers through

$$\kappa_{\ell,+}^A = 2k_\ell^A \frac{X_B}{X_A} \left(\frac{R_A}{M_A} \right)^{2\ell+1} = 2k_\ell^A \frac{X_B}{X_A} \mathcal{C}_A^{-(2\ell+1)}. \quad (4.9)$$

In terms of these variables, the LO EOB tidal contribution is given by $\kappa_2^T = \kappa_{2,+}^A + \kappa_{2,+}^B$. Similarly, the EOB magnetic tidal coefficients are typically denoted as $\kappa_{\ell,-}^i$, and given by:

$$\kappa_{\ell,-}^A = \frac{1}{2} j_\ell^A \frac{X_B}{X_A} \left(\frac{R_A}{M_A} \right)^{2\ell+1} = \frac{1}{2} j_\ell^A \frac{X_B}{X_A} \mathcal{C}_A^{-(2\ell+1)}. \quad (4.10)$$

4.1 Resonant tides

Tidal resonances in coalescing compact binaries have been studied for a long time in connection to GW observations [414, 416, 417, 423] (See also [424–427] for earlier work on tidally generated radiation.) During the coalescence process, the proper oscillation modes of a NS can be resonantly excited by the orbital frequency. For a quasi-circular orbit, the energy transfer between the orbit and the mode can change the rate of inspiral and alter the phase of the chirping GWs [417]. In general, the impact of the tidal resonance on the GWs depends on the duration of the resonance, and it is stronger the slower the orbital decay is. Initial studies focused on the excitation g -modes at frequencies $\lesssim 100$ Hz, but the resonance effect was found negligible due to the weak coupling between the mode and the tidal potential [414]. In contrast, f -modes have stronger tidal coupling but also higher frequencies $\sim (GM_A/R_A^3)^{1/2}$, thus falling in the kilo-Hertz regime for typical NS masses M_A and radii R_A of the star A . These frequencies are too large for the resonance to occur during the inspiral [417]; their value actually approaching (or being larger than) the merger frequency [428].

NR simulations of quasi-circular NS mergers conducted so far do not show decisive evidence for the presence of f -mode resonances. On the one hand, some GW models including f -mode resonances have been shown to reproduce the NR waveform phasing near merger [134, 418, 419]. On the other hand, the same data can be reproduced at

the same accuracy without assuming the presence of a f -mode resonance nor additional parameters [142, 143, 418, 429]. Moreover, it is well known that the two NSs come in contact well before the resonance condition is met [130, 184] (see also discussion below in Sec. 4.1.1). Interestingly, f -mode excitations are instead observed in NR simulations of highly eccentric compact binaries composed of BH–NS [430] and two NSs [431, 432]. In these mergers, each close passage triggers the NS’s oscillation on proper modes; the GW between two successive bursts (corresponding to the passages) clearly shows f -mode oscillations (see Fig. 4.5 below). Note however that the excitation does not meet the resonant condition [431]: the close periastron passage exerts a tidal perturbation which excites the axisymmetric ($m = 0$) $\ell = 2$ mode [427].

Recent studies after GW170817 [12, 19, 369] re-considered waveform models with f -mode resonances and demonstrated the possibility of GW asteroseismology with BNS inspiral signals [433–435]. In particular, the prospect study in Ref. [435] demonstrates that neglecting dynamical tidal effects associated with the fundamental mode could lead to systematic biases in the inference of the tidal polarizability parameters and thus the NS equation of state. Since GW analyses are performed with matched filtering, these studies *postulate* the validity of resonant models to merger or contact and a sufficient accuracy of the GW template. While it is, in principle, possible to observationally verify the necessity of a f -mode resonance model in a particular observation (e.g. via hypothesis ranking), the quality of current GW data *and* templates at high-frequencies is still insufficient [251]. The potential relevance of resonant tides for GW astronomy and the above considerations motivates further detailed comparisons between the current analytical results and NR simulations.

Here, we consider state-of-art models for the compact binary dynamics with tidal resonances in the EOB framework and critically assess their validity against NR data. In Sec. 4.1.1 we briefly summarize the effective Love number model proposed in Refs. [134, 135] that can be efficiently coupled to any EOB implementation to generate precise inspiral-merger waveforms. This model prescribes a dynamical Love number (or tidal coupling constant) as function of the quasi-circular orbital frequency that, while approaching merger, enhances the effect of tidal interaction. Qualitatively, this effect is known also from studies of tidally interacting compact binaries with affine models [436–440]. On physical ground, tidal interactions stronger than those expected by adiabatic and PN models are expected towards merger [129]. For example, early EOB/NR comparisons for quasi-circular mergers found that the description of tidal effects after contact and towards merger requires to enhance the attractive character

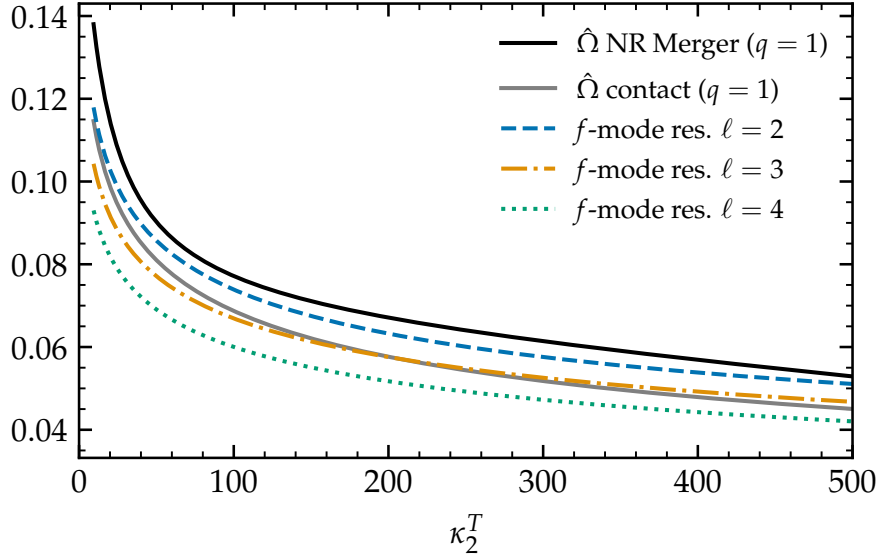


FIGURE 4.1: Mass-rescaled orbital merger frequency, contact frequency and resonant conditions for $\ell = 2, 3, 4$ modes for equal-mass binaries with different tidal coupling constant κ_2^T . The merger frequency is computed from the NR quasi-universal fits of Ref. [428]. The contact frequency is estimated as in [128] using the quasi-universal relations $C_A(\Lambda_2^{(A)})$ of [262].

of the EOB tidal potential in PN form [130, 429, 441]. In these studies, it was also pointed out that a key diagnostic to robustly assess tidal effects in NR data is the use of gauge-invariant energetics [336], see also Sec. 1.5.

Here, we compare different EOB tidal models to selected, high-resolution NR simulations considering both energetics and GW phasing. In particular, we consider quasi-circular mergers and show that the f -mode resonance does not give a consistently accurate description of both energetics and the waveform. Similarly, we also consider a highly eccentric merger and show that a f -mode resonance model does not qualitatively capture the “free-oscillation” feature observed in the frequency-evolution of the NR waveform. Notably however – modulo this effect – the EOB waveform and (orbital) frequency closely follow the NR quantities up to \sim one orbit before merger, attesting to the goodness of the dynamics description provided by the model even for these extreme systems.

In Sec. 4.1.3 we then perform Bayesian analyses and model selection on GW170817 data using the various EOB models introduced in Sec. 4.1.1. We find that f -mode augmented models are not favored with respect to models which only implement adiabatic tidal effects. The f -mode resonant frequencies cannot be measured in GW170817, as

also observed in [433]. This is expected, since f -mode inference is mostly informative at frequencies larger than $\sim 1\text{kHz}$ (for comparable and canonical NS masses), and GW170817 may not contain enough high-frequency information to allow for such a measurement.

4.1.1 Effective Love number model

The model of Refs. [134, 135] describes the resonant excitation of the NS f -mode by a *circular* orbit based on an *effective* quadrupolar Love number. The latter is defined by an approximate, Newtonian solution of

$$k_2^{\text{eff}} = \frac{E_{ij}Q^{ij}}{E^2}, \quad (4.11)$$

where $E_{ij} = \partial_i\partial_j\phi$ is the external quadrupolar field derived from the Newtonian potential ϕ and Q_{ij} is the NS's quadrupole. The resonance of a NS's modes is triggered by the condition

$$m\hat{\Omega} X_A = \bar{\omega}_{fA}^{(\ell)}, \quad (4.12)$$

and its net effect is an enhancement of the Love number $k_\ell^{(A)}$. This results in a simple prescription to obtain ‘‘dynamical tides’’ based on the formal substitution of the Love numbers (or equivalently the tidal coupling constants) with their effective values:

$$k_\ell^{(A)} \mapsto k_\ell^{\text{eff}(A)} := \alpha_{\ell m}(\nu, \hat{\Omega}, \bar{\omega}_{fA}^{(\ell)}, X_A) k_\ell^{(A)} \quad (4.13)$$

where the dressing factor $\alpha_{\ell m}$ in Eq. (4.13) is a multipolar correction valid for $\ell = m$.

In this work, the model with $\ell = 2, 3, 4$ resonances is incorporated in `TEOBResumS-GIOTTO` [142, 144, 258, 285, 286, 296, 332, 337]. Tidal interactions are described by additive contribution A_T to the EOB metric potential [128]. Different choices for A_T are considered: (i) a PN baseline expression including NNLO gravitoelectric corrections [130] (as also employed in Refs. [134, 135]) and LO gravitomagnetic terms [143], (ii) a resummed expression of high-order gravitoelectric $\ell = 2$ PN terms obtained from gravitational self-force computations [429, 442], hereafter referred to as $\text{GSF}2^{(+)}\text{PN}^{(-)}$ (See Tab.I of [143]); (iii) a resummed expression of high-order gravitoelectric $\ell = 2, 3$ PN terms obtained from gravitational self-force computations, $\text{GSF}23^{(+)}\text{PN}^{(-)}$ (see Sec. 4.2 below).

For typical binaries the resonant condition in Eq. (4.12) is met before the moment of merger (defined as the peak of the $\ell = m = 2$ mode of the strain). This is shown

in Fig. 4.1 for equal-mass mergers, where the merger frequency (solid black line) is computed in terms of the tidal coupling constant κ_2^T using the quasi-universal relations of Ref. [428]. The contact frequency (gray solid line) is estimated as in Eq. (78) of [128]; this simple expression is known to overestimate the values extracted from the simulations¹ – e.g. $\hat{\Omega} \sim 0.04$ for equal mass NSs with $\kappa_2^T \sim 180$, effectively corresponding to the last 2-3 GW cycles to the moment of merger [130] – but provides a sufficient estimate for this work.

Colored (dashed) lines indicate that the resonant excitation for the $\ell = 2, 3, 4$ f -mode happens progressively earlier in the merger process. While the $\ell = 2$ f -mode is excited shortly before merger (approximately corresponding to the last GW cycles) and after contact, the octupolar and hexapolar $\ell = 3, 4$ mode resonances are reached before the NSs’ contact. This has two important implications. First, the predicted resonance phenomenon can be directly tested with NR simulations and should, if significant, be visible in the gauge-invariant energetics of the dynamics from the simulations. Second, the dominant $\ell = 2$ resonance happens in a regime in which the model itself is not valid since the NSs are not isolated nor “orbiting” anymore; the matter dynamics being governed by hydrodynamical processes.

The typical behavior of the dressing factors $\alpha_{\ell m}$ during the quasi-circular merger process is shown in Fig. 4.2 for a fiducial binary (that reproduces Fig. 1 of [135] with our implementation). After the resonance, the dressing factors decrease and become smaller than one or even negative for typical BNS parameters. Since the post-resonance behavior is not directly modeled in the effective Love number model it is unclear to what extent this effect is physical. However, given that the resonances happen before merger, this trend affects the accuracy of the EOB waveforms that adopt this f -mode model.

Indeed, the behavior of the dressing factors after the resonance can introduce unphysical features in the EOB dynamics by affecting the EOB light ring, r_{LR} . When using the PN expanded tidal model with dressed tides, the peak of the orbital frequency typically happens *after* the resonance, i.e. at $\hat{\Omega}_{\text{peak}} > \hat{\Omega}_f^{(2)}$. Since $\hat{\Omega}_{\text{peak}}$ (the EOB light ring) is the natural point to stop the EOB dynamics, the earlier resonance generates an unphysical step increase of the waveform’s amplitude approaching merger. In order to minimize this behavior, the EOB model of [134, 135] terminates the EOB dynamics at the NR merger using the quasi-universal fits of [140, 428] for which $\hat{\Omega}_{\text{mrg}}^{\text{NR}} < \hat{\Omega}_{\text{peak}}$. We follow here the same procedure, but emphasize that this solution is not satisfactory

¹A better representation would be obtained accounting also for the shape love number of the stars, h [128, 130]

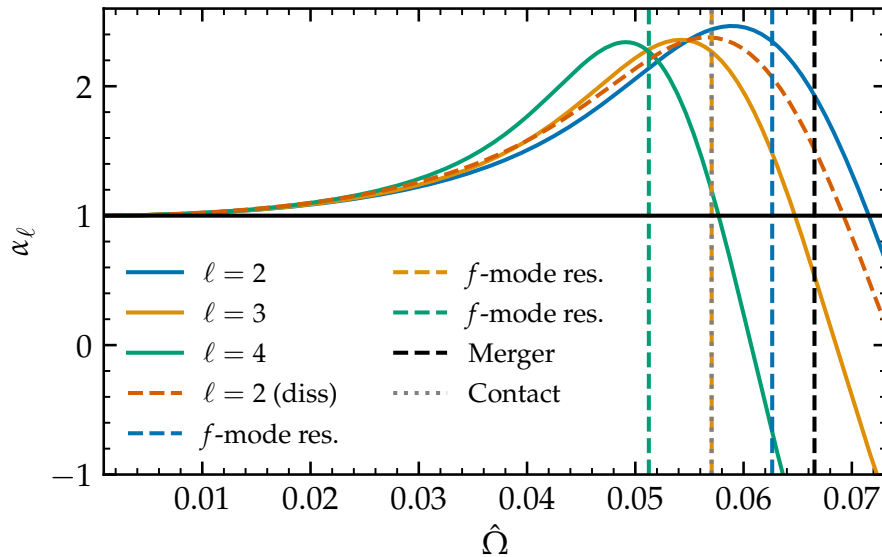


FIGURE 4.2: Dressing factors prescribed by the effective Love number model as a function of the orbital frequency and for a fiducial binary. Vertical lines mark the resonances and the merger frequency. The dashed red line is the waveform’s amplitude correction due to dynamical tides. The dotted gray line, which happens to be superimposed to the green $\ell = 3$ resonance, corresponds to the contact frequency of the stars.

since a well-designed EOB model should not break before its light ring (this is true for `TEOBResumS` even in the BBH case). Further, we manually impose that $\alpha_{\ell m} \geq 1$ post-resonance.

4.1.2 Comparison with numerical-relativity data

We contrast different EOB tidal models to selected NR simulations considering both gauge-invariant energy-angular momentum energetics [336] and the $\ell = m = 2$ waveform mode phasing. We consider the NNLO [130], $\text{GSF2}^{(+)}\text{PN}^{(-)}$ [429, 442], and $\text{GSF23}^{(+)}\text{PN}^{(-)}$ [143] prescriptions for the EOB tidal potential with and without the f -mode resonance model described above. We consider NR data from quasi-circular and highly eccentric mergers computed respectively in Ref. [167, 443] and Ref. [432] using Jena’s BAM code [121, 184]. The binding energy E_b and the specific angular momentum j are computed as described in [130, 336]. The tidal contribution E_b^{T} to the energy curves is isolated by subtracting the relative BBH contribution as described in [130, 429, 441]. For the NR data we use the equal mass, non-spinning BBH SXS simulation `SXS:BBH:0002`. For TD waveforms comparison, the arbitrary time and

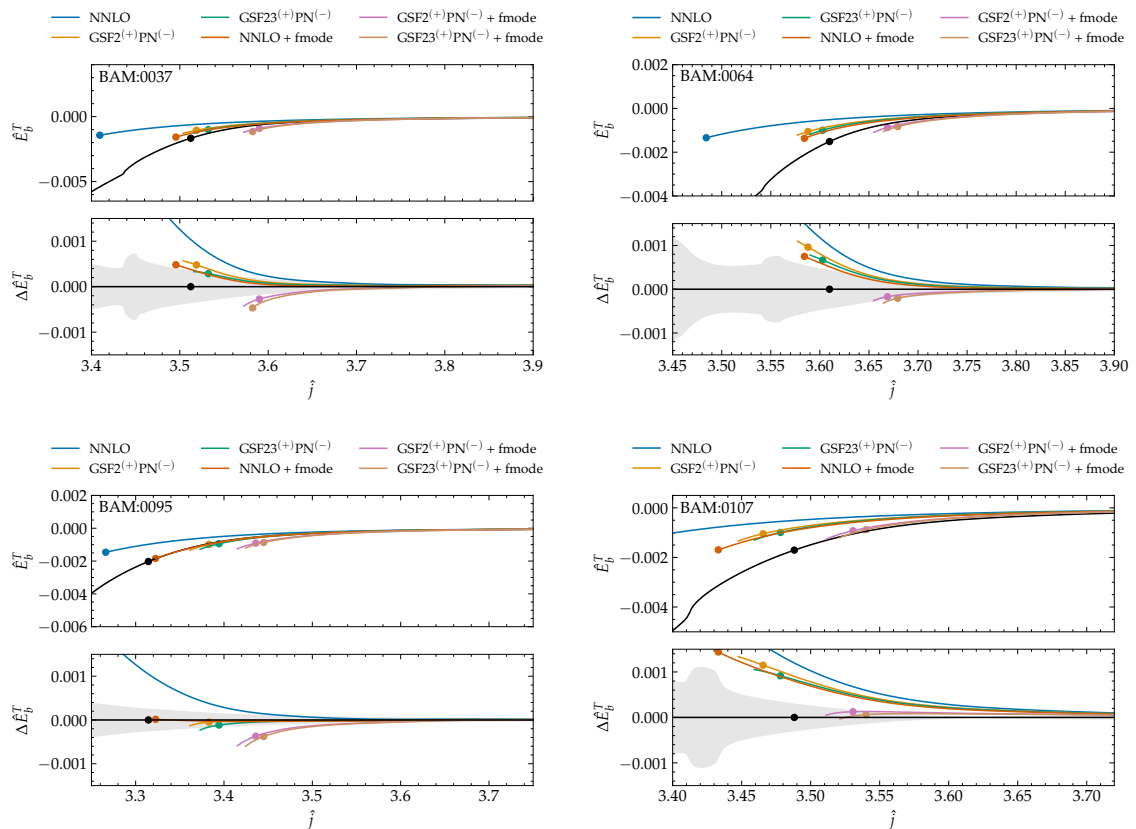


FIGURE 4.3: \hat{E}_b^T and $\Delta\hat{E}_b^T$ as functions of the angular momentum \hat{j} of the system for the equal mass BAM simulations considered in this paper (black) and the respective TEOBResumS simulations. The latter are computed using different baseline tidal models (NNLO, GSF2⁽⁺⁾PN⁽⁻⁾, GSF23⁽⁺⁾PN⁽⁻⁾) and f-mode contributions. The EOB and NR mergers are denoted via dots, while shaded gray bands indicate the NR error.

phase relative shifts are determined by minimizing the phase difference $\Delta\phi^{\text{EOBNR}}$ over a fixed time interval Δt , e.g. [168, 444].

Quasi-circular mergers We consider the simulations of the CoRe collaboration named BAM:0037 [167], BAM:0064 [167], BAM:0095 [167] and BAM:0107 [443] corresponding to non-spinning mergers with $\kappa_2^T = 187, 287, 73, 136$ and $q = 1, 1, 1, 1.224047$ respectively. These data are computed at multiple resolutions and show convergent properties that allowed a clear assessment of the errorbars [143]. Hence, these are some of the most challenging NR waveforms to reproduce with analytical models.

Figure 4.3 shows the tidal contribution to the binding energy for the NR data and for all the considered models (top panels) and the differences $\Delta E_b^T = E_b^{\text{EOB}} - E_b^{\text{NR}}$

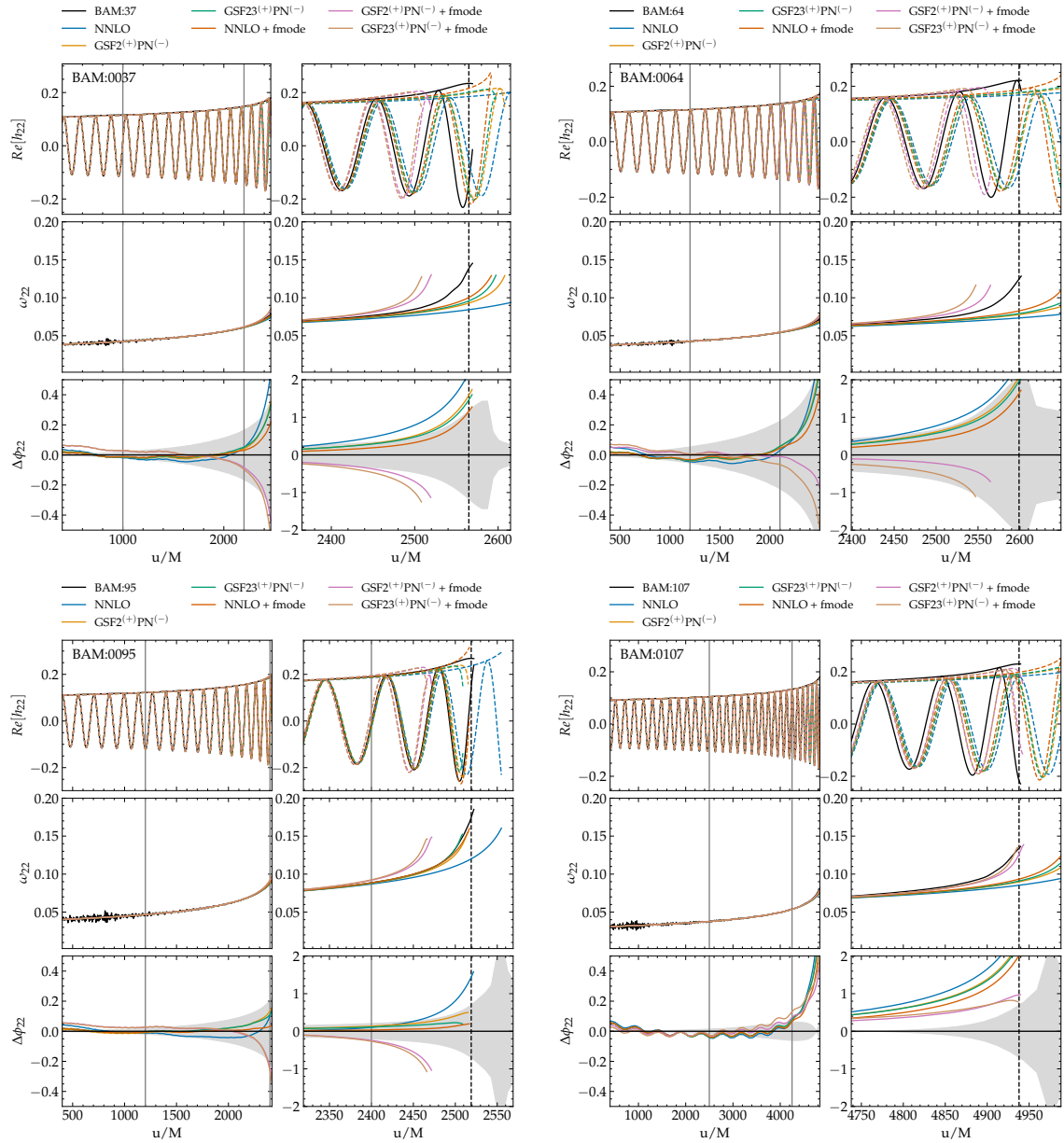


FIGURE 4.4: Waveforms (top panels), frequency evolution $\hat{\omega}_{22}$ (middle panels) and EOB/NR phase difference $\Delta\phi^{\text{EOB/NR}}$ (bottom panels) for all the non spinning BNS simulations considered in Fig. 4.3. The GSF+ f -mode tidal model is the closest to NR for the BAM:0064 and BAM:0107 simulations, while for BAM:0037 and BAM:0095 the NNLO+ f -mode and the GSF models without dynamical tides deliver the best waveforms.

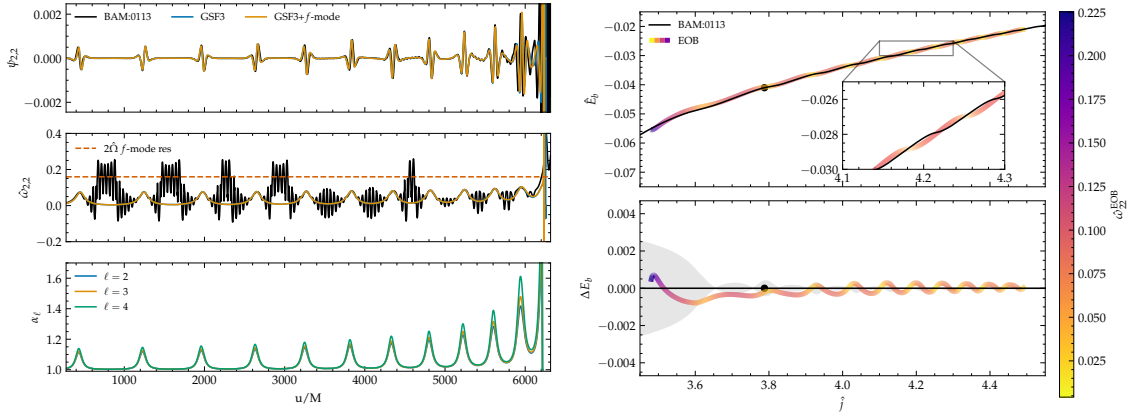


FIGURE 4.5: Left: EOB/NR comparison between the multipolar Weyl scalars $\psi_{2,2}$ (top panel) and their respective frequency evolutions $\hat{\omega}_{22}$ (middle panel). The f -mode excitations that are typically observed in NR simulations between two close encounters are not captured by the f -mode resonance model which prescribes $k_\ell \mapsto \alpha_\ell k_\ell$. Right: EOB/NR comparison between the evolution of the binding energy \hat{E}_b of the system as a function of its orbital angular momentum \hat{j} for the same binary shown in the left panel. The colorbar additionally indicates the EOB frequency evolution along the dynamics. The energy difference that we obtain is $\mathcal{O}(10^{-4})$, compatible with the estimates of the energy carried by f -mode oscillations via Eq. 17 of [432].

(bottom panels). The EOB model based on the NNLO PN expansion of the A_T potential significantly underestimates the actual tidal interaction, as it is well known from previous results [130, 429]. Augmenting the NNLO model with f -mode resonance terms improves the agreement with NR, but the energetics are compatible only for BAM:0095 while for the other three binaries the disagreement remains significant. Further, without forcibly stopping the evolution at the NR merger (see Sec. 4.1.1) the amplitude of the waveform, too, would be largely overestimated near merger. Note the NNLO+ f -mode is the model employed in `SEOBNRv4` [134, 135, 419]. The $\text{GSF2}^{(+)}\text{PN}^{(-)}$ and $\text{GSF23}^{(+)}\text{PN}^{(-)}$ models behave very similarly to the NNLO+ f -mode model, improving the NNLO behavior but also departing from the NR data for BAM:0064 and BAM:0107. The $\text{GSF23}^{(+)}\text{PN}^{(-)}$ is currently the default choice in `TEOBResumS` [143, 429]. If these GSF-model are augmented with the f -mode the dynamics becomes too attractive and departs from the NR data in all the considered binaries but BAM:0107 and BAM:0064.

Figure 4.4 shows the GW phasing analysis for all the simulations considered; the top, middle and bottom panel show the evolution of the waveform's amplitude, the waveform's frequency and the phase differences $\Delta\phi = \phi^{\text{EOB}} - \phi^{\text{NR}}$ respectively. For BAM:0107, the frequency evolution of the NNLO model significantly differs out of the

alignment interval and is not sufficiently rapid to follow the NR data. This is in agreement with the relative energetics discussed above. The NNLO+ f -mode and the GSF (without f -mode) models improve over the NNLO phasing but, again, the frequency evolution remains too slow to capture the NR tides. On the contrary, the GSF2+ f -mode models describe very closely the frequency evolution of the NR data, and give the best approximation of the waveform for this binary. This behavior is consistent with what observed in the energetics above, although the merger – approximated by the EOB light ring – is reached too early in the coalescence.

The BAM:0037 and BAM:0064 phasing analyses are qualitatively analogous to one another, and no model is able to reproduce the NR frequency evolution, although the phase of the corresponding waveform might fall within the NR error. Tidal effects are too attractive for f -mode augmented GSF models, and not attractive enough for the remaining models.

Differently from the others, for the BAM:0095 simulation the NNLO+ f -mode and the GSF (no f -mode) models are the closest to the NR data and within the error bars. In this case, the GW phasing analysis is compatible with the results of the energetics.

The results discussed above highlight that establishing the presence of f -mode resonances in quasi-circular merger computed in NR is not straightforward. On the one hand, the inclusion of this interaction in EOB models can help to obtain analytical waveforms more faithful to NR, at least for some binaries. This is evident in the analysis of the equal-mass, non-spinning merger BAM:0095, where the inclusion of the f -mode resonance in the NNLO EOB model shows an excellent agreement to NR data in both energetics and phasing as opposed to the NNLO EOB baseline. On the other hand, the f -mode resonance does not capture well the waveforms of other binaries and the EOB/NR waveform agreement does not always correspond to an improvement of the energetics (i.e. the Hamiltonian). For example, the NNLO+ f -mode model does not perform uniformly well with the other equal-mass, non-spinning binaries. The GSF+ f -mode models, instead, give a very attractive interaction close to merger and significantly depart from NR for case studies BAM:0037 and BAM:0095.

Highly eccentric encounters We consider the BAM:0113 simulation of Ref. [432], where constraint satisfying initial data are prepared and evolved for a highly eccentric ($e_{\text{NR}} \sim 0.45$) merger. The binary undergoes eleven periastron passages before merging; each passage is characterized by a burst of GW radiation, as shown in Fig. 4.5. Between each burst, the GW shows oscillations compatible with the axisymmetric f -mode of

the (nonrotating) NS component. The oscillation frequency can be identified also in the fluid density, and it is triggered by the close passage to the companion [431].

TEOBResumS can model these types of mergers [145, 146, 148]. Although previous works focused on BBH systems, the extension of TEOBResumS to eccentric and hyperbolic binaries including NSs is straightforward, and we have it implemented in this work. The EOB/NR comparison with these types of NR data requires to fine-tune the EOB initial conditions because no analytical map is known between EOB and the initial data employed in the simulation [445]. In order to reproduce the NR waveform, we fix the NS masses and quadrupolar tidal parameters to those employed in the NR simulation and vary independently the nominal EOB eccentricity and initial frequency until an acceptable EOB/NR phase agreement is found. This procedure is equivalent to fixing the initial frequency of the waveform and varying independently the mean anomaly and the eccentricity of the system. For this work we do not implement a minimization procedure, we instead find that manually tuning the parameters to $\hat{\omega}_0 = 0.0058$ and $e_{\text{EOB}}^0 = 0.58$ is enough to obtain a good visual EOB/NR agreement that is sufficient for our purposes.

The waveform comparison is performed in terms of the multipole $\psi_{22} = \ddot{h}_{22}$ of the Weyl pseudo-scalar Ψ_4 since this quantity best highlights the f -mode oscillations between the bursts. As shown in the top and middle panels of Fig. 4.5, the EOB ψ_{22}^{EOB} closely matches the NR data in both amplitude and phase showing an excellent agreement during the ten periastron passages and up to merger. However, the middle panel also shows that the EOB f -mode model does not capture the high frequency oscillations in the GW frequency $\hat{\omega}_{22}$. This might not be surprising: as shown in the bottom panel of Fig. 4.5, the f -mode model prescribes significant variations of the dressing factors only around the peaks of the (orbital) frequency while it is close to one in-between the peaks. By contrast, in the NR data the high-frequency oscillations are observed mainly at times between two close passages². Further, by comparing the orbital frequency evolution to the resonant frequency condition, we observe that throughout the inspiral the resonance is never fully crossed. To model this behavior, it seems necessary to consider more complex models which consider the post-resonance dynamics – not included in our effective model – and for which the tidal response is

²We note that in order to correctly compute the f -mode induced amplitude oscillations, Ref. [432] corrected the multipoles for displacement-induced mode mixing [446]. Although we mainly focus on the frequency of the waveform, rather than the amplitude, Ref. [432] suggests that this quantity too might be influenced by such an effect, which we do not account for here.

evolved together with the orbital dynamics of the system [427, 447, 448] and incorporate those models in the EOB.

We complement the GW phasing analysis with a discussion on the energetics. Figure 4.5 shows the binding energy of the highly eccentric system as a function of the orbital angular momentum. The decrease of $\hat{E}_b(\hat{j})$ presents clear oscillations that can be reconducted to the close encounters. During each passage both \hat{E}_b and \hat{j} decrease but the times at which the two NSs are apart are characterized by approximate “plateaus” (moments of approximately constant energy and angular momentum, see the inset). From this interpretation, it appears that the EOB and NR curves, although close, are not perfectly compatible: the encounters do not always align in the $\hat{E}_b(\hat{j})$ curves.

Finally, we stress that, modulo the small f -mode feature, our EOB waveforms *quantitatively* reproduce highly eccentric NR simulations up to few orbits before merger. Ours is the first EOB model capable of describing highly eccentric comparable-mass system including NSs, and this is to our knowledge the first EOB/NR comparison of this kind. The striking agreement between EOB and NR in Fig. 4.5 attests to the goodness of the radiation reaction model employed within `TEOBResumS`.

4.1.3 Model selection on GW170817

We now apply our models to GW170817, using the `BAJES` pipeline [34] and the `dynesty` [204] sampler. We consider 128 seconds of data around GW170817 GPS time, and analyze frequencies between 23 Hz and 2048 Hz. The employed prior is uniform in component masses and tidal parameters, isotropic in spin components and volumetric in luminosity distance. It spans the ranges of chirp mass $\mathcal{M}_c \in [1.1, 1.3]$, mass ratio $q \in [1, 3]$, spin magnitudes $\chi_i \in [0, 0.05]$, tidal parameters $\Lambda_i \in [0, 5000]$ and distance $D_L \in [20, 100]$ Mpc. We consider three models for our analysis: the `GSF23(+)PN(-)` model, the `GSF23(+)PN(-)` model augmented with dynamical tides and the NNLO model, also augmented with dynamical tides³. When using the f -mode resonance model, we either fix the values of $\bar{\omega}_{fA}^{(2)}$, $\bar{\omega}_{fB}^{(2)}$ via the quasi-universal relation of [449] or we infer them independently of Λ , imposing uniform priors on $\bar{\omega}_{fi}^{(2)} \in [0.04, 0.14]$ with $i = A, B$.

³For computational convenience we do not employ dressed spin-quadrupole parameters

TABLE 4.1: Logarithmic evidences $\log Z$ of the five models employed in our GW170817 reanalysis and their Bayes' factors computed against the GSF model. The GSF model is slightly favored over the GSF + f -mode model both when we do and do not attempt to infer $\bar{\omega}_f^{(2)}$ from the GW data. NNLO + f -mode models, instead, appear mildly disfavored with respect to those employing the adiabatic GSF tidal baseline.

Model (X)	$\log Z$	$\log \mathcal{B}_{\text{GSF}}^{\text{X}}$
GSF	480.23 ± 0.18	0
GSF + f -mode	479.61 ± 0.18	-0.62
GSF + f -mode + sampling	479.57 ± 0.18	-0.66
PN + f -mode + sampling	479.22 ± 0.18	-1.01
PN + f -mode	479.15 ± 0.18	-1.08

The evidences recovered with the five models are reported in Tab. 4.1. The data mildly favors the GSF tidal model and the GSF model augmented by f -mode resonances with respect to the NNLO dynamical tides model. When sampling the resonance frequencies (see Fig 4.6), we find that it is not possible to precisely determine $\bar{\omega}_f^{(2)}$ from GW170817 data. For both tidal baselines, the recovered $\bar{\omega}_B^{(2)}$ distribution is consistent with the flat prior imposed. The distribution of $\bar{\omega}_A^{(2)}$, instead, allows only to impose an upper or lower bound on the f -mode frequency, depending on whether the GSF or NNLO tidal model is employed. This is consistent with what previously observed in Ref. [435]: it is not possible to accurately determine $\bar{\omega}_f^{(2)}$ from GW170817 data.

A simple Fisher Matrix study (right panel of Fig. 4.6) immediately clarifies the reason for the fact illustrated above. Following Ref. [129], we compute the diagonal Fisher Matrix (normalized) integrands $\gamma(f)fv^p$:

$$\gamma(f) = \frac{f^{-7/3}/S_n(f)}{\int_{f_{\min}}^{f_{\max}} f^{-7/3}/S_n(f)}, \quad (4.14)$$

where $v = (M\pi f)^{1/3}$ and p depends on the parameter considered. Employing the PN FD model of Ref. [450] and considering only the LO for each of the studied parameters, one finds that $p_{\mathcal{M}} = -10$, $p_\nu = -6$, $p_{\bar{\Lambda}} = 10$ and $p_{\bar{\omega}_f} = 22$. This indicates that f -mode parameters are determined close to the resonance frequency, where the effect of the model is strongest ($\alpha_\ell > 1$). For GW170817, such frequencies are dominated by the detectors' noise.

It is worth noting that in the region where dynamical effects become more prominent (above the frequency of contact between the two stars), the model itself is not physically grounded. PE studies such as the ones presented in [433, 435, 451] circle

this issue by generating waveforms exclusively up to the contact frequency, measuring the secular accumulated phase difference due to the effect of dynamical tides away from the resonance over a very large number of GW cycles. Directly testing the physical validity of this approach is challenging, as it would require extremely long NR simulations which are currently unavailable. Within our EOB model, we find an accumulated phase difference due to dynamical tides of $\sim 0.5 - 1$ rad at contact for a $1.35M_{\odot} + 1.35M_{\odot}$ reference binary from 20 Hz. Most of the phase is accumulated above 300 Hz. This phase difference might become measurable with third generation detectors [173], although biases due to an imperfect knowledge of the point mass and (adiabatic) tidal sectors of the models could affect future measurements. Overall, while the f -mode model can be effective in improving the agreement between NR and EOB after contact and to merger, it is not clear whether this corresponds to the actual resonant effect or if it is rather an effective description for the hydrodynamics-dominated regime of the merger. Hence, caution should be applied whenever trying to extract actual physical information (i.e., the f -mode resonant frequencies) from a matched filtered analysis using templates that include f -mode resonances. More advanced, general-relativistic models of f -mode resonances coupled to EOB waveform appear necessary for applications in GW astronomy with next generation detectors and observations.

4.2 A new tidal model for TEOBResumS

In this section we focus on improving the tidal sector of TEOBResumS [143, 144, 259, 328], and provide a phenomenological representation of it for spinning BNS systems. The improvements concern (i) the computation and inclusion of additional higher order analytical information in the metric and waveform multipoles, and (ii) the inclusion of NR information via next to quasi-circular (NQC) parameters and through an additional NR-calibrated parameter, which enters the tidal part of the radial metric potential. For equal mass binaries, this parameter is clearly correlated with the effective tidal parameter of the system, and given a large enough number of high-quality simulations can be fit directly to NR.

4.2.1 EOB Tidal model

Below, we discuss the model used for BNS systems, highlighting improvements and differences with respect to the previous model of [143].

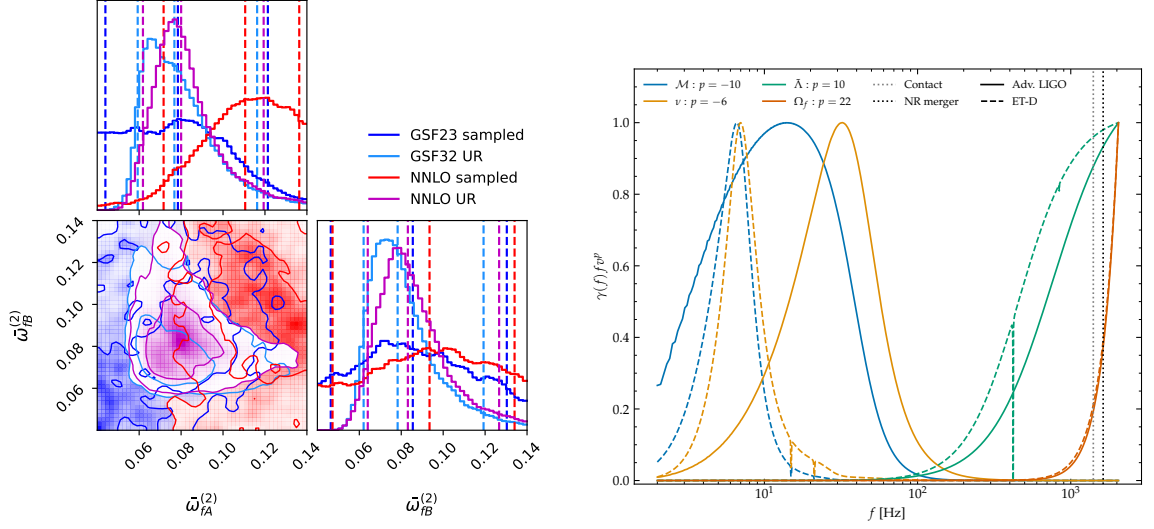


FIGURE 4.6: Left: posterior samples for $\bar{\omega}_{fA}^{(2)}$ and $\bar{\omega}_{fB}^{(2)}$ extracted from GW170817 via direct sampling (blue, red) or by applying quasi-universal relations to the mass and tidal parameters recovered (cyan, magenta). The sampled values span the entire interval investigated, indicating that we are not able to precisely extract the $\ell = 2$ resonance frequency from GW170817 data. Right: Fisher matrix integrands, computed as in [129], evaluated considering the LO phase contribution for chirp mass, symmetric mass ratio, effective tidal parameter and f -mode frequency. Straight curves are computed using advanced LIGO PSD [335], while dashed lines are estimated with Einstein Telescope PSD [334]. Notably, the f -mode resonance frequency is informed mainly by very high frequencies, larger than merger or contact.

Hamiltonian In order to account for tidal and self-spin effects, the effective EOB Hamiltonian of Eq. 1.5 needs to be modified. Following the notation of [143], electric (+) and magnetic (−) tidal interactions are generally included within the $A(r)$ and $B(r)$ potential as

$$A = A_0 + A_T^+ + A_T^-, \quad (4.15)$$

$$B = B_0 + B_T^+ + B_T^-. \quad (4.16)$$

where A_0, B_0 are the point mass BBH baselines of the metric potentials. The tidal part of $A(r)$ is then typically further factorized as

$$A_T^\pm(u) = \sum_{\ell \geq 2} A_A^{(\ell \pm) \text{LO}}(u) \hat{A}_A^{\ell \pm}(u) + (A \leftrightarrow B) \quad (4.17)$$

where $u = 1/r$ is the inverse of the EOB radial coordinate and A, B label the bodies. The LO coefficients are straightforwardly given by

$$A_A^{(\ell+)\text{LO}}(u) = -\kappa_A^{(\ell+)} u^{2\ell+2}, \quad (4.18)$$

and

$$A_A^{(\ell-)\text{LO}}(u) = -\kappa_A^{(\ell-)} u^{2\ell+3}. \quad (4.19)$$

Within `TEOBResumS`, we consider LO electric contributions up to $\ell = 8$ [452], extending the previous model of [143] that only included them up to $\ell = 4$, and magnetic contributions up to $\ell = 3$.

The higher order corrections to Eq. 4.17 are known up to 2PN (NNLO) [70]. Notably however, rather than relying on the simple PN-expanded expressions above for $\hat{A}_A^{(2+)}$ and $\hat{A}_A^{(3+)}$, the `TEOBResumS` model implements a GSF-informed resummation of the potential:

$$\hat{A}_A^{(\ell\pm)}(u) = \hat{A}_A^{(\ell\pm)0\text{GSF}} + X_A \hat{A}_A^{(\ell\pm)1\text{GSF}} + X_A^2 \hat{A}_A^{(\ell\pm)2\text{GSF}}. \quad (4.20)$$

The expressions for the GSF coefficients can be read in Eq. (23)-(28) of Ref. [143]. Notably, all terms explicitly depend on the light ring radius r_{LR} , which determines the position of the pole in $A(u)$, and a ‘‘GSF exponent’’ p , which appears in the 2GSF terms. The former used to be set by computing the adiabatic light ring of the $A(u)$ potential with 2PN tidal terms; the latter was fixed to $p = 4$ independently of the binary parameters. Here, we make full use of the flexibility provided by the GSF resummation, fix $p = 9/2$ and determine r_{LR} via comparisons to NR data (see Sec. 4.2.3 below).

The $B(u)$ potential includes tidal effects to LO in the electric and magnetic tidal parameters [71, 143]:

$$B_T^+(u) = 3(3 - 5\nu)(\kappa_{2,+}^A + \kappa_{2,+}^B)u^6, \quad (4.21)$$

$$B_T^-(u) = 5(\kappa_{2,-}^A + \kappa_{2,-}^B)u^6. \quad (4.22)$$

The magnetic term is – to the best of our knowledge – presented here for the first time. Its computation used the results of Ref. [75], and follows standard techniques. We compute the Legendre transformation of the harmonic center of mass 1PN Lagrangian of Ref. [75] proceeding order-by-order, recovering the ADM Hamiltonian in the point mass sector. To obtain information about the EOB coefficients entering \hat{H}_{eff} we need

to express both the Hamiltonian $\hat{H}_{\text{ADM-like}}$ just obtained and \hat{H}_{eff} in the same set of coordinates. We do so by employing a canonical transformation, following closely the procedure outlined in [124]. We parameterize the 1PN generating function $G_{1\text{PN}}(\mathbf{q}, \mathbf{p}')$, where (\mathbf{q}, \mathbf{p}) are the original (ADM-like) coordinates and $(\mathbf{q}', \mathbf{p}')$ are the desired EOB coordinates. We then compute:

$$\mathbf{q}' = \mathbf{q} + \frac{\partial G}{\partial \mathbf{p}'}, \quad (4.23)$$

$$\mathbf{p} = \mathbf{p}' + \frac{\partial G}{\partial \mathbf{q}}, \quad (4.24)$$

and compare

$$\hat{H}_{\text{eff}}^2(q', p') = \left[1 + \hat{H}_{\text{ADM-like}}(q, p) + \alpha_1 \hat{H}_{\text{ADM-like}}(q, p)^2 \right]^2. \quad (4.25)$$

Here, the A and B potentials are expanded to 1PN, and the LO magnetic and electric terms in B are parameterized via two unknown coefficients χ_2 and β_2 , respectively. We then find

$$\beta_2 = 3(3 - 5\nu), \quad (4.26)$$

$$\chi_2 = 5. \quad (4.27)$$

thus confirming the result of Vines et. al. [71] and of Bini et. al. [70], and computing χ_2 for the first time. Notably, $B(u)$ is typically computed as the ratio of the EOB $D(u)$ BBH potential and the $A(u)$ potential discussed above. Since $A(u)$ already contains tidal corrections, in order to obtain the correct $B(u)$ PN LO one needs to correct the ratio $D(u)/A(u)$ with an additional term $B'_T(u)$, so that in practice

$$B_T(u) = \frac{D(u)}{A(u)} + B'_T(u)$$

$$B'_T(u) = (\kappa_{2,+}^A + \kappa_{2,+}^B)(8 - 15\nu)u^6 + B_T^-(u).$$

Regarding spinning BNSs, self-spin effects are included within the definition of the centrifugal radius r_c [296], which for BNS systems is modified to

$$r_c^2 = r^2 + \tilde{a}_Q^2 \left(1 + \frac{2}{r} \right) + \frac{\delta \hat{a}_{\text{NLO}}^2}{r} + \frac{\delta \hat{a}_{\text{NNLO}}^2}{r^2}, \quad (4.28)$$

where \tilde{a}_Q is an effective spin parameter that accounts for the EOS-dependent spin-monopole interaction [328] and reduces to the effective Kerr spin \tilde{a}_0 for BBH systems. Beyond LO, spin-squared contributions are included in $\delta\hat{a}_{\text{NLO}}^2$ and $\delta\hat{a}_{\text{NNLO}}^2$, which can be read e.g. in [142, 328]. Finally, we mention that we include and inverse-resum $\hat{G}_{\hat{s}}$ and $\hat{G}_{\hat{s}_*}$ up to 5.5PN order [304], improving on the previous model which only accounted for PN terms up to NNLO. Differently from BBH models, we do not employ any NR-informed coefficient in the gyro-gravitomagnetic terms.

Waveform and radiation reaction We remind the reader that the BBH EOB waveform is given by

$$h_{\ell m}^0 = c_{\ell+\epsilon}(\nu) h'_{\ell m}{}^{(N,\epsilon)} S^{(\epsilon)} h_{\ell m}^{\text{tail}} f_{\ell m} = h'_{\ell m}{}^{(N,\epsilon)} \hat{h}_{\ell m}^0. \quad (4.29)$$

where $h'_{\ell m}{}^{(N,\epsilon)}$ is a Newtonian prefactor, $S^{(\epsilon)}$ is the source term, $h_{\ell m}^{\text{tail}}$ includes tail contributions and $f_{\ell m}$ resums the residual terms [279, 296, 310, 311, 453, 454]. Tidal contributions are included in the EOB multipoles $h_{\ell m}$ via a simple additive correction to the BBH baseline, $h_{\ell m} = h_{\ell m}^0 + h_{\ell m}^{\text{tidal}}$. The tidal part of the waveform multipoles does not follow the standard EOB factorization, and is instead simply given by:

$$h_{\ell m}^{\text{tidal}} = h'_{\ell m}{}^{(N,\epsilon)} \hat{h}_{\ell m}^{\text{tidal}}, \quad (4.30)$$

$$\hat{h}_{\ell m}^{\text{tidal}} = c_{\ell m}^{\text{LO}} \kappa_A (1 + \beta_{\ell m}^1 x + \beta_{\ell m}^2 x^2) + (A \leftrightarrow B). \quad (4.31)$$

where $c_{\ell m}^{\text{LO}}$ and $\beta_{\ell m}^n$ parameterize the LO and n -th PN corrections to the waveform amplitude. These terms were previously known up to NLO [71, 128, 129]; here we exploit the results of Ref. [77] to compute and include also the LO correction to h_{44} and h_{42} and the subleading terms β_{22}^2 and β_{21}^1 .

To obtain the desired terms, we first evaluate the multipolar fluxes $F_{\ell m}$, parameterized by the unknown coefficients, via

$$F_{\ell m} = F_{\ell m}^{(N,\epsilon)} |\hat{h}_{\ell m}|^2 = F_{\ell m}^{(N,\epsilon)} |\hat{h}_{\ell m}^0 + \hat{h}_{\ell m}^{\text{tidal}}|^2. \quad (4.32)$$

The Newtonian flux prefactors $F_{\ell m}^{(N,\epsilon)}$ can be found in e.g. App. A of [311]. Note however that, with respect to the definition given in Ref. [311], the term $c_{\ell+\epsilon}(\nu)$ is here factored out and included directly in the definition of $\hat{h}_{\ell m}^0$. We then compare our results to the multipolar fluxes computed in Ref. [77], and thus extract the desired parameters. We find:

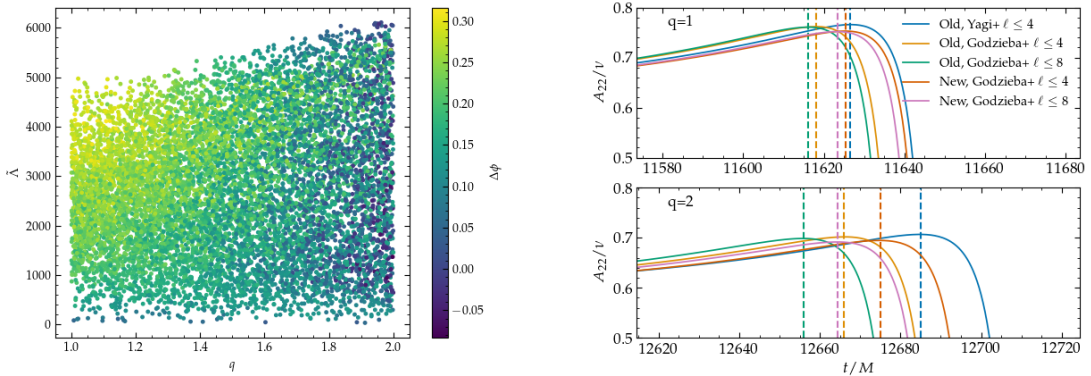


FIGURE 4.7: Impact of the new analytical information included in the model. Left: phase differences $\Delta\phi = \phi^{\text{old}} - \phi^{\text{new}}$ between the model without (“old”) and with (“new”) the newly added information. Right: time evolution of the (2, 2) amplitude for two non-spinning BNSs with $\tilde{\Lambda} = 2500$ and $q = 1$ (top) and $q = 2$ (bottom).

$$\beta_{22}^2 = \frac{-1096X_A^5 + 2567X_A^4 + 8198X_A^3 - 17052X_A^2 + 1439X_A + 1735}{504(2X_A - 3)}, \quad (4.33)$$

$$\beta_{21}^1 = \frac{-220X_A^3 - 130X_A^2 + 203X_A + 15}{126 - 168X_A}, \quad (4.34)$$

$$c_{44}^{\text{LO}} = 2(5 - 9X_A + 6X_A^2), \quad (4.35)$$

$$c_{42}^{\text{LO}} = 3584(5 - 9X_A + 6X_A^2). \quad (4.36)$$

When specifying β_{22}^2 to the equal mass case ($X_A = X_B = 1/2$) we find $\beta_{22}^2 = 167/256 \sim 0.653$. This value is extremely close, but not exactly equal, to the β_{22}^2 estimated in Ref. [77] when comparing their results with Ref. [129]. We attribute this discrepancy to possible computation errors in Ref. [129], which was also found to be incorrect in the 7.5PN tail term. Crucially, with respect to previous versions of the model, we do not propagate the tail contribution $h_{\ell m}^{\text{tail}}$ to the tidal amplitudes, in order to correctly recover the LO 6.5PN tail terms. Given the new tidal terms contributing to the waveform amplitudes $\hat{h}_{\ell m}$, the radiation reaction force $\hat{\mathcal{F}}_\varphi$ is extended straightforwardly.

4.2.2 Effect of the analytical information

The left panel of Fig. 4.7 shows the impact of the additional analytical information included in the Hamiltonian and the waveform for 10^4 systems with varying mass ratios, tidal parameters and spins. Such a difference is here quantified in terms of

the phase difference at merger $\Delta\phi = \phi^{\text{old}} - \phi^{\text{new}}$, where “new” and “old” indicate the models with and without the extra terms discussed in the previous subsections. Note that, in both cases, $\ell > 2$ multipolar tidal parameters are estimated via the fits from Ref. [262, 452]. From this comparison it appears that: (i) the (absolute) values of the phase differences are smallest for binaries with small tidal parameters or larger mass ratios, and maximal for equal mass binaries with large tidal parameters; (ii) the phase difference is positive over a considerable portion of the parameter space, implying that the new tidal model prescribes weaker matter effects than the previous. The facts observed above are, at first impact, rather puzzling: while it is expected for the models to differ the most for large values of $\tilde{\Lambda}$, it is not immediately clear why they should agree for high mass ratios, or – conversely – why they should differ the most for equal mass BNSs.

To further understand this picture, then, we consider two representative cases: an equal mass, non-spinning binary with $\tilde{\Lambda} = 2500$, and a $q = 2$ binary with the same tidal parameters and spins. For each, we also compute the waveform and frequency evolution combining the “new” and “old” model with different fits for the multipolar tidal parameters Λ_ℓ . The right panel of Fig. 4.7 shows the $(2, 2)$ amplitude evolution for the system considered. By comparing curves we note that the largest effect for this binary is given by choice of the fit for $\Lambda_{3,4}$. The inclusion of Λ_ℓ terms with $\ell \geq 5$, too, has a considerable effect on the waveform. Contrasting models based on the same fits and with identical Λ_ℓ content, it appears that the tidal contributions to the B potential, the new tidal contributions to h_{22} itself and the lack of propagation of $T_{\ell m}$ to the multipolar waveforms have an overall repulsive effect on the dynamics. When the mass ratio is increased the importance of higher modes also grows, and differences between models are attenuated.

Qualitatively, moving from the old model (which used the fits of Ref. [455]), to a model which includes more analytical information and is based on the fits from Ref. [262, 452] represents a step towards the right direction: previous EOB-NR comparisons highlighted how the models fail to capture the last few cycles before merger, with tidal effects not being attractive enough. Quantitatively, however, the new contributions are relatively small: the dephasing at merger varies between -0.05 and 0.3 rad. The inclusion of the analytical information discussed in the previous section to the conservative and radiative sectors of the model therefore does not, unfortunately, provide corrections to the final waveform that are large enough to fill the gap with NR simulations, as observed in e.g. [143, 264].

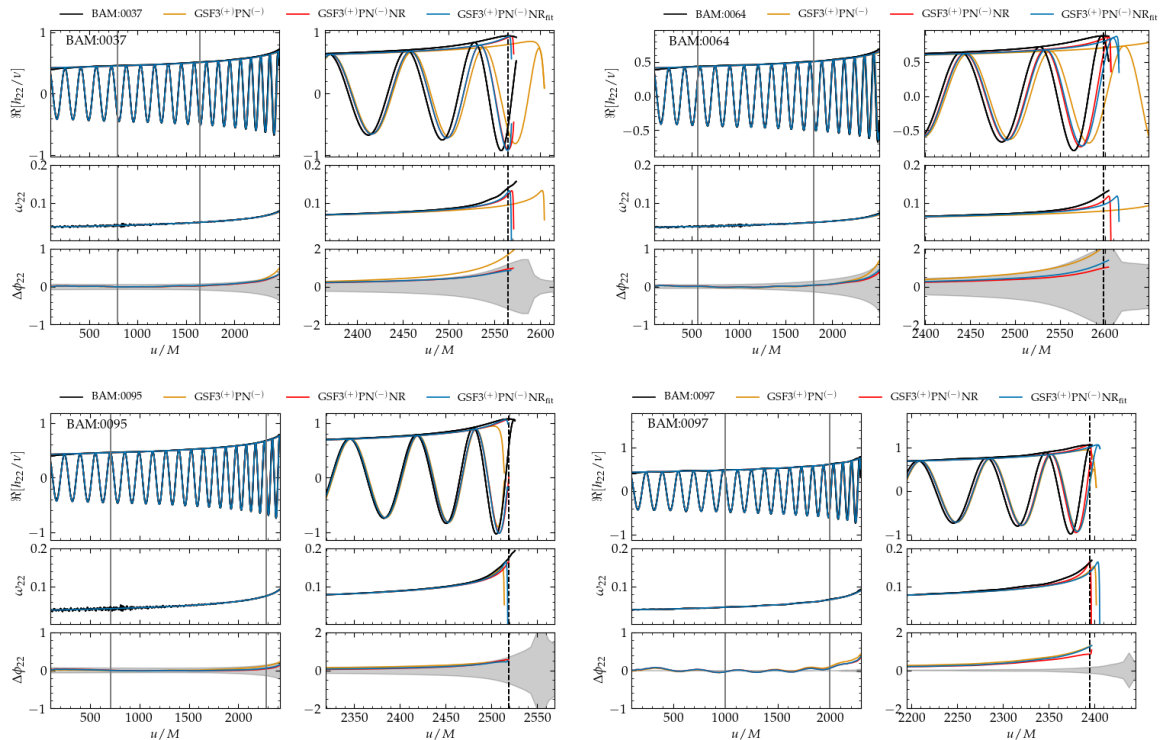


FIGURE 4.8: Comparison between the TEOBResumS model and the four equal mass NR simulations employed to tune the tidal parameter α_T

X	a_1^X	a_2^X	a_3^X	a_4^X	b_1^X	b_2^X	b_3^X	b_4^X
M	-1.7988	—	—	—	—	—	—	—
S	0.3555	—	—	—	-7.1674	—	—	—
T	0.0314	0	0.1714	0.0006	-6.8144	1.0	5.1651	-1.0333

TABLE 4.2: The coefficients for $\hat{\omega}_{\text{mrg}}^{\text{NR}}$ from Eq. 4.48. The fitted value of a_0 is $a_0 = 0.0074$.

4.2.3 Numerically informing the model

The need of employing some NR information to improve our model in the last few cycles before merger appears inevitable. We proceed on two different fronts. First, we include some NQCs corrections in our waveform, in order to ensure that the expected NR-prescribed values of amplitude and frequency at merger are reached by our waveforms. Then, we employ the flexibility of the tidal model described in Sec. 4.2.1 provided by the light ring radius r_{LR} or the GSF-inspired exponent p_{GSF} . These parameters effectively determine the strength of tidal interactions by shifting the position of the pole in the tidal potential (r_{LR}) or the degree of the singularity (p_{GSF}).

NQC model for BNS systems NQCs have proven to be fundamental in the creation of faithful IMR BBH waveform models [141, 142, 286, 324]. Here, we apply NQC corrections to BNS systems for the dominant $\ell = m = 2$ mode, making use of the merger fits provided by [456].

We remind the reader than NQC corrections enter the factorized EOB waveform as a multiplicative term $\hat{h}_{\ell m}^{\text{NQC}}$, which in the general case explicitly reads:

$$\hat{h}_{\ell m}^{\text{NQC}} = (1 + a_1 n_1 + a_2 n_2) e^{i(b_1 n_3 + b_2 n_4)}. \quad (4.37)$$

n_1, n_2, n_3, n_4 are the NQC basis functions, given by:

$$n_1 = \frac{p_{r^*}^2}{r^2 \omega^2}, \quad (4.38)$$

$$n_2 = \frac{\ddot{r}}{r \omega^2}, \quad (4.39)$$

$$n_3 = \frac{p_{r^*}}{r \omega}, \quad (4.40)$$

$$n_4 = n_3 r^2 \omega^2. \quad (4.41)$$

The NQC coefficients a_i, b_i are determined by imposing that the EOB amplitude \hat{A}_{22} , its time derivative $\dot{\hat{A}}_{22}$, the frequency $\hat{\omega}_{22}$ and the frequency time derivative $\dot{\hat{\omega}}_{22}$ extracted $3M$ before the peak of the EOB orbital frequency are equal to the same NR quantities extracted at the NR NQC time $t_{\text{NQC}}^{\text{NR}}$, which is here identified with the merger, $t_{\text{NQC}}^{\text{NR}} = t_{\text{mrg}}^{\text{NR}}$.

$$\hat{A}_{22}^{\text{EOB}}(t_{\Omega\text{peak}} - 3) = \hat{A}_{22}^{\text{NR}}(t_{\text{mrg}}), \quad (4.42)$$

$$\dot{\hat{A}}_{22}^{\text{EOB}}(t_{\Omega\text{peak}} - 3) = \dot{\hat{A}}_{22}^{\text{NR}}(t_{\text{mrg}}) = 0, \quad (4.43)$$

$$\hat{\omega}_{22}^{\text{EOB}}(t_{\Omega\text{peak}} - 3) = \hat{\omega}_{22}^{\text{NR}}(t_{\text{mrg}}), \quad (4.44)$$

$$\dot{\hat{\omega}}_{22}^{\text{EOB}}(t_{\Omega\text{peak}} - 3) = \dot{\hat{\omega}}_{22}^{\text{NR}}(t_{\text{mrg}}), \quad (4.45)$$

$$(4.46)$$

This choice of the extraction point is slightly different with respect to the BBH case, where $t_{\text{NQC}}^{\text{NR}} = t_{\text{mrg}}^{\text{NR}} + 2M$, and is motivated by the desire of employing already existing fits to the desired NR quantities when they are specified at merger. In detail, we supplement the fits presented in Ref. [456] for $\hat{A}_{22}^{\text{NR}}(t_{\text{mrg}})$ and $\hat{\omega}_{22}^{\text{NR}}(t_{\text{mrg}})$ with new ones for $\dot{\hat{\omega}}_{22}^{\text{NR}}(t_{\text{mrg}})$. Following Ref. [456], we assume a functional form of the type:

$$\dot{\hat{\omega}}_{\text{mrg}}^{\text{NR}} = a_0 Q^M(X) Q^S(\hat{S}, X) Q^T(\kappa_2^T, X), \quad (4.47)$$

with

$$Q^M = 1 + a_1^M X \quad (4.48)$$

$$Q^S = 1 + a_1^S(1 + b_1^S X)\hat{S} \quad (4.49)$$

$$Q^T = \frac{1 + a_1^T(1 + b_1^T X)^T \kappa_2^T + a_2^T(1 + b_2^T X)\kappa_2^{T^2}}{1 + a_3^T(1 + b_3^T X)\kappa_2^T + a_4^T(1 + b_4^T X)\kappa_2^{T^2}}, \quad (4.50)$$

and $X \equiv (1 - 4\nu)$. The coefficients of the fit are collected in Tab. 4.2.

Light ring singularity The GSF-informed resummation introduced in [143] naturally introduced a *pole* in the denominator of the \hat{A}^{XGSF} terms, with $X = 0, 1, 2$. The precise location of this pole is however quite uncertain: the analytical GSF expressions placed the pole at $r = 3M$, where the BBH light ring is situated. However, clearly, given that we are not describing coalescing BHs, this value can be modified at will. One possibility is to employ the light ring radius r_{LR} implied by the A potential augmented by NNLO tidal effects. The value of r_{LR} so estimated is generally larger than the BBH light ring, effectively enhancing the tidal terms close to the end of the evolution, in the last few orbital cycles before the peak of the EOB orbital frequency⁴. Such an enhancement was shown to improve the agreement between NR and EOB, although it was still not sufficient to reproduce NR within its error bars in most of the cases studied.

Here, we build on this approach by multiplying the light ring radius estimated from the NNLO A potential by a parameter α , to be determined case-by-case by comparing our model to high resolution NR simulations after alignment. We start from the equal mass, non-spinning case, and consider the public CoRe simulations BAM:0037, BAM:0064, BAM:0095, and BAM:0097. All simulations show clear convergence properties, with the latter displaying evident 4th order convergence thanks to the Entropy-Flux-Limited (EFL) method developed in [457, 458] and improved in [459]. Given the multiple available resolutions and extraction radii associated to each simulation, we estimate the total error budget on the waveform phase as the sum in quadrature of the resolution and finite extraction error. The former is computed by evaluating the phase difference between the highest and second-highest resolutions; the latter by estimating the phase difference between the waveform extrapolated to infinity and extracted at the largest finite radius.

⁴The EOB dynamics never crosses r_{LR} in the physically meaningful region, see Fig. 1 of [143]

Comparisons between our α -calibrated and uncalibrated EOB model with the NR waveforms above are shown in Fig. 4.8. The calibrated model can reproduce all the simulations shown within their NR error, except for `BAM:0097`. Notably, even when the phase error at merger is within the NR errorbars, the NQCs-enhanced and NR-tuned EOB model still does not seem to be able to fully capture the frequency evolution over the last two cycles. Nonetheless, the introduction of the α parameter noticeably improves the EOB/NR agreement for binaries with large effective tidal parameters, such as `BAM:0037` and `BAM:0064`. A trend in α is also easily identifiable: it is clear that to match the simulations with larger tidal parameters, larger values of α are necessary. Conversely, given that we set $p = 9/2$, values of $\alpha < 1$ need to be chosen in order to obtain agreement with those simulations with $\kappa_2^T \leq 100$. Using the four simulations shown in Fig. 4.8 we fit

$$\alpha = \frac{a_1 \kappa_2^T}{1 + a_2 \kappa_2^T}, \quad (4.51)$$

finding $a_1 = 0.06306$ and $a_2 = 0.05732$.

Beyond our calibration set, we determine α for ~ 10 additional lower-resolution non-spinning simulations and compare the extracted values with the α computed via Eq. 4.51. This investigation indicates that the trend we identified is maintained when considering other equal-mass configurations, with the largest $\Delta\alpha/\alpha$ amounting to about 13%. Concerning unequal mass and spinning simulations, instead, we do not attempt to fit these contributions to α due to the large uncertainties affecting the simulations. However, we mention that even in this scenario by modifying α it is usually possible to reproduce the NR waveforms within their estimated error bands.

4.2.4 EOB/NR comparisons

New simulations

We present 14 new simulations of unequal mass, spinning binaries. The initial data for these simulations has been computed using the SGRID library [445, 460, 461], and eccentricity reduction has been performed in order to minimize residual spurious artifacts in the waveform [462, 463]. The constraint-satisfying data is then evolved with the `BAM` code [121, 184, 464]. All simulations are run at multiple resolutions, with $\{96, 104, 128, 144\}$ points per directions in the finest (moving) mesh refinement level covering the individual NSs and using a high-order hydrodynamics scheme [465].

ID	EOS	$M\omega_0$	M	q	Λ_2^A	Λ_2^B	χ_A	χ_B	$\bar{\mathcal{F}}_{old}$	$\bar{\mathcal{F}}_{new}$
ER01	H4	0.0373	2.77	1.02	888	1007	0.03	0.07	0.0119	0.0039
ER02	H4	0.0339	2.6	1.26	719	2789	0.04	0.13	0.0225	0.0045
ER03	H4	0.0339	2.6	1.26	718	2794	0.11	0.05	0.0219	0.009
ER04	H4	0.0373	2.77	1.02	887	1008	0.06	0.03	0.0132	0.0032
ER05	H4	0.0382	2.82	1.06	718	1008	0.11	0.05	0.008	0.0024
ER06	MS1b	0.0369	2.77	1.02	1268	1420	0.1	0.03	0.0059	0.0169
ER10	MS1b	0.0347	2.65	1.21	1048	2854	0.03	0.14	0.0339	0.0072
ER11	MS1b	0.0379	2.82	1.06	1048	1418	0.03	0.1	0.0045	0.0267
ER12	MS1b	0.0379	2.82	1.06	1048	1417	0.03	0.13	0.0203	0.0014
ER13	MS1b	0.0378	2.82	1.06	1047	1420	0.09	0.03	0.018	0.0044
ER14	MS1b	0.0379	2.82	1.06	1046	1420	0.12	0.03	0.0164	0.0026
ER15	H4	0.0382	2.82	1.05	719	1006	0.04	0.11	0.0075	0.0019
ER17	H4	0.0373	2.77	1.02	888	1006	0.05	0.11	0.0109	0.0068
ER18	H4	0.0373	2.77	1.02	886	1008	0.11	0.05	0.0128	0.0054

TABLE 4.3: New spinning, unequal mass NR simulations used to test **TEOBResumS**. The new model has lower unfaithfulness than the previous one in all but two cases.

Time-domain phasing To validate our new model in a regime far from the one considered in our calibration set, we align in the TD the GSF3 and the GSF3NR models with the NR simulations described in the previous section. When using the GSF3NR model, we iterate on the NQCss 5 times, employing them also in the flux, before performing the alignment. The results of our alignment procedure can be inspected from Fig. 4.9 and Fig. 4.10 for the H4 and MS1b simulations, respectively. Notably, we do not present results for the ER06 and ER11 simulations, as we were not able to correctly align them to the EOB model. Overall, we observe that although no unequal mass or spin-dependent corrections have been introduced to the GSF23NR⁽⁺⁾PN⁽⁻⁾ model, it improves over the previous one in all the comparisons presented. The EOB/NR phase difference at merger is smaller than the estimated NR error in eight out of twelve cases displayed, with an average $\Delta\phi^{\text{EOBNR}} \sim 0.5$ rad at merger. Unsurprisingly, the two cases for which significant disagreement – larger than the NR error – is found are both high q , large spins ones with the H4 EOS. Notably, as was also the case for the simulations of Fig. 4.8, we observe again a faster increase of the NR frequency over the last two cycles with respect to the one predicted by the EOB model. This is especially evident in the ER05, ER13, ER14, ER15 and ER18 simulations, where $\Delta\phi^{\text{EOB/NR}}$ is smaller than the NR error in the inspiral and at merger, but larger than this quantity approaching the end of the coalescence. This indicates that our model is not fully capturing the physics of the system beyond the contact of the two bodies.

TABLE 4.4: The coefficients of Ψ_Λ and Ψ_{MQ} as defined in equations 4.56.

	Ψ^Λ				Ψ^{MQ}			
	d_1	d_2	$n_{5/2}$	n_3	d_1	d_2	d_3	n_4
$\nu = 1/4$	99.80	1560.60	-2191.56	5307.07	-9.61	23.12	3.90	-27.50
$\nu \neq 1/4$	4.08	39.67	-86.62	158.92	-2.84	28.93	63.34	-58.83

Unfaithfulness Applying Eq. (1.24), we find that our model is either comparable with or improves the previous one in all but four cases, with typical mismatches below 1%. Note that this number provides a conservative limit on the NR-faithfulness of our model, as little to no early inspiral is included in our simulations. If hybrid waveforms were to be considered, the mismatch of `TEOBResumS` would decrease as well. This result confirms and complements the TD phasing analysis discussed in the previous paragraph (see Tab. 4.3).

4.3 Closed form representation of tidal sector

Following the ideas proposed in Ref. [167] (see also [168, 466, 467]), we develop a FD *closed-form* representation of the tidal sector of `TEOBResumS` that can be employed to augment any point-particle model of choice to include the effects of tides. This representation is faithful ($\bar{\mathcal{F}} \sim \mathcal{O}(10^{-3})$ or lower) for $\Lambda \in [10, 3000]$, mass ratios $q \in [1, 2.5]$ and spins $|\chi_i| \lesssim 0.35$.

Phenomenological representations of tidal approximants are usually built from hybrid PN-EOB-NR waveforms by (i) subtracting the point-mass (BBH) and (ii) fitting the differences in phase and amplitude. The use of NR data at high-frequencies potentially improves the accuracy with respect to the “exact” (unknown) waveform, but also implies a limitation in the parameter space coverage. For example, neither the `NRTidal` model nor its improved version `NRTidalv2` [168] incorporate mass-ratio induced corrections, and take into account spin-quadrupole effects only in the phase difference through the PN expression of [328]. Moreover, the use of different approximants in the hybrid construction and in the subtraction step can result in inconsistencies and systematic effects. The phenomenological representation of `TEOBResumS` does not have these drawbacks, although it retains the uncertainties of `TEOBResumS` in the merger description when compared to NR waveforms [130, 143, 429].

4.3.1 Phase

The phase of the (2, 2) FD waveform is modeled as the sum of the contributions due to pure orbital interactions (O), pure tidal effects (Λ), spin orbit and spin-spin effects (S), and self-spin couplings, also known as monopole-quadrupole (MQ) terms. It formally reads

$$\Psi(f) = \Psi_{\text{O}} + \Psi_{\Lambda} + \Psi_S + \Psi_{\text{MQ}}. \quad (4.52)$$

Under the simplifying assumption that these contributions can, indeed, be clearly separated, the contribution to the phasing due to tidal effects can be expressed as:

$$\Delta\Psi(f) = \Psi^{\text{BNS}}(f) - \Psi^{\text{BBH}}(f) \approx \Psi_{\Lambda} + \Psi_{\text{MQ}}. \quad (4.53)$$

The PN expression valid in the low-frequency, weak-field regime of Ψ^{Λ} at incomplete 7.5PN accuracy was originally obtained in [129], and is of the form

$$\Psi_{\Lambda} = c_{\text{LO}}^{\Lambda} x^{5/2} (1 + c_1^{\Lambda} x + c_{3/2}^{\Lambda} x^{3/2} + c_2^{\Lambda} x^2 + c_{5/2}^{\Lambda} x^{5/2}), \quad (4.54)$$

while the self-spin contributions Ψ_{MQ} at 3.5PN accuracy is given by [328, 468, 469]

$$\Psi_{\text{MQ}} = \frac{3}{128\nu} c_{\text{LO}}^{\text{MQ}} x^{-1/2} (1 + c_1^{\text{MQ}} x + c_{3/2}^{\text{MQ}} x^{3/2}), \quad (4.55)$$

The functional form of our representations is obtained by the Padé resummation of the PN expression,

$$\Psi_{\Lambda} = c_{\text{LO}}^{\Lambda} x^{5/2} \frac{1 + \sum_{i=2}^6 n_{i/2}^{\Lambda} x^{i/2}}{1 + \sum_{i=2}^4 d_{i/2}^{\Lambda} x^{i/2}} \quad (4.56a)$$

$$\Psi_{\text{MQ}} = \frac{3}{128\nu} c_{\text{LO}}^{\text{MQ}} x^{-1/2} \frac{1 + \sum_{i=2}^3 n_{i/2}^{\text{MQ}} x^{i/2}}{1 + \sum_{i=2}^4 d_{i/2}^{\text{MQ}} x^{i/2}}. \quad (4.56b)$$

The PN limit requires the following constraints on the pure tidal and spin-quadrupole coefficients:

$$n_1^\Lambda = c_1^\Lambda + d_1^\Lambda \quad (4.57a)$$

$$n_{3/2}^\Lambda = (c_1^\Lambda c_{3/2}^\Lambda - c_{5/2}^\Lambda - c_{3/2}^\Lambda d_1^\Lambda + n_{5/2}^\Lambda) / c_1^\Lambda \quad (4.57b)$$

$$n_2^\Lambda = c_2^\Lambda + c_1^\Lambda d_1^\Lambda + d_2^\Lambda \quad (4.57c)$$

$$d_{3/2}^\Lambda = - (c_{5/2}^\Lambda + c_{3/2}^\Lambda d_1^\Lambda - n_{5/2}^\Lambda) / c_1^\Lambda \quad (4.57d)$$

$$n_1^{\text{MQ}} = c_1^{\text{MQ}} + d_1^{\text{MQ}} \quad (4.57e)$$

$$n_{3/2}^{\text{MQ}} = c_{3/2}^{\text{MQ}} + d_2^{\text{MQ}}. \quad (4.57f)$$

The remaining coefficients are fitted to `TEOBResumSPA`. To incorporate corrections due to unequal-mass effects we parameterize the free coefficients as a $\nu = 1/4$ contribution plus a factor proportional to $\sqrt{1 - 4\nu}$. In particular, denoting a generic coefficient n_i^Λ, d_i^Λ or $n_i^{\text{MQ}}, d_i^{\text{MQ}}$ as p_i^Λ and p_i^{MQ} , we have:

$$p_i^\Lambda = p_i^{(\nu=1/4)} + \frac{\kappa_1 - \kappa_2}{\kappa_1 + \kappa_2} p_i^{(\nu \neq 1/4)} \sqrt{1 - 4\nu} \quad (4.58a)$$

$$p_i^{\text{MQ}} = p_i^{(\nu=1/4)} + \frac{(C_{Q1} \tilde{a}_1^2 - C_{Q2} \tilde{a}_2^2)}{(C_{Q1} \tilde{a}_1^2 + C_{Q2} \tilde{a}_2^2)} p_i^{(\nu \neq 1/4)} \sqrt{1 - 4\nu}. \quad (4.58b)$$

These functional forms are inspired by the expressions of the coefficients known from PN theory.

We then proceed as follows: (i) we compute the phase difference between a set of $\nu = 1/4$, non-spinning waveforms, and fit the values of $(d_1^\Lambda, d_2^\Lambda, n_{5/2}^\Lambda, n_3^\Lambda)^{(\nu=1/4)}$; (ii) we consider a set of unequal mass, non-spinning waveforms and fit $(d_1^\Lambda, d_2^\Lambda, n_{5/2}^\Lambda, n_3^\Lambda)^{(\nu \neq 1/4)}$, setting the $\nu = 1/4$ coefficients to the values found in the previous point; (iii) we fit equal mass, spinning waveforms, and find the values of $(d_1^{\text{MQ}}, d_2^{\text{MQ}}, n_4^{\text{MQ}}, d_3^{\text{MQ}})^{(\nu=1/4)}$ using again the equal-mass coefficients of (i); (iv) we use all information found up to now, and fit unequal mass, spinning waveforms to find $(d_1^{\text{MQ}}, d_2^{\text{MQ}}, n_4^{\text{MQ}}, d_3^{\text{MQ}})^{(\nu \neq 1/4)}$. The values of all fitted coefficients, obtained from a dataset of ~ 1000 waveforms, are summarized in Table 4.4.

4.3.2 Amplitude

We proceed analogously for the amplitude, whose FD tidal and self-spin terms are modeled as

$$\tilde{A}^\Lambda = \sqrt{\frac{2\nu}{3}} \pi x^{13/4} c_5^\Lambda \frac{1 + \frac{c_6^\Lambda}{c_5^\Lambda} x + \frac{22672}{9} x^{2.89}}{1 + d_4^\Lambda x^4} \quad (4.59)$$

$$\tilde{A}_{\text{MQ}} = -\sqrt{\frac{3\nu}{2}} \pi x^{1/4} \frac{(C_{Q1} \tilde{a}_1^2 + C_{Q2} \tilde{a}_2^2)}{1 + e_4 x^4}. \quad (4.60)$$

The PN limit of the above expressions can be obtained via a simple SPA. Denoting the TD amplitude of the 22 mode as A_{22} , one has that

$$\tilde{A}_{22} = A_{22}(t_f) \sqrt{\frac{\pi}{\ddot{\phi}(t_f)}} \quad (4.61a)$$

$$\ddot{\phi}(x) = -\frac{3}{2} x^{1/2} \frac{\mathcal{F}(x)}{E'(x)} \quad (4.61b)$$

Where $E(x)$ and $\mathcal{F}(x)$ denote, respectively, the energy and its flux. We employ expressions for A_{22} , $E(x)$ and $\mathcal{F}(x)$ which contain point-particle and spin-orbit corrections known up to 3.5 PN [331, 413, 470], spin-quadrupole corrections up to relative 1PN [311, 468], and pure tidal corrections up to relative 1PN [72, 129, 376]. Expanding Eq. (4.61a), we find that the waveform amplitude is given by

$$\tilde{A}_{22}(x) = \sqrt{\frac{2\nu}{3}} \pi x^{-7/4} \sum_{i=0}^{i=X} c_{i/2} x^{i/2} \quad (4.62)$$

The coefficients of the point mass and spinning terms are given in e.g. [155]. Spin-quadrupole and tidal effects enter the amplitude at relative 2 and 5 PN orders. While the latter are known in the literature, the former are here computed for the first time, and read:

$$c_2^{\text{MQ}} = -\frac{3}{2} (C_{Q1} \tilde{a}_1^2 + C_{Q2} \tilde{a}_2^2) \quad (4.63a)$$

$$c_{5/2}^{\text{MQ}} = -C_{Q1} \tilde{a}_1^2 \left(\frac{12247}{1344} - \frac{2221}{672} \sqrt{1-4\nu} + \frac{53}{336} \nu \right) - C_{Q2} \tilde{a}_2^2 \left(\frac{12247}{1344} + \frac{2221}{672} \sqrt{1-4\nu} + \frac{53}{336} \nu \right) \quad (4.63b)$$

In Eq. (4.60) we incorporate only LO PN information for the spin sector, as we find that, while the addition of the NLO term slightly improves the low frequency

behavior of our fits, it also negatively impacts the overall agreement in the high-frequency regime. The unknown coefficients are fit by following the same procedure of the previous paragraph. We find:

$$d_4^{(\nu=1/4)} = 5009.8736694 \quad (4.64a)$$

$$d_4^{(\nu \neq 1/4)} = -4017.88863642, \quad (4.64b)$$

$$e_4^{(\nu=1/4)} = 5.98351934 \quad (4.64c)$$

$$e_4^{(\nu \neq 1/4)} = 20.04283392 \quad (4.64d)$$

4.3.3 Validation

We compute the unfaithfulness between the BNS `TEOBResumS` model and the BBH model augmented by the phenomenological description of tides. We consider 10^4 systems with masses uniformly distributed between $[1, 2.5] M_\odot$, dimensionless spins uniformly distributed in $[-0.35, 0.35]$ and tidal parameters in $[10, 3000]$. When restricting the calculation to non-spinning binaries with $\tilde{\Lambda} < 1000$ and $m_{1,2} \in [1, 2.5] M_\odot$ we find a maximum unfaithfulness of 2×10^{-3} . Widening the range of tidal parameters, we find that the faithfulness degrades for tidal deformabilities larger than roughly ~ 2000 . The worst matches ($\bar{\mathcal{F}} \sim 2\%$) are obtained, as expected, for unequal mass configurations with large $\tilde{\Lambda}$. When also considering spins, we find that the largest differences are obtained with configurations having at least one rapidly spinning NS. In this scenario, unfaithfulness values can increase above the nominal 1% threshold. When the spins of the NS are moderate, instead, we find mismatch values around $\mathcal{O}(10^{-3})$ or lower.

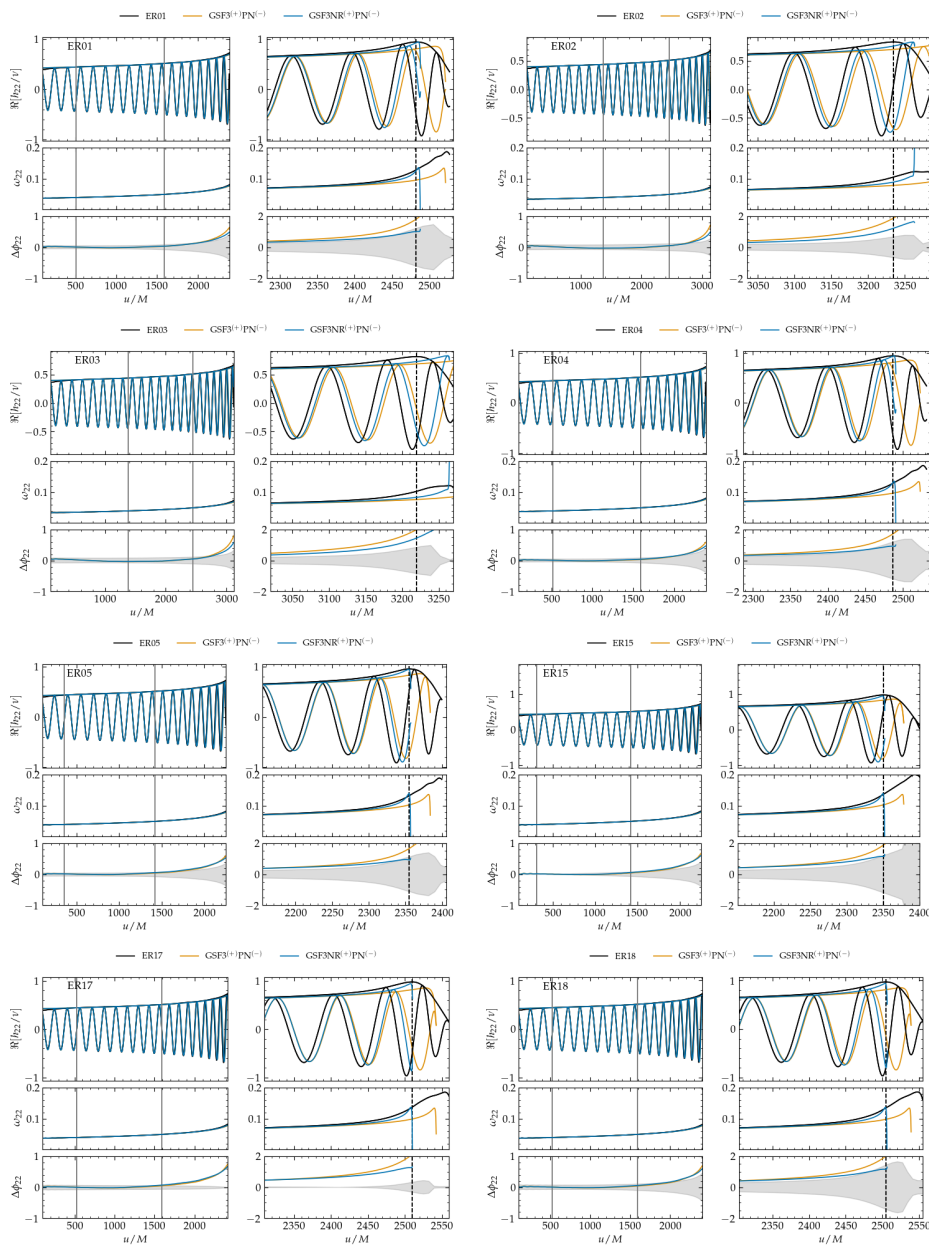


FIGURE 4.9: Comparison between the two tidal flavors of the TEOBResumS model, GSF23(+)-PN(-) (orange lines) and GSF23NR(+)-PN(-) (blue lines), and the eight H4 unequal mass, spinning NR simulations summarized in Tab. 4.3 (black lines). In each subfigure, the upper-left panel shows the TEOBResumS waveforms overlaid on top of the NR data during the early inspiral of the system. The upper-right panel shows instead the merger and few cycles preceding it. The middle and bottom panels, instead, show the frequency evolution and EOB/NR phase difference $\Delta\phi^{\text{EOB/NR}}$. The alignment region is delimited by two gray vertical lines, while merger is indicated with a dashed black line. In the bottom panels, the gray area denotes the NR error, estimated as described in the text.

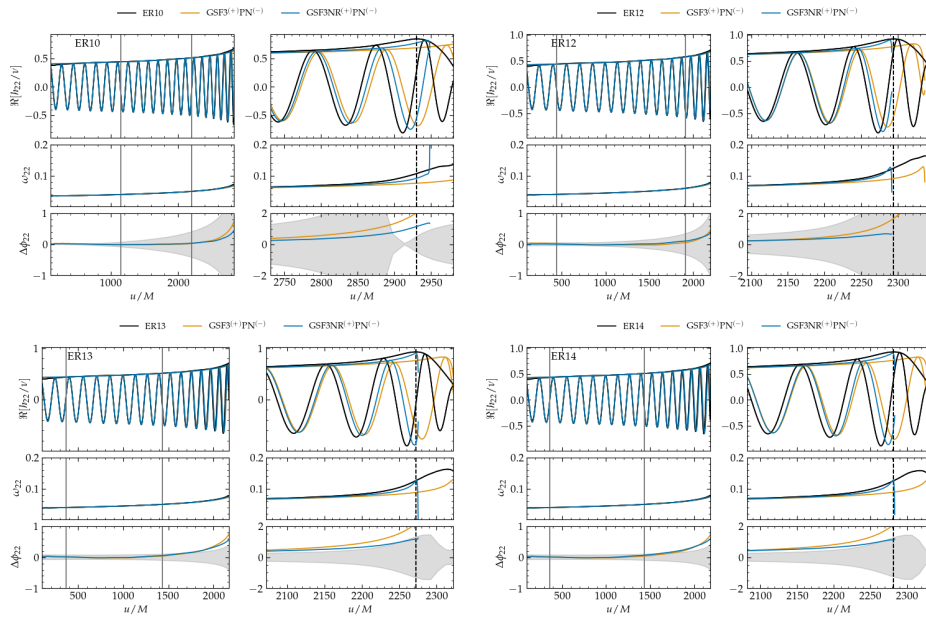


FIGURE 4.10: Same as Fig. 4.9, for the five converged MS1b simulations of Tab. 4.3.

Conclusions

In this *Thesis* we improved the performance of **TEOBResumS**, a fast and accurate waveform model for generic compact binaries (BBHs and BNSs). We presented the first multipolar frequency domain model for precessing BNSs, obtained the first NR-informed EOB model for BNS systems and discussed the importance of resonant tidal effects for current and next generation detectors. Employing our model within Bayesian frameworks to link signals measured by the LIGO-Virgo-Kagra detectors to their astrophysical sources, we suggested that GW190521 may have been caused by the dynamical capture of two BHs. The development of faithful models is of paramount importance to avoid the issue of waveform systematics, and make the most of the information contained in the data of current and future interferometers.

Spin precession When compared to 121 SXS simulations, spanning a large portion of the precessing BBHs parameter space, **TEOBResumS** was found to yield mismatches below the 3% threshold for $\iota = 0$ ($\iota = \pi/3$) for 96% (99%) of the total simulations considered. The worsening of the unfaithfulness for increasing inclination is expected, as for more edge-on binaries geometrical effects enhance the importance of higher modes and precession. This result is comparable to the one obtained via the phenomenological waveform approximant **IMRPhenomXPHM**, indicating that **TEOBResumS** represents an efficient and faithful alternative to current state-of-the-art models. When applied to the PE of real signals, we find results that are overall consistent with those obtained by LVK. Marginal differences appear in the posterior distributions of χ_p and χ_{eff} for GW190412. Critically, these studies demonstrate that **TEOBResumS** can be directly applied to PE, even of computationally challenging BNS systems, without the need for additional surrogates or reduced order models.

The degradation of the performance of the model at high masses seen in Fig. 2.3, however, indicates the need for an improved merger-ringdown description of the precessing waveform. This could come from a combination of three different avenues: (i) an improved description of the ringdown of spin-aligned $(\ell, m) \neq (2, 2)$ modes; (ii) a more accurate model for the evolution of the Euler angles α, β above merger; (iii) an

improved (analytical) fit for the remnant spin χ_f (see Fig. 2.1). Regarding the first point, in particular, we mention that the modelling of the $(\ell, m) = (2, 1)$ is a known criticality of `TEOBResumS`, as the latter is known to misbehave at merger for large misaligned spins. This known issue is potentially even more important for precessing systems. That is because, clearly, the *twisted* modes are obtained as a superposition of spin aligned multipoles. Hence, the $(2, 1)$ mode directly affects also the $(2, 2)$ and $(2, 0)$ multipolar waveforms. However, once an appropriate solution for the issue is found for the spin-aligned case, this will immediately have a positive impact on the precessing model. Similarly, any improvement of the spin-aligned model (addition of analytical information, re-calibrations of the NR informed parameters, improved merger-ringdown) will *immediately* be reflected on the precessing waveform, thanks to the modular nature of our approximant. With respect to the second point, instead, we observe that [243] recently proposed a phenomenological model to extend the Euler angles above merger, directly fit on numerical relativity simulations. Applying such a model to other approximants, such as the here employed `IMRPhenomXPHM`, brought very relevant improvements when computing unfaithfulness against NR simulations. Since the spin-evolution is independently evolved in our model, it is in principle straightforward to apply the prescription of [243] to our EOB waveform. Similarly, improved modeling of the co-precessing frame modes which does not impose symmetry between the $\pm m$ modes for fixed ℓ is expected to further improve agreement with NR.

Generic orbits The results obtained from the re-analysis of GW190521 – assuming that it was caused by the dynamical capture of two BHs – are consistent with the fact that burst-like waveforms from highly eccentric or head-on BBH collision may be confused with mildly precessing quasi-circular binaries [240] and vice-versa. Regarding other possible scenarios, a quantitative comparison is currently not possible since they have not been analyzed with full Bayesian studies and/or complete waveform templates [238, 241, 399]. While our analysis selects a two-encounters merger as best-fitting capture scenario (Fig. 3.9), the orbital dynamics of these encounters is rather sensitive to changes in both the conservative and non-conservative part of the dynamics [146], as also evident from Fig. 11 of [146]. Going beyond the conservative assumptions behind our analysis, future work will explore the impact of spin and of higher waveform multipoles, as well as consider systematic comparisons between our (improved [148]) EOB model and a larger number of NR simulations. The inclusion of additional, physically motivated, degrees of freedom (e.g., BH spins) is expected to further shed light on the nature of GW190521.

Resonant tides A critical assessment of the importance of resonant tidal effects, performed via phasing and energetics comparisons to NR waveforms, highlighted that while models based on f -mode excitations certainly represent a viable *effective* tidal model for the later stages of the coalescence, caution should be applied when trying to extract physical information from them via GW data analysis of real events. No clear signature of the presence of f -mode resonances after the NS contact can be assessed from NR simulations of quasi-circular binaries. For highly eccentric binaries, instead, the effective f -mode model does not capture the oscillations in the NR data (small oscillations in amplitude and frequency of the waveform centered around the proper mode star frequency). This is not unexpected because (i) the f -mode model considered in this *Thesis* was specifically computed for quasi-circular orbits, and (ii) the resonant condition is not met during the close passages. Aside from the small oscillation feature, we demonstrated that our `TEOBResumS` model for generic orbits quantitatively reproduces the NR waveform and frequency evolution with high-accuracy up to merger. To our knowledge, this was the first EOB/NR comparison of highly eccentric BNS mergers.

NR informed matter model While the inclusion of high order tidal effects in our model (leading order magnetic tidal corrections to the B EOB potential, 2PN electric tidal terms in the $(\ell, m) = \{(2, 2), (2, 1), (4, 2), (4, 4)\}$ waveform multipoles, 5.5PN spin-orbit terms in the gyro-gravitomagnetic coefficients entering the EOB Hamiltonian, electric tidal coefficients up to $\ell = 8$) positively impacts the overall agreement between `TEOBResumS` and NR, the need of incorporating some NR information in the model appears unavoidable. By adding NQCs to the quadrupolar $(2, 2)$ mode and a new NR-informed parameter, α , we are able to improve on the previous model's performance in terms of both mismatches and time-domain phasing. This improvement is also summarized in a new a frequency domain closed form representation of `TEOBResumS`, This phenomenological representation faithfully approximates the baseline model with $\bar{\mathcal{F}} < 0.001$ over a considerable portion of the parameter space, with the worst mismatches obtained for strongly asymmetric systems with large spins.

Outlook Thanks to the modular nature of our model, most of the effects studied in this *Thesis* can be combined in a straightforward manner. For instance, the advancements presented in Chapter 4 regarding the tidal sector can be immediately included when considering systems coalescing along generic orbits or quasi circular, precessing BNS with higher modes (see Chapter 2). When considering spins precession

and generic orbits, notably, such an extension is not as straightforward. Within our framework, this is due to two main reasons: (i) the PN description of $\dot{\omega}$ employed to evolve the spins cannot be immediately applied to obtain a good description of generic orbits, and (ii) the PN equations themselves that we employ to compute the evolution of the spins need to be extended to also account for non-circular effects. Both points, however, are rather straightforward to address, and we plan to do so in future publications. Beyond the simultaneous description of precession and eccentricity, we are also working towards an improved plunge-to-ringdown model for highly eccentric, aligned-spins BBHs. Preliminary studies highlighted that the quasi-circular ringdown template employed in `TEOBResumS` appears sufficient for binaries which tend to circularize before merger. On the other hand, for systems that merge head-on, or – more generically – that are characterized by sufficiently low values of orbital angular momentum, the merger amplitude predicted by the current template tends to underestimate the one found from NR simulations. We plan to develop a general NQCs and ringdown model, informed by test mass and NR simulations, which reduces to the current quasi-circular description in the correct limit. Moving to BNS systems, other planned improvements regard the beyond-contact regime. Indeed, in spite of the model’s performance being overall satisfactory ($\Delta\phi^{\text{EOBNR}} < \text{NR error}$) for most of the system we inspected in Chapter 4, our study highlighted how improvements are still necessary in the last few cycles before merger. Comparisons between our model and NR waveforms highlight that the frequency evolution of the NR waveforms close to merger is steeper with respect to the one provided by the models. This will require large amounts of sufficiently accurate NR data, spanning large portions of the BNS parameter space. This will enable precise inference of the equation of state of cold, dense matter with NG detectors such as Einstein Telescope (ET) [256] and Cosmic Explorer (CE) [471]. Overall, although much work will be needed to make the most of the rich landscape of future observations, the future of GW astronomy is bright and the development of physically complete models at reach.

Appendix A

Waveform Systematics for BNS systems

NG detectors such as ET [253, 256] and CE [471] are expected to start taking data in the late 2020s. Their increased sensitivity at high frequencies will significantly improve the detection of tidal signatures in the inspiral, and even allow the detection of GWs from the remnant. Typical SNRs expected for GW170817-like events detected by ET are of the order of 1700. As a consequence, the importance of waveform systematics is expected to further increase with respect to second generation detectors. In this picture, the SNR ρ of a detected event impacts the measurement of the effective tidal parameter $\tilde{\Lambda}$ mainly by determining the width of the distribution of $\tilde{\Lambda}$, $\sigma_{\tilde{\Lambda}} = \tilde{\Lambda}^{95\text{th}\%ile} - \tilde{\Lambda}^{5\text{th}\%ile}$.

To obtain a qualitative estimate of $\sigma_{\tilde{\Lambda}}$ for NG detectors, we perform an injection-recovery study (see Fig. A.1) using aLIGO noise curve and employing two GW models, `PhenomPv2NRTidal` and `TaylorF2`. We fit the width of the found $\tilde{\Lambda}$ distributions and extrapolate them to higher SNRs, finding that a good approximation of the behavior of $\sigma_{\tilde{\Lambda}}$ over the SNR range considered ($\rho \sim 70 - 90$) is obtained by assuming that

$$\sigma_{\tilde{\Lambda}}(\rho) = \frac{c}{\rho - \rho_0}. \quad (\text{A.1})$$

This functional form is valid only for $\rho > \rho_0$, in which case the denominator can be expanded as a geometrical series, and incorporates the corrections to the leading order $1/\rho$ asymptotical behavior expected from the Fisher Matrix analysis. Fitting Eq.(A.1) to the data, we find $(c, \rho_0) = (7497.97, 63.09)$ for `TaylorF2` and $(4372.21, 66.78)$ for `PhenomPv2NRTidal`. To obtain a unique estimate of $\sigma_{\tilde{\Lambda}}$, we compute the average value $\bar{\sigma}_{\tilde{\Lambda}} = (\sigma_{\tilde{\Lambda}}^{\text{Phenom}} + \sigma_{\tilde{\Lambda}}^{\text{TaylorF2}})/2$.

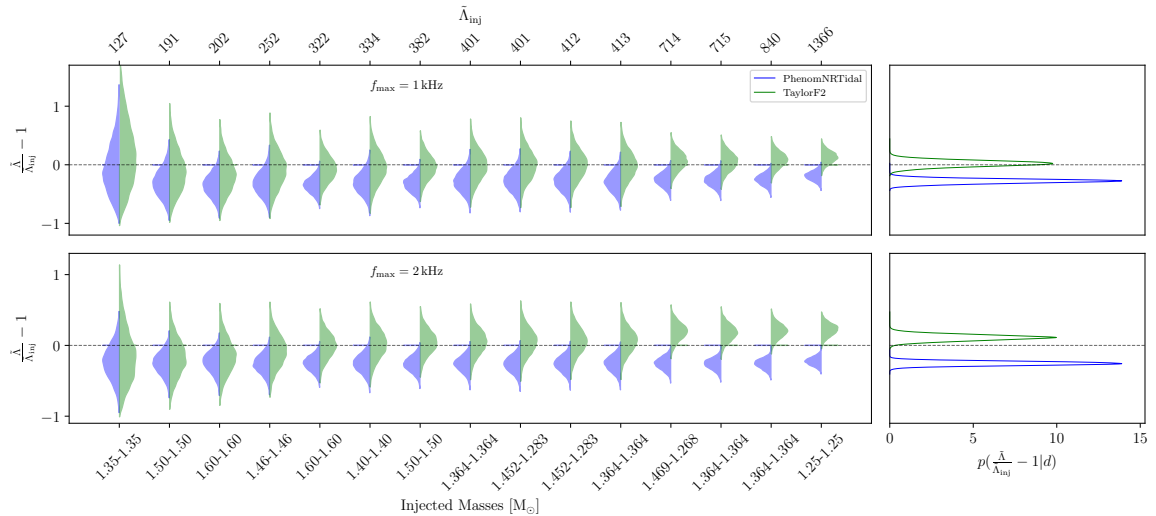


FIGURE A.1: Fractional deviation between the true “injected” values of $\tilde{\Lambda}$ and the reconstructed posteriors for a set of 15 different simulated GW signals. Each signal is generated with the EOB TEOBResumS model, and recovered with a phenomenological (blue) and a PN approximant (green).

This expression of $\bar{\sigma}_{\tilde{\Lambda}}$ can then be used to compute the SNR at which two independent measurements of $\tilde{\Lambda}$, whose difference we denote as $\Delta\tilde{\Lambda}$, become statistically inconsistent. Figure A.2 shows the quantity $\Delta\tilde{\Lambda}/\bar{\sigma}_{\tilde{\Lambda}}$ as a function of the optimal SNR ρ for values of $\Delta\tilde{\Lambda} \in [-100, 100]$. When $\Delta\tilde{\Lambda}/\bar{\sigma}_{\tilde{\Lambda}} \approx 1$, statistical fluctuations are of the same order of magnitude as systematical effects. For $|\Delta\tilde{\Lambda}| \approx 100$, we see that this condition is satisfied already at the threshold $\rho \approx 125$. As $|\Delta\tilde{\Lambda}|$ decreases, the threshold SNR increases, reaching $\rho \approx 300$ in correspondence of a $\Delta\tilde{\Lambda} \approx 20$.

The above considerations are independent of the exact waveform models employed, and do not tackle the issue of estimating the $\Delta\tilde{\Lambda}$ associated with two specific chosen approximants. While it is clear from Fig. A.1 that large $\Delta\tilde{\Lambda}$ are to be expected when employing TaylorF2 and NRTidal, we take a step further and qualitatively estimate $\Delta\tilde{\Lambda}$ for two additional state-of-the-art approximants, PhenomPv2NRTidalv2 [168] and SEOBNRv4Tsurrogate [136]. Given a baseline waveform d with fixed effective tidal parameter $\tilde{\Lambda}_d$ and a template waveform h , we estimate the “best-fitting” $\tilde{\Lambda}_h^{\text{best}}$ by maximizing the faithfulness between the two waveforms over a one-dimensional interval of $\tilde{\Lambda}_h$ values. The difference $\Delta\tilde{\Lambda}$ is then simply obtained as $\Delta\tilde{\Lambda} = \tilde{\Lambda}_d - \tilde{\Lambda}_h^{\text{best}}$.

We then compare PhenomPv2NRTidalv2, SEOBNRv4Tsurrogate and TEOBResumS and report the differences with respect to two baselines (TEOBResumS and SEOBNRv4Tsurrogate). We consider baseline values of $\tilde{\Lambda}$ equal to 400, 800 and 1000, and employ the ET PSD [472]. We compute waveforms from 30 to 2048 Hz or 1024 Hz. Results are again

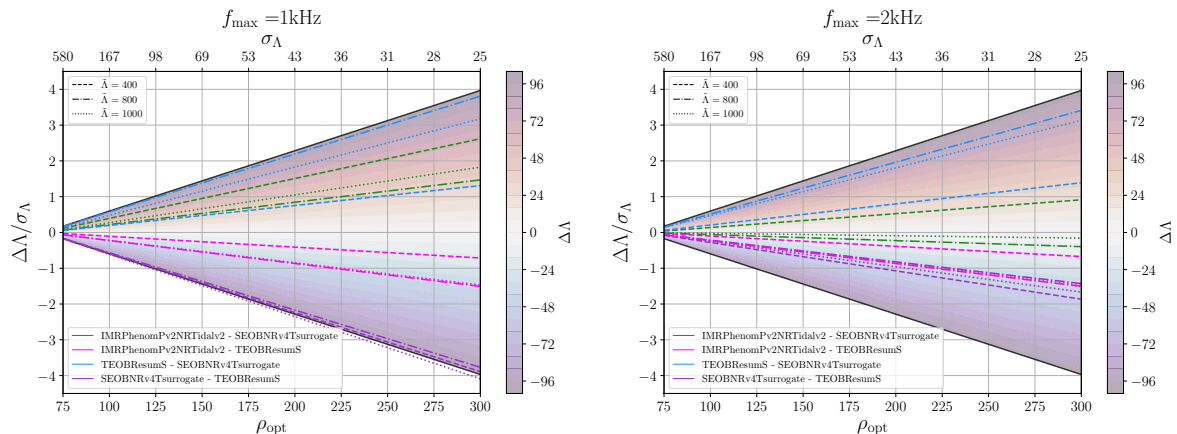


FIGURE A.2: Ratio between systematic ($\Delta\tilde{\Lambda}$) and statistical ($\sigma_{\tilde{\Lambda}}$) errors on the effective tidal parameter $\tilde{\Lambda}$ for BNSs detected with ET employing frequencies up to 1 kHz (left panel) or 2 kHz (right panel). For $|\Delta\tilde{\Lambda}| \approx 100$, systematic errors are larger than statistical ones at SNRs larger than ~ 125 .

displayed in Fig. A.2. We find that both `SEOBNRv4Tsurrogate` and `PhenomPv2NRTidalv2` “underestimate” the values of $\tilde{\Lambda}$ of the `TEOBResumS` baseline (right panel), and that the $|\Delta\tilde{\Lambda}|$ found are always below ≈ 100 . This indicates that tides are stronger in the `SEOBNRv4Tsurrogate` and `PhenomPv2NRTidalv2` models than in `TEOBResumS`. When restricting below 1kHz the systematic bias in $\tilde{\Lambda}$ due to the differences between `IMRPhenomPv2NRTidalv2` and `TEOBResumS` is $\lesssim 2\sigma$ corresponding to $\Delta\tilde{\Lambda} \pm 50$, while it varies $\sim 2 - 4\sigma$ when considering differences with respect to `SEOBNRv4Tsurrogate`. This indicates that the differences between `PhenomPv2NRTidalv2` and `TEOBResumS` are mostly related to the modeling of tides at high-frequencies, while the tides in the EOB models differ from each other already at lower frequencies. Some caution is needed when interpreting the results obtained for the different waveform approximants: the estimated $\Delta\tilde{\Lambda}$ provides only a rough estimate of the expected difference in the models. Nonetheless, we expect the behavior of the approximants (i.e., their being more/less attractive) to be correctly captured. Overall, our findings indicate that above $\text{SNR} \approx 100 - 200$, $\sigma_{\tilde{\Lambda}}$ will be small enough that the models will appear to be fully inconsistent with each other. The estimated systematic biases reflect differences in the tidal modeling at frequencies corresponding to the very last orbits and thus accessible to NR. We stress that at frequencies $\hat{\omega} \gtrsim 0.06$ the NS are in contact and the waveform modeling based on tidal interactions can only be considered an effective description, since the dynamics are dominated by hydrodynamics [130]. We demonstrate below that current NR simulations may not be sufficiently accurate to produce faithful waveforms. New,

more precise NR simulations appear crucial to further develop tidal waveform models for future detectors.

A.1 Faithfulness of Numerical Relativity waveforms

Numerical Relativity (NR) simulations are fundamental for understanding the merger physics and the waveform morphology in the high-frequencies regime. They incorporate hydrodynamical effects, and can model not only the late-inspiral-merger parts of the coalescence, but also the postmerger phase. While NR waveforms are often regarded as exact with respect to the ones provided by waveform approximants in the same regime, the complex 3D simulations can introduce significant uncertainties, e.g. [130, 444, 465, 473, 474]. The latter are both due to systematics (finite radius extraction of the GWs, numerical dissipation, etc.) and to finite grid resolution. Systematics are difficult to control, but finite resolution errors can be studied by simulating at different resolutions and performing convergence tests.

In this appendix, we test the accuracy of a set of state-of-the-art NR waveforms taken from the CoRe database [277], with the aim of guiding future efforts. In particular, we consider multi-orbit and eccentricity reduced simulations performed with the BAM code, and focus on late inspiral-merger where waveforms are shown to be convergent. To the best of our knowledge, accuracy standard for BNS NR waveforms at multiple grid resolutions have been computed only in [444] for data that are currently superseded by the those produced with simulations employing high-order numerical fluxes [465, 473] and higher resolutions than we consider here. We use here a sample of CoRe waveforms computed at multiple resolution and produced in [167, 418, 428, 443, 475].

Table A.1 displays the faithfulness values computed for a set of BAM waveforms. Each value is obtained by comparing the two highest-resolution simulations available for each considered set of intrinsic parameters. For each resolution R , the simulations compute the multipoles $h_{\ell m}(t)$; the waveform polarizations h_+^R, h_\times^R are reconstructed from

$$h_+^R - ih_\times^R = D_L^{-1} \sum_{\ell=2}^{\infty} \sum_{m=-\ell}^{\ell} h_{\ell m}(t) {}_{-2}Y_{\ell m}(t, \psi) \quad (\text{A.2})$$

where ${}_{-2}Y_{\ell m}(t, \psi)$ are the spin weighted spherical harmonics of spin $s = -2$ and D_L is the luminosity distance. Considering only the dominant multipole $(\ell, |m|) = (2, 2)$ and assuming that the radiation is emitted along the z -axis, perpendicular to the orbital

plane, one has that $\iota = \psi = 0$ and ${}_{-2}Y_{2\pm 2}(0, 0) = \sqrt{5/(64\pi)}(1 \pm 1)^2$. Matches are computed over a frequency range $f \in [f_{\text{low}}, f_{\text{mrg}}]$, where f_{low} is defined as the frequency at which the amplitude of the fourier transform $\text{FT}[\text{Re}(h_{22})]$ is highest and f_{mrg} is the merger frequency, i.e. the instantaneous frequency corresponding to the peak of the amplitude $|h_{22}(t)|$. Such values are then contrasted to a ‘‘threshold faithfulness’’ \mathcal{F}_{thr} given by

$$\mathcal{F}_{\text{thr}} = \frac{\epsilon^2}{2\text{SNR}^2}. \quad (\text{A.3})$$

We choose ϵ^2 to be equal to one, for a stricter requirement, or to the number of intrinsic parameters of a BNS system ($\epsilon^2 = 6$). Note that while $\mathcal{F} < \mathcal{F}_{\text{thr}}$ is a necessary but not sufficient condition for biases to appear, $\mathcal{F} > \mathcal{F}_{\text{thr}}$ is a sufficiently strong requirement to ensure that two waveforms are faithful. While for low SNR signals most of the waveforms considered are accurate enough, we find that – out of the twelve simulations examined – none passes the accuracy test when (SNR 80, $\epsilon^2 = 1$), and only one (BAM:0095) manages to pass it when (SNR 80, $\epsilon^2 = 6$) and (SNR 30, $\epsilon^2 = 1$). Note the stars are resolved in this case with $\gtrsim 200$ grid points.

Our findings indicate that the largest portion of the NR simulations available to date may not be yet sufficiently accurate for GW data-analysis purposes. High-order methods for hydrodynamics and resolutions > 200 grid points per star appear necessary for GW modeling.

TABLE A.1: Faithfulness values \mathcal{F} computed considering frequencies from f_{low} to f_{mrg} between simulations with the same intrinsic parameters and two different resolutions, extracted at $r/M = 1000$. The source is situated in the same sky location as GW170817, and the waveform polarizations h_+ and h_\times are computed and projected on the Livingston detector. We employ the aLIGODesignSensitivityP1200087 [8] PSD from pycbc [476] to compute the matches, and compare the values obtained to the thresholds \mathcal{F}_{thr} calculated with Eq. A.3 with $\epsilon^2 = 1$ or $\epsilon^2 = 6$. A tick \checkmark indicates that $\mathcal{F} > \mathcal{F}_{\text{thr}}$. Conversely, a cross \times indicates that $\mathcal{F} < \mathcal{F}_{\text{thr}}$.

Sim	n ¹	\mathcal{F}	SNR						
			14		30		80		
			6	1	6	1	6	1	
BAM:0011	[96, 64]	0.991298	\checkmark	\times	\times	\times	\times	\times	\times
BAM:0017	[96, 64]	0.985917	\checkmark	\times	\times	\times	\times	\times	\times
BAM:0021	[96, 64]	0.957098	\times	\times	\times	\times	\times	\times	\times
BAM:0037	[216, 144]	0.998790	\checkmark	\checkmark	\checkmark	\times	\times	\times	\times
BAM:0048	[108, 72]	0.983724	\times	\times	\times	\times	\times	\times	\times
BAM:0058	[64, 64]	0.999127	\checkmark	\checkmark	\checkmark	\times	\times	\times	\times
BAM:0064	[240, 160]	0.997427	\checkmark	\times	\checkmark	\times	\times	\times	\times
BAM:0091	[144, 108]	0.997810	\checkmark	\checkmark	\checkmark	\times	\times	\times	\times
BAM:0094	[144, 108]	0.996804	\checkmark	\times	\checkmark	\times	\times	\times	\times
BAM:0095	[256, 192]	0.999550	\checkmark	\checkmark	\checkmark	\checkmark	\checkmark	\checkmark	\times
BAM:0107	[128, 96]	0.995219	\checkmark	\times	\times	\times	\times	\times	\times
BAM:0127	[128, 96]	0.999011	\checkmark	\checkmark	\checkmark	\times	\times	\times	\times

Bibliography

- [1] R. Abbott et al. “Open data from the third observing run of LIGO, Virgo, KAGRA and GEO”. In: (Feb. 2023). arXiv: 2302.03676 [gr-qc].
- [2] Rich Abbott et al. “Open data from the first and second observing runs of Advanced LIGO and Advanced Virgo”. In: *SoftwareX* 13 (2021), p. 100658. ISSN: 2352-7110. DOI: <https://doi.org/10.1016/j.softx.2021.100658>. URL: <https://www.sciencedirect.com/science/article/pii/S2352711021000030>.
- [3] A. Einstein. “The Foundation of the General Theory of Relativity”. In: *Annalen Phys.* 49.7 (1916). Ed. by J.-P. Hsu and D. Fine, pp. 769–822. DOI: 10.1002/andp.19163540702.
- [4] R. Hulse and J. Taylor. “Discovery of a pulsar in a binary system”. In: *Astrophys.J.* 195 (1975), pp. L51–L53. DOI: 10.1086/181708.
- [5] R. A. Hulse. “The discovery of the binary pulsar”. In: *Rev. Mod. Phys.* 66 (1994), pp. 699–710. DOI: 10.1103/RevModPhys.66.699.
- [6] T. Damour. “Gravitational radiation reaction in the binary pulsar and the quadrupole formula controversy”. In: *Phys.Rev.Lett.* 51 (1983), pp. 1019–1021. DOI: 10.1103/PhysRevLett.51.1019.
- [7] T. Damour and J. H. Taylor. “On the orbital period change of the binary pulsar PSR-1913+16”. In: *Astrophys. J.* 366 (1991), pp. 501–511. DOI: 10.1086/169585.
- [8] J. Aasi et al. “Advanced LIGO”. In: *Class. Quant. Grav.* 32 (2015), p. 074001. DOI: 10.1088/0264-9381/32/7/074001. arXiv: 1411.4547 [gr-qc].
- [9] F. Acernese et al. “Advanced Virgo: a second-generation interferometric gravitational wave detector”. In: *Class. Quant. Grav.* 32.2 (2015), p. 024001. DOI: 10.1088/0264-9381/32/2/024001. arXiv: 1408.3978 [gr-qc].

- [10] B. P. Abbott et al. “GWTC-1: A Gravitational-Wave Transient Catalog of Compact Binary Mergers Observed by LIGO and Virgo during the First and Second Observing Runs”. In: *Phys. Rev. X* 9.3 (2019), p. 031040. DOI: 10.1103/PhysRevX.9.031040. arXiv: 1811.12907 [astro-ph.HE].
- [11] R. Abbott et al. “GWTC-3: Compact Binary Coalescences Observed by LIGO and Virgo During the Second Part of the Third Observing Run”. In: (Nov. 2021). arXiv: 2111.03606 [gr-qc].
- [12] B. P. Abbott et al. “GW170817: Observation of Gravitational Waves from a Binary Neutron Star Inspiral”. In: *Phys. Rev. Lett.* 119.16 (2017), p. 161101. DOI: 10.1103/PhysRevLett.119.161101. arXiv: 1710.05832 [gr-qc].
- [13] B. P. Abbott et al. “Multi-messenger Observations of a Binary Neutron Star Merger”. In: *Astrophys. J. Lett.* 848.2 (2017), p. L12. DOI: 10.3847/2041-8213/aa91c9. arXiv: 1710.05833 [astro-ph.HE].
- [14] B. P. Abbott et al. “GW190425: Observation of a Compact Binary Coalescence with Total Mass $\sim 3.4M_{\odot}$ ”. In: *Astrophys. J. Lett.* 892.1 (2020), p. L3. DOI: 10.3847/2041-8213/ab75f5. arXiv: 2001.01761 [astro-ph.HE].
- [15] R. Abbott et al. “Observation of Gravitational Waves from Two Neutron Star–Black Hole Coalescences”. In: *Astrophys. J. Lett.* 915.1 (2021), p. L5. DOI: 10.3847/2041-8213/ac082e. arXiv: 2106.15163 [astro-ph.HE].
- [16] B. Abbott et al. “Binary Black Hole Population Properties Inferred from the First and Second Observing Runs of Advanced LIGO and Advanced Virgo”. In: *Astrophys. J. Lett.* 882.2 (2019), p. L24. DOI: 10.3847/2041-8213/ab3800. arXiv: 1811.12940 [astro-ph.HE].
- [17] R. Abbott et al. “Population Properties of Compact Objects from the Second LIGO-Virgo Gravitational-Wave Transient Catalog”. In: *Astrophys. J. Lett.* 913.1 (2021), p. L7. DOI: 10.3847/2041-8213/abe949. arXiv: 2010.14533 [astro-ph.HE].
- [18] B. P. Abbott et al. “A gravitational-wave standard siren measurement of the Hubble constant”. In: *Nature* (2017). DOI: 10.1038/nature24471. arXiv: 1710.05835 [astro-ph.CO].
- [19] B. P. Abbott et al. “GW170817: Measurements of neutron star radii and equation of state”. In: *Phys. Rev. Lett.* 121.16 (2018), p. 161101. DOI: 10.1103/PhysRevLett.121.161101. arXiv: 1805.11581 [gr-qc].

- [20] E. Annala et al. “Gravitational-wave constraints on the neutron-star-matter Equation of State”. In: *Phys. Rev. Lett.* 120.17 (2018), p. 172703. DOI: 10.1103/PhysRevLett.120.172703. arXiv: 1711.02644 [astro-ph.HE].
- [21] D. Radice et al. “Binary Neutron Star Mergers: Mass Ejection, Electromagnetic Counterparts and Nucleosynthesis”. In: *Astrophys. J.* 869.2 (2018), p. 130. DOI: 10.3847/1538-4357/aaf054. arXiv: 1809.11161 [astro-ph.HE].
- [22] S. De et al. “Tidal Deformabilities and Radii of Neutron Stars from the Observation of GW170817”. In: *Phys. Rev. Lett.* 121.9 (2018). [Erratum: *Phys. Rev. Lett.* 121,no.25,259902(2018)], p. 091102. DOI: 10.1103/PhysRevLett.121.259902, 10.1103/PhysRevLett.121.091102. arXiv: 1804.08583 [astro-ph.HE].
- [23] F. J. Fattoyev, J. Piekarewicz, and C. J. Horowitz. “Neutron skins and neutron stars in the multi-messenger era”. In: *Phys. Rev. Lett.* 120.17 (2018), p. 172702. DOI: 10.1103/PhysRevLett.120.172702. arXiv: 1711.06615 [nucl-th].
- [24] E. R. Most et al. “New constraints on radii and tidal deformabilities of neutron stars from GW170817”. In: *Phys. Rev. Lett.* 120.26 (2018), p. 261103. DOI: 10.1103/PhysRevLett.120.261103. arXiv: 1803.00549 [gr-qc].
- [25] C. Raithel, F. Özel, and D. Psaltis. “Tidal deformability from GW170817 as a direct probe of the neutron star radius”. In: *Astrophys. J. Lett.* 857.2 (2018), p. L23. DOI: 10.3847/2041-8213/aabcbf. arXiv: 1803.07687 [astro-ph.HE].
- [26] I. Tews, J. Margueron, and S. Reddy. “Critical examination of constraints on the equation of state of dense matter obtained from GW170817”. In: *Phys. Rev.* C98.4 (2018), p. 045804. DOI: 10.1103/PhysRevC.98.045804. arXiv: 1804.02783 [nucl-th].
- [27] J. Meidam et al. “Testing the no-hair theorem with black hole ringdowns using TIGER”. In: *Phys. Rev.* D90.6 (2014), p. 064009. DOI: 10.1103/PhysRevD.90.064009. arXiv: 1406.3201 [gr-qc].
- [28] B. P. Abbott et al. “Tests of general relativity with GW150914”. In: *Phys. Rev. Lett.* 116.22 (2016). [Erratum: *Phys. Rev. Lett.* 121,no.12,129902(2018)], p. 221101. DOI: 10.1103/PhysRevLett.116.221101, 10.1103/PhysRevLett.121.129902. arXiv: 1602.03841 [gr-qc].
- [29] B. P. Abbott et al. “Tests of General Relativity with GW170817”. In: *Phys. Rev. Lett.* 123.1 (2019), p. 011102. DOI: 10.1103/PhysRevLett.123.011102. arXiv: 1811.00364 [gr-qc].

- [30] T. Damour, B. R. Iyer, and B. S. Sathyaprakash. “Improved filters for gravitational waves from inspiralling compact binaries”. In: *Phys. Rev. D* 57 (1998), pp. 885–907. DOI: 10.1103/PhysRevD.57.885. arXiv: gr-qc/9708034 [gr-qc].
- [31] H. Gabbard et al. “Matching matched filtering with deep networks for gravitational-wave astronomy”. In: *Phys. Rev. Lett.* 120.14 (2018), p. 141103. DOI: 10.1103/PhysRevLett.120.141103. arXiv: 1712.06041 [astro-ph.IM].
- [32] J. Veitch et al. “Parameter estimation for compact binaries with ground-based gravitational-wave observations using the LALInference software library”. In: *Phys. Rev. D* 91.4 (2015), p. 042003. DOI: 10.1103/PhysRevD.91.042003. arXiv: 1409.7215 [gr-qc].
- [33] G. Ashton et al. “BILBY: A user-friendly Bayesian inference library for gravitational-wave astronomy”. In: *Astrophys. J. Suppl.* 241.2 (2019), p. 27. DOI: 10.3847/1538-4365/ab06fc. arXiv: 1811.02042 [astro-ph.IM].
- [34] M. Breschi, R. Gamba, and S. Bernuzzi. “Bayesian inference of multimessenger astrophysical data: Methods and applications to gravitational waves”. In: *Phys. Rev. D* 104.4 (2021), p. 042001. DOI: 10.1103/PhysRevD.104.042001. arXiv: 2102.00017 [gr-qc].
- [35] L. D. Landau and E. M. Lifshitz. *The Classical Theory of Fields*. 4th ed. Butterworth-Heinemann, Jan. 1980. ISBN: 0750627689. URL: <http://www.worldcat.org/isbn/0750627689>.
- [36] J Droste. In: *Versl. K. Akad. Wet. Amsterdam* 19 (1916), pp. 447–455.
- [37] W. de Sitter. “Einstein’s theory of gravitation and its astronomical consequences”. In: *Mon. Not. Roy. Astron. Soc.* 76 (June 1916), pp. 699–728. DOI: 10.1093/mnras/76.9.699.
- [38] J Chazy. *La théorie de la Relativité et la Mécanique Céleste*. Gauthier-Villars, Paris, 1928 and 1930.
- [39] T. Levi-Civita. In: *Am. J. Math.* 59 (1937), pp. 9–22.
- [40] A. Einstein, L. Infeld, and B. Hoffmann. “The Gravitational Equations and the Problem of Motion”. In: *Annals of Mathematics* 39.1 (1938), pp. 65–100. ISSN: 0003486X. URL: <http://www.jstor.org/stable/1968714> (visited on 02/22/2023).

- [41] A. Hewish and S. E. Okoye. “Evidence for an Unusual Source of High Radio Brightness Temperature in the Crab Nebula”. In: *nat* 207.4992 (July 1965), pp. 59–60. DOI: 10.1038/207059a0.
- [42] S. J. Bell Burnell. “Little Green Men, White Dwarfs or Pulsars”. In: *Annals of the New York Academy of Sciences* ().
- [43] J. Ehlers et al. “Comments on gravitational radiation damping and energy loss in binary systems.” In: *Astrophys. J. Lett.* 208 (Sept. 1976), pp. L77–L81. DOI: 10.1086/182236.
- [44] T. Damour and N. Deruelle. “Radiation reaction and angular momentum loss in small angle gravitational scattering”. In: *Physics Letters A* 87.3 (Dec. 1981), pp. 81–84. DOI: 10.1016/0375-9601(81)90567-3.
- [45] T. Damour. “Gravitational radiation and the motion of compact bodies”. In: *Gravitational Radiation*. Ed. by N. Deruelle and T. Piran. North-Holland, Amsterdam, 1983, pp. 59–144.
- [46] G Schafer. “Gravitational quadrupole radiation-reaction force and the canonical formalism of ADM”. In: *Ann. Phys. (N. Y.); (United States)* 161:1 (Apr. 1985). DOI: 10.1016/0003-4916(85)90337-9. URL: <https://www.osti.gov/biblio/5467543>.
- [47] L. Blanchet. “Gravitational Radiation from Post-Newtonian Sources and Inspiralling Compact Binaries”. In: *Living Rev. Relativity* 17 (2014), p. 2. DOI: 10.12942/lrr-2014-2. arXiv: 1310.1528 [gr-qc].
- [48] M. E. Pati and C. M. Will. “Post-Newtonian gravitational radiation and equations of motion via direct integration of the relaxed Einstein equations: Foundations”. In: *Physical Review D* 62.12 (2000), p. 124015.
- [49] P. Jaranowski and G. Schaefer. “Third postNewtonian higher order ADM Hamilton dynamics for two-body point mass systems”. In: *Phys. Rev. D* 57 (1998). [Erratum: *Phys. Rev. D* 63,029902(2001)], pp. 7274–7291. DOI: 10.1103/PhysRevD.57.7274, 10.1103/PhysRevD.63.029902. arXiv: gr-qc/9712075 [gr-qc].
- [50] L. Blanchet and G. Faye. “General relativistic dynamics of compact binaries at the third postNewtonian order”. In: *Phys. Rev. D* 63 (2001), p. 062005. DOI: 10.1103/PhysRevD.63.062005. arXiv: gr-qc/0007051.

-
- [51] T. Damour, P. Jaranowski, and G. Schaefer. “Dimensional regularization of the gravitational interaction of point masses”. In: *Phys. Lett. B* 513 (2001), pp. 147–155. DOI: 10.1016/S0370-2693(01)00642-6. arXiv: gr-qc/0105038.
- [52] P. Jaranowski and G. Schafer. “Towards the 4th post-Newtonian Hamiltonian for two-point-mass systems”. In: *Phys. Rev. D* 86 (2012), p. 061503. DOI: 10.1103/PhysRevD.86.061503. arXiv: 1207.5448 [gr-qc].
- [53] S. Foffa and R. Sturani. “Dynamics of the gravitational two-body problem at fourth post-Newtonian order and at quadratic order in the Newton constant”. In: *Phys. Rev. D* 87.6 (2013), p. 064011. DOI: 10.1103/PhysRevD.87.064011. arXiv: 1206.7087 [gr-qc].
- [54] P. Jaranowski and G. Schäfer. “Dimensional regularization of local singularities in the 4th post-Newtonian two-point-mass Hamiltonian”. In: *Phys. Rev. D* 87 (2013), p. 081503. DOI: 10.1103/PhysRevD.87.081503. arXiv: 1303.3225 [gr-qc].
- [55] D. Bini and T. Damour. “Analytical determination of the two-body gravitational interaction potential at the fourth post-Newtonian approximation”. In: *Phys. Rev. D* 87.12 (2013), p. 121501. DOI: 10.1103/PhysRevD.87.121501. arXiv: 1305.4884 [gr-qc].
- [56] T. Damour, P. Jaranowski, and G. Schäfer. “Nonlocal-in-time action for the fourth post-Newtonian conservative dynamics of two-body systems”. In: *Phys. Rev. D* 89.6 (2014), p. 064058. DOI: 10.1103/PhysRevD.89.064058. arXiv: 1401.4548 [gr-qc].
- [57] P. Jaranowski and G. Schäfer. “Derivation of local-in-time fourth post-Newtonian ADM Hamiltonian for spinless compact binaries”. In: *Phys. Rev. D* 92.12 (2015), p. 124043. DOI: 10.1103/PhysRevD.92.124043. arXiv: 1508.01016 [gr-qc].
- [58] L. Bernard et al. “Fokker action of nonspinning compact binaries at the fourth post-Newtonian approximation”. In: *Phys. Rev. D* 93.8 (2016), p. 084037. DOI: 10.1103/PhysRevD.93.084037. arXiv: 1512.02876 [gr-qc].
- [59] T. Damour, P. Jaranowski, and G. Schäfer. “Conservative dynamics of two-body systems at the fourth post-Newtonian approximation of general relativity”. In: *Phys. Rev. D* 93.8 (2016), p. 084014. DOI: 10.1103/PhysRevD.93.084014. arXiv: 1601.01283 [gr-qc].

- [60] L. Bernard et al. “Energy and periastron advance of compact binaries on circular orbits at the fourth post-Newtonian order”. In: *Phys. Rev. D* 95.4 (2017), p. 044026. DOI: 10.1103/PhysRevD.95.044026. arXiv: 1610.07934 [gr-qc].
- [61] T. Damour and P. Jaranowski. “Four-loop static contribution to the gravitational interaction potential of two point masses”. In: *Phys. Rev. D* 95.8 (2017), p. 084005. DOI: 10.1103/PhysRevD.95.084005. arXiv: 1701.02645 [gr-qc].
- [62] T. Marchand et al. “Ambiguity-Free Completion of the Equations of Motion of Compact Binary Systems at the Fourth Post-Newtonian Order”. In: *Phys. Rev. D* 97.4 (2018), p. 044023. DOI: 10.1103/PhysRevD.97.044023. arXiv: 1707.09289 [gr-qc].
- [63] L. Bernard et al. “Center-of-Mass Equations of Motion and Conserved Integrals of Compact Binary Systems at the Fourth Post-Newtonian Order”. In: *Phys. Rev. D* 97.4 (2018), p. 044037. DOI: 10.1103/PhysRevD.97.044037. arXiv: 1711.00283 [gr-qc].
- [64] S. Foffa and R. Sturani. “Conservative dynamics of binary systems to fourth Post-Newtonian order in the EFT approach I: Regularized Lagrangian”. In: *Phys. Rev. D* 100.2 (2019), p. 024047. DOI: 10.1103/PhysRevD.100.024047. arXiv: 1903.05113 [gr-qc].
- [65] D. Bini, T. Damour, and A. Geralico. “Sixth post-Newtonian local-in-time dynamics of binary systems”. In: *Phys. Rev. D* 102.2 (2020), p. 024061. DOI: 10.1103/PhysRevD.102.024061. arXiv: 2004.05407 [gr-qc].
- [66] D. Bini, T. Damour, and A. Geralico. “Sixth post-Newtonian nonlocal-in-time dynamics of binary systems”. In: *Phys. Rev. D* 102.8 (2020), p. 084047. DOI: 10.1103/PhysRevD.102.084047. arXiv: 2007.11239 [gr-qc].
- [67] J. Blümlein et al. “Testing binary dynamics in gravity at the sixth post-Newtonian level”. In: *Phys. Lett. B* 807 (2020), p. 135496. DOI: 10.1016/j.physletb.2020.135496. arXiv: 2003.07145 [gr-qc].
- [68] E. Poisson. “Gravitational waves from inspiraling compact binaries: The Quadrupole moment term”. In: *Phys. Rev. D* 57 (1998), pp. 5287–5290. DOI: 10.1103/PhysRevD.57.5287. arXiv: gr-qc/9709032 [gr-qc].
- [69] E. E. Flanagan and T. Hinderer. “Constraining neutron star tidal Love numbers with gravitational wave detectors”. In: *Phys. Rev. D* 77 (2008), p. 021502. DOI: 10.1103/PhysRevD.77.021502. arXiv: 0709.1915 [astro-ph].

-
- [70] D. Bini, T. Damour, and G. Faye. “Effective action approach to higher-order relativistic tidal interactions in binary systems and their effective one body description”. In: *Phys.Rev.* D85 (2012), p. 124034. DOI: 10.1103/PhysRevD.85.124034. arXiv: 1202.3565 [gr-qc].
- [71] J. E. Vines and E. E. Flanagan. “Post-1-Newtonian quadrupole tidal interactions in binary systems”. In: *Phys. Rev.* D88 (2010), p. 024046. DOI: 10.1103/PhysRevD.88.024046. arXiv: 1009.4919 [gr-qc].
- [72] J. Vines, E. E. Flanagan, and T. Hinderer. “Post-1-Newtonian tidal effects in the gravitational waveform from binary inspirals”. In: *Phys. Rev.* D83 (2011), p. 084051. DOI: 10.1103/PhysRevD.83.084051. arXiv: 1101.1673 [gr-qc].
- [73] P. Landry. “Rotational-tidal phasing of the binary neutron star waveform”. In: (2018). arXiv: 1805.01882 [gr-qc].
- [74] B. Banihashemi and J. Vines. “Gravitomagnetic tidal effects in gravitational waves from neutron star binaries”. In: (2018). arXiv: 1805.07266 [gr-qc].
- [75] Q. Henry, G. Faye, and L. Blanchet. “Tidal effects in the equations of motion of compact binary systems to next-to-next-to-leading post-Newtonian order”. In: *Phys. Rev. D* 101.6 (2020), p. 064047. DOI: 10.1103/PhysRevD.101.064047. arXiv: 1912.01920 [gr-qc].
- [76] Q. Henry, G. Faye, and L. Blanchet. “Hamiltonian for tidal interactions in compact binary systems to next-to-next-to-leading post-Newtonian order”. In: *Phys. Rev. D* 102.12 (2020), p. 124074. DOI: 10.1103/PhysRevD.102.124074. arXiv: 2009.12332 [gr-qc].
- [77] Q. Henry, G. Faye, and L. Blanchet. “Tidal effects in the gravitational-wave phase evolution of compact binary systems to next-to-next-to-leading post-Newtonian order”. In: *Phys. Rev. D* 102.4 (2020), p. 044033. DOI: 10.1103/PhysRevD.102.044033. arXiv: 2005.13367 [gr-qc].
- [78] B. Bertotti. “On gravitational motion”. In: *Nuovo Cim.* 4.4 (1956), pp. 898–906. DOI: 10.1007/bf02746175.
- [79] B. Bertotti and J. Plebanski. “Theory of gravitational perturbations in the fast motion approximation”. In: *Annals Phys.* 11.2 (1960), pp. 169–200. DOI: 10.1016/0003-4916(60)90132-9.

- [80] A. Rosenblum. “Gravitational Radiation Energy Loss in Scattering Problems and the Einstein Quadrupole Formula”. In: *Phys. Rev. Lett.* 41 (15 1978), pp. 1003–1005. DOI: 10.1103/PhysRevLett.41.1003. URL: <https://link.aps.org/doi/10.1103/PhysRevLett.41.1003>.
- [81] K. Westpfahl and M. Goller. “GRAVITATIONAL SCATTERING OF TWO RELATIVISTIC PARTICLES IN POSTLINEAR APPROXIMATION”. In: *Lett. Nuovo Cim.* 26 (1979), pp. 573–576. DOI: 10.1007/BF02817047.
- [82] L. Bel et al. “Poincaré-invariant gravitational field and equations of motion of two pointlike objects: The postlinear approximation of general relativity”. In: *Gen. Rel. Grav.* 13 (1981), pp. 963–1004. DOI: 10.1007/BF00756073.
- [83] T. Damour. “Gravitational scattering, post-Minkowskian approximation and Effective One-Body theory”. In: *Phys. Rev.* D94.10 (2016), p. 104015. DOI: 10.1103/PhysRevD.94.104015. arXiv: 1609.00354 [gr-qc].
- [84] T. Damour. “High-energy gravitational scattering and the general relativistic two-body problem”. In: *Phys. Rev.* D97.4 (2018), p. 044038. DOI: 10.1103/PhysRevD.97.044038. arXiv: 1710.10599 [gr-qc].
- [85] Z. Bern et al. “Scattering Amplitudes and the Conservative Hamiltonian for Binary Systems at Third Post-Minkowskian Order”. In: *Phys. Rev. Lett.* 122.20 (2019), p. 201603. DOI: 10.1103/PhysRevLett.122.201603. arXiv: 1901.04424 [hep-th].
- [86] T. Damour and P. Retegno. “Strong-field scattering of two black holes: Numerical Relativity meets Post-Minkowskian gravity”. In: (Nov. 2022). arXiv: 2211.01399 [gr-qc].
- [87] Y. Mino, M. Sasaki, and T. Tanaka. “Gravitational radiation reaction to a particle motion”. In: *Phys. Rev.* D55 (1997), pp. 3457–3476. DOI: 10.1103/PhysRevD.55.3457. arXiv: gr-qc/9606018 [gr-qc].
- [88] T. C. Quinn and R. M. Wald. “Axiomatic approach to electromagnetic and gravitational radiation reaction of particles in curved spacetime”. In: *Phys. Rev. D* 56 (6 1997), pp. 3381–3394. DOI: 10.1103/PhysRevD.56.3381. URL: <https://link.aps.org/doi/10.1103/PhysRevD.56.3381>.
- [89] R. M. Wald. “Introduction to Gravitational Self-Force”. In: *Fundam. Theor. Phys.* 162 (2011). Ed. by L. Blanchet, A. Spallicci, and B. Whiting, pp. 253–262. arXiv: 0907.0412 [gr-qc].

- [90] A. Pound. “Motion of small objects in curved spacetimes: An introduction to gravitational self-force”. In: *Fund. Theor. Phys.* 179 (2015). Ed. by D. Pützfeld, C. Lämmerzahl, and B. Schutz, pp. 399–486. DOI: 10.1007/978-3-319-18335-0_13. arXiv: 1506.06245 [gr-qc].
- [91] A. Pound. “Nonlinear gravitational self-force: second-order equation of motion”. In: *Phys. Rev. D* 95.10 (2017), p. 104056. DOI: 10.1103/PhysRevD.95.104056. arXiv: 1703.02836 [gr-qc].
- [92] L. Barack and A. Pound. “Self-force and radiation reaction in general relativity”. In: *Rept. Prog. Phys.* 82.1 (2019), p. 016904. DOI: 10.1088/1361-6633/aae552. arXiv: 1805.10385 [gr-qc].
- [93] N. Warburton et al. “Gravitational-Wave Energy Flux for Compact Binaries through Second Order in the Mass Ratio”. In: *Phys. Rev. Lett.* 127.15 (2021), p. 151102. DOI: 10.1103/PhysRevLett.127.151102. arXiv: 2107.01298 [gr-qc].
- [94] B. Wardell et al. “Gravitational waveforms for compact binaries from second-order self-force theory”. In: (Dec. 2021). arXiv: 2112.12265 [gr-qc].
- [95] B. S. DeWitt and R. W. Brehme. “Radiation damping in a gravitational field”. In: *Annals of Physics* 9.2 (Feb. 1960), pp. 220–259. DOI: 10.1016/0003-4916(60)90030-0.
- [96] J. Hobbs. “A vierbein formalism of radiation damping”. In: *Annals of Physics* 47.1 (1968), pp. 141–165. ISSN: 0003-4916. DOI: [https://doi.org/10.1016/0003-4916\(68\)90231-5](https://doi.org/10.1016/0003-4916(68)90231-5). URL: <https://www.sciencedirect.com/science/article/pii/0003491668902315>.
- [97] T. Hinderer and E. E. Flanagan. “Two timescale analysis of extreme mass ratio inspirals in Kerr. I. Orbital Motion”. In: *Phys. Rev. D* 78 (2008), p. 064028. DOI: 10.1103/PhysRevD.78.064028. arXiv: 0805.3337 [gr-qc].
- [98] S. Babak et al. “Science with the space-based interferometer LISA. V: Extreme mass-ratio inspirals”. In: *Phys. Rev. D* 95.10 (2017), p. 103012. DOI: 10.1103/PhysRevD.95.103012. arXiv: 1703.09722 [gr-qc].
- [99] P. Amaro-Seoane et al. “Laser Interferometer Space Antenna”. In: *arXiv e-prints*, arXiv:1702.00786 (Feb. 2017), arXiv:1702.00786. DOI: 10.48550/arXiv.1702.00786. arXiv: 1702.00786 [astro-ph.IM].

- [100] F. Pretorius. “Evolution of binary black hole spacetimes”. In: *Phys. Rev. Lett.* 95 (2005), p. 121101. DOI: 10.1103/PhysRevLett.95.121101. arXiv: gr-qc/0507014.
- [101] J. G. Baker et al. “Consistency of post-Newtonian waveforms with numerical relativity”. In: *Phys. Rev. Lett.* 99 (2007), p. 181101. DOI: 10.1103/PhysRevLett.99.181101. arXiv: gr-qc/0612024 [gr-qc].
- [102] M. Campanelli et al. “Accurate Evolutions of Orbiting Black-Hole Binaries Without Excision”. In: *Phys. Rev. Lett.* 96 (2006), p. 111101. DOI: 10.1103/PhysRevLett.96.111101. arXiv: gr-qc/0511048.
- [103] S. G. Hahn and R. W. Lindquist. “The two-body problem in geometrodynamics”. In: *Annals of Physics* 29.2 (Sept. 1964), pp. 304–331. DOI: 10.1016/0003-4916(64)90223-4.
- [104] H. Friedrich. “On the hyperbolicity of Einstein’s and other gauge field equations”. English. In: *Communications in Mathematical Physics* 100.4 (1985), pp. 525–543. ISSN: 0010-3616. DOI: 10.1007/BF01217728. URL: <http://dx.doi.org/10.1007/BF01217728>.
- [105] L. Lindblom et al. “A New generalized harmonic evolution system”. In: *Class. Quant. Grav.* 23 (2006), S447–S462. DOI: 10.1088/0264-9381/23/16/S09. arXiv: gr-qc/0512093 [gr-qc].
- [106] T. Nakamura, K. Oohara, and Y. Kojima. “General Relativistic Collapse to Black Holes and Gravitational Waves from Black Holes”. In: *Prog. Theor. Phys. Suppl.* 90 (1987), pp. 1–218.
- [107] M. Shibata and T. Nakamura. “Evolution of three-dimensional gravitational waves: Harmonic slicing case”. In: *Phys. Rev. D* 52 (10 1995), pp. 5428–5444. DOI: 10.1103/PhysRevD.52.5428. URL: <https://link.aps.org/doi/10.1103/PhysRevD.52.5428>.
- [108] T. W. Baumgarte and S. L. Shapiro. “On the numerical integration of Einstein’s field equations”. In: *Phys. Rev. D* 59 (1999), p. 024007. DOI: 10.1103/PhysRevD.59.024007. arXiv: gr-qc/9810065.
- [109] C. Bona et al. “General-covariant evolution formalism for Numerical Relativity”. In: *Phys. Rev. D* 67 (2003), p. 104005. DOI: 10.1103/PhysRevD.67.104005. arXiv: gr-qc/0302083.

-
- [110] S. Bernuzzi and D. Hilditch. “Constraint violation in free evolution schemes: comparing BSSNOK with a conformal decomposition of Z4”. In: *Phys. Rev. D* 81 (2010), p. 084003. DOI: 10.1103/PhysRevD.81.084003. arXiv: 0912.2920 [gr-qc].
- [111] Z. Cao and D. Hilditch. “Numerical stability of the Z4c formulation of general relativity”. In: *Phys. Rev. D* 85 (2012), p. 124032. DOI: 10.1103/PhysRevD.85.124032. arXiv: 1111.2177 [gr-qc].
- [112] A. Weyhausen, S. Bernuzzi, and D. Hilditch. “Constraint damping for the Z4c formulation of general relativity”. In: *Phys. Rev. D* 85 (2012), p. 024038. DOI: 10.1103/PhysRevD.85.024038. arXiv: 1107.5539 [gr-qc].
- [113] D. Hilditch et al. “Compact binary evolutions with the Z4c formulation”. In: *Phys. Rev. D* 88 (2013), p. 084057. DOI: 10.1103/PhysRevD.88.084057. arXiv: 1212.2901 [gr-qc].
- [114] F. Estabrook et al. “Maximally Slicing a Black Hole”. In: *Phys. Rev. D* 7 (10 1973), pp. 2814–2817. DOI: 10.1103/PhysRevD.7.2814. URL: <https://link.aps.org/doi/10.1103/PhysRevD.7.2814>.
- [115] C. Bona et al. “A New formalism for numerical relativity”. In: *Phys. Rev. Lett.* 75 (1995), pp. 600–603. DOI: 10.1103/PhysRevLett.75.600. arXiv: gr-qc/9412071.
- [116] M. Alcubierre et al. “Towards a stable numerical evolution of strongly gravitating systems in general relativity: The conformal treatments”. In: *Phys. Rev. D* 62 (2000), p. 044034. DOI: 10.1103/PhysRevD.62.044034. arXiv: gr-qc/0003071.
- [117] M. Alcubierre et al. “Black Hole Excision for Dynamic Black Holes”. In: *Phys. Rev. D* 64 (2001), p. 061501. DOI: 10.1103/PhysRevD.64.061501. arXiv: gr-qc/0104020.
- [118] M. Alcubierre et al. “Gauge conditions for long term numerical black hole evolutions without excision”. In: *Phys. Rev. D* 67 (2003), p. 084023. DOI: 10.1103/PhysRevD.67.084023. arXiv: gr-qc/0206072 [gr-qc].
- [119] J. W. York. “Kinematics and Dynamics of General Relativity”. In: *Sources of gravitational radiation*. Ed. by L. L. Smarr. Cambridge, UK: Cambridge University Press, 1979, pp. 83–126. ISBN: 0-521-22778-X.

-
- [120] J. M. Bowen and J. W. York Jr. “Time asymmetric initial data for black holes and black hole collisions”. In: *Phys. Rev. D* 21 (1980), pp. 2047–2056. DOI: 10.1103/PhysRevD.21.2047.
- [121] B. Brügmann et al. “Calibration of Moving Puncture Simulations”. In: *Phys. Rev. D* 77 (2008), p. 024027. DOI: 10.1103/PhysRevD.77.024027. arXiv: gr-qc/0610128 [gr-qc].
- [122] A. Buonanno and T. Damour. “Effective one-body approach to general relativistic two-body dynamics”. In: *Phys. Rev. D* 59 (1999), p. 084006. DOI: 10.1103/PhysRevD.59.084006. arXiv: gr-qc/9811091.
- [123] A. Buonanno and T. Damour. “Transition from inspiral to plunge in binary black hole coalescences”. In: *Phys. Rev. D* 62 (2000), p. 064015. DOI: 10.1103/PhysRevD.62.064015. arXiv: gr-qc/0001013.
- [124] T. Damour, P. Jaranowski, and G. Schaefer. “On the determination of the last stable orbit for circular general relativistic binaries at the third postNewtonian approximation”. In: *Phys. Rev. D* 62 (2000), p. 084011. DOI: 10.1103/PhysRevD.62.084011. arXiv: gr-qc/0005034 [gr-qc].
- [125] T. Damour. “Coalescence of two spinning black holes: An effective one-body approach”. In: *Phys. Rev. D* 64 (2001), p. 124013. DOI: 10.1103/PhysRevD.64.124013. arXiv: gr-qc/0103018.
- [126] A. Buonanno, Y. Chen, and T. Damour. “Transition from inspiral to plunge in precessing binaries of spinning black holes”. In: *Phys. Rev. D* 74 (2006), p. 104005. DOI: 10.1103/PhysRevD.74.104005. arXiv: gr-qc/0508067.
- [127] T. Damour, P. Jaranowski, and G. Schäfer. “Fourth post-Newtonian effective one-body dynamics”. In: *Phys. Rev. D* 91.8 (2015), p. 084024. DOI: 10.1103/PhysRevD.91.084024. arXiv: 1502.07245 [gr-qc].
- [128] T. Damour and A. Nagar. “Effective One Body description of tidal effects in inspiralling compact binaries”. In: *Phys. Rev. D* 81 (2010), p. 084016. DOI: 10.1103/PhysRevD.81.084016. arXiv: 0911.5041 [gr-qc].
- [129] T. Damour, A. Nagar, and L. Villain. “Measurability of the tidal polarizability of neutron stars in late-inspiral gravitational-wave signals”. In: *Phys. Rev. D* 85 (2012), p. 123007. DOI: 10.1103/PhysRevD.85.123007. arXiv: 1203.4352 [gr-qc].

-
- [130] S. Bernuzzi et al. “Tidal effects in binary neutron star coalescence”. In: *Phys. Rev. D* 86 (2012), p. 044030. DOI: 10.1103/PhysRevD.86.044030. arXiv: 1205.3403 [gr-qc].
- [131] A. Bohé et al. “Improved effective-one-body model of spinning, nonprecessing binary black holes for the era of gravitational-wave astrophysics with advanced detectors”. In: *Phys. Rev. D* 95.4 (2017), p. 044028. DOI: 10.1103/PhysRevD.95.044028. arXiv: 1611.03703 [gr-qc].
- [132] S. Babak, A. Taracchini, and A. Buonanno. “Validating the effective-one-body model of spinning, precessing binary black holes against numerical relativity”. In: *Phys. Rev. D* 95.2 (2017), p. 024010. DOI: 10.1103/PhysRevD.95.024010. arXiv: 1607.05661 [gr-qc].
- [133] R. Cotesta et al. “Enriching the Symphony of Gravitational Waves from Binary Black Holes by Tuning Higher Harmonics”. In: *Phys. Rev. D* 98.8 (2018), p. 084028. DOI: 10.1103/PhysRevD.98.084028. arXiv: 1803.10701 [gr-qc].
- [134] T. Hinderer et al. “Effects of neutron-star dynamic tides on gravitational waveforms within the effective-one-body approach”. In: *Phys. Rev. Lett.* 116.18 (2016), p. 181101. DOI: 10.1103/PhysRevLett.116.181101. arXiv: 1602.00599 [gr-qc].
- [135] J. Steinhoff et al. “Dynamical Tides in General Relativity: Effective Action and Effective-One-Body Hamiltonian”. In: *Phys. Rev. D* 94.10 (2016), p. 104028. DOI: 10.1103/PhysRevD.94.104028. arXiv: 1608.01907 [gr-qc].
- [136] B. D. Lackey et al. “Surrogate model for an aligned-spin effective one body waveform model of binary neutron star inspirals using Gaussian process regression”. In: *Phys. Rev. D* 100.2 (2019), p. 024002. DOI: 10.1103/PhysRevD.100.024002. arXiv: 1812.08643 [gr-qc].
- [137] A. Matas et al. “Aligned-spin neutron-star–black-hole waveform model based on the effective-one-body approach and numerical-relativity simulations”. In: *Phys. Rev. D* 102.4 (2020), p. 043023. DOI: 10.1103/PhysRevD.102.043023. arXiv: 2004.10001 [gr-qc].
- [138] S. Ossokine et al. “Multipolar Effective-One-Body Waveforms for Precessing Binary Black Holes: Construction and Validation”. In: *Phys. Rev. D* 102.4 (2020), p. 044055. DOI: 10.1103/PhysRevD.102.044055. arXiv: 2004.09442 [gr-qc].

- [139] T. Damour and A. Nagar. “A new analytic representation of the ringdown waveform of coalescing spinning black hole binaries”. In: *Phys.Rev.* D90 (2014), p. 024054. DOI: 10.1103/PhysRevD.90.024054. arXiv: 1406.0401 [gr-qc].
- [140] S. Bernuzzi et al. “Modeling the Dynamics of Tidally Interacting Binary Neutron Stars up to the Merger”. In: *Phys.Rev.Lett.* 114.16 (2015), p. 161103. DOI: 10.1103/PhysRevLett.114.161103. arXiv: 1412.4553 [gr-qc].
- [141] A. Nagar, G. Riemenschneider, and G. Pratten. “Impact of Numerical Relativity information on effective-one-body waveform models”. In: *Phys. Rev.* D96.8 (2017), p. 084045. DOI: 10.1103/PhysRevD.96.084045. arXiv: 1703.06814 [gr-qc].
- [142] A. Nagar et al. “Time-domain effective-one-body gravitational waveforms for coalescing compact binaries with nonprecessing spins, tides and self-spin effects”. In: *Phys. Rev.* D98.10 (2018), p. 104052. DOI: 10.1103/PhysRevD.98.104052. arXiv: 1806.01772 [gr-qc].
- [143] S. Akcay et al. “Effective-one-body multipolar waveform for tidally interacting binary neutron stars up to merger”. In: *Phys. Rev.* D99.4 (2019), p. 044051. DOI: 10.1103/PhysRevD.99.044051. arXiv: 1812.02744 [gr-qc].
- [144] A. Nagar et al. “Multipolar effective one body waveform model for spin-aligned black hole binaries”. In: *Phys. Rev. D* 102.2 (2020), p. 024077. DOI: 10.1103/PhysRevD.102.024077. arXiv: 2001.09082 [gr-qc].
- [145] D. Chiaramello and A. Nagar. “Faithful analytical effective-one-body waveform model for spin-aligned, moderately eccentric, coalescing black hole binaries”. In: *Phys. Rev. D* 101.10 (2020), p. 101501. DOI: 10.1103/PhysRevD.101.101501. arXiv: 2001.11736 [gr-qc].
- [146] A. Nagar et al. “Effective-one-body waveforms from dynamical captures in black hole binaries”. In: *Phys. Rev. D* 103.6 (2021), p. 064013. DOI: 10.1103/PhysRevD.103.064013. arXiv: 2009.12857 [gr-qc].
- [147] S. Albanesi, A. Nagar, and S. Bernuzzi. “Effective one-body model for extreme-mass-ratio spinning binaries on eccentric equatorial orbits: Testing radiation reaction and waveform”. In: *Phys. Rev. D* 104.2 (2021), p. 024067. DOI: 10.1103/PhysRevD.104.024067. arXiv: 2104.10559 [gr-qc].

- [148] A. Nagar, A. Bonino, and P. Rettengo. “Effective one-body multipolar waveform model for spin-aligned, quasicircular, eccentric, hyperbolic black hole binaries”. In: *Phys. Rev. D* 103.10 (2021), p. 104021. DOI: 10.1103/PhysRevD.103.104021. arXiv: 2101.08624 [gr-qc].
- [149] A. Nagar and P. Rettengo. “Next generation: Impact of high-order analytical information on effective one body waveform models for noncircularized, spin-aligned black hole binaries”. In: *Phys. Rev. D* 104.10 (2021), p. 104004. DOI: 10.1103/PhysRevD.104.104004. arXiv: 2108.02043 [gr-qc].
- [150] P. Ajith et al. “Phenomenological template family for black-hole coalescence waveforms”. In: *Class.Quant.Grav.* 24 (2007), S689–S700. DOI: 10.1088/0264-9381/24/19/S31. arXiv: 0704.3764 [gr-qc].
- [151] P. Ajith et al. “A Template bank for gravitational waveforms from coalescing binary black holes. I. Non-spinning binaries”. In: *Phys.Rev.* D77 (2008), p. 104017. DOI: 10.1103/PhysRevD.77.104017, 10.1103/PhysRevD.79.129901, 10.1103/PhysRevD.77.104017. arXiv: 0710.2335 [gr-qc].
- [152] P. Ajith et al. “Inspirational-merger-ringdown waveforms for black-hole binaries with non-precessing spins”. In: *Phys.Rev.Lett.* 106 (2011), p. 241101. DOI: 10.1103/PhysRevLett.106.241101. arXiv: 0909.2867 [gr-qc].
- [153] L. Santamaria et al. “Matching post-Newtonian and numerical relativity waveforms: systematic errors and a new phenomenological model for non-precessing black hole binaries”. In: *Phys.Rev.* D82 (2010), p. 064016. DOI: 10.1103/PhysRevD.82.064016. arXiv: 1005.3306 [gr-qc].
- [154] S. Husa et al. “Frequency-domain gravitational waves from nonprecessing black-hole binaries. I. New numerical waveforms and anatomy of the signal”. In: *Phys. Rev. D* 93.4 (2016), p. 044006. DOI: 10.1103/PhysRevD.93.044006. arXiv: 1508.07250 [gr-qc].
- [155] S. Khan et al. “Frequency-domain gravitational waves from nonprecessing black-hole binaries. II. A phenomenological model for the advanced detector era”. In: *Phys. Rev. D* 93.4 (2016), p. 044007. DOI: 10.1103/PhysRevD.93.044007. arXiv: 1508.07253 [gr-qc].
- [156] G. Pratten et al. “Setting the cornerstone for a family of models for gravitational waves from compact binaries: The dominant harmonic for nonprecessing quasicircular black holes”. In: *Phys. Rev. D* 102.6 (2020), p. 064001. DOI: 10.1103/PhysRevD.102.064001. arXiv: 2001.11412 [gr-qc].

-
- [157] H. Estellés et al. “Phenomenological time domain model for dominant quadrupole gravitational wave signal of coalescing binary black holes”. In: *Phys. Rev. D* 103.12 (2021), p. 124060. DOI: 10.1103/PhysRevD.103.124060. arXiv: 2004.08302 [gr-qc].
- [158] H. Estellés et al. “New twists in compact binary waveform modeling: A fast time-domain model for precession”. In: *Phys. Rev. D* 105.8 (2022), p. 084040. DOI: 10.1103/PhysRevD.105.084040. arXiv: 2105.05872 [gr-qc].
- [159] E. Hamilton et al. “Model of gravitational waves from precessing black-hole binaries through merger and ringdown”. In: *Phys. Rev. D* 104.12 (2021), p. 124027. DOI: 10.1103/PhysRevD.104.124027. arXiv: 2107.08876 [gr-qc].
- [160] L. London et al. “First higher-multipole model of gravitational waves from spinning and coalescing black-hole binaries”. In: *Phys. Rev. Lett.* 120.16 (2018), p. 161102. DOI: 10.1103/PhysRevLett.120.161102. arXiv: 1708.00404 [gr-qc].
- [161] C. García-Quirós et al. “Multimode frequency-domain model for the gravitational wave signal from nonprecessing black-hole binaries”. In: *Phys. Rev. D* 102.6 (2020), p. 064002. DOI: 10.1103/PhysRevD.102.064002. arXiv: 2001.10914 [gr-qc].
- [162] S. Khan et al. “Including higher order multipoles in gravitational-wave models for precessing binary black holes”. In: *Phys. Rev. D* 101.2 (2020), p. 024056. DOI: 10.1103/PhysRevD.101.024056. arXiv: 1911.06050 [gr-qc].
- [163] M. Hannam et al. “Simple Model of Complete Precessing Black-Hole-Binary Gravitational Waveforms”. In: *Phys. Rev. Lett.* 113.15 (2014), p. 151101. DOI: 10.1103/PhysRevLett.113.151101. arXiv: 1308.3271 [gr-qc].
- [164] P. Schmidt, F. Ohme, and M. Hannam. “Towards models of gravitational waveforms from generic binaries II: Modelling precession effects with a single effective precession parameter”. In: *Phys. Rev. D* 91.2 (2015), p. 024043. DOI: 10.1103/PhysRevD.91.024043. arXiv: 1408.1810 [gr-qc].
- [165] S. Khan et al. “Phenomenological model for the gravitational-wave signal from precessing binary black holes with two-spin effects”. In: *Phys. Rev. D* 100.2 (2019), p. 024059. DOI: 10.1103/PhysRevD.100.024059. arXiv: 1809.10113 [gr-qc].

-
- [166] G. Pratten et al. “Computationally efficient models for the dominant and subdominant harmonic modes of precessing binary black holes”. In: *Phys. Rev. D* 103.10 (2021), p. 104056. DOI: 10.1103/PhysRevD.103.104056. arXiv: 2004.06503 [gr-qc].
- [167] T. Dietrich, S. Bernuzzi, and W. Tichy. “Closed-form tidal approximants for binary neutron star gravitational waveforms constructed from high-resolution numerical relativity simulations”. In: *Phys. Rev. D* 96.12 (2017), p. 121501. DOI: 10.1103/PhysRevD.96.121501. arXiv: 1706.02969 [gr-qc].
- [168] T. Dietrich et al. “Improving the NRTidal model for binary neutron star systems”. In: *Phys. Rev. D* 100.4 (2019), p. 044003. DOI: 10.1103/PhysRevD.100.044003. arXiv: 1905.06011 [gr-qc].
- [169] J. Blackman et al. “Sparse Representations of Gravitational Waves from Precessing Compact Binaries”. In: *Phys. Rev. Lett.* 113.2 (2014), p. 021101. DOI: 10.1103/PhysRevLett.113.021101. arXiv: 1401.7038 [gr-qc].
- [170] J. Blackman et al. “A Surrogate Model of Gravitational Waveforms from Numerical Relativity Simulations of Precessing Binary Black Hole Mergers”. In: *Phys. Rev. D* 95.10 (2017), p. 104023. DOI: 10.1103/PhysRevD.95.104023. arXiv: 1701.00550 [gr-qc].
- [171] V. Varma et al. “Surrogate model of hybridized numerical relativity binary black hole waveforms”. In: *Phys. Rev. D* 99.6 (2019), p. 064045. DOI: 10.1103/PhysRevD.99.064045. arXiv: 1812.07865 [gr-qc].
- [172] V. Varma et al. “Surrogate models for precessing binary black hole simulations with unequal masses”. In: *Phys. Rev. Research*. 1 (2019), p. 033015. DOI: 10.1103/PhysRevResearch.1.033015. arXiv: 1905.09300 [gr-qc].
- [173] D. Williams et al. “A Precessing Numerical Relativity Waveform Surrogate Model for Binary Black Holes: A Gaussian Process Regression Approach”. In: (2019). arXiv: 1903.09204 [gr-qc].
- [174] T. Goodale et al. “The Cactus Framework and Toolkit: Design and Applications”. In: *Vector and Parallel Processing – VECPAR’2002, 5th International Conference, Lecture Notes in Computer Science*. Berlin: Springer, 2003.
- [175] E. Schnetter, S. H. Hawley, and I. Hawke. “Evolutions in 3-D numerical relativity using fixed mesh refinement”. In: *Class. Quant. Grav.* 21 (2004), pp. 1465–1488. DOI: 10.1088/0264-9381/21/6/014. arXiv: gr-qc/0310042 [gr-qc].

- [176] F. Löffler et al. “The Einstein Toolkit: A Community Computational Infrastructure for Relativistic Astrophysics”. In: *Class. Quant. Grav.* 29 (2012), p. 115001. DOI: 10.1088/0264-9381/29/11/115001. arXiv: 1111.3344 [gr-qc].
- [177] D. Pollney et al. “High accuracy binary black hole simulations with an extended wave zone”. In: *Phys. Rev. D* 83 (2011), p. 044045. DOI: 10.1103/PhysRevD.83.044045. arXiv: 0910.3803 [gr-qc].
- [178] C. Reisswig et al. “Three-Dimensional General-Relativistic Hydrodynamic Simulations of Binary Neutron Star Coalescence and Stellar Collapse with Multipatch Grids”. In: *Phys. Rev. D* 87.6 (2013), p. 064023. DOI: 10.1103/PhysRevD.87.064023. arXiv: 1212.1191 [astro-ph.HE].
- [179] P. Mösta et al. “GRHydro: A new open source general-relativistic magnetohydrodynamics code for the Einstein Toolkit”. In: *Class. Quant. Grav.* 31 (2014), p. 015005. DOI: 10.1088/0264-9381/31/1/015005. arXiv: 1304.5544 [gr-qc].
- [180] D. Radice, L. Rezzolla, and F. Galeazzi. “High-Order Fully General-Relativistic Hydrodynamics: new Approaches and Tests”. In: *Class. Quant. Grav.* 31 (2014), p. 075012. DOI: 10.1088/0264-9381/31/7/075012. arXiv: 1312.5004 [gr-qc].
- [181] B. Szilagyi, L. Lindblom, and M. A. Scheel. “Simulations of Binary Black Hole Mergers Using Spectral Methods”. In: *Phys. Rev. D* 80 (2009), p. 124010. DOI: 10.1103/PhysRevD.80.124010. arXiv: 0909.3557 [gr-qc].
- [182] M. Boyle et al. “The SXS Collaboration catalog of binary black hole simulations”. In: *Class. Quant. Grav.* 36.19 (2019), p. 195006. DOI: 10.1088/1361-6382/ab34e2. arXiv: 1904.04831 [gr-qc].
- [183] L. E. Kidder et al. “SpECTRE: A Task-based Discontinuous Galerkin Code for Relativistic Astrophysics”. In: *J. Comput. Phys.* 335 (2017), pp. 84–114. DOI: 10.1016/j.jcp.2016.12.059. arXiv: 1609.00098 [astro-ph.HE].
- [184] M. Thierfelder, S. Bernuzzi, and B. Brügmann. “Numerical relativity simulations of binary neutron stars”. In: *Phys. Rev. D* 84 (2011), p. 044012. DOI: 10.1103/PhysRevD.84.044012. arXiv: 1104.4751 [gr-qc].
- [185] D. Hilditch, A. Weyhausen, and B. Brügmann. “Pseudospectral method for gravitational wave collapse”. In: *Phys. Rev. D* 93.6 (2016), p. 063006. DOI: 10.1103/PhysRevD.93.063006. arXiv: 1504.04732 [gr-qc].

- [186] M. Bugner et al. “Solving 3D relativistic hydrodynamical problems with weighted essentially nonoscillatory discontinuous Galerkin methods”. In: *Phys. Rev. D* 94.8 (2016), p. 084004. DOI: 10.1103/PhysRevD.94.084004. arXiv: 1508.07147 [gr-qc].
- [187] K. Clough et al. “GRChombo : Numerical Relativity with Adaptive Mesh Refinement”. In: (2015). arXiv: 1503.03436 [gr-qc].
- [188] B. Daszuta et al. “GR-Athena++: Puncture Evolutions on Vertex-centered Oct-tree Adaptive Mesh Refinement”. In: *Astrophys. J. Supp.* 257.2 (2021), p. 25. DOI: 10.3847/1538-4365/ac157b. arXiv: 2101.08289 [gr-qc].
- [189] C. Messick et al. “Analysis framework for the prompt discovery of compact binary mergers in gravitational-wave data”. In: *prd* 95.4, 042001 (Feb. 2017), p. 042001. DOI: 10.1103/PhysRevD.95.042001. arXiv: 1604.04324 [astro-ph.IM].
- [190] S. Sachdev et al. “The GstLAL Search Analysis Methods for Compact Binary Mergers in Advanced LIGO’s Second and Advanced Virgo’s First Observing Runs”. In: (Jan. 2019). arXiv: 1901.08580 [gr-qc].
- [191] K. Cannon et al. “GstLAL: A software framework for gravitational wave discovery”. In: *SoftwareX* 14, 100680 (June 2021), p. 100680. DOI: 10.1016/j.softx.2021.100680. arXiv: 2010.05082 [astro-ph.IM].
- [192] A. H. Nitz et al. “Detecting binary compact-object mergers with gravitational waves: Understanding and Improving the sensitivity of the PyCBC search”. In: *Astrophys. J.* 849.2 (2017), p. 118. DOI: 10.3847/1538-4357/aa8f50. arXiv: 1705.01513 [gr-qc].
- [193] T. Dal Canton et al. “Implementing a search for aligned-spin neutron star-black hole systems with advanced ground based gravitational wave detectors”. In: *Phys. Rev. D* 90.8 (2014), p. 082004. DOI: 10.1103/PhysRevD.90.082004. arXiv: 1405.6731 [gr-qc].
- [194] T Adams et al. “Low-latency analysis pipeline for compact binary coalescences in the advanced gravitational wave detector era”. In: *Classical and Quantum Gravity* 33.17 (2016), p. 175012. DOI: 10.1088/0264-9381/33/17/175012. URL: <https://dx.doi.org/10.1088/0264-9381/33/17/175012>.

- [195] J. Luan et al. “Towards low-latency real-time detection of gravitational waves from compact binary coalescences in the era of advanced detectors”. In: *Phys. Rev. D* 85 (10 2012), p. 102002. DOI: 10.1103/PhysRevD.85.102002. URL: <https://link.aps.org/doi/10.1103/PhysRevD.85.102002>.
- [196] S. Klimenko et al. “Method for detection and reconstruction of gravitational wave transients with networks of advanced detectors”. In: *Phys. Rev. D* 93.4 (2016), p. 042004. DOI: 10.1103/PhysRevD.93.042004. arXiv: 1511.05999 [gr-qc].
- [197] N. J. Cornish and T. B. Littenberg. “BayesWave: Bayesian Inference for Gravitational Wave Bursts and Instrument Glitches”. In: *Class. Quant. Grav.* 32.13 (2015), p. 135012. DOI: 10.1088/0264-9381/32/13/135012. arXiv: 1410.3835 [gr-qc].
- [198] R. Lynch et al. “Information-theoretic approach to the gravitational-wave burst detection problem”. In: *Phys. Rev. D* 95.10 (2017), p. 104046. DOI: 10.1103/PhysRevD.95.104046. arXiv: 1511.05955 [gr-qc].
- [199] J. Veitch and A. Vecchio. “Bayesian coherent analysis of in-spiral gravitational wave signals with a detector network”. In: *Phys. Rev. D* 81 (2010), p. 062003. DOI: 10.1103/PhysRevD.81.062003. arXiv: 0911.3820 [astro-ph.CO].
- [200] B. P. Abbott et al. “A guide to LIGO-Virgo detector noise and extraction of transient gravitational-wave signals”. In: (2019). arXiv: 1908.11170 [gr-qc].
- [201] D. Foreman-Mackey et al. “emcee: The MCMC Hammer”. In: *passp* 125.925 (Mar. 2013), p. 306. DOI: 10.1086/670067. arXiv: 1202.3665 [astro-ph.IM].
- [202] A. Gelman and D. B. Rubin. “Inference from Iterative Simulation Using Multiple Sequences”. In: *Statistical Science* 7.4 (1992), pp. 457–472. DOI: 10.1214/ss/1177011136. URL: <https://doi.org/10.1214/ss/1177011136>.
- [203] W. D. Pozzo and J. Veitch. <https://github.com/johnveitch/cpnest>. Parallel nested sampling algorithm in python. DOI: 10.5281/zenodo.835874.
- [204] J. S. Speagle. “dynesty: a dynamic nested sampling package for estimating Bayesian posteriors and evidences”. In: *Monthly Notices of the Royal Astronomical Society* 493.3 (2020), 3132–3158. ISSN: 1365-2966. DOI: 10.1093/mnras/staa278. URL: <http://dx.doi.org/10.1093/mnras/staa278>.

- [205] B. P. Abbott et al. “Observation of Gravitational Waves from a Binary Black Hole Merger”. In: *Phys. Rev. Lett.* 116.6 (2016), p. 061102. DOI: 10.1103/PhysRevLett.116.061102. arXiv: 1602.03837 [gr-qc].
- [206] B. P. Abbott et al. “Astrophysical Implications of the Binary Black-Hole Merger GW150914”. In: *Astrophys. J.* 818.2 (2016), p. L22. DOI: 10.3847/2041-8205/818/2/L22. arXiv: 1602.03846 [astro-ph.HE].
- [207] A. Goldstein et al. “An Ordinary Short Gamma-Ray Burst with Extraordinary Implications: Fermi-GBM Detection of GRB 170817A”. In: *Astrophys. J.* 848.2 (2017), p. L14. DOI: 10.3847/2041-8213/aa8f41. arXiv: 1710.05446 [astro-ph.HE].
- [208] V. Savchenko et al. “INTEGRAL Detection of the First Prompt Gamma-Ray Signal Coincident with the Gravitational-wave Event GW170817”. In: *Astrophys. J.* 848.2 (2017), p. L15. DOI: 10.3847/2041-8213/aa8f94. arXiv: 1710.05449 [astro-ph.HE].
- [209] D. A. Coulter et al. “Swope Supernova Survey 2017a (SSS17a), the Optical Counterpart to a Gravitational Wave Source”. In: *Science* (2017). [Science358,1556(2017)]. DOI: 10.1126/science.aap9811. arXiv: 1710.05452 [astro-ph.HE].
- [210] R. Chornock et al. “The Electromagnetic Counterpart of the Binary Neutron Star Merger LIGO/VIRGO GW170817. IV. Detection of Near-infrared Signatures of r-process Nucleosynthesis with Gemini-South”. In: *Astrophys. J.* 848.2 (2017), p. L19. DOI: 10.3847/2041-8213/aa905c. arXiv: 1710.05454 [astro-ph.HE].
- [211] M. Nicholl et al. “The Electromagnetic Counterpart of the Binary Neutron Star Merger LIGO/VIRGO GW170817. III. Optical and UV Spectra of a Blue Kilonova From Fast Polar Ejecta”. In: *Astrophys. J.* 848 (2017), p. L18. DOI: 10.3847/2041-8213/aa9029. arXiv: 1710.05456 [astro-ph.HE].
- [212] P. S. Cowperthwaite et al. “The Electromagnetic Counterpart of the Binary Neutron Star Merger LIGO/Virgo GW170817. II. UV, Optical, and Near-infrared Light Curves and Comparison to Kilonova Models”. In: *Astrophys. J.* 848.2 (2017), p. L17. DOI: 10.3847/2041-8213/aa8fc7. arXiv: 1710.05840 [astro-ph.HE].

- [213] E. Pian et al. “Spectroscopic identification of r-process nucleosynthesis in a double neutron star merger”. In: *Nature* (2017). DOI: 10.1038/nature24298. arXiv: 1710.05858 [astro-ph.HE].
- [214] S. J. Smartt et al. “A kilonova as the electromagnetic counterpart to a gravitational-wave source”. In: *Nature* (2017). DOI: 10.1038/nature24303. arXiv: 1710.05841 [astro-ph.HE].
- [215] N. R. Tanvir et al. “The Emergence of a Lanthanide-Rich Kilonova Following the Merger of Two Neutron Stars”. In: *Astrophys. J.* 848 (2017), p. L27. DOI: 10.3847/2041-8213/aa90b6. arXiv: 1710.05455 [astro-ph.HE].
- [216] M. Tanaka et al. “Kilonova from post-merger ejecta as an optical and near-infrared counterpart of GW170817”. In: *Publ. Astron. Soc. Jap.* (2017). DOI: 10.1093/pasj/psx121. arXiv: 1710.05850 [astro-ph.HE].
- [217] S. Valenti et al. “The discovery of the electromagnetic counterpart of GW170817: kilonova AT 2017gfo/DLT17ck”. In: *Astrophys. J.* 848.2 (2017), p. L24. DOI: 10.3847/2041-8213/aa8edf. arXiv: 1710.05854 [astro-ph.HE].
- [218] M. Nynka et al. “Fading of the X-Ray Afterglow of Neutron Star Merger GW170817/GRB 170817A at 260 Days”. In: *Astrophys. J. Lett.* 862.2 (2018), p. L19. DOI: 10.3847/2041-8213/aad32d. arXiv: 1805.04093 [astro-ph.HE].
- [219] A. Hajela et al. “Two Years of Nonthermal Emission from the Binary Neutron Star Merger GW170817: Rapid Fading of the Jet Afterglow and First Constraints on the Kilonova Fastest Ejecta”. In: *Astrophys. J. Lett.* 886.1 (2019), p. L17. DOI: 10.3847/2041-8213/ab5226. arXiv: 1909.06393 [astro-ph.HE].
- [220] D. Radice et al. “Probing Extreme-Density Matter with Gravitational Wave Observations of Binary Neutron Star Merger Remnants”. In: *Astrophys. J.* 842.2 (2017), p. L10. DOI: 10.3847/2041-8213/aa775f. arXiv: 1612.06429 [astro-ph.HE].
- [221] B. Margalit and B. D. Metzger. “Constraining the Maximum Mass of Neutron Stars From Multi-Messenger Observations of GW170817”. In: *Astrophys. J.* 850.2 (2017), p. L19. DOI: 10.3847/2041-8213/aa991c. arXiv: 1710.05938 [astro-ph.HE].
- [222] A. Bauswein et al. “Neutron-star radius constraints from GW170817 and future detections”. In: *Astrophys. J.* 850.2 (2017), p. L34. DOI: 10.3847/2041-8213/aa9994. arXiv: 1710.06843 [astro-ph.HE].

- [223] D. Radice et al. “GW170817: Joint Constraint on the Neutron Star Equation of State from Multimessenger Observations”. In: *Astrophys. J.* 852.2 (2018), p. L29. DOI: 10.3847/2041-8213/aaa402. arXiv: 1711.03647 [astro-ph.HE].
- [224] T. Dietrich et al. “High-resolution numerical relativity simulations of spinning binary neutron star mergers”. In: *2018 26th Euromicro International Conference on Parallel, Distributed and Network-based Processing (PDP)*. 2018, pp. 682–689. DOI: 10.1109/PDP2018.2018.00113. arXiv: 1803.07965 [gr-qc]. URL: <https://inspirehep.net/record/1663472/files/1803.07965.pdf>.
- [225] M. Breschi et al. “AT2017gfo: Bayesian inference and model selection of multicomponent kilonovae and constraints on the neutron star equation of state”. In: *Mon. Not. Roy. Astron. Soc.* 505.2 (2021), pp. 1661–1677. DOI: 10.1093/mnras/stab1287. arXiv: 2101.01201 [astro-ph.HE].
- [226] B. P. Abbott et al. “A gravitational-wave standard siren measurement of the Hubble constant”. In: *Nature* 551.7678 (2017), pp. 85–88. DOI: 10.1038/nature24471. arXiv: 1710.05835 [astro-ph.CO].
- [227] R. Abbott et al. “GWTC-2: Compact Binary Coalescences Observed by LIGO and Virgo During the First Half of the Third Observing Run”. In: *Phys. Rev. X* 11 (2021), p. 021053. DOI: 10.1103/PhysRevX.11.021053. arXiv: 2010.14527 [gr-qc].
- [228] R. Abbott et al. “GW190412: Observation of a Binary-Black-Hole Coalescence with Asymmetric Masses”. In: *Phys. Rev. D* 102.4 (2020), p. 043015. DOI: 10.1103/PhysRevD.102.043015. arXiv: 2004.08342 [astro-ph.HE].
- [229] R. Abbott et al. “GW190521: A Binary Black Hole Merger with a Total Mass of $150 M_{\odot}$ ”. In: *Phys. Rev. Lett.* 125.10 (2020), p. 101102. DOI: 10.1103/PhysRevLett.125.101102. arXiv: 2009.01075 [gr-qc].
- [230] R. Abbott et al. “Properties and astrophysical implications of the 150 Msun binary black hole merger GW190521”. In: *Astrophys. J. Lett.* 900 (2020), p. L13. DOI: 10.3847/2041-8213/aba493. arXiv: 2009.01190 [astro-ph.HE].
- [231] E. González et al. “Intermediate-mass Black Holes from High Massive-star Binary Fractions in Young Star Clusters”. In: *Astrophys. J. Lett.* 908.2 (2021), p. L29. DOI: 10.3847/2041-8213/abdf5b. arXiv: 2012.10497 [astro-ph.HE].

- [232] K. Belczynski. “The most ordinary formation of the most unusual double black hole merger”. In: *Astrophys. J. Lett.* 905.2 (2020), p. L15. DOI: 10.3847/2041-8213/abcbf1. arXiv: 2009.13526 [astro-ph.HE].
- [233] M. Mapelli et al. “Hierarchical black hole mergers in young, globular and nuclear star clusters: the effect of metallicity, spin and cluster properties”. In: *Mon. Not. R. Astron. Soc.* 505.1 (2021), pp. 339–358. DOI: 10.1093/mnras/stab1334. arXiv: 2103.05016 [astro-ph.HE].
- [234] M. A. Sedda et al. “Breaching the limit: formation of GW190521-like and IMBH mergers in young massive clusters”. In: (May 2021). arXiv: 2105.07003 [astro-ph.GA].
- [235] H. Tagawa et al. “Signatures of Hierarchical Mergers in Black Hole Spin and Mass distribution”. In: (Apr. 2021). arXiv: 2104.09510 [astro-ph.HE].
- [236] M. Dall’Amico et al. “GW190521 formation via three-body encounters in young massive star clusters”. In: (May 2021). arXiv: 2105.12757 [astro-ph.HE].
- [237] G. Fragione, A. Loeb, and F. A. Rasio. “On the Origin of GW190521-like Events from Repeated Black Hole Mergers in Star Clusters”. In: *Astrophys. J. Lett.* 902.1, L26 (Oct. 2020), p. L26. DOI: 10.3847/2041-8213/abbc0a. arXiv: 2009.05065 [astro-ph.GA].
- [238] V. Gayathri et al. “Eccentricity estimate for black hole mergers with numerical relativity simulations”. In: *Nature Astron.* 6.3 (2022), pp. 344–349. DOI: 10.1038/s41550-021-01568-w. arXiv: 2009.05461 [astro-ph.HE].
- [239] I. M. Romero-Shaw et al. “GW190521: orbital eccentricity and signatures of dynamical formation in a binary black hole merger signal”. In: *Astrophys. J. Lett.* 903.1 (2020), p. L5. DOI: 10.3847/2041-8213/abbe26. arXiv: 2009.04771 [astro-ph.HE].
- [240] J. C. Bustillo et al. “Confusing Head-On Collisions with Precessing Intermediate-Mass Binary Black Hole Mergers”. In: *Phys. Rev. Lett.* 126.20 (2021), p. 201101. DOI: 10.1103/PhysRevLett.126.201101. arXiv: 2009.01066 [gr-qc].
- [241] M. Shibata et al. “Alternative possibility of GW190521: Gravitational waves from high-mass black hole-disk systems”. In: *Phys. Rev. D* 103.6 (2021), p. 063037. DOI: 10.1103/PhysRevD.103.063037. arXiv: 2101.05440 [astro-ph.HE].

-
- [242] A. H. Nitz and C. D. Capano. “GW190521 may be an intermediate mass ratio inspiral”. In: *Astrophys. J. Lett.* 907.1 (2021), p. L9. DOI: 10.3847/2041-8213/abccc5. arXiv: 2010.12558 [astro-ph.HE].
- [243] H. Estellés et al. “A detailed analysis of GW190521 with phenomenological waveform models”. In: (May 2021). arXiv: 2105.06360 [gr-qc].
- [244] R. Dudi et al. “Relevance of tidal effects and post-merger dynamics for binary neutron star parameter estimation”. In: (2018). arXiv: 1808.09749 [gr-qc].
- [245] A. Samajdar and T. Dietrich. “Waveform systematics for binary neutron star gravitational wave signals: effects of the point-particle baseline and tidal descriptions”. In: *Phys. Rev.* D98.12 (2018), p. 124030. DOI: 10.1103/PhysRevD.98.124030. arXiv: 1810.03936 [gr-qc].
- [246] A. Samajdar and T. Dietrich. “Waveform systematics for binary neutron star gravitational wave signals: Effects of spin, precession, and the observation of electromagnetic counterparts”. In: *Phys. Rev.* D100.2 (2019), p. 024046. DOI: 10.1103/PhysRevD.100.024046. arXiv: 1905.03118 [gr-qc].
- [247] F. Messina et al. “Quasi-5.5PN TaylorF2 approximant for compact binaries: point-mass phasing and impact on the tidal polarizability inference”. In: *Phys. Rev.* D99 (2019), p. 124051. DOI: 10.1103/PhysRevD.99.124051. arXiv: 1904.09558 [gr-qc].
- [248] M. Agathos et al. “Inferring Prompt Black-Hole Formation in Neutron Star Mergers from Gravitational-Wave Data”. In: *Phys. Rev.* D101.4 (2020), p. 044006. DOI: 10.1103/PhysRevD.101.044006. arXiv: 1908.05442 [gr-qc].
- [249] T. Narikawa et al. “Reanalysis of the binary neutron star mergers GW170817 and GW190425 using numerical-relativity calibrated waveform models”. In: *Phys. Rev. Res.* 2.4 (2020), p. 043039. DOI: 10.1103/PhysRevResearch.2.043039. arXiv: 1910.08971 [gr-qc].
- [250] A. Chen et al. “Distinguishing high-mass binary neutron stars from binary black holes with second- and third-generation gravitational wave observatories”. In: *Phys. Rev. D* 101.10 (2020), p. 103008. DOI: 10.1103/PhysRevD.101.103008. arXiv: 2001.11470 [astro-ph.HE].

- [251] R. Gamba et al. “Waveform systematics in the gravitational-wave inference of tidal parameters and equation of state from binary neutron star signals”. In: *Phys. Rev. D* 103.12 (2021), p. 124015. DOI: 10.1103/PhysRevD.103.124015. arXiv: 2009.08467 [gr-qc].
- [252] N. Kunert et al. “Quantifying modeling uncertainties when combining multiple gravitational-wave detections from binary neutron star sources”. In: *Phys. Rev. D* 105.6 (2022), p. L061301. DOI: 10.1103/PhysRevD.105.L061301. arXiv: 2110.11835 [astro-ph.HE].
- [253] B. Sathyaprakash et al. “Scientific Potential of Einstein Telescope”. In: *46th Rencontres de Moriond on Gravitational Waves and Experimental Gravity*. Aug. 2011, pp. 127–136. arXiv: 1108.1423 [gr-qc].
- [254] B. P. Abbott et al. “Prospects for Observing and Localizing Gravitational-Wave Transients with Advanced LIGO, Advanced Virgo and KAGRA”. In: *Living Rev. Rel.* 21 (2018). [Living Rev. Rel.19,1(2016)], p. 3. DOI: 10.1007/s41114-018-0012-9, 10.1007/lrr-2016-1. arXiv: 1304.0670 [gr-qc].
- [255] G. M. Harry. “Advanced LIGO: The next generation of gravitational wave detectors”. In: *Class. Quant. Grav.* 27 (2010), p. 084006. DOI: 10.1088/0264-9381/27/8/084006.
- [256] M. Maggiore et al. “Science Case for the Einstein Telescope”. In: *JCAP* 03 (2020), p. 050. DOI: 10.1088/1475-7516/2020/03/050. arXiv: 1912.02622 [astro-ph.CO].
- [257] M. Pürrer and C.-J. Haster. “Gravitational waveform accuracy requirements for future ground-based detectors”. In: *Phys. Rev. Res.* 2.2 (2020), p. 023151. DOI: 10.1103/PhysRevResearch.2.023151. arXiv: 1912.10055 [gr-qc].
- [258] S. Akcay, R. Gamba, and S. Bernuzzi. “A hybrid post-Newtonian – effective-one-body scheme for spin-precessing compact-binary waveforms”. In: *Phys. Rev. D* 103.2 (2021), p. 024014. DOI: 10.1103/PhysRevD.103.024014. arXiv: 2005.05338 [gr-qc].
- [259] R. Gamba et al. “Effective-one-body waveforms for precessing coalescing compact binaries with post-Newtonian twist”. In: *Phys. Rev. D* 106.2 (2022), p. 024020. DOI: 10.1103/PhysRevD.106.024020. arXiv: 2111.03675 [gr-qc].

- [260] R. Gamba et al. “GW190521 as a dynamical capture of two nonspinning black holes”. In: *Nat. Astron.* (2022). DOI: 10.1038/s41550-022-01813-w. arXiv: 2106.05575 [gr-qc].
- [261] A. Bonino et al. “Inferring eccentricity evolution from observations of coalescing binary black holes”. In: *Phys. Rev. D* 107.6 (2023), p. 064024. DOI: 10.1103/PhysRevD.107.064024. arXiv: 2207.10474 [gr-qc].
- [262] D. A. Godzieba et al. “Updated universal relations for tidal deformabilities of neutron stars from phenomenological equations of state”. In: *Phys. Rev. D* 103.6 (2021), p. 063036. DOI: 10.1103/PhysRevD.103.063036. arXiv: 2012.12151 [astro-ph.HE].
- [263] M. Breschi et al. “Kilohertz Gravitational Waves from Binary Neutron Star Mergers: Inference of Postmerger Signals with the Einstein Telescope”. In: (May 2022). arXiv: 2205.09979 [gr-qc].
- [264] R. Gamba and S. Bernuzzi. “Resonant tides in binary neutron star mergers: Analytical-numerical relativity study”. In: *Phys. Rev. D* 107.4 (2023), p. 044014. DOI: 10.1103/PhysRevD.107.044014. arXiv: 2207.13106 [gr-qc].
- [265] T. Chu, H. P. Pfeiffer, and M. A. Scheel. “High accuracy simulations of black hole binaries: spins anti-aligned with the orbital angular momentum”. In: *Phys. Rev. D* 80 (2009), p. 124051. DOI: 10.1103/PhysRevD.80.124051. arXiv: 0909.1313 [gr-qc].
- [266] G. Lovelace, M. Scheel, and B. Szilagyi. “Simulating merging binary black holes with nearly extremal spins”. In: *Phys. Rev. D* 83 (2011), p. 024010. DOI: 10.1103/PhysRevD.83.024010. arXiv: 1010.2777 [gr-qc].
- [267] G. Lovelace et al. “Accurate gravitational waveforms for binary-black-hole mergers with nearly extremal spins”. In: *Class. Quant. Grav.* 29 (2012), p. 045003. DOI: 10.1088/0264-9381/29/4/045003. arXiv: 1110.2229 [gr-qc].
- [268] L. T. Buchman et al. “Simulations of non-equal mass black hole binaries with spectral methods”. In: *Phys. Rev. D* 86 (2012), p. 084033. DOI: 10.1103/PhysRevD.86.084033. arXiv: 1206.3015 [gr-qc].
- [269] D. A. Hemberger et al. “Final spin and radiated energy in numerical simulations of binary black holes with equal masses and equal, aligned or anti-aligned spins”. In: *Phys. Rev. D* 88 (2013), p. 064014. DOI: 10.1103/PhysRevD.88.064014. arXiv: 1305.5991 [gr-qc].

- [270] M. A. Scheel et al. “Improved methods for simulating nearly extremal binary black holes”. In: *Class. Quant. Grav.* 32.10 (2015), p. 105009. DOI: 10.1088/0264-9381/32/10/105009. arXiv: 1412.1803 [gr-qc].
- [271] J. Blackman et al. “Fast and Accurate Prediction of Numerical Relativity Waveforms from Binary Black Hole Coalescences Using Surrogate Models”. In: *Phys. Rev. Lett.* 115.12 (2015), p. 121102. DOI: 10.1103/PhysRevLett.115.121102. arXiv: 1502.07758 [gr-qc].
- [272] G. Lovelace et al. “Nearly extremal apparent horizons in simulations of merging black holes”. In: *Class. Quant. Grav.* 32.6 (2015), p. 065007. DOI: 10.1088/0264-9381/32/6/065007. arXiv: 1411.7297 [gr-qc].
- [273] A. H. Mroue et al. “A catalog of 174 binary black-hole simulations for gravitational-wave astronomy”. In: *Phys.Rev.Lett.* 111 (2013), p. 241104. DOI: 10.1103/PhysRevLett.111.241104. arXiv: 1304.6077 [gr-qc].
- [274] P. Kumar et al. “Accuracy and precision of gravitational-wave models of inspiraling neutron star-black hole binaries with spin: Comparison with matter-free numerical relativity in the low-frequency regime”. In: *Phys. Rev.* D92.10 (2015), p. 102001. DOI: 10.1103/PhysRevD.92.102001. arXiv: 1507.00103 [gr-qc].
- [275] T. Chu et al. “On the accuracy and precision of numerical waveforms: Effect of waveform extraction methodology”. In: *Class. Quant. Grav.* 33.16 (2016), p. 165001. DOI: 10.1088/0264-9381/33/16/165001. arXiv: 1512.06800 [gr-qc].
- [276] *SXS Gravitational Waveform Database*. URL: <https://data.black-holes.org/waveforms/index.html>.
- [277] T. Dietrich et al. “CoRe database of binary neutron star merger waveforms”. In: *Class. Quant. Grav.* 35.24 (2018), 24LT01. DOI: 10.1088/1361-6382/aaebc0. arXiv: 1806.01625 [gr-qc].
- [278] A. Gonzalez et al. “Second release of the CoRe database of binary neutron star merger waveforms”. In: (Oct. 2022). arXiv: 2210.16366 [gr-qc].
- [279] T. Damour, B. R. Iyer, and A. Nagar. “Improved resummation of post-Newtonian multipolar waveforms from circularized compact binaries”. In: *Phys. Rev.* D79 (2009), p. 064004. DOI: 10.1103/PhysRevD.79.064004. arXiv: 0811.2069 [gr-qc].

- [280] T. Damour, P. Jaranowski, and G. Schäfer. “Effective one body approach to the dynamics of two spinning black holes with next-to-leading order spin-orbit coupling”. In: *Phys.Rev.* D78 (2008), p. 024009. DOI: 10.1103/PhysRevD.78.024009. arXiv: 0803.0915 [gr-qc].
- [281] E. Barausse and A. Buonanno. “An Improved effective-one-body Hamiltonian for spinning black-hole binaries”. In: *Phys.Rev.* D81 (2010), p. 084024. DOI: 10.1103/PhysRevD.81.084024. arXiv: 0912.3517 [gr-qc].
- [282] T. Damour. “Gravitational Self Force in a Schwarzschild Background and the Effective One Body Formalism”. In: *Phys. Rev.* D81 (2010), p. 024017. DOI: 10.1103/PhysRevD.81.024017. arXiv: 0910.5533 [gr-qc].
- [283] J. Vines. “Scattering of two spinning black holes in post-Minkowskian gravity, to all orders in spin, and effective-one-body mappings”. In: *Class. Quant. Grav.* 35.8 (2018), p. 084002. DOI: 10.1088/1361-6382/aaa3a8. arXiv: 1709.06016 [gr-qc].
- [284] A. Nagar and P. Retegno. “Efficient effective one body time-domain gravitational waveforms”. In: *Phys. Rev.* D99.2 (2019), p. 021501. DOI: 10.1103/PhysRevD.99.021501. arXiv: 1805.03891 [gr-qc].
- [285] A. Nagar et al. “A Multipolar Effective One Body Model for Non-Spinning Black Hole Binaries”. In: (2019). arXiv: 1904.09550 [gr-qc].
- [286] G. Riemenschneider et al. “Assessment of consistent next-to-quasicircular corrections and postadiabatic approximation in effective-one-body multipolar waveforms for binary black hole coalescences”. In: *Phys. Rev. D* 104.10 (2021), p. 104045. DOI: 10.1103/PhysRevD.104.104045. arXiv: 2104.07533 [gr-qc].
- [287] S. Foffa et al. “Static two-body potential at fifth post-Newtonian order”. In: *Phys. Rev. Lett.* 122.24 (2019), p. 241605. DOI: 10.1103/PhysRevLett.122.241605. arXiv: 1902.10571 [gr-qc].
- [288] J. Blümlein, A. Maier, and P. Marquard. “Five-Loop Static Contribution to the Gravitational Interaction Potential of Two Point Masses”. In: *Phys. Lett. B* 800 (2020), p. 135100. DOI: 10.1016/j.physletb.2019.135100. arXiv: 1902.11180 [gr-qc].

- [289] D. Bini, T. Damour, and A. Geralico. “Novel approach to binary dynamics: application to the fifth post-Newtonian level”. In: *Phys. Rev. Lett.* 123.23 (2019), p. 231104. DOI: 10.1103/PhysRevLett.123.231104. arXiv: 1909.02375 [gr-qc].
- [290] D. Bini, T. Damour, and A. Geralico. “Binary dynamics at the fifth and fifth-and-a-half post-Newtonian orders”. In: *Phys. Rev. D* 102.2 (2020), p. 024062. DOI: 10.1103/PhysRevD.102.024062. arXiv: 2003.11891 [gr-qc].
- [291] A. Nagar. “Effective one body Hamiltonian of two spinning black-holes with next-to-next-to-leading order spin-orbit coupling”. In: *Phys.Rev.* D84 (2011), p. 084028. DOI: 10.1103/PhysRevD.84.084028. arXiv: 1106.4349 [gr-qc].
- [292] P. Rettegno et al. “Comparing Effective One Body Hamiltonians for spin-aligned coalescing binaries”. In: (2019). arXiv: 1911.10818 [gr-qc].
- [293] E. Barausse, E. Racine, and A. Buonanno. “Hamiltonian of a spinning test-particle in curved spacetime”. In: *Phys. Rev.* D80 (2009), p. 104025. DOI: 10.1103/PhysRevD.80.104025. arXiv: 0907.4745 [gr-qc].
- [294] E. Barausse and A. Buonanno. “Extending the effective-one-body Hamiltonian of black-hole binaries to include next-to-next-to-leading spin-orbit couplings”. In: *Phys.Rev.* D84 (2011), p. 104027. DOI: 10.1103/PhysRevD.84.104027. arXiv: 1107.2904 [gr-qc].
- [295] S. Balmelli and P. Jetzer. “Effective-one-body Hamiltonian with next-to-leading order spin-spin coupling for two nonprecessing black holes with aligned spins”. In: *Phys. Rev.* D87.12 (2013). [Erratum: *Phys. Rev.* D90,no.8,089905(2014)], p. 124036. DOI: 10.1103/PhysRevD.87.124036, 10.1103/PhysRevD.90.089905. arXiv: 1305.5674 [gr-qc].
- [296] T. Damour and A. Nagar. “New effective-one-body description of coalescing nonprecessing spinning black-hole binaries”. In: *Phys.Rev.* D90.4 (2014), p. 044018. DOI: 10.1103/PhysRevD.90.044018. arXiv: 1406.6913 [gr-qc].
- [297] T. Damour and G. Schafer. “Higher-order relativistic periastron advances and binary pulsars.” In: *Nuovo Cimento B Serie* 101B.2 (Jan. 1988), pp. 127–176. DOI: 10.1007/BF02828697.

- [298] T. Damour, P. Jaranowski, and G. Schäfer. “Hamiltonian of two spinning compact bodies with next-to-leading order gravitational spin-orbit coupling”. In: *Phys. Rev. D* 77 (2008), p. 064032. DOI: 10.1103/PhysRevD.77.064032. arXiv: 0711.1048 [gr-qc].
- [299] J. Hartung and J. Steinhoff. “Next-to-next-to-leading order post-Newtonian spin-orbit Hamiltonian for self-gravitating binaries”. In: *Annalen Phys.* 523 (2011), pp. 783–790. DOI: 10.1002/andp.201100094. arXiv: 1104.3079 [gr-qc].
- [300] R. A. Porto. “Post-Newtonian corrections to the motion of spinning bodies in NRGR”. In: *Phys. Rev. D* 73 (2006), p. 104031. DOI: 10.1103/PhysRevD.73.104031. arXiv: gr-qc/0511061.
- [301] J. Hartung, J. Steinhoff, and G. Schäfer. “Next-to-next-to-leading order post-Newtonian linear-in-spin binary Hamiltonians”. In: *Annalen Phys.* 525 (2013), pp. 359–394. DOI: 10.1002/andp.201200271. arXiv: 1302.6723 [gr-qc].
- [302] M. Levi and J. Steinhoff. “Next-to-next-to-leading order gravitational spin-squared potential via the effective field theory for spinning objects in the post-Newtonian scheme”. In: *JCAP* 1601 (2016), p. 008. DOI: 10.1088/1475-7516/2016/01/008. arXiv: 1506.05794 [gr-qc].
- [303] M. Levi and J. Steinhoff. “Complete conservative dynamics for inspiralling compact binaries with spins at fourth post-Newtonian order”. In: (2016). arXiv: 1607.04252 [gr-qc].
- [304] M. Khalil. “Gravitational spin-orbit dynamics at the fifth-and-a-half post-Newtonian order”. In: *Phys. Rev. D* 104.12 (2021), p. 124015. DOI: 10.1103/PhysRevD.104.124015. arXiv: 2110.12813 [gr-qc].
- [305] J. Steinhoff, S. Hergt, and G. Schäfer. “On the next-to-leading order gravitational spin(1)-spin(2) dynamics”. In: *Phys. Rev. D* 77 (2008), p. 081501. DOI: 10.1103/PhysRevD.77.081501. arXiv: 0712.1716 [gr-qc].
- [306] J. Steinhoff, S. Hergt, and G. Schäfer. “Spin-squared Hamiltonian of next-to-leading order gravitational interaction”. In: *Phys. Rev. D* 78 (2008), p. 101503. DOI: 10.1103/PhysRevD.78.101503. arXiv: 0809.2200 [gr-qc].
- [307] A. Taracchini et al. “Prototype effective-one-body model for nonprecessing spinning inspiral-merger-ringdown waveforms”. In: *Phys. Rev. D* 86 (2012), p. 024011. DOI: 10.1103/PhysRevD.86.024011. arXiv: 1202.0790 [gr-qc].

-
- [308] T. Damour and A. Nagar. “Faithful Effective-One-Body waveforms of small-mass-ratio coalescing black-hole binaries”. In: *Phys. Rev. D* 76 (2007), p. 064028. DOI: 10.1103/PhysRevD.76.064028. arXiv: 0705.2519 [gr-qc].
- [309] T. Damour and A. Nagar. “Comparing Effective-One-Body gravitational waveforms to accurate numerical data”. In: *Phys. Rev. D* 77 (2008), p. 024043. DOI: 10.1103/PhysRevD.77.024043. arXiv: 0711.2628 [gr-qc].
- [310] A. Nagar and A. Shah. “Factorization and resummation: A new paradigm to improve gravitational wave amplitudes”. In: *Phys. Rev. D* 94.10 (2016), p. 104017. DOI: 10.1103/PhysRevD.94.104017. arXiv: 1606.00207 [gr-qc].
- [311] F. Messina, A. Maldarella, and A. Nagar. “Factorization and resummation: A new paradigm to improve gravitational wave amplitudes. II: the higher multipolar modes”. In: *Phys. Rev. D* 97.8 (2018), p. 084016. DOI: 10.1103/PhysRevD.97.084016. arXiv: 1801.02366 [gr-qc].
- [312] E. Berti, V. Cardoso, and C. M. Will. “On gravitational-wave spectroscopy of massive black holes with the space interferometer LISA”. In: *Phys. Rev. D* 73 (2006), p. 064030. DOI: 10.1103/PhysRevD.73.064030. arXiv: gr-qc/0512160.
- [313] E. Berti, V. Cardoso, and A. O. Starinets. “Quasinormal modes of black holes and black branes”. In: *Class. Quant. Grav.* 26 (2009), p. 163001. DOI: 10.1088/0264-9381/26/16/163001. arXiv: 0905.2975 [gr-qc].
- [314] J. G. Baker et al. “Mergers of non-spinning black-hole binaries: Gravitational radiation characteristics”. In: *Phys. Rev. D* 78 (2008), p. 044046. DOI: 10.1103/PhysRevD.78.044046. arXiv: 0805.1428 [gr-qc].
- [315] E. Barausse, V. Morozova, and L. Rezzolla. “On the mass radiated by coalescing black-hole binaries”. In: (2012). arXiv: 1206.3803 [gr-qc].
- [316] A. Taracchini et al. “Effective-one-body model for black-hole binaries with generic mass ratios and spins”. In: *Phys. Rev. D* 89.6 (2014), p. 061502. DOI: 10.1103/PhysRevD.89.061502. arXiv: 1311.2544 [gr-qc].
- [317] W. Del Pozzo and A. Nagar. “Analytic family of post-merger template waveforms”. In: *Phys. Rev. D* 95.12 (2017), p. 124034. DOI: 10.1103/PhysRevD.95.124034. arXiv: 1606.03952 [gr-qc].
- [318] F. Hofmann, E. Barausse, and L. Rezzolla. “The final spin from binary black holes in quasi-circular orbits”. In: *Astrophys. J.* 825.2 (2016), p. L19. DOI: 10.3847/2041-8205/825/2/L19. arXiv: 1605.01938 [gr-qc].

-
- [319] X. Jiménez-Forteza et al. “Hierarchical data-driven approach to fitting numerical relativity data for nonprecessing binary black holes with an application to final spin and radiated energy”. In: *Phys. Rev. D* 95.6 (2017), p. 064024. DOI: 10.1103/PhysRevD.95.064024. arXiv: 1611.00332 [gr-qc].
- [320] A. Nagar, T. Damour, and A. Tartaglia. “Binary black hole merger in the extreme mass ratio limit”. In: *Class. Quant. Grav.* 24 (2007), S109–S124. DOI: 10.1088/0264-9381/24/12/S08. arXiv: gr-qc/0612096.
- [321] T. Damour et al. “Faithful Effective-One-Body waveforms of equal-mass coalescing black-hole binaries”. In: *Phys. Rev. D* 77 (2008), p. 084017. DOI: 10.1103/PhysRevD.77.084017. arXiv: 0712.3003 [gr-qc].
- [322] T. Damour et al. “Accurate Effective-One-Body waveforms of inspiralling and coalescing black-hole binaries”. In: *Phys. Rev. D* 78 (2008), p. 044039. DOI: 10.1103/PhysRevD.78.044039. arXiv: 0803.3162 [gr-qc].
- [323] T. Damour and A. Nagar. “An improved analytical description of inspiralling and coalescing black-hole binaries”. In: *Phys. Rev. D* 79 (2009), p. 081503. DOI: 10.1103/PhysRevD.79.081503. arXiv: 0902.0136 [gr-qc].
- [324] A. Albertini et al. “Waveforms and fluxes: Towards a self-consistent effective one body waveform model for nonprecessing, coalescing black-hole binaries for third generation detectors”. In: (Nov. 2021). arXiv: 2111.14149 [gr-qc].
- [325] T. Damour, A. Nagar, and S. Bernuzzi. “Improved effective-one-body description of coalescing nonspinning black-hole binaries and its numerical-relativity completion”. In: *Phys. Rev. D* 87 (2013), p. 084035. DOI: 10.1103/PhysRevD.87.084035. arXiv: 1212.4357 [gr-qc].
- [326] M. Pürrer. “Frequency domain reduced order models for gravitational waves from aligned-spin compact binaries”. In: *Class. Quant. Grav.* 31.19 (2014), p. 195010. DOI: 10.1088/0264-9381/31/19/195010. arXiv: 1402.4146 [gr-qc].
- [327] R. Smith et al. “Fast and accurate inference on gravitational waves from precessing compact binaries”. In: *Phys. Rev. D* 94.4 (2016), p. 044031. DOI: 10.1103/PhysRevD.94.044031. arXiv: 1604.08253 [gr-qc].
- [328] A. Nagar et al. “Nonlinear-in-spin effects in effective-one-body waveform models of spin-aligned, inspiralling, neutron star binaries”. In: *Phys. Rev. D* 99 (2019), p. 044007. DOI: 10.1103/PhysRevD.99.044007. arXiv: 1812.07923 [gr-qc].

- [329] T. Damour, B. R. Iyer, and B. Sathyaprakash. “Frequency domain P approximant filters for time truncated inspiral gravitational wave signals from compact binaries”. In: *Phys.Rev.* D62 (2000), p. 084036. DOI: 10.1103/PhysRevD.62.084036. arXiv: gr-qc/0001023 [gr-qc].
- [330] T. Damour, B. R. Iyer, and B. S. Sathyaprakash. “A Comparison of search templates for gravitational waves from binary inspiral”. In: *Phys. Rev.* D63 (2001). [Erratum: *Phys. Rev.* D72,029902(2005)], p. 044023. DOI: 10.1103/PhysRevD.63.044023, 10.1103/PhysRevD.72.029902. arXiv: gr-qc/0010009 [gr-qc].
- [331] A. Buonanno et al. “Comparison of post-Newtonian templates for compact binary inspiral signals in gravitational-wave detectors”. In: *Phys.Rev.* D80 (2009), p. 084043. DOI: 10.1103/PhysRevD.80.084043. arXiv: 0907.0700 [gr-qc].
- [332] R. Gamba, S. Bernuzzi, and A. Nagar. “Fast, faithful, frequency-domain effective-one-body waveforms for compact binary coalescences”. In: *Phys. Rev. D* 104.8 (2021), p. 084058. DOI: 10.1103/PhysRevD.104.084058. arXiv: 2012.00027 [gr-qc].
- [333] J. Tissino et al. “Combining effective-one-body accuracy and reduced-order-quadrature speed for binary neutron star merger parameter estimation with machine learning”. In: (Oct. 2022). arXiv: 2210.15684 [gr-qc].
- [334] S. Hild et al. “Sensitivity Studies for Third-Generation Gravitational Wave Observatories”. In: *Class. Quant. Grav.* 28 (2011), p. 094013. DOI: 10.1088/0264-9381/28/9/094013. arXiv: 1012.0908 [gr-qc].
- [335] *Updated Advanced LIGO sensitivity design curve.* <https://dcc.ligo.org/LIGO-T1800044/public>.
- [336] T. Damour et al. “Energy versus Angular Momentum in Black Hole Binaries”. In: *Phys.Rev.Lett.* 108 (2012), p. 131101. DOI: 10.1103/PhysRevLett.108.131101. arXiv: 1110.2938 [gr-qc].
- [337] A. Nagar et al. “Energetics and phasing of nonprecessing spinning coalescing black hole binaries”. In: *Phys. Rev.* D93.4 (2016), p. 044046. DOI: 10.1103/PhysRevD.93.044046. arXiv: 1506.08457 [gr-qc].
- [338] S. Ossokine et al. “Assessing the Energetics of Spinning Binary Black Hole Systems”. In: *Phys. Rev.* D98.10 (2018), p. 104057. DOI: 10.1103/PhysRevD.98.104057. arXiv: 1712.06533 [gr-qc].

- [339] A. V. Tutukov and L. R. YungelSon. “The merger rate of neutron star and black hole binaries”. In: *Monthly Notices of the Royal Astronomical Society* 260.3 (Feb. 1993), pp. 675–678. ISSN: 0035-8711. DOI: 10.1093/mnras/260.3.675. eprint: <https://academic.oup.com/mnras/article-pdf/260/3/675/3837145/mnras260-0675.pdf>. URL: <https://doi.org/10.1093/mnras/260.3.675>.
- [340] V. Kalogera. “Spin orbit misalignment in close binaries with two compact objects”. In: *Astrophys. J.* 541 (2000), pp. 319–328. DOI: 10.1086/309400. arXiv: astro-ph/9911417.
- [341] K. Belczynski et al. “Evolutionary roads leading to low effective spins, high black hole masses, and O1/O2 rates for LIGO/Virgo binary black holes”. In: *Astron. Astrophys.* 636 (2020), A104. DOI: 10.1051/0004-6361/201936528. arXiv: 1706.07053 [astro-ph.HE].
- [342] S. Stevenson et al. “Formation of the first three gravitational-wave observations through isolated binary evolution”. In: *Nature Commun.* 8 (2017), p. 14906. DOI: 10.1038/ncomms14906. arXiv: 1704.01352 [astro-ph.HE].
- [343] M. Zaldarriaga, D. Kushnir, and J. A. Kollmeier. “The expected spins of gravitational wave sources with isolated field binary progenitors”. In: *Mon. Not. Roy. Astron. Soc.* 473.3 (2018), pp. 4174–4178. DOI: 10.1093/mnras/stx2577. arXiv: 1702.00885 [astro-ph.HE].
- [344] D. Gerosa et al. “Spin orientations of merging black holes formed from the evolution of stellar binaries”. In: *Phys. Rev. D* 98.8 (2018), p. 084036. DOI: 10.1103/PhysRevD.98.084036. arXiv: 1808.02491 [astro-ph.HE].
- [345] S. F. Portegies Zwart and S. L. W. McMillan. “The Runaway growth of intermediate-mass black holes in dense star clusters”. In: *Astrophys. J.* 576 (2002), pp. 899–907. DOI: 10.1086/341798. arXiv: astro-ph/0201055.
- [346] F. Antonini and F. A. Rasio. “Merging black hole binaries in galactic nuclei: implications for advanced-LIGO detections”. In: *Astrophys. J.* 831.2 (2016), p. 187. DOI: 10.3847/0004-637X/831/2/187. arXiv: 1606.04889 [astro-ph.HE].
- [347] C. L. Rodriguez et al. “Black holes: The next generation—repeated mergers in dense star clusters and their gravitational-wave properties”. In: *Phys. Rev. D* 100.4 (2019), p. 043027. DOI: 10.1103/PhysRevD.100.043027. arXiv: 1906.10260 [astro-ph.HE].

- [348] D. Gerosa and M. Fishbach. “Hierarchical mergers of stellar-mass black holes and their gravitational-wave signatures”. In: *Nature Astron.* 5.8 (2021), pp. 749–760. DOI: 10.1038/s41550-021-01398-w. arXiv: 2105.03439 [astro-ph.HE].
- [349] Y. Pan et al. “Inspirational-merger-ringdown multipolar waveforms of nonspinning black-hole binaries using the effective-one-body formalism”. In: *Phys.Rev.* D84 (2011), p. 124052. DOI: 10.1103/PhysRevD.84.124052. arXiv: 1106.1021 [gr-qc].
- [350] P. Ajith. “Addressing the spin question in gravitational-wave searches: Waveform templates for inspiralling compact binaries with nonprecessing spins”. In: *Phys.Rev.* D84 (2011), p. 084037. DOI: 10.1103/PhysRevD.84.084037. arXiv: 1107.1267 [gr-qc].
- [351] E. Racine. “Analysis of spin precession in binary black hole systems including quadrupole-monopole interaction”. In: *Phys. Rev.* D78 (2008), p. 044021. DOI: 10.1103/PhysRevD.78.044021. arXiv: 0803.1820 [gr-qc].
- [352] T. A. Apostolatos et al. “Spin induced orbital precession and its modulation of the gravitational wave forms from merging binaries”. In: *Phys. Rev.* D49 (1994), pp. 6274–6297. DOI: 10.1103/PhysRevD.49.6274.
- [353] P. Schmidt et al. “Tracking the precession of compact binaries from their gravitational-wave signal”. In: *Phys. Rev.* D84 (2011), p. 024046. DOI: 10.1103/PhysRevD.84.024046. arXiv: 1012.2879 [gr-qc].
- [354] P. Schmidt, M. Hannam, and S. Husa. “Towards models of gravitational waveforms from generic binaries: A simple approximate mapping between precessing and non-precessing inspiral signals”. In: *Phys. Rev.* D86 (2012), p. 104063. DOI: 10.1103/PhysRevD.86.104063. arXiv: 1207.3088 [gr-qc].
- [355] M. Boyle, R. Owen, and H. P. Pfeiffer. “A geometric approach to the precession of compact binaries”. In: *Phys. Rev.* D84 (2011), p. 124011. DOI: 10.1103/PhysRevD.84.124011. arXiv: 1110.2965 [gr-qc].
- [356] R. O’Shaughnessy et al. “Efficient asymptotic frame selection for binary black hole spacetimes using asymptotic radiation”. In: *Phys. Rev.* D84 (2011), p. 124002. DOI: 10.1103/PhysRevD.84.124002. arXiv: 1109.5224 [gr-qc].

- [357] A. Buonanno, Y.-b. Chen, and M. Vallisneri. “Detecting gravitational waves from precessing binaries of spinning compact objects: Adiabatic limit”. In: *Phys. Rev. D* 67 (2003). [Erratum: *Phys. Rev. D* 74,029904(2006)], p. 104025. DOI: 10.1103/PhysRevD.67.104025, 10.1103/PhysRevD.74.029904. arXiv: gr-qc/0211087 [gr-qc].
- [358] L. Gualtieri et al. “Transformation of the multipolar components of gravitational radiation under rotations and boosts”. In: *Phys. Rev. D* 78 (2008), p. 044024. DOI: 10.1103/PhysRevD.78.044024. arXiv: 0805.1017 [gr-qc].
- [359] Y. Pan et al. “Inspirals-merger-ringdown waveforms of spinning, precessing black-hole binaries in the effective-one-body formalism”. In: *Phys. Rev. D* 89 (2014), p. 084006. DOI: 10.1103/PhysRevD.89.084006. arXiv: 1307.6232 [gr-qc].
- [360] K. Chatziioannou et al. “Gravitational Waveforms for Precessing, Quasicircular Compact Binaries with Multiple Scale Analysis: Small Spin Expansion”. In: *Phys. Rev. D* 88.6 (2013), p. 063011. DOI: 10.1103/PhysRevD.88.063011. arXiv: 1307.4418 [gr-qc].
- [361] Y. Pan et al. “Stability of nonspinning effective-one-body model in approximating two-body dynamics and gravitational-wave emission”. In: *Phys. Rev. D* 89 (2014), p. 061501. DOI: 10.1103/PhysRevD.89.061501. arXiv: 1311.2565 [gr-qc].
- [362] V. Varma et al. “High-accuracy mass, spin, and recoil predictions of generic black-hole merger remnants”. In: *Phys. Rev. Lett.* 122.1 (2019), p. 011101. DOI: 10.1103/PhysRevLett.122.011101. arXiv: 1809.09125 [gr-qc].
- [363] R. O’Shaughnessy et al. “Precession during merger: Strong polarization changes are observationally accessible features of strong-field gravity during binary black hole merger”. In: *Phys. Rev. D* 87.4 (2013), p. 044038. DOI: 10.1103/PhysRevD.87.044038. arXiv: 1209.3712 [gr-qc].
- [364] B. Zackay, L. Dai, and T. Venumadhav. “Relative Binning and Fast Likelihood Evaluation for Gravitational Wave Parameter Estimation”. In: (June 2018). arXiv: 1806.08792 [astro-ph.IM].
- [365] S. Vinciguerra, J. Veitch, and I. Mandel. “Accelerating gravitational wave parameter estimation with multi-band template interpolation”. In: *Class. Quant. Grav.* 34.11 (2017), p. 115006. DOI: 10.1088/1361-6382/aa6d44. arXiv: 1703.02062 [gr-qc].

- [366] I. Harry et al. “Searching for Gravitational Waves from Compact Binaries with Precessing Spins”. In: *Phys. Rev. D* 94.2 (2016), p. 024012. DOI: 10.1103/PhysRevD.94.024012. arXiv: 1603.02444 [gr-qc].
- [367] *SXS collaboration catalog tools*. https://github.com/sxs-collaboration/catalog_tools.
- [368] P. Schmidt, I. W. Harry, and H. P. Pfeiffer. “Numerical Relativity Injection Infrastructure”. In: (Mar. 2017). arXiv: 1703.01076 [gr-qc].
- [369] B. P. Abbott et al. “Properties of the binary neutron star merger GW170817”. In: *Phys. Rev. X* 9.1 (2019), p. 011001. DOI: 10.1103/PhysRevX.9.011001. arXiv: 1805.11579 [gr-qc].
- [370] B. P. Abbott et al. “Properties of the Binary Black Hole Merger GW150914”. In: *Phys. Rev. Lett.* 116.24 (2016), p. 241102. DOI: 10.1103/PhysRevLett.116.241102. arXiv: 1602.03840 [gr-qc].
- [371] T. Islam et al. “Improved analysis of GW190412 with a precessing numerical relativity surrogate waveform model”. In: *Phys. Rev. D* 103.10 (2021), p. 104027. DOI: 10.1103/PhysRevD.103.104027. arXiv: 2010.04848 [gr-qc].
- [372] M. Colleoni et al. “Towards the routine use of subdominant harmonics in gravitational-wave inference: Reanalysis of GW190412 with generation X waveform models”. In: *Phys. Rev. D* 103.2 (2021), p. 024029. DOI: 10.1103/PhysRevD.103.024029. arXiv: 2010.05830 [gr-qc].
- [373] J. W. T. Hessels et al. “A radio pulsar spinning at 716-hz”. In: *Science* 311 (2006), pp. 1901–1904. DOI: 10.1126/science.1123430. arXiv: astro-ph/0601337 [astro-ph].
- [374] M. Kramer and N. Wex. “The double pulsar system: A unique laboratory for gravity”. In: *Class. Quant. Grav.* 26 (2009), p. 073001. DOI: 10.1088/0264-9381/26/7/073001.
- [375] K. Stovall et al. “PALFA Discovery of a Highly Relativistic Double Neutron Star Binary”. In: *Astrophys. J.* 854.2 (2018), p. L22. DOI: 10.3847/2041-8213/aaad06. arXiv: 1802.01707 [astro-ph.HE].
- [376] L. Wade et al. “Systematic and statistical errors in a bayesian approach to the estimation of the neutron-star equation of state using advanced gravitational wave detectors”. In: *Phys. Rev. D* 89.10 (2014), p. 103012. DOI: 10.1103/PhysRevD.89.103012. arXiv: 1402.5156 [gr-qc].

- [377] A. Rasskazov and B. Kocsis. “The rate of stellar mass black hole scattering in galactic nuclei”. In: *Astrophys. J.* 881 (2019), p. 20. DOI: 10.3847/1538-4357/ab2c74. arXiv: 1902.03242 [astro-ph.HE].
- [378] H. Tagawa, Z. Haiman, and B. Kocsis. “Formation and Evolution of Compact Object Binaries in AGN Disks”. In: *Astrophys. J.* 898.1 (2020), p. 25. DOI: 10.3847/1538-4357/ab9b8c. arXiv: 1912.08218 [astro-ph.GA].
- [379] M. Zevin et al. “Eccentric Black Hole Mergers in Dense Star Clusters: The Role of Binary–Binary Encounters”. In: *Astrophys. J.* 871.1 (2019), p. 91. DOI: 10.3847/1538-4357/aaf6ec. arXiv: 1810.00901 [astro-ph.HE].
- [380] J. Samsing and D. J. D’Orazio. “Black Hole Mergers From Globular Clusters Observable by LISA I: Eccentric Sources Originating From Relativistic N -body Dynamics”. In: *Mon. Not. Roy. Astron. Soc.* 481.4 (2018), pp. 5445–5450. DOI: 10.1093/mnras/sty2334. arXiv: 1804.06519 [astro-ph.HE].
- [381] R. M. O’Leary, B. Kocsis, and A. Loeb. “Gravitational waves from scattering of stellar-mass black holes in galactic nuclei”. In: *Monthly Notices of the Royal Astronomical Society* 395.4 (May 2009), pp. 2127–2146. ISSN: 0035-8711. DOI: 10.1111/j.1365-2966.2009.14653.x. eprint: <https://academic.oup.com/mnras/article-pdf/395/4/2127/2931749/mnras0395-2127.pdf>. URL: <https://doi.org/10.1111/j.1365-2966.2009.14653.x>.
- [382] S. Mukherjee, S. Mitra, and S. Chatterjee. “Detectability of hyperbolic encounters of compact stars with ground-based gravitational waves detectors”. In: (Oct. 2020). arXiv: 2010.00916 [gr-qc].
- [383] M. Punturo et al. “The third generation of gravitational wave observatories and their science reach”. In: *Class. Quant. Grav.* 27 (2010), p. 084007. DOI: 10.1088/0264-9381/27/8/084007.
- [384] P. Amaro-Seoane. “Detecting Intermediate-Mass Ratio Inspirals From The Ground And Space”. In: *Phys. Rev. D* 98.6 (2018), p. 063018. DOI: 10.1103/PhysRevD.98.063018. arXiv: 1807.03824 [astro-ph.HE].
- [385] W. E. East et al. “Observing complete gravitational wave signals from dynamical capture binaries”. In: *Phys. Rev.* D87.4 (2013), p. 043004. DOI: 10.1103/PhysRevD.87.043004. arXiv: 1212.0837 [gr-qc].
- [386] N. Loutrel. “Repeated Bursts: Gravitational Waves from Highly Eccentric Binaries”. In: (Sept. 2020). arXiv: 2009.11332 [gr-qc].

- [387] R. Gold and B. Brügmann. “Eccentric black hole mergers and zoom-whirl behavior from elliptic inspirals to hyperbolic encounters”. In: *Phys. Rev. D* 88.6 (2013), p. 064051. DOI: 10.1103/PhysRevD.88.064051. arXiv: 1209.4085 [gr-qc].
- [388] P. E. Nelson et al. “Induced Spins from Scattering Experiments of Initially Nonspinning Black Holes”. In: *Phys. Rev. D* 100.12 (2019), p. 124045. DOI: 10.1103/PhysRevD.100.124045. arXiv: 1909.08621 [gr-qc].
- [389] Y.-B. Bae, H. M. Lee, and G. Kang. “Gravitational Wave Capture in Spinning Black Hole Encounters”. In: *Astrophys. J.* 900.2 (2020), p. 175. DOI: 10.3847/1538-4357/aba82b. arXiv: 2007.14019 [gr-qc].
- [390] T. Damour et al. “Strong-Field Scattering of Two Black Holes: Numerics Versus Analytics”. In: *Phys. Rev. D* 89.8 (2014), p. 081503. DOI: 10.1103/PhysRevD.89.081503. arXiv: 1402.7307 [gr-qc].
- [391] J. Healy and C. O. Lousto. “Fourth RIT binary black hole simulations catalog: Extension to eccentric orbits”. In: *Phys. Rev. D* 105.12 (2022), p. 124010. DOI: 10.1103/PhysRevD.105.124010. arXiv: 2202.00018 [gr-qc].
- [392] D. Bini and T. Damour. “Gravitational radiation reaction along general orbits in the effective one-body formalism”. In: *Phys. Rev. D* 86 (2012), p. 124012. DOI: 10.1103/PhysRevD.86.124012. arXiv: 1210.2834 [gr-qc].
- [393] F. Pretorius and D. Khurana. “Black hole mergers and unstable circular orbits”. In: *Class. Quant. Grav.* 24 (2007), S83–S108. DOI: 10.1088/0264-9381/24/12/S07. arXiv: gr-qc/0702084 [GR-QC].
- [394] J. Healy, J. Levin, and D. Shoemaker. “Zoom-Whirl Orbits in Black Hole Binaries”. In: *Phys. Rev. Lett.* 103 (2009), p. 131101. DOI: 10.1103/PhysRevLett.103.131101. arXiv: 0907.0671 [gr-qc].
- [395] U. Sperhake et al. “Cross section, final spin and zoom-whirl behavior in high-energy black hole collisions”. In: *Phys. Rev. Lett.* 103 (2009), p. 131102. DOI: 10.1103/PhysRevLett.103.131102. arXiv: 0907.1252 [gr-qc].
- [396] S. Hopper, A. Nagar, and P. Rettengo. “Strong-field scattering of two spinning black holes: Numerics versus Analytics”. In: (Apr. 2022). arXiv: 2204.10299 [gr-qc].

- [397] A. Placidi et al. “Exploiting Newton-factorized, 2PN-accurate waveform multipoles in effective-one-body models for spin-aligned noncircularized binaries”. In: *Phys. Rev. D* 105.10 (2022), p. 104030. DOI: 10.1103/PhysRevD.105.104030. arXiv: 2112.05448 [gr-qc].
- [398] S. Albanesi et al. “New avenue for accurate analytical waveforms and fluxes for eccentric compact binaries”. In: *Phys. Rev. D* 105.12 (2022), p. L121503. DOI: 10.1103/PhysRevD.105.L121503. arXiv: 2203.16286 [gr-qc].
- [399] J. C. Bustillo et al. “GW190521 as a Merger of Proca Stars: A Potential New Vector Boson of 8.7×10^{-13} eV”. In: *Phys. Rev. Lett.* 126.8 (2021), p. 081101. DOI: 10.1103/PhysRevLett.126.081101. arXiv: 2009.05376 [gr-qc].
- [400] C. L. Rodriguez et al. “Post-Newtonian Dynamics in Dense Star Clusters: Formation, Masses, and Merger Rates of Highly-Eccentric Black Hole Binaries”. In: *Phys. Rev. D* 98.12 (2018), p. 123005. DOI: 10.1103/PhysRevD.98.123005. arXiv: 1811.04926 [astro-ph.HE].
- [401] I. Mandel and F. S. Broekgaarden. “Rates of Compact Object Coalescences”. In: (July 2021). arXiv: 2107.14239 [astro-ph.HE].
- [402] Z. Cao and W.-B. Han. “Waveform model for an eccentric binary black hole based on the effective-one-body-numerical-relativity formalism”. In: *Phys. Rev. D* 96.4 (2017), p. 044028. DOI: 10.1103/PhysRevD.96.044028. arXiv: 1708.00166 [gr-qc].
- [403] N. Aghanim et al. “Planck 2018 results. VI. Cosmological parameters”. In: *Astron. Astrophys.* 641 (2020), A6. DOI: 10.1051/0004-6361/201833910. arXiv: 1807.06209 [astro-ph.CO].
- [404] R. Abbott et al. “Open data from the first and second observing runs of Advanced LIGO and Advanced Virgo”. In: (Dec. 2019). arXiv: 1912.11716 [gr-qc].
- [405] T. Hinderer. “Tidal Love numbers of neutron stars”. In: *Astrophys. J.* 677 (2008), pp. 1216–1220. DOI: 10.1086/533487. arXiv: 0711.2420 [astro-ph].
- [406] T. Binnington and E. Poisson. “Relativistic theory of tidal Love numbers”. In: *Phys. Rev. D* 80 (2009), p. 084018. DOI: 10.1103/PhysRevD.80.084018. arXiv: 0906.1366 [gr-qc].

- [407] T. Damour and A. Nagar. “Relativistic tidal properties of neutron stars”. In: *Phys. Rev. D* 80 (2009), p. 084035. DOI: 10.1103/PhysRevD.80.084035. arXiv: 0906.0096 [gr-qc].
- [408] C. A. Raithel. “Constraints on the Neutron Star Equation of State from GW170817”. In: *Eur. Phys. J. A* 55.5 (2019), p. 80. DOI: 10.1140/epja/i2019-12759-5. arXiv: 1904.10002 [astro-ph.HE].
- [409] C. D. Capano et al. “Stringent constraints on neutron-star radii from multimessenger observations and nuclear theory”. In: *Nature Astron.* 4.6 (2020), pp. 625–632. DOI: 10.1038/s41550-020-1014-6. arXiv: 1908.10352 [astro-ph.HE].
- [410] M. Breschi et al. “Constraints on the Maximum Densities of Neutron Stars from Postmerger Gravitational Waves with Third-Generation Observations”. In: *Phys. Rev. Lett.* 128.16 (2022), p. 161102. DOI: 10.1103/PhysRevLett.128.161102. arXiv: 2110.06957 [gr-qc].
- [411] A. Puecher et al. “Unraveling information about supranuclear-dense matter from the complete binary neutron star coalescence process using future gravitational-wave detector networks”. In: (Oct. 2022). arXiv: 2210.09259 [gr-qc].
- [412] R. Dudi et al. “High-accuracy simulations of highly spinning binary neutron star systems”. In: *Phys. Rev. D* 105.6 (2022), p. 064050. DOI: 10.1103/PhysRevD.105.064050. arXiv: 2108.10429 [gr-qc].
- [413] B. Mikoczi, M. Vasuth, and L. A. Gergely. “Self-interaction spin effects in inspiralling compact binaries”. In: *Phys. Rev. D* 71 (2005), p. 124043. DOI: 10.1103/PhysRevD.71.124043. arXiv: astro-ph/0504538.
- [414] D. Lai. “Resonant oscillations and tidal heating in coalescing binary neutron stars”. In: *Mon. Not. Roy. Astron. Soc.* 270 (1994), p. 611. DOI: 10.1093/mnras/270.3.611. arXiv: astro-ph/9404062 [astro-ph].
- [415] A. Reisenegger. “Multipole moments of stellar oscillation modes”. In: *Astrophys. J.* 432 (1994), p. 296. DOI: 10.1086/174569.
- [416] K. D. Kokkotas and G. Schäfer. “Tidal and tidal resonant effects in coalescing binaries”. In: *Mon. Not. Roy. Astron. Soc.* 275 (1995), p. 301. DOI: 10.1093/mnras/275.2.301. arXiv: gr-qc/9502034 [gr-qc].

- [417] W. C. G. Ho and D. Lai. “Resonant tidal excitations of rotating neutron stars in coalescing binaries”. In: *Mon. Not. Roy. Astron. Soc.* 308 (1999), p. 153. DOI: 10.1046/j.1365-8711.1999.02703.x. arXiv: astro-ph/9812116 [astro-ph].
- [418] T. Dietrich and T. Hinderer. “Comprehensive comparison of numerical relativity and effective-one-body results to inform improvements in waveform models for binary neutron star systems”. In: *Phys. Rev. D* 95.12 (2017), p. 124006. DOI: 10.1103/PhysRevD.95.124006. arXiv: 1702.02053 [gr-qc].
- [419] J. Steinhoff et al. “Spin effects on neutron star fundamental-mode dynamical tides: Phenomenology and comparison to numerical simulations”. In: *Phys. Rev. Res.* 3.3 (2021), p. 033129. DOI: 10.1103/PhysRevResearch.3.033129. arXiv: 2103.06100 [gr-qc].
- [420] T. Venumadhav, A. Zimmerman, and C. M. Hirata. “The stability of tidally deformed neutron stars to three- and four-mode coupling”. In: *Astrophys. J.* 781 (2014), p. 23. DOI: 10.1088/0004-637X/781/1/23. arXiv: 1307.2890 [astro-ph.HE].
- [421] N. N. Weinberg, P. Arras, and J. Burkart. “An instability due to the nonlinear coupling of p-modes to g-modes: Implications for coalescing neutron star binaries”. In: *Astrophys. J.* 769 (2013), p. 121. DOI: 10.1088/0004-637X/769/2/121. arXiv: 1302.2292 [astro-ph.SR].
- [422] N. N. Weinberg. “Growth rate of the tidal p-mode g-mode instability in coalescing binary neutron stars”. In: *Astrophys. J.* 819.2 (2016), p. 109. DOI: 10.3847/0004-637X/819/2/109. arXiv: 1509.06975 [astro-ph.SR].
- [423] A. Reisenegger and P. Goldreich. “Excitation of Neutron Star Normal Modes during Binary Inspiral”. In: *Astrophys. J.* 426 (May 1994), p. 688. DOI: 10.1086/174105.
- [424] B. Mashhoon. “Tidal Gravitational Radiation”. In: *Astrophys. J.* 185 (Oct. 1973), pp. 83–86. DOI: 10.1086/152397.
- [425] B. Mashhoon. “On tidal phenomena in a strong gravitational field.” In: *Astrophys. J.* 197 (May 1975), pp. 705–716. DOI: 10.1086/153560.
- [426] B. Mashhoon. “Tidal radiation.” In: *Astrophys. J.* 216 (Sept. 1977), pp. 591–609. DOI: 10.1086/155500.

- [427] M. Turner. “Tidal generation of gravitational waves from orbiting Newtonian stars. I - General formalism”. In: *Astrophys. J.* 216 (Sept. 1977), pp. 914–929. DOI: 10.1086/155536.
- [428] S. Bernuzzi et al. “Quasi-universal properties of neutron star mergers”. In: *Phys.Rev.Lett.* 112 (2014), p. 201101. DOI: 10.1103/PhysRevLett.112.201101. arXiv: 1402.6244 [gr-qc].
- [429] S. Bernuzzi, T. Dietrich, and A. Nagar. “Modeling the complete gravitational wave spectrum of neutron star mergers”. In: *Phys. Rev. Lett.* 115 (2015), p. 091101. DOI: 10.1103/PhysRevLett.115.091101. arXiv: 1504.01764 [gr-qc].
- [430] W. E. East, F. Pretorius, and B. C. Stephens. “Eccentric black hole-neutron star mergers: effects of black hole spin and equation of state”. In: *Phys.Rev. D* 85 (2012), p. 124009. DOI: 10.1103/PhysRevD.85.124009. arXiv: 1111.3055 [astro-ph.HE].
- [431] R. Gold et al. “Eccentric binary neutron star mergers”. In: *Phys.Rev. D* 86 (2012), p. 121501. DOI: 10.1103/PhysRevD.86.121501. arXiv: 1109.5128 [gr-qc].
- [432] S. V. Chaurasia et al. “Gravitational waves and mass ejecta from binary neutron star mergers: Effect of large eccentricities”. In: *Phys. Rev. D* 98.10 (2018), p. 104005. DOI: 10.1103/PhysRevD.98.104005. arXiv: 1807.06857 [gr-qc].
- [433] G. Pratten, P. Schmidt, and T. Hinderer. “Gravitational-Wave Asteroseismology with Fundamental Modes from Compact Binary Inspirals”. In: *Nature Commun.* 11.1 (2020), p. 2553. DOI: 10.1038/s41467-020-15984-5. arXiv: 1905.00817 [gr-qc].
- [434] S. Ma, H. Yu, and Y. Chen. “Excitation of f-modes during mergers of spinning binary neutron star”. In: *Phys. Rev. D* 101.12 (2020), p. 123020. DOI: 10.1103/PhysRevD.101.123020. arXiv: 2003.02373 [gr-qc].
- [435] G. Pratten, P. Schmidt, and N. Williams. “Impact of Dynamical Tides on the Reconstruction of the Neutron Star Equation of State”. In: (Sept. 2021). arXiv: 2109.07566 [astro-ph.HE].
- [436] B. Carter and J. P. Luminet. “Mechanics of the affine star model”. In: *Mon. Not. Roy. Astron. Soc.* 212 (Jan. 1985), pp. 23–55. DOI: 10.1093/mnras/212.1.23.

- [437] J. P. Luminet and J. A. Marck. “Tidal squeezing of stars by Schwarzschild black holes”. In: *Mon. Not. Roy. Astron. Soc.* 212 (Jan. 1985), pp. 57–75. DOI: 10.1093/mnras/212.1.57.
- [438] P. Wiggins and D. Lai. “Tidal interaction between a fluid star and a Kerr black hole: Relativistic Roche-Riemann model”. In: *Astrophys. J.* 532 (2000), p. 530. DOI: 10.1086/308565. arXiv: astro-ph/9907365.
- [439] V. Ferrari, L. Gualtieri, and F. Pannarale. “A Semi-relativistic Model for Tidal Interactions in BH-NS Coalescing Binaries”. In: *Class. Quant. Grav.* 26 (2009), p. 125004. DOI: 10.1088/0264-9381/26/12/125004. arXiv: 0801.2911 [astro-ph].
- [440] V. Ferrari, L. Gualtieri, and A. Maselli. “Tidal interaction in compact binaries: a post-Newtonian affine framework”. In: *Phys. Rev. D* 85 (2012), p. 044045. DOI: 10.1103/PhysRevD.85.044045. arXiv: 1111.6607 [gr-qc].
- [441] S. Bernuzzi et al. “Mergers of binary neutron stars with realistic spin”. In: *Phys. Rev. D* 89 (2014), p. 104021. DOI: 10.1103/PhysRevD.89.104021. arXiv: 1311.4443 [gr-qc].
- [442] D. Bini and T. Damour. “Gravitational self-force corrections to two-body tidal interactions and the effective one-body formalism”. In: *Phys. Rev. D* 90.12 (2014), p. 124037. DOI: 10.1103/PhysRevD.90.124037. arXiv: 1409.6933 [gr-qc].
- [443] T. Dietrich et al. “Numerical Relativity Simulations of Precessing Binary Neutron Star Mergers”. In: *Phys. Rev. D* 97.6 (2018), p. 064002. DOI: 10.1103/PhysRevD.97.064002. arXiv: 1712.02992 [gr-qc].
- [444] S. Bernuzzi, M. Thierfelder, and B. Brügmann. “Accuracy of numerical relativity waveforms from binary neutron star mergers and their comparison with post-Newtonian waveforms”. In: *Phys. Rev. D* 85 (2012), p. 104030. DOI: 10.1103/PhysRevD.85.104030. arXiv: 1109.3611 [gr-qc].
- [445] W. Tichy. “Constructing quasi-equilibrium initial data for binary neutron stars with arbitrary spins”. In: *Phys. Rev. D* 86 (2012), p. 064024. DOI: 10.1103/PhysRevD.86.064024. arXiv: 1209.5336 [gr-qc].
- [446] M. Boyle. “Transformations of asymptotic gravitational-wave data”. In: *Phys. Rev. D* 93.8 (2016), p. 084031. DOI: 10.1103/PhysRevD.93.084031. arXiv: 1509.00862 [gr-qc].

- [447] H. Yang et al. “Evolution of Highly Eccentric Binary Neutron Stars Including Tidal Effects”. In: *Phys. Rev. D* 98.4 (2018), p. 044007. DOI: 10.1103/PhysRevD.98.044007. arXiv: 1806.00158 [gr-qc].
- [448] A. Parisi and R. Sturani. “Gravitational waves from neutron star excitations in a binary inspiral”. In: *Phys. Rev. D* 97.4 (2018), p. 043015. DOI: 10.1103/PhysRevD.97.043015. arXiv: 1705.04751 [gr-qc].
- [449] T. K. Chan et al. “Multipolar universal relations between f-mode frequency and tidal deformability of compact stars”. In: *Phys. Rev. D* 90.12 (2014), p. 124023. DOI: 10.1103/PhysRevD.90.124023. arXiv: 1408.3789 [gr-qc].
- [450] P. Schmidt and T. Hinderer. “Frequency domain model of f -mode dynamic tides in gravitational waveforms from compact binary inspirals”. In: *Phys. Rev. D* 100.2 (2019), p. 021501. DOI: 10.1103/PhysRevD.100.021501. arXiv: 1905.00818 [gr-qc].
- [451] N. Williams, G. Pratten, and P. Schmidt. “Prospects for distinguishing dynamical tides in inspiralling binary neutron stars with third generation gravitational-wave detectors”. In: *Phys. Rev. D* 105.12 (2022), p. 123032. DOI: 10.1103/PhysRevD.105.123032. arXiv: 2203.00623 [astro-ph.HE].
- [452] D. A. Godzieba and D. Radice. “High-Order Multipole and Binary Love Number Universal Relations”. In: *Universe* 7.10 (2021), p. 368. DOI: 10.3390/universe7100368. arXiv: 2109.01159 [astro-ph.HE].
- [453] Y. Pan et al. “Post-Newtonian factorized multipolar waveforms for spinning, non-precessing black-hole binaries”. In: *Phys. Rev. D* 83 (2011), p. 064003. DOI: 10.1103/PhysRevD.83.064003. arXiv: 1006.0431 [gr-qc].
- [454] A. Nagar et al. “Factorization and resummation: A new paradigm to improve gravitational wave amplitudes. III: the spinning test-body terms”. In: *Phys. Rev. D* 100.10 (2019), p. 104056. DOI: 10.1103/PhysRevD.100.104056. arXiv: 1907.12233 [gr-qc].
- [455] K. Yagi. “Multipole Love Relations”. In: *Phys. Rev. D* 89.4 (2014), p. 043011. DOI: 10.1103/PhysRevD.89.043011. arXiv: 1311.0872 [gr-qc].
- [456] M. Breschi et al. “Kilohertz Gravitational Waves From Binary Neutron Star Mergers: Numerical-relativity Informed Postmerger Model”. In: (May 2022). arXiv: 2205.09112 [gr-qc].

- [457] J.-L. Guermond and R. Pasquetti. “Entropy-based nonlinear viscosity for Fourier approximations of conservation laws”. In: *Comptes Rendus Mathematique* 346.13 (2008), pp. 801–806. ISSN: 1631-073X. DOI: <https://doi.org/10.1016/j.crma.2008.05.013>. URL: <https://www.sciencedirect.com/science/article/pii/S1631073X08001702>.
- [458] F. Guercilena, D. Radice, and L. Rezzolla. “Entropy-limited hydrodynamics: a novel approach to relativistic hydrodynamics”. In: *Comput. Astrophys. Cosmol.* 4 (2017), p. 3. DOI: 10.1186/s40668-017-0022-0. arXiv: 1612.06251 [gr-qc].
- [459] G. Doulis et al. “Entropy-limited higher-order central scheme for neutron star merger simulations”. In: *Phys. Rev. D* 106.2 (2022), p. 024001. DOI: 10.1103/PhysRevD.106.024001. arXiv: 2202.08839 [gr-qc].
- [460] W. Tichy. “Initial data for binary neutron stars with arbitrary spins”. In: *Phys. Rev. D* 84 (2011), p. 024041. DOI: 10.1103/PhysRevD.84.024041. arXiv: 1107.1440 [gr-qc].
- [461] W. Tichy et al. “Constructing Binary Neutron Star Initial Data with High Spins, High Compactness, and High Mass-Ratios”. In: *Phys. Rev. D* 100.12 (2019), p. 124046. DOI: 10.1103/PhysRevD.100.124046. arXiv: 1910.09690 [gr-qc].
- [462] N. Moldenhauer et al. “Initial data for binary neutron stars with adjustable eccentricity”. In: *Phys. Rev. D* 90.8 (2014), p. 084043. DOI: 10.1103/PhysRevD.90.084043. arXiv: 1408.4136 [gr-qc].
- [463] T. Dietrich et al. “Binary Neutron Stars with Generic Spin, Eccentricity, Mass ratio, and Compactness - Quasi-equilibrium Sequences and First Evolutions”. In: *Phys. Rev. D* 92.12 (2015), p. 124007. DOI: 10.1103/PhysRevD.92.124007. arXiv: 1507.07100 [gr-qc].
- [464] B. Brügmann. “Adaptive mesh and geodesically sliced Schwarzschild spacetime in 3+1 dimensions”. In: *Phys. Rev. D* 54 (1996), pp. 7361–7372. DOI: 10.1103/PhysRevD.54.7361. arXiv: gr-qc/9608050.
- [465] S. Bernuzzi and T. Dietrich. “Gravitational waveforms from binary neutron star mergers with high-order weighted-essentially-noscillatory schemes in numerical relativity”. In: *Phys. Rev. D* 94.6 (2016), p. 064062. DOI: 10.1103/PhysRevD.94.064062. arXiv: 1604.07999 [gr-qc].

- [466] K. Kawaguchi et al. “Frequency-domain gravitational waveform models for inspiraling binary neutron stars”. In: *Phys. Rev. D* 97.4 (2018), p. 044044. DOI: 10.1103/PhysRevD.97.044044. arXiv: 1802.06518 [gr-qc].
- [467] T. Dietrich et al. “Matter imprints in waveform models for neutron star binaries: Tidal and self-spin effects”. In: *Phys. Rev. D* 99.2 (2019), p. 024029. DOI: 10.1103/PhysRevD.99.024029. arXiv: 1804.02235 [gr-qc].
- [468] A. Bohé et al. “Quadratic-in-spin effects in the orbital dynamics and gravitational-wave energy flux of compact binaries at the 3PN order”. In: *Class. Quant. Grav.* 32.19 (2015), p. 195010. DOI: 10.1088/0264-9381/32/19/195010. arXiv: 1501.01529 [gr-qc].
- [469] C. K. Mishra et al. “Ready-to-use post-Newtonian gravitational waveforms for binary black holes with nonprecessing spins: An update”. In: *Phys. Rev. D* 93.8 (2016), p. 084054. DOI: 10.1103/PhysRevD.93.084054. arXiv: 1601.05588 [gr-qc].
- [470] K. G. Arun et al. “Higher-order spin effects in the amplitude and phase of gravitational waveforms emitted by inspiraling compact binaries: Ready-to-use gravitational waveforms”. In: *Phys. Rev. D* 79 (2009). [Erratum: *Phys. Rev. D* 84,049901(2011)], p. 104023. DOI: 10.1103/PhysRevD.79.104023, 10.1103/PhysRevD.84.049901. arXiv: 0810.5336 [gr-qc].
- [471] D. Reitze et al. “Cosmic Explorer: The U.S. Contribution to Gravitational-Wave Astronomy beyond LIGO”. In: *Bull. Am. Astron. Soc.* 51 (July 2019), p. 035. arXiv: 1907.04833 [astro-ph.IM].
- [472] B. P. Abbott et al. “Exploring the Sensitivity of Next Generation Gravitational Wave Detectors”. In: *Class. Quant. Grav.* 34.4 (2017), p. 044001. DOI: 10.1088/1361-6382/aa51f4. arXiv: 1607.08697 [astro-ph.IM].
- [473] D. Radice, L. Rezzolla, and F. Galeazzi. “Beyond second-order convergence in simulations of binary neutron stars in full general-relativity”. In: *Mon. Not. Roy. Astron. Soc.* 437 (2014), pp. L46–L50. DOI: 10.1093/mnras1/s1t137. arXiv: 1306.6052 [gr-qc].
- [474] D. Radice, S. Bernuzzi, and C. D. Ott. “One-armed spiral instability in neutron star mergers and its detectability in gravitational waves”. In: *Phys. Rev. D* 94.6 (2016), p. 064011. DOI: 10.1103/PhysRevD.94.064011. arXiv: 1603.05726 [gr-qc].

Bibliography

- [475] T. Dietrich et al. “Gravitational waves and mass ejecta from binary neutron star mergers: Effect of the mass-ratio”. In: *Phys. Rev. D* 95.2 (2017), p. 024029. DOI: 10.1103/PhysRevD.95.024029. arXiv: 1607.06636 [gr-qc].
- [476] A. Nitz et al. *gwastro/pycbc: v2.1.1 release of PyCBC*. Version v.2.1.1. Mar. 2023. DOI: 10.5281/zenodo.7746324. URL: <https://doi.org/10.5281/zenodo.7746324>.

Curriculum Vitae

Personal details

Name Rossella
Surname Gamba
Address Fürstengraben, 07743 Jena, Germany
Email gamba.rossella@gmail.com
Birth date 12.12.1995
Nationality Italian

Education

2019–2022 *Ph.D. in Theoretical Physics*

Friedrich-Schiller-Universität Jena, Theoretisch-Physikalisches Institute, Jena, Germany

SUPERVISOR Prof. Sebastiano Bernuzzi, sebastiano.bernuzzi@uni-jena.de
PROJECT TITLE Gravitational waves from compact binary systems:
 modeling and application

2017–2019 *Master's degree in Theoretical Physics*

University of Torino, Torino, Italy

SUPERVISOR Dr. Alessandro Nagar, alessandro.nagar@gmail.com
PROJECT TITLE Systematic biases in the analysis
 of gravitational wave data of binary neutron stars
GRADUATION October 2019

2014–2017 *Bachelor's degree in Physics*

University of Torino, Torino, Italy

SUPERVISOR Prof. Giovanni Trincherò, giovanni.trincherò@unito.it
PROJECT TITLE On the asymptotic behaviour of likelihood ratio test statistics
GRADUATION October 2017

Achievements

2018 Scholarship for INFN–NSF/LIGO Exchange Summer School
at California State University Fullerton (Fullerton, CA, USA)
MENTOR: Prof. Jocelyn Read, jocelyn.read@ligo.org

Ort, Datum

Unterschrift